UNIVERSITY COLLEGE LONDON

Faculty of Mathematics and Physical Sciences

Department of Physics & Astronomy

ON THE FORMATION, EVOLUTION, AND DESTRUCTION OF MINOR PLANETARY BODIES

Thesis submitted for the Degree of Doctor of Philosophy of the University of London

by

Thomas G. Wilson

Supervisors:

Prof. Jonathan C. Rawlings

Dr. Jay Farihi

Prof. Bruce M. Swinyard

Examiners:

Prof. Geraint Jones

Dr. Steven Parsons

November 4, 2019

To mum.

I, Thomas G. Wilson, confirm that the work presented in this thesis is my own. Where information has been derived from other sources, I confirm that this has been indicated in the thesis.

Abstract

Minor planetary bodies can provide information on the history and future of planetary systems, from formation conditions in the Solar nebula to destruction processes of planets.

Comets have long been heralded as pristine objects from the formation of the Solar System. Indeed, it is possible to infer the nature of the formation conditions of the Solar System by studying comets. In this thesis, an astrochemical model is used to derive potential initial Solar System conditions from *Rosetta* data. Importantly, there is a fundamental question not yet concretely answered: are the observed compositions indicative of formation conditions or evolutionary processes? Isomeric ratios can be useful as they may not vary since formation. However, recent results suggest that the water ortho-to-para ratio cannot be used to trace formation conditions, but may be used to probe cometary comae. This thesis presents *Herschel* observations of four comets and discusses how the observed non-typical water ortho-to-para ratios can help the understanding of evolutionary processes in comets.

In addition to probing the Solar System, studying minor planetary bodies around white dwarfs can reveal the fate of these bodies. The evidence of white dwarf planetary systems have been known for a few decades and is inferred by atmospheric metals or circumstellar dust disks. By searching for destroyed planetesimals via these indicators, planetary system architectures, dynamics, and frequency can be inferred. A study of the largest, unbiased *Spitzer* and *Hubble* survey of white dwarfs to search for evidence of planetary systems is reported. Circumstellar disks have been thought of as static, however recent results have shown flux variations. In this thesis, a study of all white dwarfs debris disks using *Spitzer* and *WISE* data is detailed. Via observations over the longest baseline to date, it is possible to shed light on the destruction processes in these dynamical environments.

Impact Statement

In the work presented in this thesis I have conducted research into all stages of the life of minor planetary bodies. These studies have advanced multiple aspects of planetary science in the Solar System and in exoplanetary systems, and taken as a whole aims to continue a unified thinking of planetary systems regardless of Solar or exoplanetary. The work presented here aims to further our understanding of planetary systems and answer fundamental questions such as "How do planetary systems form and evolve?" that may lead to a better understanding about "What are conditions necessary for an Earth-like planet to form and for life to develop?"

As a part of the study of planetary system and minor planetary body formation a physical and chemical model of the collapse from a molecular cloud to the proto-Solar and protoplanetary disk was developed. I utilised this model to infer the initial conditions of the Solar System and the chemical and physical evolution during the collapse phase via comparison with molecular abundance seen in comet 67P/ChuryumovGerasimenko. This model has the potential to be used by the community for further work aiming to study planetary system formation from cometary observations.

The evolution of minor planetary bodies was investigated via the water isomeric, ortho-to-para, ratio in four Solar System comets. During this project I developed a radiative transfer code, CRETE, to simulate the cometary comae for comparison with the observations. This model has subsequently been published for use by the community for further analysis of volatiles in comets. In this study the lowest cometary ortho-to-para ratios ever seen were determined. These results have provided evidence that this isomeric ratio may not be used to determine comet formation location, but rather could potentially be used to research cometary coma.

On the topic of the destruction of minor planetary bodies I have analysed observations of 236 white dwarfs in order to detect destroyed planetesimals and to determine the unbiased planetary system frequency around single stars and, for the first time, in binary systems. It is possible to infer planetary system architecture and it is shown that in binaries, the companion to the white dwarf is unlikely to be the cause of the gravitational perturbation that eventually leads to the destruction of the planetary body. Furthermore, I conducted analysis of all known planetary debris disks around white dwarfs in order to study variation of the disks that formed from the destroyed planetesimals. For the first time disk colour variation was detected meaning that the temperature or location of the dust is changing. Detailed modelling of this variation could lead to understanding of the structure and evolution of these planetary debris disks.

Outside of academia, research into planetary science are of definite interest to the general public due to the fundamental questions it asks about the nature of planets and life. To stoke this interest, and to inspire the next generation of scientists, I have conducted outreach disseminating these results on multiple occasions to audiences with a broad range of backgrounds.

Acknowledgements

Over the course of the PhD I have been fortunate to work with and be supported by many people both at UCL and the ING. Firstly, I would like to thank Bruce Swinyard for taking me under his wing, teaching me a lot, and providing very good supervision during the limited time we worked together. I'd like to also thank Jonathan Rawlings for his support and encouragement for the length of the PhD, and for his help with the thesis. I want to thank Jay Farihi for providing me with many research and observing opportunities and avenues to explore. Furthermore, I would like to thank Ian Howarth and Serena Viti for many very supportive and invaluable discussions over the course of the PhD that helped greatly in many aspects. Lastly, I'd like to thank Ovidiu Vaduvescu for his involvement and support during my time at the ING, and for inviting me to contribute in the EURONEAR collaboration and the discovery of NEAs.

A considerable thanks goes to Mum for her vast support and encouragement over the decades. A lot of work went into obtaining the PhD both during my time at UCL and the ING, and prior to it, and none of it would have been possible without her support. Thanks also go to my brother and sister for at least listening to me rant on about whatever physics or astrophysics idea had enthused me that week.

While friends come and go, I want to thank all of them for keeping me sane and giving me great memories over the past half a decade and before. Finally, I'd like to thank Ingrid for all her help and support during the final years of the PhD, without which it would have been much more stressful.

One doesn't discover new lands without consenting to lose sight,
for a very long time,
of the shore.

André Paul Guillaume Gide (1925)

Contents

List of Figures

List of Tables

Chapter 1

Introduction

OBSERVATORY, n.

A place where astronomers conjecture away the guesses of their predecessors.

Ambrose Gwinnett Bierce (1911)

Minor planetary bodies in the Solar System have been observed from afar for centuries (Brahe 1603; Halley 1705; Huggins 1868), with detailed fly-by or rendezvous missions probing comets over the last few decades (Reinhard 1986; Brownlee et al. 2003; Taylor et al. 2017). Exoplanetary research, on the other hand, is still a young, albeit rapidly growing, field in comparison. Since the first detected exoplanets over 30 years ago (Wolszczan & Frail 1992; Mayor & Queloz 1995) thousands more have been found with the main focus of the field shifting to characterisation of exoplanet atmospheres, and detection of exomoons and exorings (Mamajek et al. 2012; Teachey & Kipping 2018; Madhusudhan 2019).

Although they can be thought of as disparate fields, the study of the Solar System can yield results that are beneficial for exoplanetary systems, and vice versa. The understanding of Solar System formation and evolution has benefited from the study of exoplanetary systems whereby the wide variety of architectures has led to dynamical models, such as the Grand Tack (Walsh et al. 2011), that aim to explain both the present day architecture of the Solar System and exoplanetary systems (Gomes et al. 2005; Morbidelli et al. 2005; Tsiganis et al. 2005). Conversely, detailed knowledge of the composition of Solar System asteroids, comets, and meteorites has informed studies of destroyed planetary bodies

in white dwarf systems by providing abundance ratios that can be used to interpret the compositions of exoplanetary bodies (Lodders 2003; Xu et al. 2013; Jura & Young 2014). Therefore, the once separate fields of Solar System and exoplanetary research are coming together to answer many questions about the formation, evolution, and destruction of minor planetary bodies.

This thesis presents work probing both the formation and evolution of minor planetary bodies (comets) in the Solar System in Chapters 2 and 3, and the destruction of minor planetary bodies (exoplanetesimals) around white dwarf stars in Chapters 4 and 5. To place this body of work into the broader context of Solar System and exoplanetary research the introduction is divided in two; Section 1.1 outlines current knowledge of Solar System comets and Section 1.2 provides a review of white dwarf exoplanetary systems.

1.1 A Review of Comets and Cometary Volatiles

It is important to first highlight some nomenclature of the types and structure of comet that will be used in this introduction. Comets have three main regions; the nucleus, the coma, and the tail(s). The nucleus is a small, typically on the order of one to 10s of km, rocky and icy body that is composed of refractory and volatile elements. The main constituents of the ice are H_2O, CO, and CO_2 (Bockelée-Morvan & Biver 2017). Upon entering the inner Solar System, these ices are sublimated to form a coma that can extend up to 10^7 km from the nucleus. As the comet travels through the Solar System, dust and ion tails are created and can extend up to several AU (Fulle 2004; Ip 2004).

Dynamically, comets can be split into two main classes; short-period (also known as Jupiter-Family comets) and long-period (also known as Oort-Cloud comets). Short-period comets are periodic with orbits of less than 200 years and are thought to form in the trans-Neptunian region (Dones et al. 2015), whereas long-period comets have longer orbital periods (or may be unbound from the Solar System). Long-period comets were thought to form in between Uranus and Neptune, and subsequently scattered during planetary migration (Dones et al. 2015). However recent observations have suggested that all comets may be formed in the same extended region of the outer Solar System (Brasser & Morbidelli 2013; Altwegg et al. 2015). Regardless of formation location, it is worth noting that short-period comets have undergone substantially more thermal processing since formation than long-period comets due to many more perihelion passes. Historically, comets with orbital

periods similar to comet 1P/Halley (hereafter Halley) are also called Halley-Type comets.

1.1.1 An Introduction to Comet Research

Cometesimals formed out of the Solar nebula in the outer Solar System, beyond the snow line, where volatiles can freeze out. During planet formation these icy bodies either became the building blocks of the giant planets, were ejected from the Solar System, or were gravitationally perturbed into the Oort Cloud and Kuiper Belt regions as comets. As ices in cometary nuclei are believed to have not undergone thermal processing during formation, observations can potentially shed light on the formation conditions of planetary bodies in the outer Solar System and can help constrain models of the Solar nebula. However, the importance of evolutionary effects cannot be ruled out and thus, it is important to determine if the observed cometary features are indicative of the primitive Solar System or from subsequent evolutionary processes.

For almost 70 years the prevailing description of cometary nuclei was that of a "dirty snowball" (Whipple 1950) composed of dust and ices. However, in recent years the picture has significantly changed due to the *Rosetta* spacecraft with the nucleus of comet 67P/Churyumov-Gerasimenko (hereafter 67P) more accurately described as a "snowy dirtball". As comets enter the inner Solar System they are heated by Solar radiation and the ices sublimate. Comet nuclei are not massive and have radii typically on the order of one to 10s of km, therefore the majority of the sublimated ices are not gravitationally bound to the nucleus and expand to form comae and tails. As well as volatiles, sublimation can cause the ejection of refractory dust grains, and conglomerations of ices and dust grains from the nucleus. Rendezvous missions, such as *Rosetta*, *Stardust*, and *Giotto*, can provide direct observations of the nucleus composition, however, the majority of observations are conducted from afar and thus, comet compositions must be inferred from gas in the coma.

Through observations of cometary comae, some broad regions of differing physical and chemical environments have been discovered. In the inner coma there is the "collisional zone" in which gas densities are sufficiently high that chemical reactions are facilitated by collisions. For typical comets, this region is on the order of 1 000 km and the timescale that ejected gases remain in this zone is tens of minutes. Radially exterior to this area is the "radiative zone" where photochemistry processes can alter the observed composition.

Spectroscopic observations of comets provide a wealth of information about cometary comae with gases and dust observed via line and continuum emission respectively. This

introduction and the relevant chapters will focus on the observations and chemistry of gas-phase molecules in cometary comae. For a recent review of cometary dust see Wooden, Ishii & Zolensky (2017). It is worth noting that gas produced via sublimation of nuclei ices are called "parent species", whereas molecules in the coma that are produced via collisional or photochemical processes are called "daughter species".

Comets have been observed spectroscopically in the optical since the 1800s with many daughter molecules seen, whereas in the ultraviolet, infrared, submillimetre, and radio both parent and daughter species are present. For observations of daughter molecules chemical networks and molecular lifetimes must be used to infer parent species. In order to detect all species in a comet they need to be observed across the whole spectrum as molecular structure affects the observable energy levels. For example, molecules with a permanent dipole moment can be observed in the submillimetre and radio, whereas non-dipolar molecules can only be seen through transitions in the infrared, and atomic species can be observed in the ultraviolet. From initial studies it was discovered that the spectra of different comets were similar with the same molecules species present. However, the emission line strengths, and therefore molecular abundances, varied between comets and over heliocentric distance. This discovery prompted the discussion of whether or not there are different classes of comets. The question of; "*can comets be divided into different compositional families?*" directly relates to our understanding of the primordial versus evolutionary nature of the observations of comets. One promising avenue of research is the study of isotopic and isomeric ratios as these values can potentially provide understanding of the formation and evolution. Thus, in order to answer this question detailed observations are needed to understand evolutionary processes and to potentially determine the primordial composition.

In this introduction section, a review of the historical observations of volatiles in cometary comae will be presented in Section 1.1.2. In Section 1.1.3 the current state of knowledge on the chemical composition of comets will be discussed. Section 1.1.4 will cover the recent advancements in water ortho-to-para ratio (OPR) research. Finally, an overview on radiative transfer modelling of cometary comae is given in Section 1.1.5.

1.1.2 Cometary Observations

Due to their small size and albedo, A, typically on the order of one to 10s of km with $A = 0.01 - 0.07$, observations of cometary nuclei from Earth are very challenging. In

order to study the bodies directly spacecraft fly-bys or landings are needed. However, due to their icy nature, comets form comae and tails that can be observed in order to potentially reveal substantial knowledge about the physics and chemistry of a plethora of atoms, molecules, and ions from observations at different wavelengths.

Comets have been observed in the optical since the 1800s resulting in a large number of comets studied in this wavelength range. Fainter comets are more easily observed in the optical than at other wavelengths allowing for comets to be observed at greater heliocentric distances. Gas-phase molecules seen in the optical are typically daughter species of molecules that have undergone photolysis. These are observable due to electronic band emission caused by resonance fluorescence (Feldman et al. 2004). This excitation method is described in more detail along with the radiative transfer model in Section 1.1.5.

Historically, both low- and high-resolution spectroscopy has provided a wealth of knowledge about cometary comae. Low-resolution observations allow for multiple species to be studied simultaneously with hundreds of comets observed in large surveys in the past half a century (Newburn & Spinrad 1984, 1989; Fink & Hicks 1996; Fink 2009; Langland-Shula & Smith 2011; Cochran, Barker & Gray 2012; Hyland, Fitzsimmons & Snodgrass 2019). High-resolution spectra permit detailed research of distinct cometary properties such as specific isotopic ratios (Arpigny et al. 2003; Cochran & Cochran 2001; Manfroid et al. 2005; Capria et al. 2005; Cochran 2008; McKay et al. 2012, 2018; Decock et al. 2015).

It is important to note that spectroscopy at any wavelength, in general, assumes that comae are symmetric in nature, however this is not necessarily the case (Cochran et al. 2012). This has been highlighted in a recent study of comet 67P that has shown that the abundances of H_2O, CO_2, and CO are highly asymmetric (Hässig et al. 2015). Therefore, for comet studies that do not map the composition of the comae, observations can only reveal information about the bulk compositions. While this knowledge can be useful for studying cometary formation conditions, conclusions about physical and chemical conditions of the comae may need to be treated with caution.

Optical and Ultraviolet Observations

Over the decades of optical spectroscopy observations an interesting trend has been noted. Multiple studies have discovered and confirmed that the majority of comets have similar compositions and abundance ratios (A'Hearn & Millis 1980; Newburn & Spinrad 1984; Cochran 1987). However, it was seen that at least a quarter of all comets are depleted

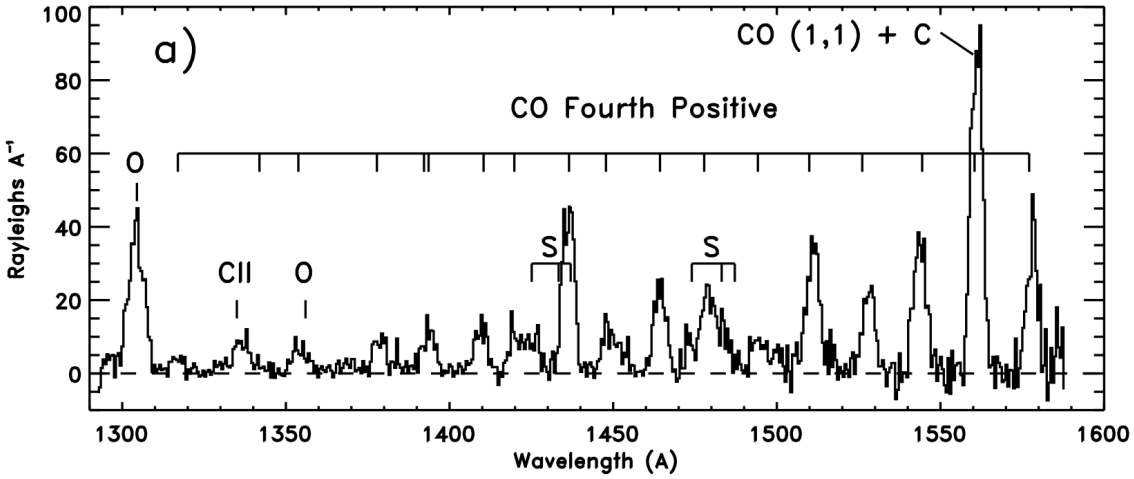

Figure 1.1. Representative UV cometary spectrum. *Hubble Space Telescope* (*HST*) UV spectra of comet C/1996 B2 Hyakutake showing emission features of CO, C, O, and S. This figure is adapted from Weaver (1998), Fig. 6

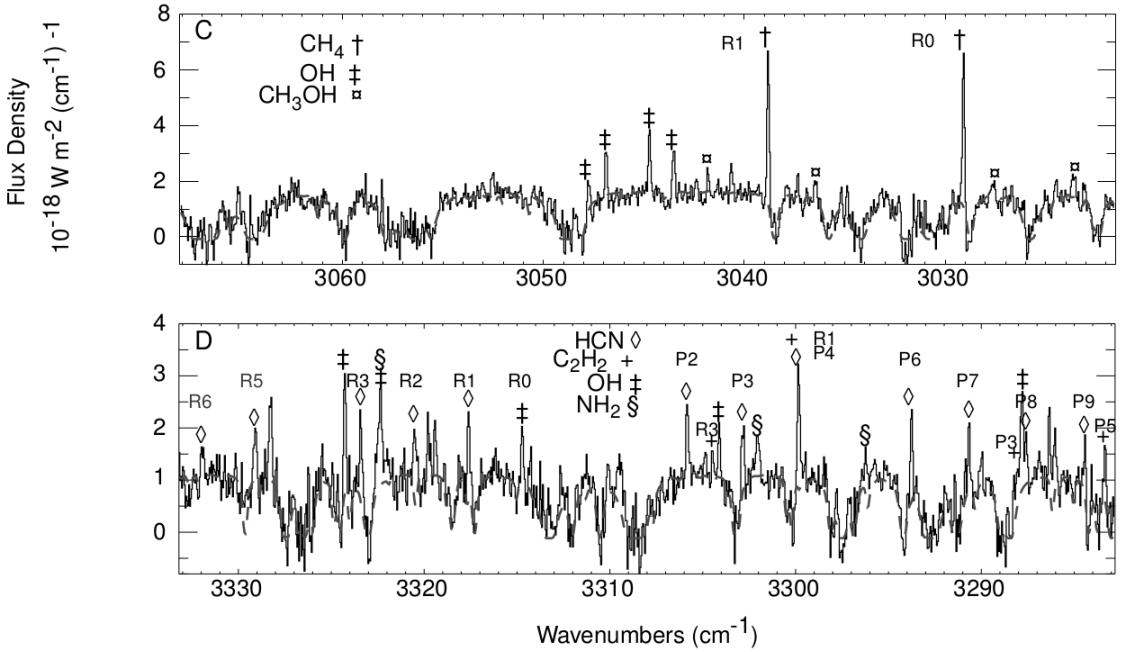

Figure 1.2. Representative IR cometary spectrum. NIRSPEC IR spectra of comet C/1999 H1 (Lee) exhibiting multiple emission lines. This figure is adapted from Mumma et al. (2001), Fig. 3.

in C_2 and C_3 compared to CN (A'Hearn et al. 1995; Fink 2009; Langland-Shula & Smith 2011; Cochran et al. 2012; Schleicher & Bair 2014).

As the Earth's atmosphere is opaque at ultraviolet wavelengths, space-based telescopes are needed to study atomic species in comae. The presence of diatomic molecules, such as H_2, OH, and CS, can be inferred as Solar ultraviolet dissociation of these molecules produces atomic daughter species such as H, O, and C seen via electronic transitions (Feldman et al. 2004). In the ultraviolet the Solar flux is relatively weak and thus, observations of the line emission of parent molecules via the radiative excitation are rare.

Early ultraviolet observations used the *Orbiting Astronomical Observatory* (*OAO*) and the *International Ultraviolet Explorer* (*IUE*) with the main conclusion from these studies being; the composition of all comets is similar (Festou 1998). More recent work has used the *HST* (Meier & A'Hearn 1997; Lupu et al. 2007), the *Far Ultraviolet Spectroscopic Explorer* (*FUSE*; Feldman 2005; Feldman et al. 2009), and the *Galaxy Evolution Explorer* (*GALEX*; Morgenthaler et al. 2009) to expand the number of molecules and atoms observed. Using radiative transfer and collisional models, S and CO abundances relative to water have been determined for tens of comets (Weaver et al. 2011). To illustrate cometary emission features seen in the UV, a *HST* spectrum of comet C/1996 B2 Hyakutake is given in the upper panel of Fig. 1.1, adapted from Weaver (1998), Fig. 6, that shows typical cometary emission lines of CO, C, O, and S.

Infrared Observations

Whilst observations in the optical and radio can probe the physics and chemistry of molecules with a permanent dipole moment, many cometary species are non-dipolar and can only be observed in the infrared via vibrational transitions. These transitions mainly occur via radiative excitation of the fundamental vibrational bands due to Solar flux, with excitation also possible via thermal emission from cometary nuclei or comae dust, and collisions (Crovisier & Encrenaz 1983).

Historically, few comets have been observed in the infrared compared to the optical due to larger telescopes needed to observe faint comets. However, recent work has resulted in infrared spectra of dozens of short- and long-period comets (DiSanti et al. 2013, 2014; Dello Russo et al. 2013, 2016*a*; Radeva et al. 2013; Paganini et al. 2013, 2015; Kawakita et al. 2014; Bonev et al. 2017). Ground-based infrared observations can be difficult due to the limited transparent wavelength regions with most observations taken between $1-5\,\mu$m.

The majority of observed molecules are parent species such as H_2O, NH_3, and HCN, but fragments of these molecules (OH, NH_2, and CN) have also been seen (Mumma et al. 2001; Dello Russo et al. 2016*b*). Radiative transfer models must be developed in order to determine molecular production ratios with a detailed focus on excitation via fluorescence needed (Bockelée-Morvan 1987). CO_2 is typically the second most abundant molecule in comae and cannot be observed from the ground in the infrared. Observations with *AKARI* showed that beyond 3 AU it is the main driver of activity (Ootsubo et al. 2012), whereas interior to this heliocentric distance H_2O becomes the most abundant gas-phase molecule. This is unsurprising as CO_2 is more volatile than H_2O. A NIRSPEC spectrum of comet C/1999 H1 (Lee) is provided in the lower panels of Fig. 1.2, adapted from Mumma et al. (2001), Fig. 3. A plethora of typical cometary emission features, such as OH, HCN, and NH_2, are observed in the IR.

One final area of infrared-based study to note is research into cometary OPRs. This will be discussed in more detail below as it is the focus of one of the main chapters. Briefly, for molecules with symmetric H atoms, it is the ratio of the amount of molecules with aligned hydrogen spins (ortho) to those with opposite spins (para). Importantly, in the gas-phase, nuclear-spin conversion between these two isomers is forbidden due to the large timescales needed for it to occur with photodestruction likely to occur before conversion between the isomers. The H_2O OPR was first determined in comet Halley using the *Kuiper Airborne Observatory* (*KAO*; Mumma, Weaver & Larson 1987) with it thought that this ratio can reveal the formation temperature of comets. However, this idea has been challenged in recent years as will be discussed below.

Radio and Submillimetre Observations

As mentioned previously, molecules with a permanent dipole moment can be detected in the radio and submillimetre via rotational transitions. These transitions are typically caused by collisional excitation via interactions with the dominant gas-phase components of comae, H_2O and electrons, and potentially CO at large heliocentric distances. Radiative excitation of rotational transitions is rare due to weak Solar radiation in the radio, however at large heliocentric distances excitation from the cosmic microwave background can occur.

High-resolution radio and submillimetre spectroscopy have allowed detailed studies of physical conditions in cometary comae, such as gas expansion velocity. However, radio beams are typically larger than the comae and so a symmetric outflow has to be

assumed and only bulk abundances can be inferred. In recent years interferometric observations at Institut de Radio Astronomie Millimetrique (IRAM) and Atacama Large Millimeter/submillimeter Array (ALMA) have permitted mapping of comae (Bockelée-Morvan et al. 2009; Boissier et al. 2012; Cordiner et al. 2014, 2017).

The history of gas-phase cometary studies in the radio can be traced as a series of detections of molecules of increasing complexity. In the 1970s the first observation of the OH radical, a daughter species of H_2O, was seen in comet C/1973 E1 (Kohoutek) using the Nançay radio telescope (Biraud et al. 1974). A decade later comet Halley was studied by five spacecraft and a global observing campaign. OH was detected and mapped by Nançay and the Very Large Array (VLA) (de Pater, Palmer & Snyder 1991; Crovisier et al. 2002), and HCN was observed for the first time in a comet by the IRAM 30 m telescope (Despois et al. 1986). This discovery is important as it began the study of parent molecules in comets using radio spectroscopy.

Comet C/1995 O1 (Hale−Bopp) (hereafter Hale−Bopp) proved to be a landmark comet in cometary research. It was observed over the entire spectrum with over 20 molecules never previously seen in cometary spectra discovered (Biver et al. 2002*a*). These included larger carbon, nitrogen, and sulfur-based molecules such as $HCOOCH_3$, NH_2CHO, and H_2CS, and also allowed for the determinations of the isotopic ratios deuterium/hydrogen (D/H), $^{12}C/^{13}C$, and $^{14}N/^{15}N$ (Biver et al. 1997*a*; Bockelée-Morvan et al. 2000; Crovisier et al. 2004). The water production rate of comet Hale−Bopp was 10 times greater than comet Halley meaning that this comet could be studied at greater heliocentric distances, and over a larger range of distances, that were then analysed to study how the molecular production rates and gas expansion velocity change with heliocentric distance (Biver et al. 2002*a*).

Observations of Water in Comets

While dozens of molecules have been observed from the ground, space-based telescopes are required to observe the rotational lines of water. The ground level, $1_{10}-1_{01}$, transition at 557 GHz was detected for the first time by the *Submillimeter Wave Astronomy Satellite* (*SWAS*) and *Odin* telescopes (Lecacheux et al. 2003; Biver et al. 2007). Furthermore, $H_2^{18}O$ had been observed allowing for the determination of the $^{18}O/^{16}O$ ratio. The larger mirror of the *Herschel Space Observatory* permitted observations of faint comets and weaker transitions, and allowed for the determinations of water isotopic and isomeric ratios (Har-

togh et al. 2010, 2011; Bockelée-Morvan et al. 2012). These will be discussed in detail in Chapter 3. Recently, *Rosetta* has provided detailed observations of H_2O in comet 67P using the Microwave Instrument for the Rosetta Orbiter (MIRO) radio telescope (Gulkis et al. 2015).

Remote observations of comets can provide overarching knowledge on many comets, but in-situ observations can give very detailed information on one or two bodies, and importantly can differentiate between nuclei and comae. In order for cometary science to advance both are necessary. To date there have been several spacecraft rendezvous and fly-by missions, but for the study of volatiles only two have had mass spectrometers capable of analysing gas-phase molecules. The *Giotto* spacecraft flew past comet Halley and obtained the first direct measurement of the abundances of ten parent molecules (Eberhardt 1999). Furthermore, it was shown that there was an extended source of CO and H_2CO in the coma, potential daughter products of CO_2 (Eberhardt et al. 1987; Eberhardt 1999). *Giotto* also provided the first measurement of the cometary water D/H ratio with a value of 3×10^{-4}, twice the terrestrial value, reported (Balsiger et al. 1995; Eberhardt et al. 1995).

Rosetta has considerably advanced cometary science in recent years with the Rosetta Orbiter Spectrometer for Ion and Neutral Analysis (ROSINA; Balsiger et al. 2007) mass spectrometer playing a key role. A variety of molecules have been discovered in comet 67P such as a plethora of complex organic molecules, $HCOOCH_3$, NH_2CHO, and H_2CS, detected for the first time in comets (Altwegg et al. 2015; Hässig et al. 2015; Rubin et al. 2015*b*, 2018; Bieler et al. 2015; Calmonte et al. 2016). Interestingly, the amino acid, glycine, was discovered suggesting that comets could have played a crucial role in the delivery of pre-biotic molecules to Earth (Altwegg et al. 2016).

1.1.3 Chemical Composition of Comets

Due to ground- and space-based observations there is an ever increasing list of molecules discovered in cometary comae and nuclei. Molecular abundances are determined from the derived production rates calculated by the comparison of the observations and a radiative transfer model. Typically, reported abundances are given relative to water and so knowledge of the water production rates are needed. These production rates vary with heliocentric distance (McKay et al. 2015), but usually peak in the range $\sim10^{27}-10^{29}$ molecules per s (typically given as s^{-1}). In general, the abundances of parent species relative to water range from 0.01 to 20 per cent with the more complex molecules typically having lower

abundances (Biver & Bockelée-Morvan 2016). An important result of multiple surveys is that there is a spread in the parent molecule abundances for the entire sample of comets observed (Crovisier et al. 2009; Ootsubo et al. 2012; Biver & Bockelée-Morvan 2016). Understanding any compositional difference is important, because it can potentially help reveal if the observed compositions are indicative of formation conditions or evolutionary processes. It should be noted that a recent study of comet 67P has shown that H_2O and CO_2 abundances seem to vary across the nucleus (Migliorini et al. 2016). This indicates that interpreting the bulk abundances may be more nuanced than previously thought.

Observationally, the abundance of CO has been seen to vary from $\sim 1 - 30$ per cent relative to water (Biver & Bockelée-Morvan 2016), whereas in five comets that were observed in the ultraviolet the CO_2 abundance relative to water differs from 2.5 to 12 per cent (Feldman et al. 1997). Hydrocarbon abundances observed in the infrared also show variation, however the level of diversity decreases with molecular complexity. Relative to water the abundance of CH_4 varies from 0.1 to 1.4 per cent (Gibb et al. 2003), whereas for C_2H_2 and C_2H_6 the abundances vary by less than a factor of two (Mumma et al. 2003).

Compositional diversity is also observed in short- and long-period comets at submillimetre and radio wavelengths. Various carbon and sulfur-bearing molecules have been observed with the abundance of H_2CO relative to water varying from 0.2 to 1.3 per cent and the H_2S to water abundance ratio ranging from 0.4 to 1.5 per cent (Biver et al. 2002*b*).

Compositional Families

As mentioned above, several optical studies have shown that ∼25 per cent of comets exhibit significantly lower C_2/CN and C_3/CN ratios than seen in the majority of comets. Interestingly, multiple studies have discovered a tenuous link between this compositional depletion and dynamical state (A'Hearn et al. 1995; Fink 2009; Cochran et al. 2012). Although both short- and long-period comets were seen to be depleted, a higher percentage of Jupiter-Family comets showed a dearth of C_2 and C_3 compared to long-period comets (Cochran et al. 2012). Recent work has determined that there are six separate classes of depleted comets characterised by the C_2/OH, C_3/OH, and NH/OH ratios, as can be seen in Fig. 1.3, adapted from Schleicher & Bair (2014), Fig. 1. Although the majority of comets (∼70 per cent) exhibit a typical composition (Schleicher & Bair 2014).

These observed abundance ratio differences can provide important information into a fundamental question of comet research; whether the observed composition is due to

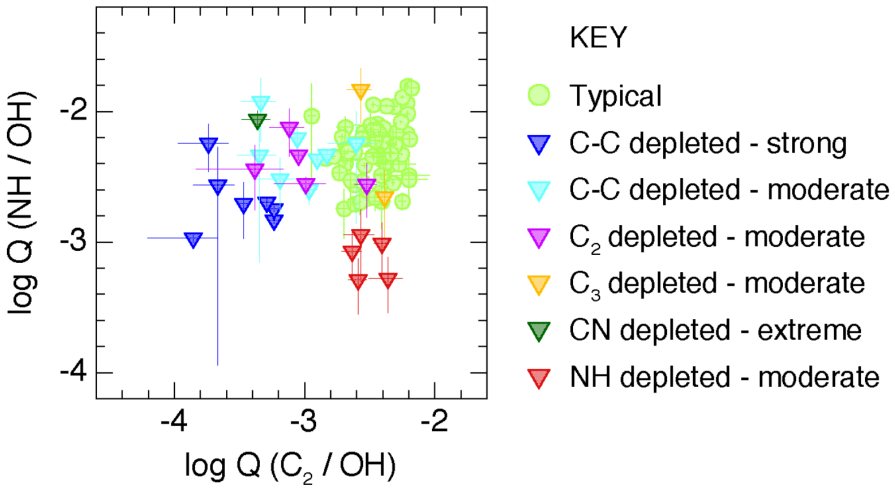

Figure 1.3. A plot of ratios of C_2 and OH production rates against ratios of NH and OH production rates of a sample of comets. Depletion in C_2 and NH compared to the sample of typical composition comets can be seen. This figure is adapted from Schleicher & Bair (2014), Fig. 1.

formation or evolution. One of the best insights into this question was provided by the splitting of comet 73P/Schwassmann-Wachmann 3 (hereafter 73P). Prior to the event, comet 73P was determined to be strongly depleted in C_2 and C_3. It is expected that if the observed depletion is from evolutionary processes that occurred during perihelion passes then the depletion would be only seen at the surface of the nucleus and the comet interior would have a typical composition. Following the splitting, the comet 73P fragments also appeared depleted (Kobayashi et al. 2007; Jehin et al. 2008; Schleicher & Bair 2011), and thus it appears that the lack of C_2 and C_3 compared to CN is from formation.

Three compositional families have been found in the infrared: typical, enriched, and depleted, similar to what is seen in the optical (Mumma & Charnley 2011). However, it is possible that a comet will not exhibit the same compositional type in both optical and infrared spectra (Bonev et al. 2008*b*). From radio observations, no compositional families based on the C_2, C_3, and CN abundances have been found (Crovisier et al. 2009).

It should be noted that whilst almost all molecules have observed composition diversity, there is no evidence that this variation is linked to dynamical class (aside from C_2 and C_3). Observations of 46 comets show that the abundance variation for each molecule can be approximated by a Gaussian distribution with no difference in the distribution for short- and long-period comets (Biver & Bockelée-Morvan 2016). It is thought that

all comets formed in the same, albeit extended, region and were subsequently scattered during planet migration (Brasser & Morbidelli 2013). If this is correct, it is not surprising that the observed chemical diversity in comets is not related to dynamical class.

In order to answer the posited formation vs evolution question there are several points that need to be considered in regards to the results presented above. As has been seen in recent *Rosetta* ROSINA & Visible and Infrared Thermal Imaging Spectrometer (VIRTIS; Coradini et al. 2007) observations, production rates for H_2O, CO_2, and CO vary diurnally due to compositional heterogeneity in the nucleus of 67P (Hässig et al. 2015; Fink et al. 2016; Migliorini et al. 2016). These results strongly indicate that the local production rates of molecules in specific areas of comae and the total production rates taken from observations of whole comae may not agree. Therefore, care may need to be taken when drawing conclusions about compositional classes from total production rates derived from remote observations. One must also consider the fact that gas-phase H_2O can be produced in the coma due to the sublimation of ice grains ejected from the nucleus (Knight & Schleicher 2013; Protopapa et al. 2014). As production rates of volatiles are often determined relative to H_2O, extended and temporary production of gas-phase H_2O could cause variation in the observed molecular abundances between comets.

Isotopic Ratios

While knowledge of the compositional diversity of parent species is important in understanding the formation and evolution of comets, studying isotopic abundances and ratios can provide additional key information on cometary history and evolutionary processes. The benefit of determining isotopic ratios is that the formation conditions of ices, such as the temperature and density, strongly affects isotopic fractionation. For example, for deuterium, this is because one of the main destruction reactions of deuterium has an activation energy barrier and in cold environments this barrier is not overcome (Ceccarelli et al. 2014). Furthermore, in dense environments, the destruction of the main producer of deuterium, H_3^+, is quenched, and more deuterium is produced. Therefore, studies have utilised this sensitivity to initial conditions to probe the early Solar System and comet formation (Ceccarelli et al. 2014). Spectral emission of isotopic species are very weak and so only observations of bright comets can shed light on isotopic fractionation (Ceccarelli et al. 2014). Due to the prevalence of water, deuterium is the most frequently observed isotope, but isotopic ratios of other elements, such as nitrogen, carbon, oxygen, and sulfur

(Stawikowski & Greenstein 1964; Owen 1973; Danks et al. 1974; Eberhardt et al. 1995; Balsiger et al. 1995; Jewitt et al. 1997; Ziurys et al. 1999), can provide insight into formation conditions, but these isotopes are not commonly observed due to weak emission.

Observations of comet Halley using *Giotto* provided the first determination of the cometary water D/H ratio from the H_2DO^+/H_3O^+ ratio (Balsiger et al. 1995; Eberhardt et al. 1995). Initial analysis found this value to be 3×10^{-4}, roughly twice the Vienna Standard Mean Ocean Water (VSMOW) value of 1.6×10^{-4} (typically used as the standard for Earth water). However re-analysis of the data revised this ratio to 2.1×10^{-4} (Brown et al. 2012). It should be noted that, in order to gain knowledge about the delivery of water to Earth, it is typical to compare comet D/H ratios against the VSMOW D/H value.

From remote observations the D/H ratio is typically determined via the detection of HDO. The fundamental rotational line ($1_{01}-0_{00}$) of HDO in comets Hale−Bopp and C/1996 B2 Hyakutake was detected in observations taken with the Caltech Submillimeter Observatory and the James Clerk Maxwell Telescope (JCMT; Meier et al. 1998; Bockelée-Morvan et al. 1998). D/H ratios for these two long-period comets agree well with the initial measurement in comet Halley. More recently, observations of 23 infrared ro-vibrational transitions of HDO in comet 8P/Tuttle using the Very Large Telescope's (VLT) Cryogenic high-resolution Infrared Echelle Spectrograph (CRIRES) revealed a D/H ratio of 4.1×10^{-4} (Villanueva et al. 2009). The D/H ratio can also be determined via the photodissociation products of water, OH and atomic hydrogen, and their deuterated counterparts with similar ratios seen (Hutsemékers et al. 2008; Weaver et al. 2008). Therefore, interestingly, there is variation in the water isotopic fractionation in comets.

The *Herschel Space Observatory* has taken observations of the ground rotational lines of water ($1_{10}-1_{01}$), HDO ($1_{10}-1_{01}$), and $H_2^{18}O$ ($1_{10}-1_{01}$) of the short-period comet 103P/Hartley 2 (hereafter Hartley 2) and the long-period comet C/2009 P1 (Garradd) (hereafter C/2009 P1) using the Heterodyne Instrument for the Far-Infrared (HIFI) (Hartogh et al. 2011; Bockelée-Morvan et al. 2012). This allowed for a more reliable determination of the D/H ratio as the fundamental transitions of $H_2^{16}O$ in comets are optically thick, whereas lines of $H_2^{18}O$ are optically thin. For comet Hartley 2 the HDO/$H_2^{18}O$ ratio was determined to be 0.161 (Hartogh et al. 2011), in excellent agreement to the VSMOW value of 0.155, whereas the value of this ratio in comet C/2009 P1 is 0.215 (Bockelée-Morvan et al. 2012).

An interesting result of the *Rosetta* mission was the determination of a D/H ratio of 5.3×10^{-4} in comet 67P using the ROSINA mass spectrometer (Altwegg et al. 2015). This

is substantially greater than values determined for other short-period comets, that had measured values closer to the VSMOW value. Dynamical work has shown that the orbit of comet 67P has previously been altered via a gravitational perturbation by Jupiter in 1959 (Maquet 2015). Therefore, the dynamical and thermal history is likely different to other short-period comets and the D/H ratio in 67P may not be indicative of all short-period comets. Another interpretation is that both short- and long-period comets were formed in the same extended region with both families inheriting a broad range of D/H ratios.

As the isotopic ratio is sensitive to formation conditions, especially temperature, it has been used as a proxy for formation location. In addition, there has been considerable work studying isomeric ratios in comets, notably the water OPR, as it has previously been thought that this ratio is also indicative of formation location.

1.1.4 Ortho-to-Para Ratio Introduction

Molecules with symmetric hydrogen atoms (e.g. H_2, H_2O, and NH_3) have different nuclear-spin species (or isomers) that are produced depending on the sum of their hydrogen spins, given by the total nuclear-spin value, I. For molecules with two hydrogen atoms the molecule is either in the ortho (spins aligned, $I = 1$, triplet) or para (spins anti-aligned, $I = 0$, singlet) state (Mumma et al. 1987). Diagrams of these spins states are shown in Fig. 1.4, adapted from Hama et al. (2018), Fig. 1. It is common to write the rotational states of a molecule as $J_{\mathrm{K_aK_c}}$ where J is the total rotational angular momentum, and K_a and K_c are J projected onto the molecular a- and c-axes (Tennyson et al. 2001). For H_2O, the a-axis is in the molecular plane, perpendicular to the bisector of the H−O−H angle, with the c-axis perpendicular to the molecular plane. A schematic of a H_2O molecule is given in Fig. 1.5, adapted from Hama & Watanabe (2013), Fig. 32. The spin symmetry can be given by the sum of K_a and K_c, with ortho states: $K_\mathrm{a}+K_\mathrm{c}$ = odd, and para states: $K_\mathrm{a}+K_\mathrm{c}$ = even (Tennyson et al. 2001).

For an isolated, gaseous system in thermal equilibrium with a temperature, T, the OPR can be calculated using;

$$\mathrm{OPR} = \frac{(2\mathrm{I_o}+1)\sum\limits_{\mathrm{o}}(2\mathrm{J}+1)\exp\left(-\frac{\mathrm{E_o}}{\mathrm{kT}}\right)}{(2\mathrm{I_p}+1)\sum\limits_{\mathrm{p}}(2\mathrm{J}+1)\exp\left(-\frac{\mathrm{E_p}}{\mathrm{kT}}\right)} \tag{1.1}$$

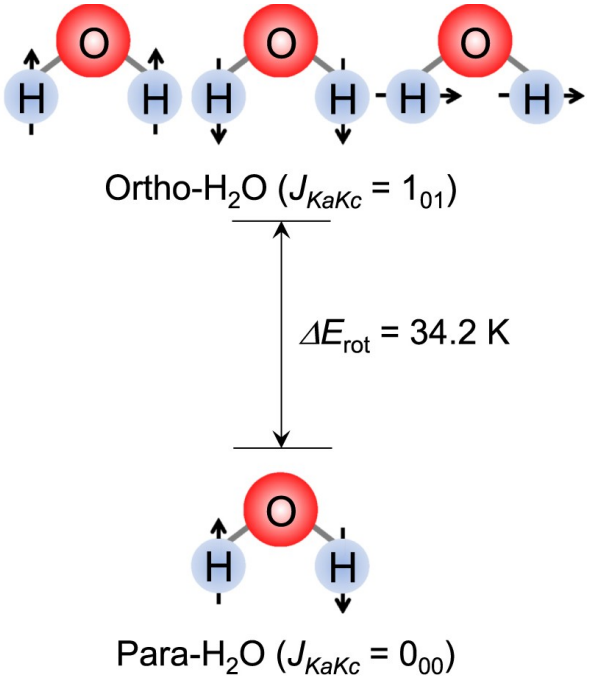

Figure 1.4. A diagram of the three triplet states of ortho-H_2O showing the aligned spins with the rightmost molecule indicating the superposition state of the two other ortho-H_2O spin states, and of the para-H_2O singlet state. The ground states for both isomers in $J_{K_aK_c}$ notation and the energy difference between them is given. This figure is adapted from Hama et al. (2018), Fig. 1.

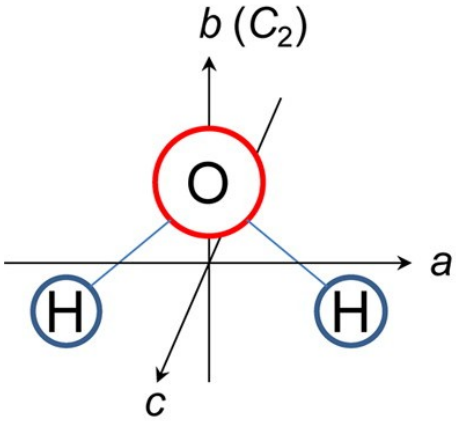

Figure 1.5. A schematic of a H_2O molecule showing the a, b, and c-axes. As the principal axis of rotation is the b-axis the projection of J onto the b-axis is invariant with rotation and thus the rotational state can be described by the the projection of J onto the a and c-axes. This figure is adapted from Hama & Watanabe (2013), Fig. 32.

where the o and p subscripts denote the ortho and para states. E is the energy level, and k is the Boltzmann constant (Mumma et al. 1987). This equation includes degeneracies as the values of J will include I_o and I_p. Interestingly, due to the relationship between OPR and temperature, the OPR will equilibrate to the statistical value with increasing temperature. For H_2O, the statistical equilibrium is $(2I_o+1)/(2I_p+1) = 3$. Compared to other molecules (Crovisier 1998), H_2O equilibrates rapidly as the ground ortho level, 1_{01}, has an energy state 34.2 K above the ground para level, 0_{00} (Tennyson et al. 2001). This means the OPR of H_2O can potentially be useful in probing cold environments.

Previous Ortho-to-Para Ratio Determinations

The first determination of the OPR was obtained from *KAO* observations of the $v3$ band at 2.7μm in comet Halley with a measurement of 2.7±0.2 reported (Mumma et al. 1987). This band has also been observed in comets C/1986 P1 (Wilson), Hale−Bopp, and Hartley 2 using the *KAO* and the *Infrared Space Observatory* (*ISO*) with water OPRs of 3.2±0.2, 2.5±0.1, and 2.8±0.1 calculated (Mumma et al. 1988; Crovisier et al. 1997, 1999). NH_3 OPR can also be determined with values in the long-period comets, C/1999 S4 (LINEAR) and C/2001 A2 (LINEAR) (hereafter C/2001 A2), found to be 1.17±0.04 and 1.12±0.03 (Kawakita et al. 2001, 2002), which are close to the statistical equilibrium value of 1. Interestingly, recent surveys have found no difference in OPR between short- and long-period comets (Shinnaka et al. 2011, 2016). In theory, any molecule with symmetric hydrogen atoms can be used to determine OPR, however to date no detections of the isomers of methane and formaldehyde have been made.

Ortho-to-Para Ratio Variation via Nuclear-Spin Conversion

Interestingly, nuclear-spin conversion between the isomers, ortho- and para-water, in an isolated, gas-phase, for example in the interstellar medium or protoplanetary disks, are forbidden (Mumma et al. 1987, 1993). This is because the timescales for nuclear-spin conversion between the isomers via radiative transitions or collisions are orders of magnitude larger than other processes such as photodissociation. Therefore, due to the relationship between the OPR and temperature this ratio has been used as a proxy for the H_2O temperature. In cometary studies, the OPR was previously thought to be related to the local temperature of the gas when frozen out during comet formation, and therefore could be used to trace formation location (Mumma et al. 1987).

However, a recent study has found that nuclear-spin conversion between the isomers can occur rapidly for molecules in the solid-phase (Hama et al. 2016). It was found that the H_2O OPR is normalised to the statistical equilibrium value of 3 after the freeze out of gas-phase volatiles during comet formation. Thus, the interpretation of the OPR is not clear, but it has been proposed that this ratio could trace: the comet formation temperature, internal temperature of cometary nucleus, the surface temperature during sublimation, or the temperature in comae during observations (Mumma et al. 1993; Irvine et al. 2000; Kawakita et al. 2004; Kawakita & Kobayashi 2009; Mumma & Charnley 2011; Shinnaka et al. 2011). Key to discerning which of these scenarios is correct is understanding the process of nuclear-spin conversion in both the gas- and solid-phase.

Nuclear-Spin Conversion in the Gas-Phase

In a collisional environment, gas-phase nuclear-spin conversion is known to occur for several molecules, including H_2O, via the quantum-relaxation model (Curl et al. 1967; Chapovsky & Ilisca 2001; Sun et al. 2005; Tudorie et al. 2006). If, following a collision, an ortho- (para-) water molecule has the energy approximately equal to a para (ortho) state then wave function mixing of nuclear-spin states induced by intra-molecular magnetic interactions will occur. After the conversion the molecule must undergo relaxation via a further collision in order for energy to be conserved (Curl et al. 1967; Chapovsky 1991). For low collision environments such as the outer coma, nuclear-spin conversion via this method is unlikely (Cacciani, Cosléou & Khelkhal 2012). However it has been proposed that proton-exchange interactions between H_2O and H^+ could cause the OPR to fall below the corresponding value for the temperature (Emprechtinger et al. 2010; Lis et al. 2010).

Nuclear-Spin Conversion in the Solid-Phase

In addition to nuclear-spin conversion of H_2O in the gas-phase, conversion could occur in the solid-phase. In bulk H_2O ice the hydrogen bond is important as it can cause a restriction to molecular rotation. This rotation barrier results in the difference between the rotational energy of ortho- and para-water decreasing substantially, that yields a more efficient and quicker nuclear-spin conversion (Limbach et al. 2006; Buntkowsky et al. 2008). Furthermore, it has been shown that as the amount of hydrogen bonds increases, to the level of the number typically seen in crystalline ice, the difference in the energy of the lowest ortho and para states narrows to become quasi-degenerate (Petrenko & Whitworth 1999;

Pérez et al. 2012). In bulk H_2O ice, the energy gap between the fundamental spin states is 5×10^{-13} K (Buntkowsky et al. 2008) much smaller than in the gas-phase, 34.2 K (Mumma et al. 1987). This substantial decrease means that nuclear-spin conversion between the different isomers can occur very rapidly, on the order of 10^{-5}–10^{-4} s (Buntkowsky et al. 2008), and proceeds via intermolecular spin-magnetic interactions.

Recently, laboratory research has been conducted to test the proposed rapid nuclear-spin conversion in ices (Hama et al. 2016). In a landmark study, H_2O ice was created from the freeze out of H_2O gas via several methods in conditions that aimed to mimic the outer Solar System conditions, $T = 8$ K and an ultrahigh vacuum (Hama et al. 2016). Following thermal desorption of the ice at 150 K, the H_2O gas was analysed spectroscopically. Regardless of formation procedure, the OPR in all experiments was observed to be consistent with the statistical equilibrium value (Hama et al. 2016). Therefore, it seems that rapid nuclear-spin conversion in the ices normalised the OPR and no record of the initial formation temperature of the H_2O was observed in the sublimated gas. This finding has important implications for the interpretation of the OPR in cometary studies as it means that the OPR cannot be used as a diagnostic of cometary formation temperature.

For the study of cometary OPRs, knowledge of nuclear-spin conversion in gases and bulk ices is important, it should be noted that research into conversion in more specialised environments has been conducted that may be useful (Hallam 1973; Abouaf-Marguin et al. 2007, 2009; Ceponkus et al. 2010; Kuyanov-Prozument et al. 2010; Sliter et al. 2011; Beduz et al. 2012). For isolated H_2O dimers and for H_2O monomers trapped in noble gas matrices, nuclear-spin conversion can happen efficiently over timescales from 1 to 10^5 s (Miyamoto et al. 2008; Kuyanov-Prozument et al. 2010). The timescale is shorter than the gas-phase due to rotational impedance and the conversion is thought to proceed via the quantum-relaxation model as outlined above (Abouaf-Marguin et al. 2009).

Therefore, there is now a substantial body of work that shows that, while gas-phase nuclear-spin conversion in isolation is forbidden, conversion between ortho- and para-water can occur very rapidly in a plethora of other environments. This means that, as the OPR should be normalised to the statistical equilibrium value of 3 in cometary ices, the previous paradigm of the OPR tracing the formation temperature of comets has to be revised.

Studying Ortho-to-Para Ratio Variation in Cometary Comae

Interestingly, observations of cometary comae have yielded OPRs lower than 3. This seems to imply that there is a process altering this ratio that is occurring after the ices have been sublimated. To test this, two comets have been observed to study the OPR at a range of nucleocentric distances. Comet 73P−B/Schwassmann-Wachmann 3 (hereafter 73P−B) was observed at nucleocentric distances of $5 - 30\,\mathrm{km}$ (Bonev et al. 2008*a*) with the OPR determined to be 3. Spectra of comet C/2004 Q2 (Machholz) were taken at distances of $100 - 1\,000\,\mathrm{km}$ from the nucleus and analysed to find an OPR of 2.86±0.06 (Bonev et al. 2007).

Taken together these results seem to suggest that OPR variation does not occur in the inner coma, but in order to explain other lower values it could occur at mid to large nucleocentric distances. If this is the case it may provide a method to probe the evolutionary processes in cometary comae. However, it has been suggested that the collisional rate between H_2O molecules with other molecules, electrons, and ions is too low for efficient nuclear-spin conversion via the collisional quantum-relaxation model to occur (Crovisier 1984; Mumma et al. 1987). It has been proposed that proton-transfer interactions with ions (Irvine et al. 2000), or collisions with water clusters (Crifo & Slanina 1991; Crifo 1992), ice grains (Davies et al. 1997; Lellouch et al. 1998; Kawakita et al. 2004; Schulz et al. 2006), or dust (Agarwal et al. 2007; Tenishev et al. 2011) in the collisional (Combi et al. 2004; Rodgers et al. 2004) comae could decrease the observed OPR, but considerable work still needs to be done to discern what role OPR can play in understanding the evolutionary processes in cometary comae. Interestingly, recent work may have found sublimating ice grains in the comae of comet 67P (Gicquel et al. 2016). If this is common then the presence of an additional source of gas-phase molecules may produce the collisional environment needed to cause nuclear-spin conversion.

1.1.5 Cometary Comae Modelling using Radiative Transfer

In order to accurately interpret spectroscopic observations and to study the physical and chemical environments in cometary comae, such as parent molecule production rates, radiative transfer models need to be developed. Essential to these models is the understanding of excitation processes (both radiative and collisional) in comae.

Excitation of Electronic and Vibrational Bands

Prior to discussing rotational excitation, the processes that produce ortho- and para-water emission, it is worth discussing the excitation processes of the electronic and vibrational bands. Due to low temperatures in cometary comae (Combi et al. 2004) collisional excitation of the electronic and vibrational bands does not typically occur. Instead excitation is caused by radiative processes driven by Solar radiation. Molecular electronic bands are observable in the ultraviolet, however at these wavelengths the Solar flux is relatively weak and thus the excitation rates of electronic transitions are much lower than for vibrational excitation (Crovisier & Le Bourlot 1983; Tozzi, Feldman & Festou 1998).

Over the past four decades there has been considerable advancement in the study of radiative vibrational excitation. The majority of the vibration transitions observed in the infrared are due to excitation from Solar radiation (Mumma 1982; Yamamoto 1982; Weaver & Mumma 1984), however it can also be caused by the thermal emission of dust in cometary comae (Crovisier & Encrenaz 1983).

Rotational Excitation

The main driver of rotational excitation in the inner and mid coma is collisions between the sublimated molecules, and H_2O molecules and electrons (Xie & Mumma 1992). However, at large heliocentric distances the CO production rate is higher than H_2O, and therefore collisions with CO can become important (Biver et al. 1996). For molecules in the fundamental vibrational state, collisions act to thermalise the rotational states of molecules to the local kinetic temperature in the coma, with the collision rate dependent on the collisional cross-section, the local density of the colliding bodies, and the relative velocities. Initial studies of comet Halley using *Giotto* data have found that in the inner coma (nucleocentric distance $\leq$3 000 km) H_2O-H_2O collisions dominate the excitation due to higher densities of H_2O compared to electrons. At greater nucleocentric distances excitation is mainly driven by H_2O-e^- collisions (Xie & Mumma 1992; Biver et al. 1999). Collisions between H_2O and the Solar wind may cause the destruction of H_2O, however the destruction rate is considerably lower than other processes, such as photochemistry, and therefore it is not thought to play an important role (Combi et al. 2004).

Radiative rotational excitation due to Solar radiation is low, because of the weak Solar flux in the submillimetre and radio. However, at large heliocentric distances, >3 AU, the

cosmic microwave background can cause rotational excitation (Biver et al. 1999). For the study of the H_2O rotational lines self-absorption effects must be taken into account (Bockelée-Morvan 1987). In the submillimetre, the fundamental rotational H_2O lines are optically thick due to the high H_2O densities in the inner coma. Following the emission of a photon, radiation trapping can occur, where a nearby H_2O molecule may absorb the emitted photon and transition to an excited state. This results in a delay to radiative relaxation and a higher local thermal equilibrium than would be expected if the H_2O was optically thin. This effect can occur up to nucleocentric distances of 10^4 km for comets with a high H_2O production rate (Weaver & Mumma 1984; Bockelée-Morvan 1987).

Calculating Molecular Production Rates

For optically thin rotational lines, observed line intensities can be converted into column densities, and therefore molecular production rates, abundances, and ratios (Bockelée-Morvan et al. 1994), using;

$$\langle \mathrm{N_u} \rangle = \frac{8\pi\nu^2 \mathrm{k}}{\mathrm{hc^3 A_{ul}}} \int \mathrm{T_b d}\nu \tag{1.2}$$

where $\langle N_\mathrm{u} \rangle$ is the column density, ν is the transition frequency, A_ul is the Einstein-A coefficient, and T_b is the brightness temperature, with $\int T_\mathrm{b} d\nu$ term representing the line intensity. The remaining variables are the standard physical constants. For optically thick rotational lines, such as the fundamental lines of H_2O, detailed radiative transfer models of cometary comae that include the excitation methods and radiation trapping described above must be developed (Chiu et al. 2001; Lecacheux et al. 2003; Bensch & Bergin 2004).

In general, the cometary radiative transfer models used to study fundamental rotational transitions aim to model the coma using a range of physical and orbital parameters that feeds into an excitation model that calculates rotational level populations in the ground vibrational level and computes the observed line emission after solving the radiative transfer equations and convolving the emission with the beam. Two main comet radiative transfer models have been developed. The modelling of the physical coma environment and the excitation processes are the same for both models, however the radiative transfer equations are solved in different ways; one via the Sobolev escape probability method (Bockelée-Morvan 1987; Biver et al. 1997*a*) and the other using an Accelerated

Monte Carlo method (Hogerheijde & van der Tak 2000; Bensch & Bergin 2004). This introduction will focus on the later model as it was the basis of the radiative transfer model developed for analysis of the *Herschel* Spectral and Photometric Imaging Receiver (SPIRE) spectra in Chapter 3 (De Val-Borro & Wilson 2016). It has been shown that both methods agree within ∼20 per cent (Zakharov et al. 2007), which is typical of the uncertainties in the derived production rates.

Modelling Cometary Comae

The radial distribution of molecules is typically modelled using a standard Haser distribution (Haser 1957). The model assumes a symmetric distribution of molecules sublimated from the nucleus at a constant rate with a constant expansion velocity. For H_2O it is;

$$\mathrm{n_{H_2O}(r)} = \frac{\mathrm{Q_{H_2O}}}{4\pi \mathrm{r_{nuc}^2 v_{exp}}} \exp\Big(- \frac{\mathrm{r_{nuc}} \beta_{\mathrm{H_2O}}}{\mathrm{v_{exp}}} \Big) \tag{1.3}$$

where $Q_{\mathrm{H_2O}}$ is the H_2O production rate, r_{nuc} is the nucleocentric distance, v_{exp} is the expansion velocity, and $\beta_{\mathrm{H_2O}}$ is the photodestruction rate due to Solar ultraviolet radiation. Thus, the exponential term in equation 1.3 determines the lifetime of H_2O in the coma, whereas the fractional term describes amount of H_2O as a function of r_{nuc} due to a symmetric sublimation from the nucleus at a constant rate and velocity. Recent observations have shown that comae are not symmetric in nature (Hässig et al. 2015), however for observations of the entire coma assuming a symmetric expansion allows for accurate determinations of global molecular production rates. If the transitions are optically thin and spectroscopically resolved the gas expansion velocity can be determined via modelling. For optically thick lines the expansion velocity can potentially be estimated by determining the width of the red-shifted half of the emission lines in velocity space (Hartogh et al. 2010). The blue-shifted half of the emission cannot typically be used as it will be affected by coma self-absorption processes. Typical values for comets in the inner Solar System ($r_{\mathrm{h}} < 3\,\mathrm{AU}$) are $0.5 < v_{\mathrm{exp}} < 1.5\,\mathrm{km\,s^{-1}}$ (Crovisier et al. 1995; Biver et al. 1999) and are related to the heliocentric distance by $v_{\mathrm{exp}} \sim 1.1 r_{\mathrm{h}}^{-0.4}$, an empirically derived relationship from observations of comet Hale−Bopp (Biver et al. 1997*b*). While $\beta_{\mathrm{H_2O}}$ at the comet is related to r_{h}, it is sensitive to the strength of the Solar activity (Crovisier 1989).

To derive rotational level populations, and therefore molecular production rates, ac-

curate values of level energies and Einstein coefficients of the transitions must be known. These have been produced experimentally in laboratory studies for most commonly observed molecules (Pickett et al. 1998; Müller et al. 2013). In order to study the OPR of H_2O, energy states and transitions of both isomers need to be included in the model. The rotational energy diagram for the fundamental rotational levels of H_2O can be seen in Chapter 3, Fig. 3.2. Level populations are then calculated using the excitation processes outlined above. In the inner coma excitation of H_2O is driven by H_2O-H_2O collisions which is determined by the gas density and the kinetic temperature of the neutral gas, $T_{\rm kin}$. Temperatures are thought to decrease rapidly with increasing nucleocentric distance (Marconi & Mendis 1984), however it has been shown that for regions in which H_2O-H_2O collisions dominate $T_{\rm kin}$ can be approximated as a constant at $\leq$100 K (Combi et al. 1999). The boundary between the H_2O-H_2O collision dominant region and the H_2O-e^{-1} collision dominant region is called the contact surface radius, $R_{\rm con}$, and is determined by the molecular production rate and a scaling factor, $x_{\rm r_e}$, that was introduced in modelling to account for the uncertainty in $R_{\rm con}$ (Biver 1997). Observations of comet Halley by *Giotto* have shown that $x_{\rm r_e} \sim 1$ which results in typical $R_{\rm con}$ at nucleocentric distances of $\sim$ 1 000 km (Balsiger 1990; Festou 1990). To calculate level populations at nucleocentric radii, the electron temperature and density profiles must be modelled. The radial dependence of the electron temperature is given by $T_{\rm kin}$ for $r < R_{\rm con}$ and arbitrarily set at 10^4 K for $r > 2R_{\rm con}$. Between these limits it is modelled as;

$$\mathrm{T_e(r) = T_{kin} + (10^4 - T_{kin})\Big(\frac{r}{R_{con}} - 1\Big)} \tag{1.4}$$

that simulates the increasing electron temperature at larger $r_{\rm nuc}$ as the decreasing gas density is insufficient in collisionally cooling the electrons. To model the electron density as a function of nucleocentric distance, the recombination surface radius, $R_{\rm rec}$, must be calculated (Biver 1997). This radius is a function of production rate and the $x_{\rm r_e}$ scaling factor. Beyond this radius Solar radiation becomes the main driver of excitation (Bockelée-Morvan 1987; Neufeld et al. 2000). Knowledge of the photoionization rate, $k_{\rm ion}$, and the recombination rate, $k_{\rm rec}$, means that the electron density profile can be modelled by;

$$\mathrm{n_e(r)} = \mathrm{x_{n_e}}\Big(\frac{\mathrm{Q_{H_2O}k_{ion}}}{\mathrm{v_{exp}k_{rec}r_{nuc}^2r_h^2}}\Big)^{0.5}\mathrm{T_e^{0.15}R_{rec}}\Big[1-\exp\Big(-\frac{\mathrm{r}}{\mathrm{R_{rec}}}\Big)\Big] \tag{1.5}$$

where $x_{\mathrm{n_e}}$ is the electron density scaling factor, previously introduced to account for uncertainties in the electron density. The radial electron density profile is mainly determined by the production of electrons via photoionization of neutral molecules and the destruction of electrons by ion recombination. This is represented in equation 1.5 by the parameters in the fractional term. Photoionization depends on the density of the neutral molecule, here calculated using the terms from equation 1.3, and is controlled by k_{ion} and decreases with heliocentric distance, r_{h}. Whereas, the amount of electrons destroyed by recombination is a factor of k_{rec} and T_{e}. Observations have reproduced emission lines using $x_{\mathrm{n_e}} = 0.2$ or 1.0 (Biver 1997; Biver et al. 2007; Hartogh et al. 2010).

The two methods of collisional excitation outlined so far allow calculation of the rotational level populations in the ground vibrational state. However, for studying H_2O in the outer coma, fluorescence of H_2O molecules from the ground vibrational state to an excited vibrational state by Solar radiation must be considered (Crovisier & Encrenaz 1983; Bockelée-Morvan 1987; Bockelée-Morvan & Crovisier 1989; Neufeld et al. 2000). In this radiative transfer model the fluorescence is simulated by effective pumping rates (Bensch & Bergin 2004). For example, when fluorescence occurs H_2O may be excited from the ground rotational level in the ground vibrational level to an excited vibrational level and subsequently relaxes into a different rotational level in the ground vibrational level. The effective pumping in this model simulates this by ignoring the excitation and relaxation to an excited vibrational level, and instead calculated the rates between different rotational states of ground vibrational state directly.

Using the model outlined above, the rotational level populations are calculated by solving the radiative transfer equations in spatially separate cells which provides a degree of spatial resolution to the model, however there is a trade-off with computational time (Hogerheijde & van der Tak 2000; Zakharov et al. 2007). The size of these cells is determined by the observational aperture and the number of shells desired by the user. The radiation that escapes the outermost shell of cells is the line emission that would be seen for an observer at the edge of the cometary coma. The radiation is then convolved with the telescope beam at the observer-comet distance to produce the predicted line emission

(Bensch & Bergin 2004; De Val-Borro & Wilson 2016). Thus, it can be seen that from knowledge of orbital parameters and chemical networks, by varying the H_2O production rate and comparing the modelled submillimetre line emission to *Herschel* observations the water environment in cometary comae can be analysed.

1.2 A Review of White Dwarf Debris Disks

In this half of the introduction a review of planetary debris disks around white dwarf stars will be presented. Firstly, it is worth outlining the general scenario that is thought to be occurring in these systems. Following a gravitational interaction with nearby stars or planets, minor planetary bodies that have survived the stellar giant phases are perturbed either out of the system, into other planetary bodies, or towards the white dwarf (Debes & Sigurdsson 2002; Debes et al. 2012; Veras et al. 2013; Mustill et al. 2014). If a perturbed planetary body passes within the Roche limit of the white dwarf then tidal forces disrupt the planetary "parent" body which subsequently forms a circumstellar debris disk (Jura 2003). The dust in the debris disk then accretes onto the white dwarf via Poynting-Robertson (PR) drag (Rafikov 2011*a*; Bochkarev & Rafikov 2011; Metzger et al. 2012). As white dwarf atmospheres are primarily made up of hydrogen or helium diffusion timescales are orders of magnitude smaller than the cooling age of the white dwarf, and thus any observed metals must be currently or recently accreting from a disk (Koester et al. 1997; Koester 2009). Following the nomenclature in the literature, "polluted" white dwarfs are white dwarfs with atmospheric metals observed spectroscopically, whereas "dusty" white dwarfs are those with a circumstellar debris disk observed photometrically in the infrared.

1.2.1 Introduction to White Dwarf Planetary Systems

The study of (exo)planetary systems around white dwarfs is a relatively young field, but has advanced rapidly over the past two decades. While "tradtional" exoplanet studies have been successful in discovering exoplanets using the transit, radial velocity, and direct imaging methods, research into white dwarf planetary systems can provide information not currently obtainable by other methods. For example, by studying white dwarf atmospheres, detailed minor planetary body compositions can be determined (Xu et al. 2014; Hollands et al. 2018*a*) and from knowledge of debris disks, the architectures of planetary systems can be probed using dynamical models (Debes et al. 2012; Veras et al. 2013).

Thus, research into the destruction of minor planetary bodies around white dwarfs can yield substantial knowledge that is useful not only for understanding the fate of planetary systems, but also in gaining information about planetary systems during the main sequence.

White Dwarf Properties

Prior to reviewing white dwarf planetary systems it is worth summarising a general overview of white dwarfs to provide context for their studying planetary systems. White dwarfs are formed when a star with mass $< 8M_{\odot}$ evolves off the main sequence, through the giant phases, and ejects the envelope leaving the stellar core which forms the white dwarf (Koester 2013). The structure and composition is: white dwarfs with a mass of $< 1M_{\odot}$ will have a carbon-oxygen core due to burning helium and carbon during the main sequence, whereas higher mass degenerates that could also burn oxygen will have a neon-oxygen core (Althaus et al. 2010). The majority of stars are low mass and thus, will form carbon-oxygen white dwarfs. The core is surrounded by a convective helium shell and, for most white dwarfs, a hydrogen atmosphere (Althaus et al. 2010; Koester 2013).

White dwarfs are delineated into classes based on the observed spectral absorption features in their atmospheres (Sion et al. 1983). Representative spectra of white dwarf classes and subclasses taken by the Sloan Digital Sky Survey (SDSS) are shown in Fig. 1.6, adapted from Gentile Fusillo et al. (2019), Fig. 11. For white dwarfs with a hydrogen dominant atmosphere the classification is DA, where D signifies that the star is degenerate, for a helium rich atmosphere it is DB, for a carbon dominant atmosphere it is DQ, and for a metal rich atmosphere it is DZ. White dwarfs are classified depending on the most prominent spectral feature and if a spectrum exhibits more than one element the classification letters are listed in decreasing strength. For example, G 29−38 is a DAZ star (Zuckerman et al. 2003) and Procyon B is a DQZ (Provencal et al. 2002). White dwarfs with featureless spectra are DC and those with an observable magnetic field are DxH, where x represents the dominant spectral feature. As these classifications are based on the relative strength of the features one should be careful in drawing conclusions about the white dwarf structure or composition based on the classification alone without spectral modelling. 80−85 per cent of known white dwarfs are DAs (Koester 2013).

In addition to composition, white dwarfs physical parameters can be determined via observation. After the giant phases a white dwarf enters a cooling state as fusion in

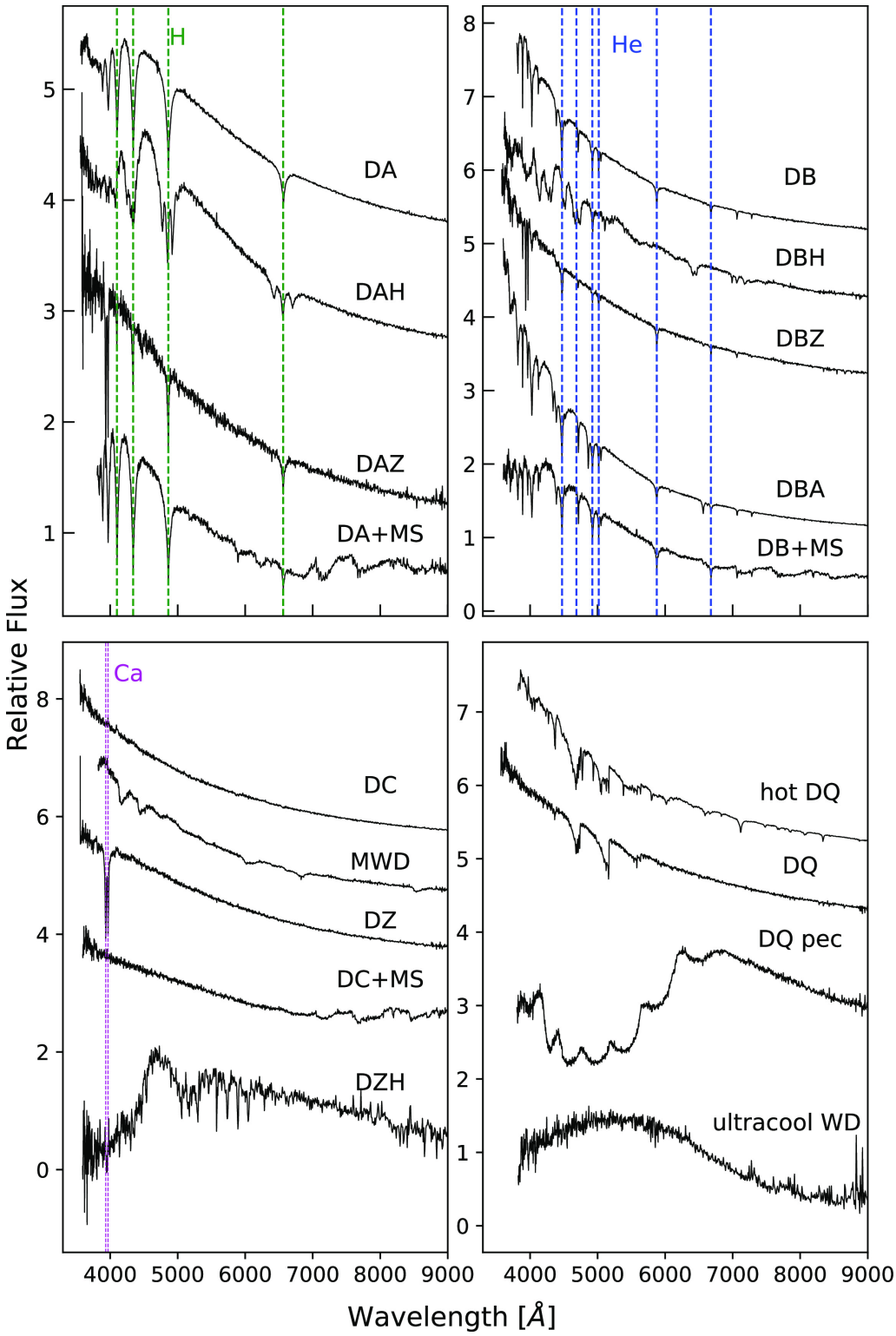

Figure 1.6. SDSS spectra of white dwarfs representative of the classification subclasses including degenerates with; (top left) hydrogen dominant atmospheres indicated by the Balmer lines, (top right) helium dominant atmospheres, (bottom left) continuum and metal-polluted white dwarfs indicated by the Ca H&K lines, and (bottom right) atmospheres showing carbon features. This figure is adapted from Gentile Fusillo et al. (2019), Fig. 11.

the core no longer occurs (Koester 2013). The white dwarf cools for its entire lifetime, with this period called the cooling age. It can be calculated from the stellar mass and temperature that can be determined by modelling the stellar spectrum (Bergeron et al. 1992; Fontaine et al. 2001). To determine the white dwarf luminosity, the stellar radius should be known which can be calculated via the mass-radius relationship (Nauenberg 1972; Tremblay et al. 2017). Population studies have shown that the white dwarf mass distribution peaks at $0.6\,M_{\odot}$ with Gaussian-like tails to $0.4\,M_{\odot}$ and $1.4\,M_{\odot}$ (Liebert et al. 2005; Livio et al. 2005; Althaus et al. 2010; Kleinman et al. 2013; Hollands et al. 2018*b*). Using the initial-final mass relationship, the main sequence mass of white dwarfs can be determined (Meng et al. 2008; El-Badry, Rix & Weisz 2018). Interestingly, this results in a white dwarf mass lower limit ($M > 0.4\,M_{\odot}$) that is constrained by the age of the universe. White dwarfs with a mass lower than this value have been observed, although this may be due to binary interaction with a companion (Nelemans & Tauris 1998).

White Dwarf Planetary Systems

The vast majority of stars (> 90 per cent) in the Milky Way, including the Sun, will become white dwarfs, studying their planetary systems provides valuable insights into the fate of the majority of planets and our Solar System.

There are several observational features of remnant planetary bodies in white dwarf systems. The most commonly seen features are metals in the white dwarf atmosphere (Zuckerman et al. 2003) and dust in the circumstellar debris disk (Zuckerman & Becklin 1987), although gas in the debris disk (Gänsicke et al. 2006) and direct observation of transiting debris have also been observed (Vanderburg et al. 2015). Due to the pristine hydrogen or helium atmospheres and the high gravity of white dwarfs, any atmospheric metals are thought to have been accreted from a circumstellar debris disk (Jura 2003; Jura et al. 2007*a*). Spectroscopy can reveal the presence of accreted elements with over 2 000 polluted white dwarfs known (Zuckerman et al. 2003, 2010; Koester et al. 2014).

Circumstellar debris disks are created from the destruction of a minor planetary body as it passes the white dwarf Roche limit and can have two components; the main, typically flat and opaque, dust disk and occasionally a tenuous gas disk that is radially co-spatial, but vertically extended compared to the dust. Dust disks have been discovered at roughly 40 white dwarfs via infrared photometric or spectroscopic observations (Zuckerman & Becklin 1987; Reach et al. 2005; von Hippel et al. 2007; Jura et al. 2007*a*; Debes et al.

2007; Farihi et al. 2008, 2010; Xu & Jura 2012; Girven et al. 2012; Rocchetto et al. 2015; Barber et al. 2016). The gas component of a debris disk has only been observed at eight stars via detection of the Ca II triplet using optical spectroscopy (Gänsicke et al. 2006, 2007, 2008; Melis et al. 2012*a*; Farihi et al. 2012*a*; Wilson et al. 2014; Guo et al. 2015).

Interestingly, planetesimals, either disrupted or stable, have been observed around three stars, WD 1145+017, SDSS J122859.93+104032.9 (hereafter SDSS J1228+1040), and ZTF J013906.17+524536.89, via the detection of transiting debris or variable circumstellar gas (Vanderburg et al. 2015; Manser et al. 2019; Vanderbosch et al. 2019). Therefore, planetary systems around white dwarf stars can be observed via multiple different methods that can probe the physical and chemical nature of these planetary bodies and can ultimately be related to Solar System minor planetary bodies.

In this introduction section, a review of the observational studies of these planetary systems will be given in Section 1.2.2. Section 1.2.3 will present theoretical work of the planetary systems and circumstellar disks. In Section 1.2.4 the frequency of planetary systems around white dwarfs is discussed with Section 1.2.5 covering observational and theoretical work on debris disk variation.

1.2.2 White Dwarf Atmospheric Metals and Circumstellar Debris Disks

While a lot of research has been focused on detecting exoplanets around main sequence stars, work has also been done discovering and studying exoplanetary systems around white dwarfs. The two main detection methods used to infer the presence of minor (and major) planetary bodies are searching for atmospheric metals and circumstellar debris disks. Discovery of exoplanets via the traditional methods (transit, radial velocity, etc.) has occurred since the 1990s (Mayor & Queloz 1995), however the detection of planetary material in white dwarf systems occurred with the first detection of a debris disk in 1987 (Zuckerman & Becklin 1987) and the first atmospheric metals observed in 1917 (van Maanen 1917). This subsection focus on the observations of evidence of white dwarf planetary systems with theoretical studies discussed in a following subsection.

Circumstellar Dust Debris Disks

As white dwarfs are more luminous at bluer wavelengths than in the infrared, cooler circumstellar objects can be detected at infrared wavelengths due to heating from stellar radiation and subsequent re-radiation (Probst 1981, 1983). Using white dwarf atmospheric

models, spectral energy distributions (SEDs) can be constructed with an excess amount of infrared flux above that predicted by the stellar model indicating the presence of a cooler component. The first circumstellar disk was discovered around G 29−38 (Zuckerman & Becklin 1987) using Infrared Telescope Facility (IRFT) near-infrared photometry that showed an infrared excess. This excess was successfully modelled by a static, optically thick, geometrically flat disk (geometrically analogous to the rings of Saturn) created via the tidal disruption of a planetesimal passing within the Roche limit of the star (Jura 2003). This seminal work has become the paradigm with all white dwarf planetary debris disks thought to form from the tidal disruption of planetesimals, asteroids, or comets.

To date, over 40 white dwarfs with circumstellar dust disks have been observed in the infrared (Becklin et al. 2005; Reach et al. 2005; von Hippel et al. 2007; Jura et al. 2007*a*; Debes et al. 2007; Farihi et al. 2008; Farihi 2009; Farihi et al. 2010; Xu & Jura 2012; Bergfors et al. 2014; Rocchetto et al. 2015; Barber et al. 2016) with the *Spitzer Space Telescope* (Werner et al. 2004) playing a key role in their discovery. Interestingly, a circumbinary dust disk has been found (Farihi et al. 2017), with the remaining disks found around single stars. The dust has also been directly observed using *Spitzer* spectroscopy. The 10 μm silicate emission feature, caused by the stretching of the Si-O bond, was observed that has been found to be consistent with amorphous olivine dust grains typically detected in inner Solar System bodies (Reach et al. 2005; Jura et al. 2007*b*).

All known disks are detectable at 3−8 μm and need to be observed from space, whereas roughly half of all disks emit strongly at 2 μm and can be seen via ground-based observations (Kilic et al. 2006; Kilic & Redfield 2007). These wavelengths indicate blackbody temperatures of 400−1500 K. Interestingly, no dust disks are only observable at wavelengths longer than 8 μm indicating that either cooler dust reservoirs do not exist or they are currently unobservable (Farihi et al. 2014).

Whilst the flat disk model has been supported by observations via well fitted SEDs, theoretical work has also reinforced this picture. Due to low white dwarf luminosities radiation pressure cannot effectively eject optically thin dust from the system (Farihi et al. 2008). Instead micron-sized unshielded dust will be accreted onto the white dwarf over decadal timescales via PR-drag, depending on the white dwarf luminosity and dust orbital radius (Burns et al. 1979; Hansen et al. 2006). In the geometrically flat disk model, the majority of dust is shielded from stellar radiation and only a small fraction of the dust undergoes PR-drag (Jura 2003). Thus, this model can also explain the survivability of

circumstellar dust over decades as, for example, the disk around G 29−38 has been detected for over 30 years. The flux of a flat disk (Jura 2003) is given by:

$$\mathrm{F_{disk}} = 12\pi^{1/3}\frac{\mathrm{R_*^2 cos\,i}}{\mathrm{D^2}}\left(\frac{2\mathrm{k_B T_*}}{3\mathrm{h}\nu}\right)^{8/3}\frac{\mathrm{h}\nu^3}{\mathrm{c^2}}\int_{\mathrm{x_{in}}}^{\mathrm{x_{out}}}\frac{\mathrm{x}^{5/3}}{\mathrm{e^x}-1}\mathrm{dx} \tag{1.6}$$

where R_* is the white dwarf radius, i is the disk inclination, D is the observer-white dwarf distance, T_* is the stellar effective temperature, ν is the frequency, and $x = h\nu/k_\mathrm{B}T_\mathrm{disk}$, where T_disk is the disk temperature. The remaining parameters, k_B, h, and c, are the Boltzmann constant, the Planck constant, and the speed of light. In this equation the Planck function is used to model the flux emitted by the debris disk by integrating between the inner and outer radii of the disk. The temperature of the dust in the disk (and the proxy x variable) is related to the physical radial distance (Chiang & Goldreich 1997), and therefore the total emitted flux can be determined by integrating between x_in and x_out. The effect of inclination on the observable emitting surface area is given by the cosine term, with the observed flux decreasing by the square of D.

The flat disk model is degenerate between the disk inclination, and inner and outer disk radii as both the inclination and radial width determines the observable emitting surface area of the disk. However, some constraints can be placed. The inner disk radius, that can be well modelled by accurate near-infrared data, is typically at the distance that corresponds to a disk temperature of 1200−1500 K as this is the sublimation temperature range of dust grains (Jura 2003; Jura et al. 2007*a*). Thus, the dust disk does not extend to the white dwarf, but instead the inner region is entirely gaseous. The outer disk radius is typically less constrained due to poor longer wavelength data and the aforementioned degeneracy resulting in many scenarios that could fit the data (Girven et al. 2012; Bergfors et al. 2014), although narrow disks are thought to be common that may break this degeneracy (Rocchetto et al. 2015). It has been seen that the outer disk radii can extend to roughly 1 $\mathrm{R_\odot}$ (Farihi et al. 2008), which is also the Roche limit for typical asteroid densities, and white dwarf masses and radii (Farihi et al. 2008). Therefore, it appears that circumstellar debris disks are usually completely within the Roche limit of the star.

The majority of debris disks have been well fitted by the flat disk model. However, infrared excesses seen in two stars, GD 56 and GD 362, cannot be fitted well by this model alone, but they may be explained by a flared or warped disk (Jura et al. 2007*a*,*b*). In other

systems, narrow dust disks have been observed at $4-8\,\mu$m suggesting that there is a lack of dust in the radially inner section of these disks (Bergfors et al. 2014). Furthermore, the lack of detectable infrared excesses at the majority of polluted DA white dwarfs implies that the material is being accreted from a narrow or optically thin disk (Rocchetto et al. 2015). Recent work has shown that most dust debris not is static, but are varying in dust surface area (Swan et al. 2019). Thus, it is becoming apparent that the canonical flat disk model will need to be built upon in order to explain these new observations.

Circumstellar Gas

As well as the observed dust disks, eight stars also exhibit a gas component to the debris disk detected via double-peaked Ca II triplet emission (Gänsicke et al. 2006, 2007, 2008; Melis et al. 2012*a*; Farihi et al. 2012*a*; Wilson et al. 2014; Guo et al. 2015). Currently, only stars with atmospheric metals and a dust disk have been seen to have circumstellar gas. The Ca II emission has been observed to be velocity broadened and shifted, and, assuming Keplerian orbits, the orbital radii of the gas can be determined (Gänsicke et al. 2008). Interestingly, it has been found that the dust and gas radially overlap (Brinkworth et al. 2009; Melis et al. 2010) with the observed maximum gas velocity corresponding to an inner radius of $10-20\,\mathrm{R_{WD}}$. This is also the typical inner dust radius as interior to this the dust grains will sublimate. As the observed Ca II is not emitted from gas interior to this radius it cannot be caused by the dust sublimation, but rather, it could potentially be due to processes occurring within the debris disk (Jura 2008; Metzger et al. 2012; Kenyon & Bromley 2017*b*). This somewhat links the circumstellar dust and gas, although it is not known why circumstellar gas is not seen at all white dwarfs that have a dust disk.

Atmospheric Metals

It should be noted that all planetary debris disk hosting white dwarfs have atmospheric metals, however not all polluted white dwarfs have observable debris disks. The first to exhibit both was G 29−38 with Ca, Mg, and Fe detected in 1997 (Koester et al. 1997).

Following the accretion of material from the circumstellar debris disk onto the white dwarf atmosphere, metal absorption features can be seen. Although this process was unknown at the time, the first white dwarf with atmospheric metals was seen in 1917 with Ca H & K lines detected (van Maanen 1917). While dedicated studies discovered metals in specific white dwarfs, in 2003 the first large search for heavy elements in DA

white dwarfs was conducted and found several new DAZs (Zuckerman et al. 2003). It has now been well established that the observed absorption lines in most white dwarfs are due to the ongoing accretion of circumstellar material (von Hippel et al. 2007; Farihi et al. 2008). This is due to short diffusion timescales that cause heavy elements to rapidly sink out of the observable atmosphere on timescales orders of magnitude shorter than the cooling age (Koester 2009). However, depending on the age and composition of the white dwarf, this inference of ongoing accretion from a debris disk may not always be the case. For DA white dwarfs with a cooling age of tens or hundreds of Myr and no or small convection zones (Althaus et al. 2010), diffusion timescales are on the order of one year (Koester 2009). However as the convection zone increases with age, older DAs have longer diffusion timescales. DBs have large convection zones and typically have diffusion timescales up to 10^6 years (Koester 2009). Therefore, for young DA any observed atmospheric metals are from ongoing accretion, whereas for DBs or older DAs, metals may still remain in the photosphere from a previous accretion event(s). For DAs younger than tens of Myr radiative levitation of atmospheric metals occurs and thus, observed metals may be retained from previously accreted bodies (Koester et al. 2014). For stars older than several hundred Myr, atmospheric carbon may be seen due to dredge up from the core (Koester et al. 1982; Koester & Kepler 2019).

This means that any observed heavy elements are potentially indicative of the composition of the accreted body. To date, 20 heavy elements have been detected in the atmospheres of white dwarfs (Zuckerman et al. 2007, 2011; Gänsicke et al. 2012; Xu et al. 2013, 2017; Hollands et al. 2018*a*), including volatiles (C, N, P, S), rock-forming elements (Mg, Si, Fe, O), refractory lithophiles (Al, Ca, Ti), and siderophiles (Cr, Mn, Ni).

The largest variety of heavy elements in a white dwarf is GD 362 with 16 (Gianninas et al. 2004). The most common absorption features are that of Ca (H & K lines) followed by Mg and Fe (Jura & Xu 2013). Due to the strength of the Ca lines they can typically be detected via low-resolution spectroscopy with over 1500 polluted white dwarfs discovered. One of the largest surveys of white dwarfs was done using SDSS (Ahn et al. 2012) observations with multiple studies detecting calcium and other elements in hundreds of white dwarfs (Dufour et al. 2007; Koester et al. 2011). Observations as a part of the Supernova 1a Progenitor Survey (SPY), using the VLT, discovered calcium and occasionally magnesium in hundreds of stars (Koester et al. 2005*a*). Dedicated surveys have been undertaken using the *HST* and the Keck telescopes to detect silicon and calcium, (Zuckerman et al. 2003,

2010; Koester et al. 2014), with the aim of determining the frequency of the occurrence of atmospheric metals.

Due to the large number of polluted white dwarfs observed, conclusions about the accreted parent body compositions can be reached. It should be noted that accurate compositions of Solar System bodies have been useful in the interpretation of white dwarf observations (Lodders 2003). For stars with atmospheric Mg, Al, Fe, and O, it has been found that the compositions of the accreted bodies are similar to the bulk Earth (Jura & Xu 2013; Wilson et al. 2016; Hollands et al. 2018*a*). However, a compositional variety of accreted planetesimals exists that is comparable to the Solar System meteorite, asteroid, and minor planetary body families (Gänsicke et al. 2012; Xu et al. 2013; Jura et al. 2015).

Furthermore, several white dwarfs have been observed with parent body compositions that are indicative of a range of planetary features. For example, by dividing the abundances of the siderophile elements to that of iron, and comparing the ratios to inner Solar System samples it has been claimed that planet cores have been accreted in multiple systems (Melis et al. 2011; Gänsicke et al. 2012). By comparing the abundances of rock-forming elements to the refractory lithophiles it has been seen that accreted bodies around some white dwarfs exhibit the same composition as crustal rocks in the Solar System (Zuckerman et al. 2011; Kawka & Vennes 2016). This indicates that planetary body differentiation has occurred in these exoplanets. While it has been found that most bodies are dry in nature (Jura & Xu 2012), two white dwarfs seemingly have an oxygen excess (Farihi et al. 2011, 2013*b*), as found by pairing oxygen with other rock-forming elements and interpreting the excess oxygen as coming from accreted water.

Finally, one white dwarf has an accreted parent body composition very similar to comet Halley (Xu et al. 2017), showing that exocomets are formed in these systems, and have survived the giant phases. Interestingly, in a study of 230 DZs spanning a cooling age range of 1−8 Gyr, the abundances of heavy elements were seen to decrease over time implying that parent reservoirs of the bodies may be depleting (Hollands et al. 2018*a*).

1.2.3 Dynamical Studies of Disk Formation and Evolution

Important to the understanding of planetary systems around white dwarf stars is knowledge about the dynamics of the minor planetary bodies; what is the initial architecture, how are they gravitationally perturbed, how are they tidally disrupted, and how are they accreted onto the white dwarf. Briefly, it is thought that this occurs in many stages:

i) the planetary body is gravitationally perturbed into a Roche limit crossing orbit;

ii) the body fragments due to tidal forces;

iii) the debris disk forms from the remaining material;

iv) the disk is circularised and flattened;

v) the material is transported to the inner edge of the debris disk;

vi) the metals are accreted onto the white dwarf atmosphere.

From an observational perspective, information can be obtained that can shed light on a few, but not all, of these stages, whereas theoretical work has been conducted that can be combined with the observations to form a somewhat complete picture. Variability in the circumstellar environment of white dwarfs has been observed and subsequently there have also been theoretical studies into the evolution of debris disks to explain the observations.

Parent Body Perturbation

The tidal disruption model, that has provided a good basis for interpreting the observations, requires a parent reservoir that planetary bodies are perturbed from. So far, observations aimed at detecting such a reservoir, for example similar to the Solar System main belt, have been unsuccessful (Farihi et al. 2014). However, theoretical work studying the dynamics and potential architectures of these systems has continued unabated.

While the exact dynamical scenarios have many differences it is useful to highlight some commonalities between the models. The simulations typically encompass the main sequence lifetime of the star, the evolution through the giant phases, and finally the white dwarf phase. The scenarios are initially composed of major or minor planetary bodies in stable orbits, following planetary formation and clearing of the protoplanetary disk.

As the central star evolves through the giant phases, the stellar radius increases and any inner planetary bodies are engulfed (Mustill & Villaver 2012; Nordhaus & Spiegel 2013). This is important as it means that the observed debris disks must be formed from

bodies that are initially outside of the maximum stellar radius. Thus, any tidally disrupted bodies must have a high eccentricity as their initial semi-major axes would probably be beyond one AU. Stellar mass loss occurs during the giant phases (Vassiliadis & Wood 1993) that increases the orbital radii of surviving planetary bodies (Sackmann et al. 1993). This can cause bodies in previously stable orbits to become unstable during the white dwarf phase (Debes & Sigurdsson 2002). In the following scenarios there are three main outcomes following an interaction between two bodies, assuming the bodies do not collide:

i) ejection from the system;

ii) collision with an additional planet or planetesimal;

iii) collision with the white dwarf or tidal disruption of the body.

An interesting result of the stellar mass loss during the giant phases is that it can lead to the increase of the Hill stability spheres of two planets (Debes & Sigurdsson 2002). The Hill sphere is approximately the area within which a smaller mass would be substantially gravitationally attracted to a more massive body. Thus, when the Hill spheres of two bodies overlap it leads to interactions between the bodies with one potentially perturbed into the white dwarf vicinity. Research into planetary system architectures that only include multiple planets (i.e. no minor planetary body belt) has been done using: a range of the number of planets, the stellar and planetary masses, the orbital radii, and the separation between planets (Veras et al. 2013; Mustill et al. 2014). It was found that for two and three Jupiter-like planet systems, the most common occurrence is ejection from the system, although perturbation into a Roche limit crossing orbit is possible.

It seems that moons may be ejected from the planet-moon system via interactions with another planet (Payne et al. 2016, 2017). This suggests that if the moons are subsequently perturbed into orbits that pass within the Roche limit of the star they could also be the cause of the observed atmospheric metals and debris disks.

The majority of models have focused on the single white dwarf plus one planet and a minor planetary body belt scenario, such as:

- *a Jupiter-like planet with an interior asteroid belt.* Using the same physical and

orbital properties as the Solar System counterparts it was found that minor bodies within an asteroid belt that are in mean motion resonances with the planet can be easily perturbed via eccentricity pumping that may result in a Roche limit crossing orbit (Debes et al. 2012). To match the observed frequency of white dwarf planetary systems the asteroid belt would have to be up to 10^5 times the mass of the Solar System asteroid belt. This amount of material around main sequence stars has not been empirically rejected (Wyatt 2008), although it is not known if such a belt can survive into the white dwarf phase. This architecture has been generalised for a range of major planet masses and eccentricities (Frewen & Hansen 2014).

- *a Neptune-like planet with an exterior Kuiper Belt.* It was found that whilst exocomets can survive into the white dwarf phase and can be scattered inward by a Neptune-like planet, additional inner major planets are needed to further perturb minor bodies into Roche limit crossing orbits (Bonsor & Wyatt 2012). Perturbation of exocomets from Kuiper Belt like reservoir into Roche limit crossing orbits is rare and cannot reproduce the total mass of planetary material seen in white dwarfs (Jura et al. 2009). This rarity may be seen in the frequency of observed exocomets (compare the number of accreted rocky bodies, e.g. Hollands et al. (2018*a*), with the one white dwarf exhibiting remnants of an accreted comet, Xu et al. (2017)).

- *minor planetary body belts interior or exterior to three planets.* By varying the planetary mass and separation, the observed atmospheric metal frequencies, discussed below, can be reproduced by a series of Super Earth to Neptune mass planets and an interior minor planetary body reservoir (Mustill et al. 2017).

- *an interior asteroid belt with two exterior planets.* It has been shown that secular resonances between the planets and the asteroid belt can cause eccentricity pumping in asteroids that leads to Roche limit crossing orbits (Smallwood et al. 2018).

Several studies have been conducted into the dynamics of major and minor planetary bodies around a white dwarf in a wide binary system. It has been suggested that for a Neptune and Kuiper Belt scenario, galactic tides may perturb the secondary star that interacts with the major planet that then perturbs the minor planetary bodies (Bonsor & Veras 2015). Another scenario that may perturb planets is Kozai−Lidov mechanism (Hamers & Portegies Zwart 2016; Petrovich & Muñoz 2017; Stephan et al. 2017). Via this

method the wide binary companion can induce a torque on planetary bodies orbiting the white dwarf that causes eccentricity pumping and can lead to Roche limit crossing orbits. These models propose the need for a stellar binary companion in order to induce Roche limit crossing orbits of planetary bodies, however it is not empirically known if a companion influences a planetary system around the white dwarf. To date, observational studies have focused on single stars and thus, observations of planets in white dwarf binaries is required to determine the viability of these dynamical models.

As will be discussed below, dynamical perturbation models are important as various planetary system architectures can perturb different amounts of minor planetary bodies to within the white dwarf Roche limit over the lifetime of the system. This can be observed as frequencies of the occurrence of atmospheric metals and debris disks over the white dwarf cooling age and compared to the model predictions in order to potentially learn about post-main sequence planetary system architectures.

Debris Disk Formation

Independent of system architecture, following the perturbation of a body beyond the Roche limit of the white dwarf it is thought that a debris disk forms via tidal disruption. For larger rocky and icy bodies fragmentation via tidal disruption is likely to occur regardless of white dwarf temperature (Brown et al. 2017), whereas smaller rocky and icy bodies might completely sublimate before a disk forms. The formation of the debris disk not well understood, but a few studies have been conducted to try to understand this process. By simulating a highly eccentric, strengthless body consisting of 5000 particles with a pericentre within the white dwarf Roche limit it was found that tidal disruption forces can create collisionless eccentric debris rings on the same orbit as the original body (Debes et al. 2012; Veras et al. 2014). It has been shown that the debris ring can then circularise and shrink via PR-drag with a timescale on the order of a million years (Veras et al. 2015). To date, contracting rings have not been observed (Farihi 2009) suggesting that other processes, such as sublimation or collisions at periastron (Wyatt et al. 2010; Debes 2011), may be acting to accelerate disk formation.

Evolution of the Disk and Accretion onto the White Dwarf

In the general picture of the optically thick, flat debris disk the dust extends from the Roche limit (or the periastron of the destroyed parent body; Veras et al. 2014) to the

sublimation radius. The dust at the inner edge is sublimated at temperatures around 1200−1500 K (von Hippel et al. 2007) with the dust at greater orbital radii shielded from the white dwarf radiation (Jura 2003). Therefore, it is thought that all white dwarfs with a debris disk have circumstellar gas interior to the sublimation radius that is then accreted onto the white dwarf (Rafikov 2011*b*), potentially detected via spectroscopy in two sources (Gänsicke et al. 2012). Interestingly, circumstellar gas at greater orbital radii, co-spatial with the dust disk, has been observed at several stars (Gänsicke et al. 2006, 2007, 2008; Melis et al. 2012*a*; Farihi et al. 2012*a*; Wilson et al. 2014; Guo et al. 2015). The source of this observed gas is currently unknown. It has been proposal that collisional cascades between dust could occur that produces gas and could also cause a variation in dust surface area and observable infrared flux (Kenyon & Bromley 2017*a*,*b*,*c*).

As the dust at the inner disk edge is sublimated it is thought that exterior, unshielded dust spirals in due to PR-drag (Rafikov 2011*a*; Bochkarev & Rafikov 2011). If there is gas co-spatial and coupled with the dust, then the dust will experience gas drag that could increase the rate at which it moves inward and is accreted (Rafikov 2011*b*; Metzger et al. 2012). Therefore, over time, the disk narrows from the outer edge inwards.

The final stage of the planetary material is the accretion onto the white dwarf. The accretion rate can be determined empirically by spectroscopic observations of atmospheric metals (Zuckerman et al. 2010; Koester et al. 2014). It has been shown that the observed accretion rates for young DAZ white dwarfs can be explained by the instantaneous accretion of material via PR-drag alone (Rafikov 2011*a*). However, for degenerates with longer diffusion timescales, higher accretion rates have been determined that are inconsistent with PR-drag (Girven et al. 2012). A method that can reproduce the observed accretion rate is that gas produced via dust sublimation interacts with the dust that increases the inward drift speed of the dust and therefore, accretion rate (Rafikov 2011*b*). As this is a positive feedback it can cause a runaway accretion episode that might result in the accretion of the entire disk (Metzger et al. 2012). However, several DBZs with high accretion rates have detected dust disks which implies that either this method is not efficient or that additional tidal disruption events have occurred that replenishes the disk (Wyatt et al. 2014).

By studying debris disk evolutionary processes it may also be possible to explain the observed circumstellar dust and gas variability. It has been proposed that collisions within the disk (Kenyon & Bromley 2017*a*,*c*), perturbations of dust out of the disk (Farihi et al.

2018), and impacts between the disk and additional bodies (Xu & Jura 2014) could be the cause of variability, however this is an active area of research and no clear picture has yet to emerge. The observations and theory of debris disk variations are discussed below.

1.2.4 The Frequency of White Dwarf Planetary Systems

As the field of white dwarf exoplanetary science developed, the focus turned from establishing a connection between atmospheric metals and debris disks to probing the overall nature of the planetary systems. Following the formation of the link between infrared excesses and atmospheric features (von Hippel et al. 2007), studies were initiated to understand the frequency of planetary systems, as a key prediction of the dynamical models is the value of this frequency and how it varies over cooling age (Debes et al. 2012; Veras et al. 2013; Mustill et al. 2014). Thus, from the frequency of the occurrence of atmospheric metals or circumstellar debris disks, it is possible to learn about planetary system architecture. These can then be compared planetary systems around main sequence stars.

Initial Findings

Firstly, it is worth highlighting several notable findings from debris disk and atmospheric metal studies. It was discovered that all white dwarfs with a debris disk observable in the infrared also exhibit atmospheric metals (von Hippel et al. 2007; Farihi et al. 2008, 2010), however many stars with atmospheric metals do not possess observable debris disks. For stars undergoing steady state accretion (such as DAZ white dwarfs), infrared excesses are only typically seen if the observed accretion rate is above $10^8\,\mathrm{g\,s^{-1}}$ (Jura et al. 2007*a*). Although this is not seen for DBZ stars, as multiple stars with an accretion rate substantial greater than $10^8\,\mathrm{g\,s^{-1}}$ do not have an observable disk in the infrared (Girven et al. 2012). However, due to the longer diffusion timescales in DBZs the observed accretion rate is an average rate, and the actual current rate may be lower (Farihi et al. 2012*b*). The opacity of white dwarf atmospheres is related to temperature and for cooler stars it is easier to detect metals (Koester & Wilken 2006). This results in the observational bias that atmospheric metals are only detected in hot white dwarfs with a high accretion rates. Therefore, due to the correlation between accretion rate and detection of a debris disk, this bias results in a higher frequency of the presence of debris disks around hotter polluted white dwarfs (Bergfors et al. 2014). Thus, in order to accurately determined the frequency of white dwarf planetary systems and infer their architectures, unbiased surveys are needed.

Larger Circumstellar Debris Disk Surveys

Following the initial studies, *Spitzer* was utilised to conduct observations of larger samples to determine infrared excess frequency. A sample of 122 white dwarfs was chosen based on Two Micron All-Sky Survey (2MASS) Ks-band brightness (Cutri et al. 2003) with *Spitzer* photometry taken at 4.5 and 7.9 μm (Mullally et al. 2007). Unlike previous studies, this sample was not selected based on the presence of atmospheric metals and thus it is unbiased in composition. Two disks were discovered resulting in a nominal debris disk frequency of 1.6 per cent. In another study, a literature search of polluted white dwarfs with *Spitzer* observations was done with a debris disk frequency range determined to be $1-3$ per cent (Farihi et al. 2009).

By selecting 117 stars from the Palomar-Green (PG) white dwarf catalogue (Liebert et al. 2005), debris disks were searched for by determining K-band excesses (Barber et al. 2012). Targets with an excess at this wavelength were then followed up with *Spitzer* observations with five disks detected yielding a frequency of 4.3 per cent. However, half of all disks are not detectable at K-band and therefore, in this study bona fide disks could have been missed in the K-band and subsequently not followed up, meaning this frequency is potentially unreliable. The *Spitzer* archive has been mined with 15 out of 381 white dwarfs found to have debris disks giving a frequency of 3.9 per cent (Barber et al. 2016). To date, the only study unbiased in atmospheric composition and infrared brightness selected 134 white dwarfs from the PG and SPY catalogues (Liebert et al. 2005; Koester et al. 2009) based on effective temperature and ultraviolet brightness (for corresponding *HST* observations). A frequency of 3.7 per cent was determined (Rocchetto et al. 2015).

Interestingly, this study also found that narrow debris disks are common (Rocchetto et al. 2015). The small radial width of disks lead to faint disks that are only observable beyond 4.5 μm and could explain white dwarf debris disks with a small fractional luminosity (the ratio between the disk and the stellar flux and can be used as a proxy of the observable emitting surface area of the dust).

Whilst *Spitzer* can provide sensitive observations it cannot cover the entire sky and thus wide-field surveys such as the UKIRT Infrared Deep Sky Survey (UKIDSS; Lawrence et al. 2007) and *Wide-field Infrared Survey Explorer* (*WISE*; Wright et al. 2010; Mainzer et al. 2011) have been used to increase the sample size by two orders of magnitude over dedicated campaigns. From a cross-correlation of DA white dwarfs in SDSS and UKIDSS,

it was found that 12 out of 1884 stars had infrared excesses in the K-band (Girven et al. 2011). However, follow-up *Spitzer* observations identified contamination in at least two targets (Farihi et al. 2012*a*). This highlights a common problem with wide-field surveys that have a relatively large point spread function (PSF) as contamination via a background object or binary companion is likely to occur. Therefore, assuming half the debris disks in the K-band are not detectable this yields a disk frequency of 0.8 per cent.

Using a cross-correlation of SDSS and *WISE*, 395 degenerates were found to be detected by *WISE* (Debes et al. 2011). 52 disk candidates were found, with six believed to be genuine disks giving a frequency of 1.5 per cent. However, previous and follow-up observations found two of these to either have a L-type companion (Steele et al. 2009) or background contamination (Barber et al. 2014) yielding a frequency of 1.0 per cent. This emphasises the need for follow-up observations of potentially contaminated targets.

WISE has also been utilised to detect infrared excesses at 1474 degenerates chosen from 2MASS and the McCook & Sion white dwarf catalogue (McCook & Sion 1999; Hoard et al. 2013). Infrared excesses were detected at twelve stars resulting in a debris disk frequency of 0.8 per cent. It should be noted that no follow-up observations of these have been conducted. One final point is, whilst *WISE* and UKIDSS covers the entire sky, they are significantly less sensitive than *Spitzer* and the upcoming *James Webb Space Telescope* (*JWST*). Therefore faint disks or disks around faint stars may be missed in these wide-field surveys, highlighting the need for follow-up, dedicated observations.

Surveys to Study Atmospheric Metals

Multiple studies have also been conducted to determine the frequency of the presence of atmospheric metals. This gives an independent check of the frequency of planetary systems around white dwarfs and can be compared to the frequency of debris disks. Ground-based surveys of both DA and DB white dwarfs indicate a nominal frequency of the presence of atmospheric metals to be 25−30 per cent, an order of magnitude higher than the debris disk frequencies mentioned above (Zuckerman et al. 2003, 2010). This is in agreement with a more sensitive, space-based study that used *HST* observations to determine that 56 per cent of DAs have evidence of an accreted planetesimal (Koester et al. 2014). As this sample included white dwarfs with $17\,000\,\mathrm{K} < T_{\mathrm{eff}} < 27\,000\,\mathrm{K}$ the effects of atmospheric radiative levitation had to be accounted for when determining which stars are currently accreting. Of the entire sample 27 per cent of stars are undergoing accretion from a circumstellar

debris disk. All of these atmospheric metal frequencies are an order of magnitude greater than the debris disk frequencies. A recent study has proposed that narrow or optically thin dust disks, or completely gaseous disks, could be the explanation for the dearth of debris disks observable in the infrared (Bonsor et al. 2017).

Binary Star Studies

All the studies mentioned previously have empirically aimed to determine the debris disk and atmospheric metal frequencies around single white dwarfs. Whilst, the debris disk frequency for binary systems has not been determined, the frequency of atmospheric metals in wide binary white dwarfs has been found to be roughly 20 per cent (Zuckerman 2014). However, as noted by that author, the targets in the study are simply white dwarfs in wide binaries with high-resolution spectroscopic observations taken from the literature and thus, the reported frequency is somewhat biased. Therefore, an unbiased survey is needed to determine the atmospheric metal frequency in binaries and probe dynamical models of pollution in binary systems (Bonsor & Veras 2015; Hamers & Portegies Zwart 2016; Petrovich & Muñoz 2017; Stephan et al. 2017; Smallwood et al. 2018).

Connections to Dynamical Studies

By comparing the aforementioned surveys it can clearly be seen that the presence of metals is a more sensitive indicator of planetary systems than an infrared emitting debris disk, as there is a dearth of detectable debris disks. Therefore, using the nominal pollution frequency and comparing to dynamical models it appears that systems with an interior asteroid belt and a Super Earth or Neptune mass planet yields the observed frequency (Mustill et al. 2017). Dynamical models typically report planetary frequency over white dwarf cooling age (Debes et al. 2012; Veras et al. 2013; Mustill et al. 2014) and thus, to compare the observations to these models larger samples are required to accurately determine the frequency of planetary systems across multiple age ranges.

1.2.5 Circumstellar Debris Disk Variability

To date, no variation in the strength of the white dwarf atmospheric metal absorption features has been seen. However, variability has been observed in other tracers of planetary systems discussed below. While there is still substantial work to be done to understand

the fate of planetary bodies around white dwarfs, observations and theory of debris disk variability may provide valuable insight into the destruction of minor planetary bodies.

Infrared Flux Variation

The first evidence of infrared flux variation attributed to a white dwarf debris disk was around WD 0959−0200 (Xu & Jura 2014). Using *Spitzer* and *WISE* photometry a 35 per cent flux decrease over 300 days was seen. Interestingly, this star also has circumstellar gas observed via Ca II triplet emission, but it has not been seen to vary (Farihi et al. 2012*a*). While it may be possible that the process(es) that cause infrared flux variation and the presence of gas may be linked, these mechanisms are currently not known. Following this discovery, multiple studies were conducted with the aim to find more systems with infrared emission variation. The polluted white dwarf GD 56 was previously noted to have an infrared excess that could not be accurately fitted by the flat disk model. *Spitzer* and *WISE* observations over 11 years show a 20 per cent flux increase and subsequent decrease (Farihi et al. 2018). This has been attributed to the production and destruction of dust in a narrow region of the disk as the infrared colour does not vary. The infrared flux dropped to pre-increase levels suggesting that any disturbed dust has settled back into the disk.

A third degenerate, G 29−38, has been observed to have infrared flux variation of the 10 μm silicate feature (Xu et al. 2018). However, this star is a ZZ Ceti (McGraw & Robinson 1975) and therefore flux variations in the infrared are challenging to interpret as they may be caused by additional heating of the dust via the increased stellar luminosity instead of any processes occurring within the debris disk. Recently, the first survey studying the long-term flux variation in debris disks was conducted (Swan et al. 2019). *WISE* photometry of 35 white dwarfs taken over seven years was analysed and it was found that the majority of these systems are significantly varying in flux. This suggests that the process(es) governing the production and destruction of dust is common.

The cause of the observed infrared flux variation is currently unknown, but the increase (decrease) of flux due to a debris disk is likely due to an increase (decrease) in the observable emitting surface area of the dust (Farihi et al. 2018). However, detailed models are needed to accurately explain the process(es) occurring. One scenario could be the impact of additional minor planetary bodies with the debris disk as the incoming body could disrupt the disk via collisions that would increase the observable surface area (Jura 2008; Xu & Jura 2014). Dust could then settle back into a flat disk to return the observed

flux back to pre-collision levels. Collisions may produce gas that could recondense into dust that would also cause variations in the emitting surface area (Metzger et al. 2012).

The modelling of the stochastic accretion of minor planetary bodies on yearly and decadal timescales has shown that it is possible to reproduce the observed amount of atmospheric metals (Wyatt et al. 2014). These events may also cause infrared flux variation due to the disruption of the dust disk. Another scenario could be the creation and destruction of dust via collisional cascades within the debris disk (Kenyon & Bromley 2017*b*). If a sufficiently large body exists within the disk, collisions may result in a periodic brightening and fading of disk luminosity. Finally, it is also possible that a large body exterior to the disk gravitationally perturbs dust in a resonance orbit out of the plane of the disk, thereby increasing the surface area of the disk (Xu et al. 2018). Understanding whether or not these processes are occurring, and at what level, is important in providing insight into the circumstellar environment in these systems.

Variation in Circumstellar Gas

In addition to infrared variation due to changes in the observable circumstellar dust, a subset of white dwarfs with a debris disk also show variability in the observed flux and shape of the double-peaked Ca II emission from the circumstellar gas. Around two stars, SDSS J084539.17+225728.0 and SDSS J104341.53+085558.2 (hereafter SDSS J0845+2257 and SDSS J1043+0855), the shape of the lines evolve over yearly and decadal timescales (Wilson et al. 2015; Manser et al. 2016*a*). The circumstellar gas in these systems is on an eccentric orbit typically within 1 $R_{\odot}$ and therefore is within the potential well of the white dwarf. Due to the effects of general relativity, the orbit of any body on an eccentric path around a massive body will precess due to the effect of space-time curvature. Thus the observed variation is due to the viewing angle rather than physical processes within the disk. Interestingly, in SDSS J161717.04+162022.4 (hereafter SDSS J1617+1620), the previously seen Ca II emission feature has disappeared over a decade (Wilson et al. 2014) that could be due to re-condensation of the gas into dust or accretion onto the star (although there is no evidence for changes in the accretion rate). Interestingly, in HE 1349−2305 changes in the strength of the Ca II lines have been seen to occur on yearly timescales (Dennihy et al. 2018). This is thought to be too short to be explained by relativistic precession, however the authors claim that density waves propagating through the gaseous debris disk potentially caused by an external perturbator such as an orbiting planet or a fly-by event.

Furthermore, variation in circumstellar gas absorption features, such as those of Fe II, have been observed in at least one system, WD 1145+017 (Redfield et al. 2017; Cauley et al. 2018), as will be discussed more below.

Notable White Dwarf Planetary Systems

Amongst the systems known to vary either photometrically or spectroscopically, two white dwarfs should be highlighted as observations of these stars have revealed considerable information about the nature of debris disks around white dwarfs. SDSS J1228+1040 is the prototype white dwarf with a gas debris disk (Gänsicke et al. 2006), and to date, has the strongest Ca II triplet emission. This star is one of the highest polluted DAs (Gänsicke et al. 2012) and infrared photometry indicates the presence of a dust debris disk (Brinkworth et al. 2009), although the observed infrared excess is not well fitted by the canonical flat disk model. Recently, it has been discovered that the dust disk is varying with a 20 per cent flux decrease found (Xu et al. 2018). Following the initial discovery of circumstellar gas, additional observations of the Ca II triplet discovered that the shape of the features was varying over the timescales of a decade due to relativistic precession (Manser et al. 2016*b*). Interestingly, spectroscopy of this object has revealed a 2 hr variation in the Ca II triplet that have been interpreted as a planetesimal orbiting on an eccentric path within the Roche limit of the star (Manser et al. 2019). It has been proposed that collisions between the planetesimal and the dust disk could be the cause of the observed gas, however both detailed models and further observations are needed to probe this idea. If this is the case then the presence of a planetesimal may explain why the gas has remained in an eccentric orbit over thousands of orbits without being circularised.

The strongly metal polluted and dust debris disk hosting WD 1145+017 showed evidence for the first white dwarf with transiting planetary debris discovered via periodic photometric dips in *Kepler* data (Vanderburg et al. 2015). Follow-up observations confirmed several main bodies (potentially solid bodies or opaque dust clouds) orbiting on a roughly 4.5 hr co-planar orbit with the transits evolving on daily timescales (Gänsicke et al. 2016; Rappaport et al. 2016). This period puts the orbiting bodies at approximately the Roche limit of the star and therefore these observations have been interpreted as a disintegrating planetesimal. Furthermore, as well as 11 heavy elements detected in the stellar atmosphere, several planet-forming elements (Mg, Ca, Ti, Cr, Mn, Fe, and Ni) have been discovered in the gas-phase orbiting the white dwarf in the debris disk (Xu et al.

2016). The emission of the circumstellar gas has been seen to vary in shape and strength on minute to monthly timescales (Redfield et al. 2017) that has been interpreted to be due to precessing eccentric gas rings (Cauley et al. 2018). Multi-band photometry has indicated that the transits are deeper in the red compared to in the blue or ultraviolet, thought to be caused by reduced circumstellar absorption during transits due to shielding by the dust (Hallakoun et al. 2017; Xu et al. 2019). Therefore the dust and gas are co-planar and both occupy the line of sight.

While certain phenomena in the thoroughly observed stars are well understood, for example the relativistic precession of circumstellar gas in SDSS J1228+1040 or the planetesimal transits in WD 1145+017, there still exists many unanswered questions about the dynamical nature of debris disks around white dwarfs. Debris disk formation and evolution models discussed in Section 1.2.3 can help inform the overall picture, but additional models are needed to explain the observations detailed above. Answering questions such as "*how is circumstellar gas produced?*" and "*what is the cause of the infrared flux variability?*" is important to advance the understanding of post-main sequence planetary systems and will likely drive the field in the upcoming years.

Chapter 2

Formation Conditions of 0_2 in Comets

The formation of planets is like a gigantic snowball fight. The balls bounce off, break apart, or stick together, but in the end they are rolled up into one enormous ball, a planet-ball that has gathered up all the snowflakes in the surrounding area.

Claude Jean Allégre (1992)

The work presented in this chapter is based on work done for the paper by Rawlings et al. 2019, MNRAS, Volume 486, Issue 1, Page 10, in collaboration with J. M. C. Rawlings and D. A. Williams, reproduced with permission.

2.1 Introduction

Cometary material formed in the early outer Solar System is believed to be pristine in nature due to the absence of thermal processing following the end of the protoplanetary disk phase and the formation of comets. Thus, it is thought that the composition of cometary ices are representative of the chemical abundances in the nascent Solar System (Bockelée-Morvan & Biver 2017). Once a comet enters the inner Solar System the ices sublimate to form a coma that can be observed spectroscopically either by ground- or space-based telescopes, or by fly-by or orbiting spacecraft.

2.1.1 The *Rosetta* Mission

Launched in 2004, the *Rosetta* spacecraft, accompanied by the *Philae* lander, rendezvoused and studied comet 67P from 2014 to 2016 using a plethora of instruments (Boehnhardt et al. 2017; Taylor et al. 2017). On a 6.45 year orbit, 67P is a Jupiter-Family comet, however it appears to have been perturbed into its current path via an interaction with Jupiter in 1959 (Maquet 2015). From analysis of *Rosetta* data it was found that the D/H ratio is roughly three times larger than the typical value for Jupiter-Family comets (Altwegg et al. 2015) and somewhat typical of Oort-Cloud comets, suggesting 67P formed in the trans-Neptunian region.

The *Rosetta* mission has revolutionised the overall picture of comets (Altwegg et al. 2017; Bockelée-Morvan & Biver 2017; Jones et al. 2017; Snodgrass et al. 2017; Wooden et al. 2017). The previously held common view of a cometary nucleus was one of a dusty-snowball (Whipple 1950), however it is now clear that the inverse is true for 67P with ices accounting for approximately 10 per cent of nucleus by mass (Fulle et al. 2016). Furthermore, studies of nucleus structure have revealed the two lobes are likely separate cometesimals that underwent a low velocity collision within the last 1 Gyr to form the "neck" of the comet (Massironi et al. 2015; Jutzi & Benz 2017). It is thought that during each perihelion pass ices are sublimated away in successive layers (Guilbert-Lepoutre et al. 2015) with a depth of tens of metres of volatiles sublimated on each orbit (Keller et al. 2015), implying that hundreds of metres of material has been lost since perturbation onto its current orbit, although dust and re-frozen ice may have fallen back onto the nucleus surface (De Sanctis et al. 2015; Filacchione et al. 2016), suggesting that during cometary formation gasses were frozen out in a layered structure. Including the aforementioned studies, considerable work has been undertaken into the formation of 67P, and comets in general. Due to the observed ice and dust layering and the structure of the lobes it is thought the nucleus is an agglomeration of material potentially hierarchical growth or collisions between millimetre-sized icy dust grains (Bentley et al. 2016; Davidsson et al. 2016; Blum et al. 2017).

2.1.2 Volatiles in 67P

In addition to the study of the nucleus, various instruments onboard *Rosetta* were used to probe the dust and gas environment of the coma. Particularly, the ROSINA device

has permitted the accurate determination of the compositional abundances of a multitude of gas-phase molecules (Bockelée-Morvan & Biver 2017), including H_2O, CO, CO_2, O_2, and N_2, and exotic compounds such glycine (a pre-biotic simple amino acid; Altwegg et al. 2016). Several studies utilised these accurate observations to determine abundance ratios between key molecules, with a noticeable result being the O_2/H_2O of 1−10 per cent (3.8±0.9 per cent on average; Bieler et al. 2015), that is at least an order of magnitude higher than detected in interstellar environments (Goldsmith et al. 2011). O_2 appears to be isotropically distributed throughout the coma and its abundance ratio with H_2O does not vary over heliocentric distance suggesting that the O_2 distribution is fairly uniform across the comet nucleus surface and depth. Interestingly, following this discovery *Giotto* data of comet Halley was reanalysed and a similar O_2/H_2O ratio of 3.7±1.7 per cent was determined (Rubin et al. 2015*b*). Therefore, these values might in fact be typical regardless of dynamical history and thus, the O_2 abundance may be pristine in origin.

The Origin of Cometary Volatiles

The nature of volatiles in comets is an active area of research as it can reveal not only the chemical composition of the early Solar System, but it can also inform formation studies as isotopic ratios can be used as a proxy for formation location. Finally, it could be used to answer the question of whether or not cometary H_2O is the source of the terrestrial oceans (Altwegg et al. 2015; Bockelée-Morvan et al. 2015*b*; Willacy et al. 2015). Thus it is important to understand the physical and chemical environment in the protoplanetary disk that comets formed out of. One potential avenue for studying this environment is the analysis of simple molecular species that are believed to be pristine, such as the O_2/H_2O ratio, as this can reveal information such as the protoplanetary disk density, temperature and chemical composition. However, an important question remains; "*how primordial are molecules such as O_2?*" For example, are they formed in the protoplanetary disk and the proto-Solar nebula, or prior to this in the dark molecular cloud? During the early Solar System there is a vast array of chemical processing occurring in the gas- and solid-phase including collisional and radiogenic heating, radiolysis, photolysis, freeze out, and sublimation. Thus, answering this question is not trivial.

Since the *Rosetta* findings, multiple studies have aimed to understand how and when the O_2 is formed. It has been found that the observed O_2 abundance can be produced by radiolysis (the chemical reaction driven by the impact of high energy particles) of H_2O ice

in the early, dense proto-Solar nebula prior to accretion into a comet in the protoplanetary disk (Mousis et al. 2016). However, it is thought that this process is slow and therefore would require a molecular cloud with a long lifetime. Additionally, to produce the observed abundance all of the energy absorbed during impact would have to be used in the chemical reactions, with none lost via ionisation or heating. Recent laboratory work has shown that during the sublimation of H_2O as the comet enters the inner Solar System O_2 can be produced by the dismutation of H_2O_2 (where the molecule is simultaneously oxidised and reduced) to H_2O and O_2 (Dulieu et al. 2017). This would explain the lack of observed H_2O_2, however the reaction requires a complete conversion of the H_2O_2 to O_2 to explain the observed abundances.

In this study it is proposed that the O_2 observed in 67P is created during the collapse from the molecular cloud into the proto-Solar and protoplanetary disk and then agglomerated into a comet and eventually sublimated during a perihelion pass. If this is the case, it may be possible to use the empirical abundance ratios to trace the chemical evolution during the collapse phase. This has recently been studied using sophisticated astrochemical model and a specific protoplanetary disk model (Taquet et al. 2016), however the aim of this study is to see if a robust model can also reproduce the *Rosetta* observations.

The work presented in this chapter aims to use molecular abundance ratios that have previously been determined from *Rosetta* observations, and a chemical and physical model of the collapse phase from a dark cloud to the protoplanetary disk in order to determine the formation conditions of minor planetary bodies in the nascent outer Solar System. In Section 2.2 an overview of the observational studies of molecules in the coma of 67P is given. The chemical and physical comet formation model that was developed as a part of this study is presented in Section 2.3 with the results of reported in Section 2.4. Conclusions are discussed in Section 2.5.

2.2 *Rosetta* Observations of Molecular Ratios in 67P

In addition to permitting ground-breaking discoveries of the shape and structure of the nucleus (Gulkis et al. 2015; Keller et al. 2015; Massironi et al. 2015; Sierks et al. 2015; Thomas et al. 2015; Hirabayashi et al. 2016; Jutzi & Benz 2017), and of the dust in the coma (Rotundi et al. 2015; Wooden et al. 2017), *Rosetta* provided an unprecedented opportunity to study the gas-phase components of the coma of 67P, primarily via the

ROSINA instrument.

An unexpected result of these observations was the determination of the gas-phase O_2/H_2O ratio in the coma to be 1−10 per cent, with an average value of 3.8±0.9 per cent (Bieler et al. 2015). This range of values is at least an order of magnitude higher than typically seen in other interstellar environments (Goldsmith et al. 2011). Re-analysis of the *Giotto* data of comet Halley found a similar value of O_2/H_2O ratio in the coma of 3.7±1.7 per cent (Rubin et al. 2015*b*) suggesting this value may indeed be indicative of a family of comets and useful in studying their formation conditions. As O_2 and H_2O are somewhat correlated in emission (Bieler et al. 2015) it is thought this ratio can be used as a metric of O_2 abundance. The HO_2/O_2 and H_2O_2/O_2 ratios have also been determined to be 0.19 per cent and 0.06 per cent, respectively. However, the surface chemistry of HO_2 and H_2O_2 is not accurately represented in the model and therefore, these ratios will not be used when comparing the results of the simulations to the observed ratios. Furthermore, although multiple sulfur molecules were observed by ROSINA (Calmonte et al. 2016), the chemistry of sulfur is complex and beyond the scope of the model presented below, and therefore these observations are not considered.

The N_2/CO, $^{36}Ar/N_2$, and $^{36}Ar/H_2O$ abundance ratios have been calculated from the ROSINA observations (Balsiger et al. 2015; Rubin et al. 2015*a*), with values of 0.2−1.6 per cent (average = 0.6 per cent), 0.9±0.03 per cent, and 0.0001−0.0023 per cent, respectively. Whilst N_2 and CO are included in the chemical network of the model, ^{36}Ar is not, however it is correlated with N_2 (potentially due to a similar volatility) and so from the ratios above the N_2/H_2O value can be calculated to be 0.01−0.26 per cent. It should be noted that N_2 and CO are not well correlated with H_2O (Bieler et al. 2015). Therefore, it has been suggested that N_2/CO is a better tracer of N_2 abundance (Rubin et al. 2015*a*).

Finally, the ROSINA instrument was able to detect CO, CO_2, and H_2O simultaneously and over a range of cometary illumination conditions. Interestingly, a rather complex relationship between CO and CO_2, and H_2O was found with the observed CO/H_2O and CO_2/H_2O ratios highly variable and dependent on position on the nucleus illuminated (Hässig et al. 2015). This results in poorly constrained abundance ratios of 13−400 per cent and 8−800 per cent, respectively, and yields a gas-phase coma-based CO/CO_2 ratio of 50−162 per cent. This is significantly higher than the nucleus-based CO/CO_2 ratio of 7 per cent determined using the Ptolemy instrument on-board *Philae* (Brugger et al. 2016).

2.3 A Chemical and Physical Model of the Formation of the Solar System

From the observed molecular ratios it is possible to learn about the initial conditions in the outer Solar System and thus the formation conditions of comets via the utilisation of a chemical and physical model. Such a model is presented below and combines a complex gas- and solid-phase chemical network with a simple physical model of the collapse from a dark molecular cloud to a proto-Solar and protoplanetary disk representing the early Solar System. Molecular abundances are traced throughout and therefore the abundances in the final phase of the simulations should be indicative of cometary values as no additional thermal processing is thought to occur following formation.

The main part of the model is simulating the collapse phase. This collapse model has successfully been used previously to simulate proto-star formation and to probe the timescale of formation and the depletion of molecules (Rawlings et al. 1992). Initially, the gas is distributed uniformly in a sphere with a defined density (and density profile) and temperature, which then collapses via a modified free-fall (Spitzer 1978) until a defined final density is met. How the collapse is integrated into the proto-Solar and protoplanetary disk formation model is described more below.

It should be noted that for the purposes of determining the initial conditions of the Solar System constrained by the *Rosetta* observations it is assumed that the reported abundance ratios are indicative of a homogeneous composition throughout the coma and nucleus. However, it appears that there is a compositional variation over the nucleus as seen via differences in molecular abundances when observing the neck and the lobes (Fougere et al. 2016). There may also be compositional variation as a function of depth (Brugger et al. 2016), but from observations of refractory elements, both lobes of the nucleus have similar compositions potentially meaning they formed in the same region (Capaccioni et al. 2015). Furthermore, recent studies have shown that there are abundance variations in the coma due to differences in the illumination of the nucleus on daily and seasonal timescales (Hässig et al. 2015; De Sanctis et al. 2015; Filacchione et al. 2016; Raponi et al. 2016). Modelling these differences is beyond the scope of this study, and for the purpose of broadly determining the chemical and physical conditions in the Solar molecular cloud, the rather simplistic physical model presented here is thought to suffice. However future work could incorporate these findings into the physical model and study

if and how these effects change the findings presented below.

2.3.1 The Chemical Model

Prior to outlining the three phase physical model of a static molecular cloud (Phase I) that collapses (Phase II) into a proto-Solar/protoplanetary disk (Phase III), the chemical network used across all three phases will be described. It is proposed that the observed molecular abundances are primordial in nature and thus, it is thought that the molecules are formed prior to the protoplanetary disk phase and then frozen out on dust grains that agglomerate to form larger bodies and eventually a comet. Therefore, as it is assumed that no solid-phase chemistry occurs after freeze out, the determined molecular abundances are related solely to the chemical and physical initial conditions of the molecular cloud and the evolutionary history of the cloud during collapse.

In the chemical network there are 96 gas-phase and 22 solid-phase species including the main molecules observed by *Rosetta*, O_2, H_2O, CO, CO_2, and N_2, and the components and products needed for the formation and destruction reactions. These reactions comprise part of the network that consists of 1296 neutral-neutral and neutral-ion reactions in the gas-phase, and 134 reactions on grain surfaces and gas-grain transitions, such as freeze out, hydrogenation, and desorption. This comprehensive chemical model covering the formation and destruction channels of the concerned molecules means that abundance determination should be reasonably accurate.

To provide an insight into the gas-phase chemical reaction network included in the model, the chemistry of the protagonistic molecule O_2 will briefly be described. There are three main competing mechanisms for the formation and destruction of this molecule in the gas-phase:

$$O + OH \rightarrow O_2 + H \tag{2.1}$$

$$O_2 + C \rightarrow CO + O \tag{2.2}$$

$$O_2 \rightarrow O_2(\text{solid}) \tag{2.3}$$

with the freeze out and hydrogenation of O:

$$O + \text{grain} \rightarrow H_2O(\text{solid}) \tag{2.4}$$

Reaction 2.1 is the main formation mechanism for O_2. Both reactants in this reaction, O and OH, can be frozen out onto dust grains and hydrogenated to form H_2O ice, i.e. in the solid-phase, as exemplified in reaction 2.4. Once formed in the gas-phase, O_2 can be destroyed to form CO (reaction 2.2) or frozen out to form O_2 ice, as shown in reaction 2.3 (Hollenbach et al. 2009). Therefore, which of these competing processes is dominant is important in calculating the abundance of O_2. When there is a reservoir of C, the destruction of O_2 via reaction 2.2 is efficient (Wirström et al. 2016), however, following the complete conversion of O_2 and C to CO any remaining gaseous O atoms should follow reaction 2.1 to form O_2. Therefore, providing O > C and reaction 2.1 is more efficient than the freeze out of O, i.e. reaction 2.4, O_2 should be readily formed in the gas-phase which will then freeze out via reaction 2.3.

For the gas-grain reactions in the model there is a plethora of processes that can lead to the desorption of a molecule from the solid-phase to the gas-phase. These include photodesorption via interstellar radiation and cosmic rays, cosmic ray heating, and formation enthalpy driven desorption. A key difference between the first couple of these mechanisms is that whilst cosmic ray heating can cause heating throughout the bulk ice (and thus desorption can occur at any point with a sufficient temperature), photodesorption only affects the upper surface of the ice. This difference is taken into account by considering the chemical composition, and desorption energies and efficiencies on a layer by layer basis, using typical desorption process yields (Hollenbach et al. 2009). A simplified network of surface chemistry is included in the model. For example, the hydrogenation of O and OH gas molecules to H_2O, and reactions between O and OH, and CO to form CO_2 are permitted.

2.3.2 The Physical Collapse Model

To simulate the transition from the dark molecular cloud to the proto-Solar and proto-planetary disk a simple three phase collapse model is used. The physical conditions, given in Table 2.1, evolve over the phases described below with the chemistry tracked for a representative point in the simulation. The DLSODE code is used to solve the relevant

chemical and dynamical differential equations (Hindmarsh 1982). The three phases are as follows:

- A static dark or diffuse molecular cloud that represents the chemical environment of the proto-Solar nebula.
- A free-fall, homologous collapse that includes a simple contraction velocity retardation parameter, B, in order to model a quasi-static collapse incorporating effects such as magnetic braking, non-spherical effects, and disk vorticity (Rawlings et al. 1992).
- A high density, static proto-Solar/protoplanetary disk that simulates conditions in the early outer Solar System.

In the simulation, Phase I is set to have a duration of 10^7 years in order to model the lifetime of a molecular cloud (Miura et al. 2012; Meidt et al. 2015). The pertinent physical parameters to be changed being the density, n_{I}, gas and dust temperatures, $T_{\mathrm{g,I}}$ and $T_{\mathrm{d,I}}$, and extinction, $A_{\mathrm{v,I}}$ as these parameters influence the desorption rate during the collapse phase. It should be noted the freeze out of the gas onto grains is highly dependent on density and thus, will not occur for the low densities simulating an initial diffuse cloud, on the order of $100\,\mathrm{cm}^{-3}$ (Yamamoto 2017), in Phase I. However, when the density rises during the collapse in Phase II, the A_{v} will increase as a function of $n^{2/3}$ (due to the spherical, homologous nature of the collapse), that results in the decrease of the dust temperature (in accordance with semi-empirical models; Keto & Caselli 2010), which reduces the rate of thermal desorption, and freeze out can occur. These relationships dictate the duration of Phase II, as the boundary conditions for entering the static Phase III are the density and temperature free parameters; n_{III}, $T_{\mathrm{g,III}}$, and $T_{\mathrm{d,III}}$.

It has been suggested that the cosmic ray ionisation rate, ζ, is variable in proto-Solar nebula conditions (Cleeves et al. 2014; Fatuzzo & Adams 2014) and therefore, for this study a range of ζ values was used. However, it was found that the determined abundances are not sensitive to a time-dependent cosmic ray ionisation rate during Phase II and thus, the value was kept constant over all phases. The parameters that are reported here and used in this model are presented in Table 2.1.

Therefore, by using this model with a range of input parameters, a plethora of output molecular ratios representing the chemical conditions of cometary formation can be calcu-

Table 2.1. Standard parameters for the nominal dynamical model.

Parameter	Symbol	Value
Phase I density	$n_{\rm I}$	$100\,{\rm cm}^{-3}$
Phase I gas temperature	$T_{\rm g,I}$	100 K
Phase I dust temperature	$T_{\rm d,I}$	50 K
Phase I extinction	$A_{\rm v,I}$	0.1 magnitudes
Phase II free-fall retardation factor	B	1.0
Phase III density	$n_{\rm III}$	$10^7\,{\rm cm}^{-3}$
Phase III gas temperature	$T_{\rm g,III}$	10 K
Phase III dust temperature	$T_{\rm d,III}$	10 K
Cosmic ray ionisation rate	ζ	$1.3{\times}10^{-17}\,{\rm s}^{-1}$

lated. A comparison with the observed ratios seen in the coma of 67P can then be made in order to determine the initial chemical and physical cometary formation conditions in the early Solar System.

2.4 Results

2.4.1 Initial Study

Using a static form of the aforementioned model, an initial study was conducted to determine which of the free parameters are important in the determination of the abundances of O_2 and other key molecules. It was found that the molecular abundances were most sensitive to:

i) the density and temperature at the end of the collapse (Phase II) and entry into the static Phase III ($n_{\rm III}$, $T_{\rm III}$);

ii) the infall collapse retardation factor (B);

iii) the cosmic ray ionisation rate (ζ).

In order to provide the broadest range of conditions possible that could reproduce the observed molecular abundances, the model was run for a range of these parameters as follows: $B = 0.1{-}1.0$, $n_{\rm III} = 10^7{-}10^{11}\,{\rm cm}^{-3}$, $T_{\rm III} = 10{-}20\,{\rm K}$, and $\zeta/\zeta_0 = 0.1{-}10.0$, where

$\zeta_0 = 1.3 \times 10^{-17}$ s^{-1}. It was found that the molecular abundances are also sensitive to the the interstellar radiation field value, G, and therefore, for the main study it was varied in the range $G/G_0 = 0.5-10.0$, where G_0 is the standard value (Draine 1978; Mathis et al. 1983). All possible parameter combinations were used. The fixed initial parameters in the model are the Phase 1 values of: $n_{\rm I} = 100\,{\rm cm}^{-3}$, $T_{\rm g,I} = 100\,{\rm K}$, $T_{\rm d,I} = 50\,{\rm K}$, and $A_{\rm v,I} = 0.1$ magnitudes, that are then allowed to evolve. The abundance ratios calculated for the full range of parameters are reported in Appendix A. A represented sample of the results that illustrates the main findings of this study is given in Table 2.2.

2.4.2 Comparison between the Observed and Modelled Abundance Ratios

To compare the modelled solid-phase molecular abundances of O_2/H_2O, N_2/H_2O, N_2/CO, and CO/H_2O to the *Rosetta* observations these ratios are recorded at the end of the collapse phase (Phase II) and at 10^8 years into Phase III. Interestingly, the observed O_2/H_2O and CO/H_2O ratios are well reproduced by the model for the vast range of input parameters with typical values of 1.5−3.7 per cent and 100−142 per cent, respectively, in good agreement with the observations of 1.0−10.0 per cent and 13−400 per cent, respectively.

However, it was found that N_2 abundances ratios determined by the model are noticeably greater than the observed values. For the N_2/CO ratio, the upper range of the empirical values (1.6 per cent), can somewhat be reproduced by the model (2.7−3.1 per cent). However, the N_2/H_2O ratio is over-estimated by the model by at least an order of magnitude. For example, the largest empirical value is 0.26 per cent, with the lowest model produced value being 3.76 per cent. These best-fit abundance ratios for were determined using the following parameter values: $B = 0.1$, $n_{\rm III} = 10^7 - 10^{11}$, $T_{\rm III} = 10$, and $\zeta/\zeta_0 = 0.1$. The disparity between the observed and model N_2/H_2O values may not be surprising, as the N_2 and H_2O emission from the nucleus of the comet are not well correlated observationally. Therefore, the abundance ratios observed in the coma may not be indicative of the ratio in the nucleus of the comet.

Overall, the presented model can reproduce the observed abundances for a wide range of physical and chemical parameter values, although the N_2 excess needs to be understood. These results suggest that the formation conditions in the protoplanetary disk had a low cosmic ray ionisation rate and a slow collapse phase (i.e. a low B value).

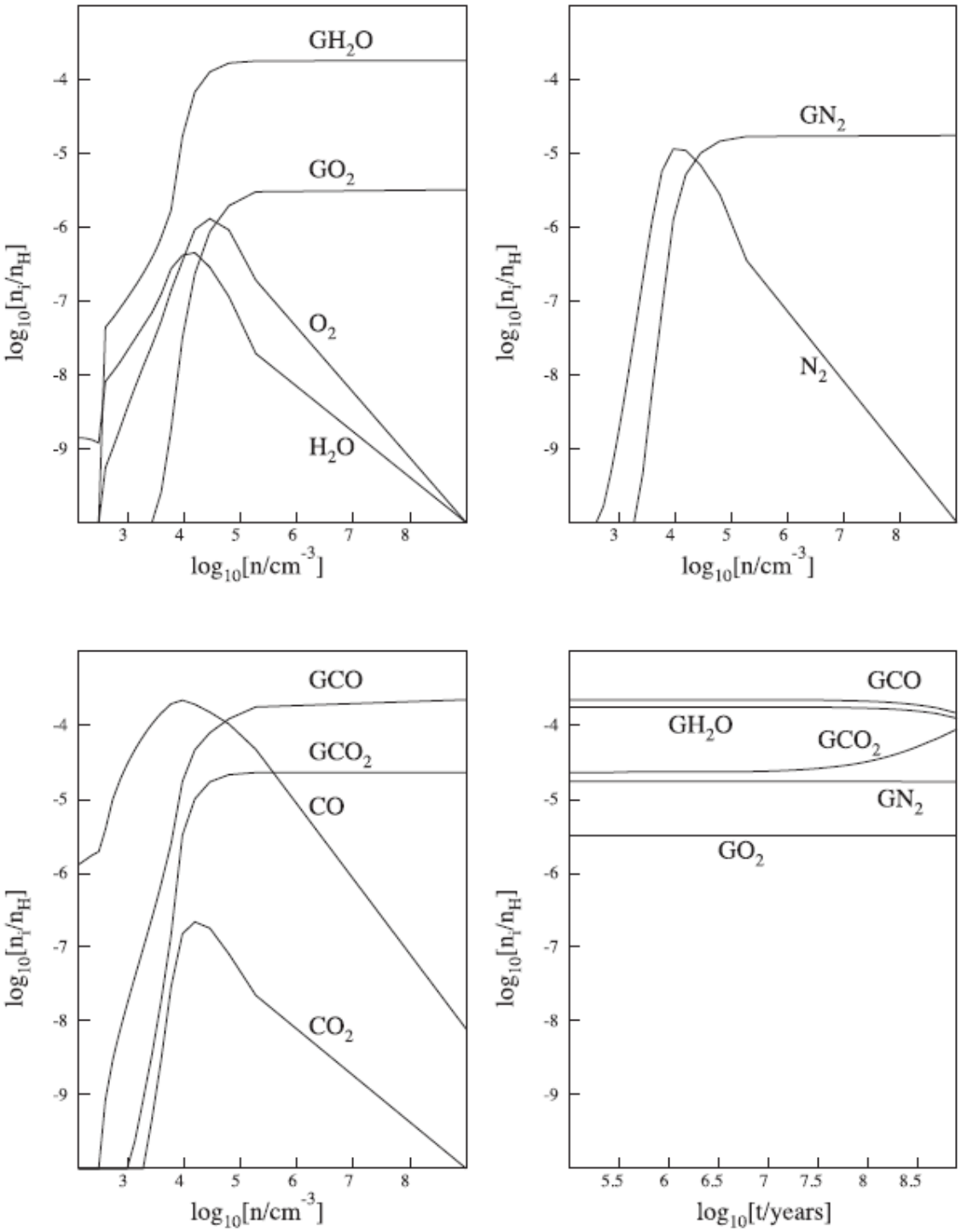

Figure 2.1. The time evolution of the molecular fractional abundances relative to hydrogen are shown for species in the gas-phase and in the solid-phase (denoted by a preceding "G" to indicate freeze out onto the grain) during the collapse phase (top row and bottom left), and the final static phase (bottom right).

2.4.3 Evolution of Physical and Chemical Conditions, and Molecular Abundances

In addition to studying the final chemical abundances of the target molecules, it is possible to study the history of the molecular abundances and the physical and chemical conditions that result in the observed abundances. It was found that when the density passes a threshold of 10^3–$10^4\,\mathrm{cm}^{-3}$ in the collapse phase there is a rapid rise in the ice formation. This is because the higher density produces a sufficiently high extinction that shields the dust from radiation which leads to a decrease in the dust temperature. Thus, the rate of desorption decreases allowing ice to form.

It is seen that during the collapse phase there are transient peaks in the abundances of the molecules in the gas-phase, see the upper row and bottom left plot of Fig. 2.1. These peaks are relatively short, in general less than 0.5 Myr, however they typically occur at roughly the same density as the threshold density that permits ice formation. This is important as it means that the molecules are frozen out onto dust grains and retained, due to the high density and low desorption rate, for the rest of Phase II and all of Phase III. So the final solid-phase abundances also reveal the gas-phase abundances after the threshold density is passed. Furthermore, it is thought that gas freezes out into stratified ices. Thus, each layer of the ices should encode information about the gas-phase abundance of the molecule at the time of freeze out. This means that the history of the chemical evolution during the collapse is recorded in the molecular abundances.

Finally, by comparing the modelled abundance ratios taken at the end of Phase II and 10^8 years into Phase III, given in Table 2.2, an interesting trend emerges for scenarios with a low final phase density ($n_{\mathrm{III}} = 10^7$) or high cosmic ray ionisation rate ($\zeta/\zeta_0 = 10.0$). In these cases, the amount of solid-phase CO decreases, as can be seen by the decreasing $\mathrm{CO/H_2O}$ value and increasing $\mathrm{N_2/CO}$ ratio. This is due to desorption processes mentioned above.

2.5 Summary and Conclusions

In this study an integrated chemical network and physical molecular cloud collapse model was used to determine molecular abundance ratios of $\mathrm{O_2/H_2O}$, $\mathrm{N_2/H_2O}$, $\mathrm{N_2/CO}$, and $\mathrm{CO/H_2O}$ in a proto-Solar/protoplanetary environment for comparison to the ratios observed in the coma of 67P. The model determines the molecular abundances in the final

state by tracking the physical and chemical properties of the evolution of the system. It is assumed that the chemistry primarily occurs during the gas-phase and that the observed abundance ratios are representative of the bulk volatile composition of the comet nucleus that is indicative of the composition of the protoplanetary disk. Therefore, on the basis that these are reasonable assumptions the model can put constraints on both the comet-forming conditions in the early Solar System and also the physical and chemical history of the Solar System prior to that stage.

It is found that, in general, the observed abundance ratios can be reproduced using a wide range of free parameters suggesting that a primordial gas-phase chemistry based origin is a robust method to produce the molecules found in cometary nuclei. The best-fit scenario is one with a low cosmic ray ionisation rate and a slow collapse velocity, given by a low free-fall collapse retardation factor. However, the N_2/H_2O ratio is over-estimated by at least an order of magnitude in this scenario. Possible explanations for this difference are that the observations are not representative of the bulk comet composition or that 67P has an anomalously low nitrogen composition. Indeed, other comets and trans-Neptunian objects (TNOs) have significantly higher nitrogen abundance that is typically one to two orders of magnitude greater than 67P, that could result in a N_2/H_2O in agreement with the model results.

As the model tracks the time-evolution of the chemistry and physics across the phases it is possible to see how molecules are formed in the gas-phase and then freeze out to form the ices that proceed to form comets. Interestingly, for the molecules focused on in this study it was found that during the collapse phase of the model when a density threshold was passed, the formation of ice occurred rapidly. It was found that the gas-phase abundances of the molecules have transient peaks which, in general, occur when the density of the system passes the ice formation threshold density. This means that gas-phase abundances of the molecules are frozen out and retained in the ices as density is high enough to quench the desorption of ices. Furthermore, as gas is frozen out into stratified layers of ice, it means that each layer of the ice records the gas-phase abundance of the molecule when freeze out occurs. Therefore, not only can the observed abundances provide knowledge about cometary formation conditions during the early Solar System, but they can also reveal the chemical and physical history of the collapse phase prior to the proto-Solar System.

Future work could analyse the volatile compositions of comets from different dynamical

families (short-period versus long-period) in order to probe the physical and chemical formation conditions for comets from (potentially) different formation locations. This future work could further constrain cometary formation conditions and the formation history of the Solar System.

Table 2.2. A sample of the results from the dynamical model. The abundance ratios in the ice for the molecular ratios are reported at: (a) the end of the collapse phase (Phase II) and (b) 10^8 years into the final steady-state phase (Phase III).

B	n_{III} (cm^{-3})	T_{III} (K)	ζ/ζ_0	G/G_0	O_2/H_2O (per cent)		N_2/H_2O (per cent)		N_2/CO (per cent)		CO/H_2O (per cent)	
					a	b	a	b	a	b	a	b
1.0	10^7	10	1.0	1.0	1.78	1.17	9.68	5.52	7.80	17.23	124.02	32.02
1.0	10^8	10	1.0	1.0	1.78	1.72	9.70	9.20	7.77	8.73	124.86	105.33
1.0	10^9	10	1.0	1.0	1.78	1.86	9.70	10.10	7.77	8.15	124.95	123.90
1.0	10^{10}	10	1.0	1.0	1.78	1.88	9.70	10.20	7.76	8.10	124.96	126.03
1.0	10^{11}	10	1.0	1.0	1.78	1.88	9.70	10.21	7.76	8.09	124.96	126.24
0.1	10^9	10	1.0	1.0	2.94	3.07	10.66	11.12	10.08	10.67	105.82	104.31
1.0	10^9	20	1.0	1.0	1.67	1.75	8.81	9.20	7.16	7.50	123.11	122.67
1.0	10^9	10	0.1	1.0	0.80	0.81	7.77	7.81	6.19	6.22	125.40	125.51
1.0	10^9	10	10.0	1.0	1.89	2.18	13.41	12.98	13.42	139.03	99.92	9.34
1.0	10^7	10	10.0	1.0	1.76	0.34	12.30	0.00	15.32	10.54	80.30	0.01
1.0	10^9	10	1.0	0.5	1.90	1.98	8.89	9.26	7.08	7.43	125.62	124.59
1.0	10^9	10	1.0	5.0	1.56	1.62	11.56	12.04	9.40	9.88	122.93	121.83
1.0	10^9	10	1.0	10.0	1.46	1.53	12.19	12.70	9.99	10.51	122.01	120.89
0.1	10^7	10	0.1	1.0	3.14	3.09	4.31	4.28	3.08	3.12	139.78	137.30
0.1	10^8	10	0.1	1.0	3.11	3.12	4.31	4.33	3.08	3.10	139.88	139.81
0.1	10^9	10	0.1	1.0	3.11	3.13	4.31	4.34	3.08	3.10	139.89	140.07
0.1	10^{10}	10	0.1	1.0	3.14	3.13	4.31	4.34	3.08	3.09	139.89	140.09
0.1	10^{11}	10	0.1	1.0	13.11	3.13	4.31	4.34	3.08	3.09	139.89	140.10
Observed abundance ratios												
					1.00−10.00		0.01−0.26		0.20−1.60		13.00-400.00	

Chapter 3

Observations of Non-Typical Cometary H_2O Ortho-to-Para Ratios

How bright and beautiful a comet is as it flies past our planet
– provided it does fly past it.

Isaac Asimov (1988)

The work presented in this chapter is based on the paper by Wilson et al. 2017, MNRAS, Volume 466, Issue 2, Page 1954, in collaboration with J. M. C. Rawlings and B. M. Swinyard.

3.1 Introduction

Comets are formed in the outer Solar System and spend the majority of their lifetimes in this region except for brief perihelion passes. Therefore, they are not subject to significant thermal processing and are believed to retain pristine material from the Solar protoplanetary disk, and potentially the pre-Solar nebula (Taquet et al. 2016). Thus, from the study of comets, knowledge can be gained about their formation conditions and the history of the

Solar System. Furthermore, information about current, evolutionary processes occurring in cometary nuclei and comae may be obtained, although it is important to exercise caution when trying to distinguish between formation conditions and evolutionary processes when interpreting comet observations. Water is the most abundant volatile in cometary nuclei, the sublimation of which drives much of the activity when comets enter the inner Solar System (heliocentric distance, $r_{\rm h}, \leq 3\,{\rm AU}$). Therefore, by studying both the physical and chemical nature of water in comets, and by comparing to protoplanetary disks and exoplanetary systems, it is potentially possible to achieve a better understanding of the formation and evolution of minor planetary bodies.

3.1.1 Cometary Observables

Observable tracers that allow for the probing of the physical and chemical nature of comets are, for example, the water production rate, $Q_{\rm H_2O}$, and the water OPR. As $Q_{\rm H_2O}$ is a measure of how much water is being sublimated from the nuclei (calculated from observations of the comae), comae physical conditions such as temperature, expansion velocity, and excitation conditions can be derived, and if other volatiles are detected, the relative abundances compared to water can shed light onto the compositional conditions in the protoplanetary disk, as was seen in Chapter 2. Moreover, for comets observed at the same $r_{\rm h}$, if there is observable $Q_{\rm H_2O}$ variation between comet families (for example, Jupiter-Family and Oort-Cloud comets) this could lead to insight into the formation of cometary ices and the evolution of the cometary bodies.

The water OPR is the ratio of the detected water isomers, ortho- and para-water. Recently, it has been of great interest as a tool to understand thermal processing and history of water in the interstellar medium, star-forming regions, and protoplanetary disks, as the local temperature will affect this ratio in the gas-phase (Lis et al. 2013*a*; Choi et al. 2014; Salinas et al. 2016). Furthermore, it was previously thought that the gas-phase OPR was retained during freeze out of the molecules into ices (Mumma et al. 1987). However, as will be discussed below, this may not be the case. Studies of water in comets also leads to the debate around the fraction of the terrestrial water reservoir that was delivered to Earth via cometary impacts (Altwegg et al. 2015; Bockelée-Morvan et al. 2015*a*; Willacy et al. 2015). This has lead many to use isotopic ratios, such as D/H, as a comparison between cometary and terrestrial water as this ratio is also dependent on temperature and is thought to preserve the formation temperature, and therefore formation location, of the

water.

In cometary comae, water molecules are collisionally excited via interactions with neutral molecules and electrons, and radiatively via Solar infrared pumping of fundamental vibration levels. For water these excitation methods primarily result in transitions between fundamental rotational levels as cometary comae are typically rotationally cold environments. The strongest rotational lines, and those focused on in this study, are detected at submillimetre and radio wavelengths, thus space-based telescopes such as the *Herschel Space Observatory* and its predecessors permit excellent opportunities at studying water in comets, yielding a better understanding of the physical and chemical environments of comae, and therefore potentially the formation and evolution of minor planetary bodies.

Cometary water was directly detected for the first time in a comet Halley by the *KAO* (Mumma, Weaver & Larson 1987) with fundamental rotational transitions of ortho-water ($2_{12}-1_{01}$ and $3_{03}-2_{12}$) first observed in comet Hale−Bopp using the *ISO* (Crovisier et al. 1997). Subsequent space-based telescopes, such as *SWAS* and *Odin* detected the former fundamental rotational line mentioned above in multiple comets (Neufeld et al. 2000; Lecacheux et al. 2003; Biver et al. 2007, 2009). However, it wasn't until the launch of *Herschel* that both ortho- ($2_{12}-1_{01}$) and para-water ($1_{11}-0_{00}$ and $2_{02}-1_{11}$) was observed in the same comet for the first time (De Val-Borro et al. 2010; Hartogh et al. 2010; Szutowicz et al. 2011; Biver et al. 2012; Bockelée-Morvan et al. 2012; De Val-Borro et al. 2012; Lis et al. 2013*b*; De Val-Borro et al. 2014). More recently, several rotational transitions have been detected with the *Rosetta* spacecraft following the initial discovery of para-water (Gulkis et al. 2015).

3.1.2 Water Molecular Structure and Ortho-to-Para Ratio Introduction

If a molecule has two hydrogen atoms then two nuclear-spin isomers of the molecule exist. As the hydrogen atoms each have a nuclear-spin angular momentum of $I = 1/2$, the spin aligned isomer (ortho) will have a total nuclear-spin angular momentum of 1 that results in a triplet state. Conversely, the spin anti-aligned isomer (para) has a total nuclear-spin angular momentum of 0 resulting in a singlet state. The ground rotational level of water is the para 0_{00} state, with the first excited state being the ortho 1_{01}. These levels have a rotational energy difference of 34.2 K, see Fig. 3.2, that means the OPR is temperature-dependent that can permit the use of this ratio as a probe of low temperature regions. The temperature dependence is shown as a solid black line in Fig. 3.3.

The water OPR can be determined if observations of rotational lines of both ortho- and para-water transitions are detected. From equation (3.1), the OPR is calculated as the ratio of sum of all the ortho line intensities divided by their branching ratios, with the sum of all the para line intensities divided by their branching ratios.

$$\mathrm{OPR} = \frac{\sum_{\mathrm{i}} \mathrm{I_o(i)/B_o(i)}}{\sum_{\mathrm{j}} \mathrm{I_p(j)/B_p(j)}} \tag{3.1}$$

where i, j indicate individual transitions, ortho and para intensities are I_o and I_p, respectively, and B_o and B_p are the branching ratios for each ortho- and para-water transition.

As ortho-water is a triplet state and para-water is a singlet state, the statistical equilibrium water OPR value is 3 that is obtained for temperatures greater than 50 K. In comets OPR values of 2.5−3.0 are typically seen (Crovisier et al. 1997; Dello Russo et al. 2005, 2007, 2008; Kawakita et al. 2006; Woodward et al. 2007; Radeva et al. 2010; Villanueva et al. 2011; DiSanti et al. 2013; Paganini et al. 2015), however lower values have been observed in a few comets. Significantly lower values (0.1−2.0) have been determined from observations of the interstellar medium, star-forming regions, and interestingly, a protoplanetary disk, indicating that these regions (that may eventually form comets) currently have very low temperatures (Lis et al. 2013*a*; Choi et al. 2014; Salinas et al. 2016). These temperatures are commonly referred to as the nuclear-spin temperatures that can be calculated from the OPR (Mumma et al. 1987).

3.1.3 Ortho-to-Para Ratio Variation via Nuclear-Spin Conversion

In the Gas-Phase

To explain OPR variations from the statistical equilibrium value nuclear-spin conversion occurs from ortho-water to para-water and vice versa. In the gas-phase nuclear-spin conversion between isomers occurs very rarely as the weak magnetic interactions between the intra-molecular hydrogen nuclear spins means that conversions happen on timescales longer than the time between photodissociation events for water molecules. However, nuclear-spin conversion can occur through hydrogen-exchange reactions between water molecules or the changing of nuclear-spin states via interactions between two water molecules. Conversion can also happen in the gas-phase via collisions, explained in the

quantum-relaxation model (Hama & Watanabe 2013). For example, following a collision, should an ortho-water molecular be energetically closer to a para state then a mixing of the ortho and para states occurs. Energy relaxation to the final state occurs via a subsequent collision and the ortho to para conversion is complete.

In the Solid-Phase

In addition to conversion in the gas-phase, it is thought that nuclear-spin conversion can happen in the solid-phase, for example, in cometary ices. This has been proposed to occur through spin-magnetic interactions between neighbouring water molecules in the ice on the timescale of $10^{-5} - 10^{-4}$ s. This rapid conversion is thought to arise on such short timescales due to a substantially reduced rotational energy difference between the ortho and para states. Compared to the difference in the ground states in the gas-phase of 34.2 K, in the solid-phase it is thought to be 5×10^{-13} K (Buntkowsky et al. 2008). This is because the hydrogen bonds between molecules in ices act as potential barriers to rotation, and thus, the energy difference between the ortho- and para-water ground states is substantially reduced.

3.1.4 Ortho-to-Para Ratio Interpretation in Comets

Water OPRs have now been determined in dozens of comets, but the exact meaning of this ratio is not known and debate over the interpretation is still ongoing. Historically, it was thought that the OPR and corresponding nuclear-spin temperature is indicative of comet ice formation temperature, and therefore comet formation location (Mumma et al. 1987). However, a recent laboratory study has found that regardless of freeze out temperature, when vapour-deposited or in-situ produced water is sublimated either by thermal desorption at 150 K or by photodissociation at 10 K the observed OPR is equal to the statistical equilibrium value of 3 (Hama et al. 2016). This study shows two things are happening under these laboratory settings:

i) rapid solid-phase nuclear-spin conversion occurs in water ice that normalises the OPR;

ii) the sublimation processes do not seem to alter the OPR.

Therefore, if these laboratory results are representative of the environment of a cometary coma it suggests that the formation temperature of the comet is not encoded and retained in the observed gas-phase OPR in comae.

Therefore, in order to explain the observed OPR that are lower than the statistical equilibrium the possibility of nuclear-spin conversion in the comae following sublimation should be discussed. Previously, it has been predicted that the collision rate of water with other water molecules, ions, and electrons is too small to induce efficient nuclear-spin conversion in cometary comae (Crovisier 1984; Mumma et al. 1987). However, should additional sources of sublimating water molecules, such as water clusters or ice, exist in comae then collisions or hydrogen-exchange reactions may occur in the collisional, fluid, coma regions near the nucleus via the quantum-relaxation model described previously (Irvine et al. 2000; Hama & Watanabe 2013; Manca Tanner et al. 2013). Therefore, nuclear-spin conversion, especially in the low temperature conditions of the coma, needs to be re-examined in order to interpret the observed OPRs as it may be possible to use the OPRs to probe the gas-phase physical conditions in comae and learn about any ongoing evolutionary processes.

Interestingly, it has been found that there is a correlation between ammonia and water OPRs from observations taken of 26 comets (Shinnaka et al. 2016). This suggests that there is a common OPR variation process for different molecules.

The chapter is laid out as followed; Section 3.2 outlines the observations with the data analysis, modelling, and results reported in Section 3.3. A discussion of the main points of the study is presented in Section 3.4 and conclusions are given in Section 3.5.

3.2 Observations

Between 2010 July 10 and 2011 October 16 observations of comets Hartley 2, 10P/Tempel 2, 45P/Honda−Mrkos−Pajdušáková, and C/2009 P1 were taken using the *Herschel* SPIRE (Griffin et al. 2010; Pilbratt et al. 2010) as a part of the *Herschel* Guaranteed Time Key project "Water and related chemistry in the Solar System" (HssO; Hartogh et al. 2009).

Spectra were obtained using the SPIRE Fourier Transform Spectrometer (FTS; Swinyard et al. 2014) that covers the spectral range 447−1568 GHz in two bands; the short (SSW, 447−1018 GHz) and long (SLW, 944−1568 GHz) wavelength channels. The high-resolution mode was used with a spectral resolution of $\Delta\nu = 1.2$ GHz. Data processing

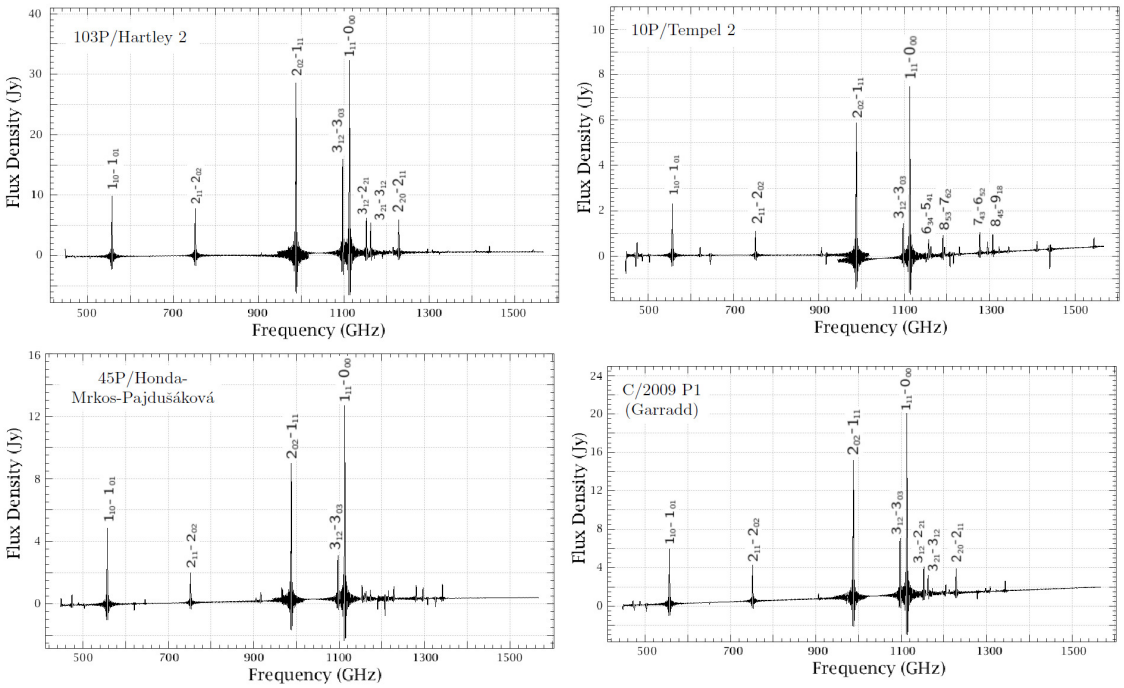

Figure 3.1. *Herschel* SPIRE spectra of the target comet nuclei that shows the fundamental rotational water lines. The observed transitions, frequencies, and isomeric forms are: $1_{10}-1_{01}$ (557 GHz, Ortho), $2_{11}-2_{02}$ (752 GHz, Para), $2_{02}-1_{11}$ (988 GHz, Para), $3_{12}-3_{03}$ (1097 GHz, Ortho), $1_{11}-0_{00}$ (1113 GHz, Para), $3_{12}-2_{21}$ (1153 GHz, Ortho), $6_{34}-5_{41}$ (1158 GHz, Ortho), $3_{21}-3_{12}$ (1163 GHz, Ortho), $8_{53}-7_{62}$ (1191 GHz, Para), $2_{20}-2_{11}$ (1229 GHz, Para), $7_{43}-6_{52}$ (1278 GHz, Ortho), $8_{45}-9_{18}$ (1308 GHz, Ortho).

was conducted in the *Herschel* Interactive Processing Environment (HIPE) v.13.0 utilising the standard SPIRE scripts and following the recommended best practices (*Herschel* Science Centre. 2014), in order to produce the flux-calibrated spectra shown in Fig. 3.1. For comets 10P/Tempel 2, 45P/Honda−Mrkos−Pajdušáková, and C/2009 P1 additional reduction via background subtraction and frequency-based mask fitting scripts were also done in order to produce a flatter continuum. The background level was estimated from the continuum in the off-axis detectors that took observations at larger nucleocentric distances, $r_{\rm nuc}$. Comet positions and relative velocities with respect to *Herschel* were calculated using JPL HORIZONS, with the spectra *Herschel*-centric velocity corrected.

The purpose of the study is to determine the H_2O OPR and Q_{H_2O} values in cometary comae at a range of $r_{\rm nuc}$ for comets that are likely have different formation conditions and evolutionary histories. Therefore, for all comets the central SSW and SLW bolometers

that observed the nuclei of the targets were ignored. This effectively created two rings of SSW detectors at $r_{\rm nuc}$ of roughly 33 and 66 arcsec and one ring of SLW detectors at a distance of 51 arcsec from the nuclei (*Herschel* Science Centre. 2014). It should be noted that this resulted in observations taken at $r_{\rm nuc}$ greater than the recombination surface for each comet (Bensch & Bergin 2004). The observation $r_{\rm nuc}$ is given in Table 3.2.

Physical and orbital properties of the target comets such as the radius of the nucleus, $r_{\rm n}$, and the orbital period, P, are given in Table 3.1. Further characteristics of the observations, for example the heliocentric distance, $r_{\rm h_{obs}}$, the *Herschel*-comet distance, $\Delta_{\rm obs}$, and the time between the observation and perihelion, $\Delta T_{\rm obs}$ (where negative and positive values are pre- and post-perihelion observations respectively), are reported in Table 3.2.

3.2.1 103P/Hartley 2

The Jupiter-Family comet Hartley 2 passed perihelion on 2010 October 28 at $r_{\rm h}$ = 1.059 AU, following the close approach to Earth on October 21 at $\Delta = 0.12$ AU. In addition to the *Herschel* observation presented here, Hartley 2 was also the target of the *EPOXI* space mission and a global observing campaign of 51 telescopes during this apparition (Meech et al. 2011). Further observations of water in Hartley 2 are shown in Table 3.3.

A single SPIRE FTS observation in both SSW and SLW set of bolometers was taken on 2010 November 9 with a duration of 7002 s for a Signal-to-Noise Ratio (S/N) of 88. The frequency range of the instrument permits detection of multiple fundamental rotational water emission lines as can be seen in the spectra of Hartley 2 in Fig. 3.1. Hartley 2 will make a close approach to Earth on 2023 September 26 at $\Delta = 0.38$ AU yielding another opportunity to study this target.

3.2.2 10P/Tempel 2

10P/Tempel 2 (hereafter Tempel 2) is a Jupiter-Family comet that passed perihelion on 2010 July 4 at $r_{\rm h} = 1.42$ AU prior to the sole SPIRE FTS observation of 5650 s on 2010 July 10 that had a S/N of 18. As with Hartley 2, Tempel 2 was observed using all SSW and SLW detectors revealing several fundamental rotational water lines as can be seen in Fig. 3.1. The next closest approach to Earth will be on 2026 August 3 at $\Delta = 0.41$ AU that will allow follow-up observations and comparison to the results presented below. Five previous studies have observed water in Tempel 2 that are presented in Table 3.3.

Table 3.1. Orbital and physical properties of the four targets in this studies, and selected constrained model parameters.

Comet	$r_{\rm n}$ (km)	P (year)	$v_{\rm exp}$ (km s^{-1})	$\beta_{\rm H_2O}$ (s^{-1})
Hartley 2	0.7	6.46	0.83	1.08×10^{-5}
Tempel 2	5.3	5.36	0.50	1.06×10^{-5}
45P	0.8	5.26	0.75	1.16×10^{-5}
C/2009 P1	<5.6	127 000	0.60	1.16×10^{-5}

3.2.3 45P/Honda−Mrkos−Pajdušáková

The comet 45P/Honda−Mrkos−Pajdušáková (hereafter 45P) is a Jupiter-Family comet that passed Earth with $\Delta = 0.06$ AU on 2011 August 15 prior to perihelion on 2011 September 28 ($r_{\rm h} = 0.53$ AU). Fig. 3.1 shows the spectra obtained on 2011 August 16 with an integration time of 4568 s and a S/N of 43. The fundamental rotational water lines detected in the comet are clearly seen in the SPIRE FTS observation with several emission features noted. In the future, 45P will pass Earth at $\Delta = 0.37$ AU on 2032 November 11 when further observations of this target could be taken. Water in 45P has been studied on two previous occasions reported in Table 3.3.

3.2.4 C/2009 P1 (Garradd)

The only long-period comet in the study, comet C/2009 P1, originates from the Oort Cloud ($i = 106°$ with respect to the ecliptic), and passed perihelion on 2011 December 23 at $r_{\rm h} = 1.55$ AU. It was observed once by SPIRE FTS on 2011 October 16 for 4568 s with a S/N of 46. As the orbital period for the target is approximately 127 000 years follow-up observations are not possible. The observations utilised the SSW and SLW bolometers covering the entire frequency range that allows for several fundamental rotational water emission features to be detected (see Fig. 3.1). During the 2011 apparition multiple other studies analysed water in C/2009 P1, as summarised in Table 3.3.

3.3 Data Analysis and Results

3.3.1 Radiative Transfer Model

In order to determine the $Q_{\rm H_2O}$ of each comet detailed radiative transfer modelling of the comae is needed to produce model water emission spectra for comparison against the

observations. The comae were modelled using the one-dimensional Accelerated Monte Carlo radiative transfer code; CRETE (De Val-Borro & Wilson 2016) that was inspired by RAT4COM (Bensch & Bergin 2004), and developed from previous work that generated synthetic water emission spectra (Hogerheijde & van der Tak 2000). The main comae excitation processes of collisions between water molecules and between water and electrons, and Solar infrared pumping of the vibrational bands and subsequent fluorescence are included.

Prior work has focused primarily on modelling ortho-water, typically considering nine rotational transitions between the seven fundamental levels in the ground vibrational state. In the updated CRETE model used in this study nine transitions between the seven fundamental rotational states of para-water are included. All ortho- and para-water transitions in the CRETE model are shown as blue arrows in Fig. 3.2, with the green arrows indicating the modelled transitions that are observed in all SPIRE detectors that are the focus of the analysis in order to determine the $Q_{\mathrm{H_2O}}$ values.

Model Description and Parameters

The standard spherically symmetric Haser distribution was used to model the radial gas expansion profile with a constant coma gas expansion velocity, v_{exp} (Haser 1957). This models the coma as a spherically symmetric outflow from the nucleus, scaled as $1/r^2$, with constant velocity and an exponential decay term, $\exp(-r\beta_{\mathrm{H_2O}}/v_{\mathrm{exp}})$, that accounts for destruction via photodissociation (with rate $\beta_{\mathrm{H_2O}}$) and ionisation by the Solar radiation field.

In the model, the constrained parameters include the orbital properties r_{h} and Δ, and the scaling factors for both $\beta_{\mathrm{H_2O}}$ and the ionisation rate, that depends on the r_{h} and Solar activity level. The reasonably well constrained physical parameters which have values for the observed comets taken from the literature include v_{exp}, the gas kinetic temperature, T_{kin}, and $\beta_{\mathrm{H_2O}}$. It has been shown that at the r_{nuc} observed in this study, the assumption of a constant $T_{\mathrm{kin}} = 40\,\mathrm{K}$ is a good approximation (Combi et al. 1999).

This leaves the electron density scaling factor, $x_{\mathrm{n_e}}$, the contact surface scaling factor, $x_{\mathrm{r_e}}$, the number of shells in the radiative transfer calculations, the OPR, and $Q_{\mathrm{H_2O}}$ as the only free parameters in the model. The scaling factors mentioned above, $x_{\mathrm{n_e}}$ and $x_{\mathrm{r_e}}$, are used in the model to determine the r_{nuc} for the recombination and contact surfaces, respectively, which are the boundaries between the three excitation processes mentioned

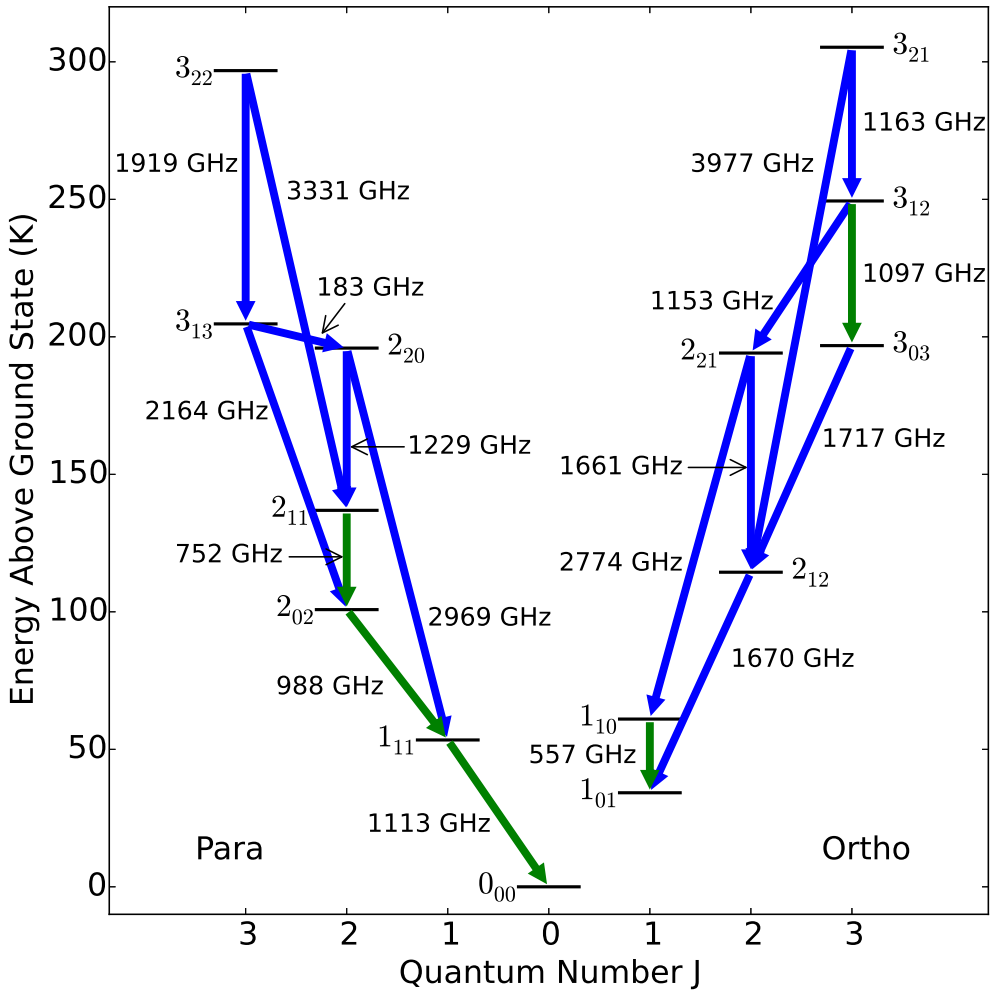

Figure 3.2. The fundamental rotational ortho- and para-water transitions in the CRETE radiative transfer model. Green arrows indicate emission lines observed in all SPIRE detectors, whereas blue arrows show transitions that were unobserved or observed in a few detectors.

previously. Via observations of the ground ortho-water line these factors have been constrained to be 0.2 and 1.0, respectively (Balsiger 1990; Festou 1990; Biver 1997; Biver et al. 2007; Hartogh et al. 2010). Based on recommendations that took into account computation time versus model accuracy, the number of shells used was set to be 1500. The adopted values for other model parameters, specific to each comet, taken from the literature are presented in Table 3.1. Finally, to determine the Q_{H_2O} values, both the empirical and the canonical (equal to 3) OPR values were used.

Whilst this model includes some simplistic assumptions such as spherically symmetric sublimation, and the lack of vibrationally excited levels and radiative transfer at infrared wavelengths, several previous studies have utilised a version of the model with considerable success (Zakharov et al. 2007; Hartogh et al. 2010; Bockelée-Morvan et al. 2012).

3.3.2 Empirical Ortho-to-Para Ratios

Due to the multiple ortho- and para-water transitions seen in the SPIRE observations of each comet, OPR values can be calculated using equation (3.1) from the total line intensities of the transitions (Mumma et al. 1987). The observed lines are labelled as ortho- or para-water in Fig. 3.1 with the OPR values for each comet in the study reported in Table 3.2. It should be noted that these OPR values are averaged over the observed range of r_{nuc}, $\sim$1 000$-$10 000 km, that predominantly cover the mid and outer coma. Importantly this means that the inner, collisionally dominant region of the coma is not probed. The r_{nuc} are presented in Table 3.2. From the OPR values the nuclear-spin temperature, i.e. the temperature at which the water was last equilibriated at, can also be determined.

Hartley 2 is a well studied comet with OPR values having been determined for the 1997 and 2010 apparitions as shown in Table 3.3. Whilst the the OPR uncertainty calculated from the SPIRE observations is somewhat substantial, the OPR value of 2.44$\pm$0.71, taken from observations at r_{nuc} of 4 100$-$8 200 km, agrees with the wide range determined previously at similar r_h (Crovisier et al. 1999; Dello Russo et al. 2011; Mumma et al. 2011; Bonev et al. 2013; Kawakita et al. 2013). This OPR corresponds to a nuclear-spin temperature of $\approx$ 28 K.

The calculated, empirical OPR for Tempel 2 is 1.59$\pm$0.23 that is significantly lower than the canonical value, and importantly it is a factor of two lower than the only previous OPR value for this comet (Paganini et al. 2012*a*), as can be seen in Table 3.3. Both observations were taken at similar r_h during the 2010 apparition that could suggest OPR

variations over the 16 day between the observations. However, interestingly, it should be noted that the previously determined, higher OPR value was calculated from on-nucleus and inner coma observations, $\leq$1 000 km (Paganini et al. 2012*a*), whereas the value reported in this study is probing the mid and outer coma at $r_{\rm nuc}$ of 17 000−35 000 km. Thus, this could be evidence of OPR variations due to coma processes. This interpretation raises further questions that will be discussed in Section 3.4.1. The OPR determined in this study results in a nuclear-spin temperature of $\approx$ 20 K.

The remaining two comets in the study, 45P and C/2009 P1, have OPR values of 2.00±0.30 and 1.36±0.22, respectively, that yield nuclear-spin temperatures of $\approx$ 22 K and $\approx$ 18 K. These OPRs were determined at $r_{\rm nuc}$ of 1 500−3 100 km and 45 000−90 000 km, thus these values probe the mid and outer comae. This is the first time OPRs have been calculated for these comets, and whilst they are significantly lower than the canonical value, they agree with previous OPR values seen in Halley and C/2001 A2 (Mumma et al. 1988; Dello Russo et al. 2005), see Fig. 3.3.

3.3.3 Water Production Rates

$Q_{\rm H_2O}$ values were determined for all comets for a range of $r_{\rm nuc}$ probed by the SSW and SLW detectors depending on the frequency of the observed transition. The values were calculated by fitting the observations with the CRETE produced model water emission profiles via a least-squares method. Table 3.2 presents the $Q_{\rm H_2O}$ values using both:

i) the empirical OPRs reported above; and

ii) the canonical OPR of 3 equal to the statistical equilibrium value

in order to compare between a typical cometary OPR value and those determined in this study.

The Hartley 2 $Q_{\rm H_2O}$ values determined using the empirical OPR are $2-8\times10^{27}$ s^{-1}, whilst for an OPR of 3 they are $2-9\times10^{27}$ s^{-1}. These values are roughly equal to previously reported values at a similar $r_{\rm h}$, as can be seen in Table 3.3 (Crovisier et al. 1999; Dello Russo et al. 2011; Combi et al. 2011; Meech et al. 2011; Mumma et al. 2011; Kawakita et al. 2013; Knight & Schleicher 2013; Gicquel et al. 2014), although these $Q_{\rm H_2O}$ values are, in general, lower than observations taken at previous apparitions. The exception is

the Q_{H_2O} value derived from the $3_{12}-3_{03}$ line that is an order of magnitude lower than the other transitions.

Using the empirical and canonical OPRs, the Q_{H_2O} values for Tempel 2 vary by an order of magnitude, $2-12\times10^{27}\,s^{-1}$ and $2-16\times10^{27}\,s^{-1}$, respectively. The upper values of this range are in agreement with previous works, see Table 3.3, but are a factor of 4 lower than the Q_{H_2O} value seen in the 1988 apparition (Roettger et al. 1990; Fink 2009; Szutowicz et al. 2011; Biver et al. 2012; Paganini et al. 2012*a*).

For 45P, the Q_{H_2O} values for the empirical and canonical OPRs are $0.6-1.4\times10^{27}\,s^{-1}$ and $0.9-2.0\times10^{27}\,s^{-1}$, respectively. These values are in good agreement with previous studies shown in Table 3.3 (Fink 2009; Lis et al. 2013*b*). Furthermore, from previous observations, it appears that there is a decrease in the Q_{H_2O} values between the 1995 and 2011 apparitions that may support the trend seen in the other Jupiter-Family comets in this study.

In the Oort-Cloud comet C/2009 P1, the Q_{H_2O} values obtained using the determined OPR are in the range $0.7-2.6\times10^{29}\,s^{-1}$, whereas when using an OPR of 3 it is $1.1-2.0\times10^{29}\,s^{-1}$. These also agree well with the values presented in previous studies (Bockelée-Morvan et al. 2012; Paganini et al. 2012*b*; Villanueva et al. 2012; Combi et al. 2013; Bockelée-Morvan et al. 2014; DiSanti et al. 2014; Feaga et al. 2014).

By looking at the sample as a whole and taking note of the fact that Q_{H_2O} values were obtained from different transitions and r_{nuc} it is possible to look for trends. Interestingly, a couple of similar features are seen across the sample:

i) whilst for Tempel 2 the rates calculated from all transitions are approximately similar, for Hartley 2, 45P, and C/2009 P1 the Q_{H_2O} values from the $3_{12}-3_{03}$ (and occasionally $2_{11}-2_{02}$) line are noticeably lower than the rates determined from other transitions;

ii) for all comets there is a correlation between Q_{H_2O} and r_{nuc}, a decreasing production rate is seen with increasing distance.

Table 3.2: The OPR values averaged over the observed comae for the four targets. The Q_{H_2O} values determined for various transitions and nucleocentric offsets using (i) the empirical OPR values and (ii) the canonical OPR value of 3.

Comet	Start Date (UT) yyyy/mm/dd.dd	ΔT_{obs} (d)	$r_{h_{obs}}$ (au)	Δ_{obs} (au)	OPR	Transition	ν_{ij} (GHz)	Ortho / Para	Offset (km)	Q_{H_2O} (10^{27} s^{-1}) (i)	(ii)
Hartley 2	2010/11/09.03	11.77	1.071	0.176	2.44±0.71	$1_{10}-1_{01}$	557	Ortho	6400	3.83±0.12	3.61±0.17
						$2_{11}-2_{02}$	752	Para	6400	1.89±0.11	2.19±0.15
						$2_{02}-1_{11}$	988	Para	4100	6.43±0.13	7.49±0.21
									6400	5.68±0.11	6.57±0.12
									8200	4.09±0.15	4.75±0.20
						$3_{12}-3_{03}$	1097	Ortho	4100	0.55±0.06	0.55±0.06
									8200	0.35±0.04	0.35±0.04
						$1_{11}-0_{00}$	1113	Para	4100	7.46±0.13	8.67±0.19
									8200	5.57±0.14	6.44±0.20
Tempel 2	2010/07/10.93	6.03	1.424	0.732	1.59 ± 0.23	$1_{10}-1_{01}$	557	Ortho	27000	11.6 ± 1.7	9.5 ± 1.4
						$2_{11}-2_{02}$	752	Para	27000	3.8 ± 1.2	5.7 ± 1.8
						$2_{02}-1_{11}$	988	Para	17000	9.5 ± 1.2	14.5 ± 1.8
									27000	5.2 ± 0.6	8.2 ± 0.9
									35000	10.2 ± 1.7	15.8 ± 2.5
						$3_{12}-3_{03}$	1097	Ortho	17000	2.9 ± 1.3	2.3 ± 1.1
									35000	2.2 ± 1.0	1.8 ± 0.8

Table 3.2 – continued from previous page

Comet	Start Date (UT) yyyy/mm/dd.dd	ΔT_{obs} (d)	$r_{h_{obs}}$ (au)	Δ_{obs} (au)	OPR	Transition	ν_{ij} (GHz)	Ortho / Para	Offset (km)	Q_{H_2O} (10^{27} s^{-1}) (i)	(ii)
						$1_{11}-0_{00}$	1113	Para	17000	8.6 ± 0.9	13.1 ± 1.3
									35000	6.0 ± 1.0	9.2 ± 1.5
45P	2011/08/16.13	−44.65	1.002	0.061	2.00 ± 0.30	$1_{10}-1_{01}$	557	Ortho	2400	1.22 ± 0.11	1.08 ± 0.09
						$2_{11}-2_{02}$	752	Para	2400	0.37 ± 0.09	0.49 ± 0.12
						$2_{02}-1_{11}$	988	Para	1500	1.25 ± 0.10	1.67 ± 0.14
									2400	0.94 ± 0.05	1.26 ± 0.06
									3100	0.68 ± 0.11	0.90 ± 0.15
						$3_{12}-3_{03}$	1097	Ortho	1500	0.19 ± 0.05	0.16 ± 0.04
									3100	0.14 ± 0.05	0.13 ± 0.05
						$1_{11}-0_{00}$	1113	Para	1500	1.53 ± 0.07	2.04 ± 0.10
									3100	0.67 ± 0.08	0.90 ± 0.11
C/2009 P1	2011/10/16.79	−68.89	1.807	1.875	1.36 ± 0.22	$1_{10}-1_{01}$	557	Ortho	69000	255 ± 10	196 ± 8
						$2_{11}-2_{02}$	752	Para	69000	22 ± 6	37 ± 11
						$2_{02}-1_{11}$	988	Para	45000	110 ± 6	187 ± 10
									69000	97 ± 3	164 ± 6
									90000	87 ± 14	147 ± 16
						$3_{12}-3_{03}$	1097	Ortho	45000	17 ± 4	13 ± 3

Table 3.2 – continued from previous page

Comet	Start Date (UT)	$\Delta T_{\rm obs}$	$r_{\rm h_{obs}}$	$\Delta_{\rm obs}$	OPR	Transition	$\nu_{\rm ij}$	Ortho	Offset	$Q_{\rm H_2O}$ (10^{27} s^{-1})	
	yyyy/mm/dd.dd	(d)	(au)	(au)			(GHz)	/ Para	(km)	(i)	(ii)
									90000	21 ± 7	16 ± 6
						$1_{11}-0_{00}$	1113	Para	45000	115 ± 5	195 ± 8
									90000	69 ± 12	116 ± 15

Potential explanations for these trends are discussed in Section 3.4.2. For the majority of the comets in the study, when using the OPR values derived from this work a more consistent, narrower range of Q_{H_2O} values is determined. This gives some support for the adoption of these OPR values. As can be seen in Table 3.2, even for low OPR values, the Q_{H_2O} values do not differ from those determined using an OPR = 3 by more than a factor of 2.

3.4 Discussion

3.4.1 Ortho-to-Para Ratio Variation

A main finding of this study is that for three comets, Tempel 2, 45P, and C/2009 P1, the empirical OPRs are significantly lower than the canonical value, see Table 3.2. However, as can be seen in Fig. 3.3, the OPR values reported here agree with values observed in other comets such as Halley and C/2001 A2 (Mumma et al. 1988; Dello Russo et al. 2005). Furthermore, and quite interestingly, the OPRs determined here agree well with those observed in the protoplanetary disk TW Hydrae, that has a range of OPR from 0.73 to 1.52 depending on the disk model (Salinas et al. 2016). From this similarity it may be tempting to conclude that the SPIRE observations are detecting OPR values preserved from the protoplanetary disk. Indeed, previously, it was thought OPR variation was caused by a low comet ice formation temperature as para-water is more stable at low temperatures (Mumma et al. 1987). However, as mentioned above, a recent laboratory study has shown that solid-phase rapid nuclear-spin conversion equilibrates the OPR to 3 (Hama et al. 2016), therefore the cause of the observed OPR variation may be due to gas-phase nuclear-spin conversion processes in the cometary comae following sublimation from the nuclei.

Ortho-to-Para Ratio Variation Over r_{nuc}

One possible approach to establish if these conversion processes are occurring in the coma is to see if the OPR of a comet varies with r_{nuc}. The sole OPR value for Tempel 2 in the literature was determined from observations centred on-nucleus and extending up to 1 500 km (Paganini et al. 2012*a*). Whereas, the SPIRE observations reported here cover the outer coma at r_{nuc} of 17 000−35 000 km. These two OPR determinations are represented by two blue bars in Fig. 3.4. It can be seen that there is a clear decrease of OPR in

Table 3.3. OPR and Q_{H_2O} values from this work and the literature, determined from observations at similar r_h, but at a range of r_{nuc}, a value of 0 means observations were on-nucleus.

Comet	Apparition	r_h (AU)	r_{nuc} (10^3 km)	OPR	Q_{H_2O} (10^{27} s^{-1})	References
Hartley 2	2010	1.07	4.1−8.2	2.44 ± 0.71	$1.89 - 7.46$	1
			4.1−8.2	3	$2.19 - 8.67$	1
	1991	0.96	–	–	≈ 63.00	2
		1.05	–	–	32.36	3
	1997	1.04	–	–	31.00 ± 2.00	4
		1.04	0	2.76 ± 0.08	12.40 ± 2.00	5
		1.06	–	–	15.14	3
		1.11	0	2.63 ± 0.18	5.40 ± 2.00	5
		1.17	–	–	18.80	6
	2010	1.06	0−1.4	3.4 ± 0.6	$8.84 - 14.00$	7
		1.06	0−0.4	2.76 ± 0.15	$8.44 - 13.60$	8
		1.06	–	–	11.48	3
		1.06	0−0.3	2.85 ± 0.20	6.78 ± 0.26	9
		1.07	–	–	7.56 ± 0.08	10
		1.07	–	–	7.32 ± 0.95	11
		1.07	0−0.4	2.88 ± 0.17	$7.60 - 16.20$	8
		1.07	–	–	≈ 10.00	12
Tempel 2	2010	1.42	17−35	1.59 ± 0.23	$2.2 - 11.6$	1
			17−35	3	$1.8 - 15.8$	1
	1988	1.41	–	–	48.7	6
	1988	1.42	–	–	$\approx 15.0 - 20.0$	13
	2010	1.42	–	–	≈ 20.0	14
	2010	1.43	–	–	22.0 ± 1.0	15
	2010	1.44	0−1.5	3.01 ± 0.18	19.0 ± 1.2	16
45P	2011	1.00	1.5−3.1	2.00 ± 0.30	$0.60 - 1.36$	1
			1.5−3.1	3	$0.90 - 2.04$	1
	1995	1.14	–	–	1.92	6
	2011	1.03	–	–	0.91	17
C/2009 P1	2011	1.81	45−90	1.36 ± 0.22	$69 - 255$	1
			45−90	3	$114 - 196$	1
	2011	1.73	–	–	108 ± 30	18
		1.76	–	–	$69 - 81$	18
		1.80	–	–	270 ± 3	19
		1.84	–	–	$90 - 106$	20
		1.88	–	–	$155 - 262$	21
		2.00	–	–	46 ± 8	22
		2.00	–	–	84 ± 7	23
		2.10	–	–	86 ± 7	24

References. (1) This work; (2) Weaver et al. (1994); (3) Knight & Schleicher (2013); (4) Colangeli et al. (1999); (5) Crovisier et al. (1999); (6) Fink (2009); (7) Dello Russo et al. (2011); (8) Kawakita et al. (2013); (9) Mumma et al. (2011); (10) Combi et al. (2011); (11) Gicquel et al. (2014); (12) Meech et al. (2011); (13) Roettger et al. (1990); (14) Szutowicz et al. (2011); (15) Biver et al. (2012); (16) Paganini et al. (2012*a*); (17) Lis et al. (2013*b*); (18) Bockelée-Morvan et al. (2014); (19) Combi et al. (2013); (20) DiSanti et al. (2014).; (21) Bockelée-Morvan et al. (2012); (22) Feaga et al. (2014); (23) Paganini et al. (2012*b*); (24) Villanueva et al. (2012).

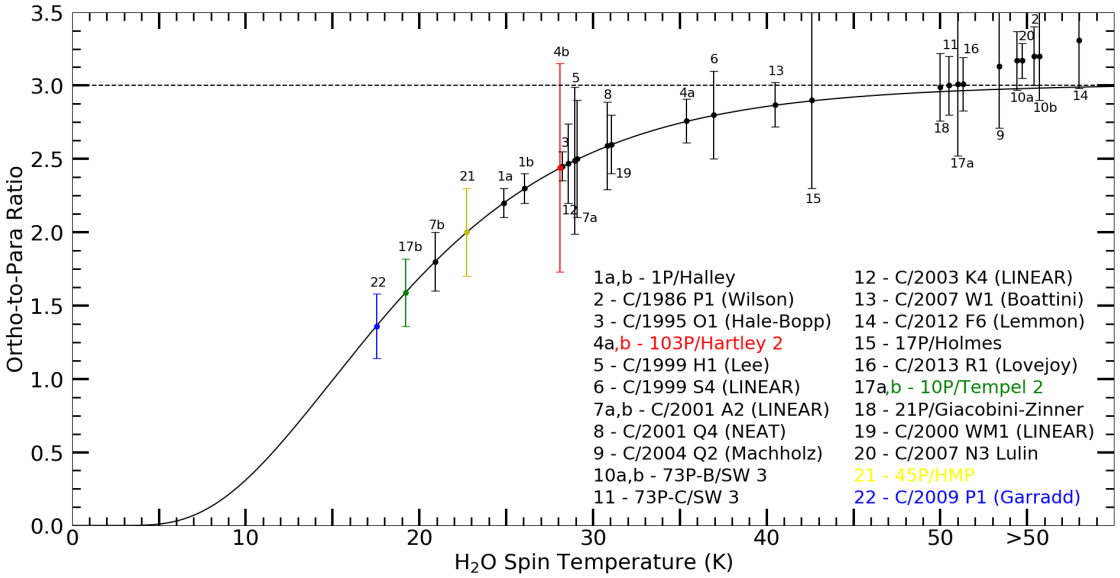

Figure 3.3. Cometary OPR values against the corresponding water spin temperature. (1a,b,2) Mumma et al. (1988); (3) Crovisier et al. (1997); (4a) Crovisier et al. (1999); (4b,17b,21,22) This work; (5,6,7a,7b) Dello Russo et al. (2005); (8) Kawakita et al. (2006); (9) Bonev et al. (2009); (10a) Bonev et al. (2008*a*); (10b,11) Dello Russo et al. (2007); (12) Woodward et al. (2007); (13) Villanueva et al. (2011); (14) Paganini et al. (2014) ; (16) Dello Russo et al. (2008); (17a) Paganini et al. (2012*a*); (18) DiSanti et al. (2013); (19) Radeva et al. (2010); (20) (Gibb et al. 2012)

Tempel 2 with increasing $r_{\rm nuc}$. Taking into account the results of the laboratory study, it would seem that the previous on-nucleus observation probed sublimated water with an OPR that was normalised to the statistical equilibrium value in the nucleus ice. Whereas, the SPIRE observation presented in this study has detected the water further out in the coma following nuclear-spin conversion via hydrogen-exchange reactions of water with H^+ and H_3O^+ or water molecule collisions with water clusters or ice.

The other comet in the study with previously determined OPRs is Hartley 2. In these studies, the observations were all centred on-nucleus and extending up to several hundred km, whereas the SPIRE observations probe $r_{\rm nuc}$ of 4 100−8 200 km. Whilst the OPR determined in this study is lower than the literature values, the large uncertainty means that the OPR reported here is in agreement with previous studies. More sensitive observations of the coma of Hartley 2 are needed to determine if any OPR variation is real. To further assess the relationship between OPR and $r_{\rm nuc}$, the on-nucleus OPR was determined for all comets in this study using the central SPIRE detectors. It was

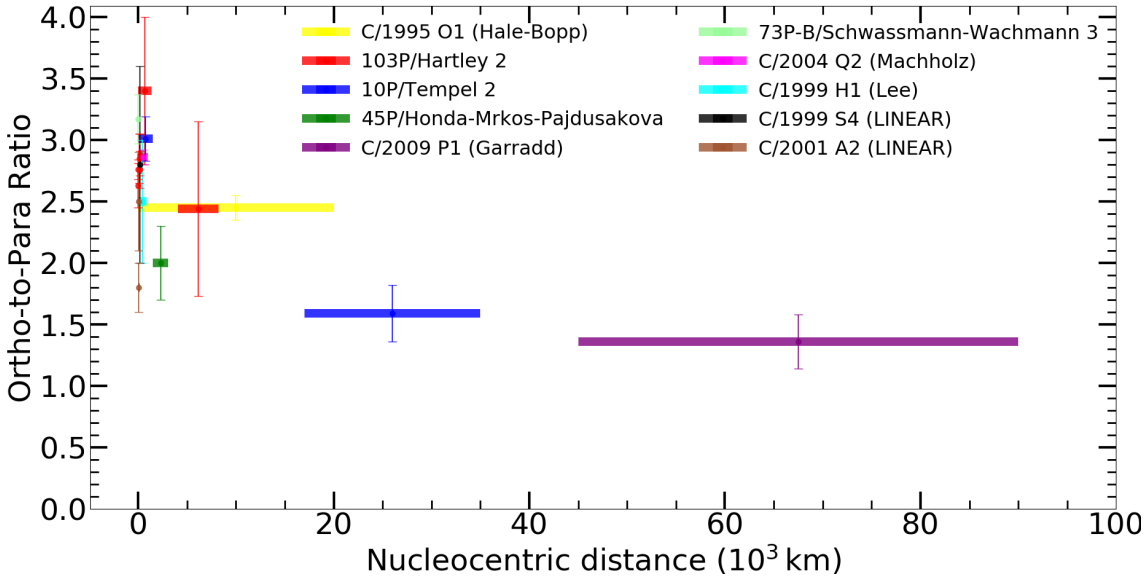

Figure 3.4. All empirical OPR values from this study and from the literature with published $r_{\rm nuc}$ of the observations. The bars in the x-axis direction indicate the range of the observations.

found that these values are in agreement with the coma observations, however, this is unsurprising as the relatively large SPIRE beam sizes result in the on-nucleus detectors also observing the comae up to $r_{\rm nuc}$ of $\sim$1000$-$10 000 km. Therefore, it seems that following sublimation, gas-phase nuclear-spin conversion is occurring within these radii.

Previous Determinations of Ortho-to-Para Ratio versus $r_{\rm nuc}$

Most previous cometary observations that have yielded OPR values are either on-nucleus or probing the very inner comae, however one of the first comets with a reported OPR was comet Hale$-$Bopp with observations taken with *ISO* extending from the nucleus to a $r_{\rm nuc}$ of approximately 20 000 km (Crovisier et al. 1997). Interestingly, an OPR of 2.45$\pm$0.10 was calculated, significantly lower than the canonical value. This seems to further support the relationship between OPR and $r_{\rm nuc}$, and hence coma-based nuclear-spin conversion. However, as this is the only reported OPR value for this comet caution should be taken when interpreting this OPR value, as other currently unknown factors that influence the OPR may have occurred in comet Hale$-$Bopp.

Several studies of the OPR in inner cometary comae have been conducted. Observations of comet 73P$-$B and C/2004 Q2 (Machholz) determined OPR values of approximately 3 and found no variation over $r_{\rm nuc}$ of 5$-$30 km and $\leq$1000 km, respectively (Bonev

et al. 2007, 2008*a*). Furthermore, on-nucleus observations, that extended up to a $r_{\rm nuc}$ of 350−1700 km, were taken of C/1999 H1 (Lee), C/1999 S4 (LINEAR), and C/2001 A2 and roughly agree with the canonical OPR value (Dello Russo et al. 2005). Although in the comet C/2001 A2 OPR variation was observed temporally over 24 hr, suggesting nuclear-spin conversion has been observed (Dello Russo et al. 2005). Therefore, these studies indicate that nuclear-spin conversion may not be happening in the inner coma, but instead it may be occurring at larger $r_{\rm nuc}$ in order to explain the observations of Tempel 2. However, this raises questions about how the conversion is happening at large radial distances outside of the higher density, collisionally dominant inner coma.

Finally, in this study no significant difference in the water OPR between the Jupiter-Family comets and the Oort-Cloud comet is found. This is consistent with a recent study of ammonia OPR in 26 comets (Shinnaka et al. 2016).

The *Herschel* SPIRE observations presented in this study seem to further support rapid solid-phase nuclear-spin conversion in cometary ice. However, these results highlight the need for further observational, laboratory, and theoretical study of nuclear-spin conversion as it has previously been proposed that the processes mentioned above would occur in the very inner coma, but from the analysis above it would seem that OPR variations occur at a range of $r_{\rm nuc}$. From an observational perspective, for one comet multiple OPR measurements at a range of $r_{\rm nuc}$ are needed in order to directly detect changes in the coma OPR. Additional laboratory studies are needed with the inclusion of a collisional, coma-like, environment that the water ice is sublimated into. On the theoretical side, if a mechanism could be identified for nuclear-spin conversion in low collision regions then that would help explain the observations reported here.

3.4.2 Water Production Rate Variation

As noted in the previous section, for all comets in the study it appears that the observed $Q_{\rm H_2O}$ decreases with increasing $r_{\rm nuc}$. There are a number of possible causes for this:

i) The coma temperature is not constant, but varies with $r_{\rm nuc}$ as line intensities are sensitive to the gas temperature profile.

ii) There is an additional source of water in comae, potentially from the sublimation of the ice clusters or icy dust grains.

iii) There is a spatial variation in the water OPR.

iv) The assumption that the sublimation outflow of water is spherically symmetric is too simplistic or indeed incorrect.

v) The radiative transfer excitation model for the water transitions may be missing important processes such as transitions from higher rotational levels.

Whilst there are not enough transitions or $r_{\rm nuc}$ offsets to discern which of these possibilities is the cause of the variation, the observation that transitions from the upper rotational levels produce significantly lower $Q_{\rm H_2O}$ values for three of the comets indicate that an over-simplified excitation model may be all or part of the cause. This is because the upper states in the radiative transfer model are populated from higher levels that are not described in the model. Observationally, analysis of *Rosetta* data of comet 67P has shown that the water outflow in the coma is asymmetric (Bockelée-Morvan et al. 2015*b*), and there also might be ongoing sublimation of ice in the coma (Gicquel et al. 2016). Therefore, the assumption of a symmetric water distribution and the additional comae water sources may also be part of the cause.

In this study, it is interesting to note that C/2009 P1, the only Oort-Cloud comet, has $Q_{\rm H_2O}$ values 1−2 orders of magnitude higher than the Jupiter-Family comets of Hartley 2, Tempel 2, and 45P. Furthermore, by comparing the results of this study with the literature it was found that only the long-period comet Hale−Bopp has a greater $Q_{\rm H_2O}$ value then C/2009 P1 at a similar $r_{\rm h}$ (Combi et al. 2000). Additionally, of all comets with known $Q_{\rm H_2O}$ values, 45P has the lowest value at the observed $r_{\rm h}$, with the short-period comet 67P having a roughly equal $Q_{\rm H_2O}$ to that of 45P, although it is known to vary (Bertaux et al. 2014). From these comparisons, and the fact that the remaining two Jupiter-Family comets in this study also have lower $Q_{\rm H_2O}$ values than any Oort-Cloud comet at the same $r_{\rm h}$, it could be concluded that Oort-Cloud comets have greater $Q_{\rm H_2O}$ values due to a greater retention of the volatiles accreted during formation due to fewer perihelion passes, if $Q_{\rm H_2O}$ is linked to amount of volatiles in the nucleus.

Finally, an interesting trend is apparent when comparing the $Q_{\rm H_2O}$ values of Hartley 2, Tempel 2, and 45P determined in this work against values calculated from previous

apparitions observed at similar values of $r_{\rm h}$. As can be seen in Table 3.3, $Q_{\rm H_2O}$ values for all three comets have decreased over time. Between 1991 and 1997, the $Q_{\rm H_2O}$ of Hartley 2 decreased by at least a factor of two, and subsequently between 1997 and 2010 it dropped by 2−7 times. For Tempel 2 the $Q_{\rm H_2O}$ decreased by a factor of 3−10 between 1988 and 2010, whereas for 45P the 1995 apparition is $\approx 1.5 - 3$ times greater than in 2011. If the outgassing rate is linked to the amount of volatiles in the comet then this provides evidence for the continued volatile loss over perihelion passes.

3.5 Summary and Conclusions

Spectroscopic data of three Jupiter-Family comets and one Oort-Cloud comet observed using *Herschel* SPIRE FTS were analysed with several fundamental rotational water lines detected in each comet. Ortho- and para-water emission were seen and water OPR values were determined. The OPR values for 45P and C/2009 P1 are reported for the first time. While the OPR for Hartley 2 is in agreement with the literature values, for Tempel 2 the calculated value is lower than previously determined. By comparing the short- and long-period comets in the study no variation in OPR is seen between different families. Whilst the OPR values for Tempel 2, 45P, and C/2009 P1 are non-typical when compared to previously determined OPRs in other comets, they are approximately equal to the OPR values determined in comets Halley and C/2001 A2, and the protoplanetary disk TW Hydrae.

Interestingly, in Tempel 2 it should be noted that the previous observation is focused on-nucleus and an OPR approximately equal to the canonical value. Whereas the observation presented here is of the cometary coma and therefore, it is thought that this difference could be due to coma-based gas-phase nuclear-spin conversion that occurred subsequent to OPR equilibrium in the solid-phase and sublimation from the nucleus. Importantly, this picture is consistent with the laboratory findings and the OPR values presented provide good evidence of post-sublimation gas-phase nuclear-spin conversion.

Using the empirical OPR values and an established radiative transfer model, the $Q_{\rm H_2O}$ values for each comet were determined at a range of $r_{\rm nuc}$ for each of the main fundamental rotational water lines.

In general, the $Q_{\rm H_2O}$ values determined from the SPIRE observations are in agreement within an order of magnitude of previous observations, however the values determined

from the $3_{12}-3_{03}$ ortho-water and the $2_{11}-2_{02}$ para-water lines are lower than literature values. This could suggest level population inaccuracies in the model, but more work is required to confirm this. Interestingly, the Q_{H_2O} values decrease with increasing r_{nuc}. This could potentially be caused by inaccuracies in the excitation model, however further observational and theoretical work is needed in order to determine if this result is linked to an apparent nucleocentric dependence for the OPR.

By comparing the comets in this study is can be seen that the only Oort-Cloud comet, C/2009 P1, has a value of Q_{H_2O} that is one to two orders of magnitude greater than the Jupiter-Family comets presented here. This correlation and difference is also seen in the literature as C/2009 P1 has one of the highest values of Q_{H_2O} of all comets at the observed r_h, whilst the three Jupiter-Family comets have some of the lowest values. Interestingly, the values of Q_{H_2O} for the three Jupiter-Family comets presented here are lower than seen in previous apparitions suggesting that short-period comets decrease in Q_{H_2O} on each apparition, that results in a lower value when compared to an Oort-Cloud comet. Therefore, it could be concluded that the Q_{H_2O} is somewhat related to comet family, and formation location and conditions. However, this study has a small sample size and so more research should be done to probe this relationship.

This page was intentionally left blank

Chapter 4

An Unbiased Survey to Determine White Dwarf Disk Frequency

Where there is an observatory and a telescope, we expect that any eyes will see new worlds at once.

Henry David Thoreau (1862)

The work presented in this chapter is based on the paper by Wilson et al. 2019, MNRAS, Volume 487, Issue 1, Page 133, in collaboration with J. Farihi, B. T. Gänsicke, and A. Swan.

4.1 Introduction

Over the past few decades thousands of exoplanetary systems have been discovered via transit and radial velocity surveys. While knowledge about exoplanet radii and masses can be gained, little is known about their precise composition. By studying protoplanetary disks it is possible to probe the chemical signatures of solids and gases that likely form minor and major planetary bodies (Bergin et al. 2015; Marty et al. 2017). However, while these techniques, combined with other methods such as direct imaging, are beginning to probe Solar System-like architectures (Gillon et al. 2017), knowledge of exoplanetary composition is important and cannot be provided by conventional means.

4.1.1 White Dwarf Planetary Systems

Recent work has shown that planetary systems can survive into the post-main sequence (Zuckerman et al. 2003, 2010; Koester et al. 2014; Vanderburg et al. 2015), and empirically provide the compositional information key to understanding the formation and bulk chemistry of large planetesimals and their associated planets. White dwarfs with atmospheric metals have been observed to host circumstellar disks which manifest via dusty and gaseous emission (Zuckerman & Becklin 1987; Becklin et al. 2005; Reach et al. 2005; Gänsicke et al. 2006; von Hippel et al. 2007; Farihi et al. 2008; Rocchetto et al. 2015; Farihi, Parsons & Gänsicke 2017). The white dwarf atmosphere distils the disk material and provides an indirect, but observable measurement of the parent body elemental composition (Jura & Young 2014; Xu et al. 2014; Wilson et al. 2016; Xu et al. 2017; Hollands et al. 2018*a*). The nature and frequency of these white dwarf planetary systems therefore plays a critical and complementary role to the study of the exoplanetary systems via other methods such as transit photometry, radial velocity variations, and direct imaging.

Theoretical Models of Parent Body Perturbation, Debris Disk Formation, and Accretion onto the White Dwarf

Dynamical studies have shown that the delivery of minor planetary bodies to the innermost orbital regions around white dwarfs can occur via planet-planetesimal perturbations (Veras et al. 2013; Mustill, Veras & Villaver 2014). In some cases the dynamics are sufficient to generate periastra within the stellar Roche limit (Debes et al. 2012; Frewen & Hansen 2014), thus leading to tidal fragmentation, while in other cases additional gravitational encounters are necessary to create sufficiently close passes (Bonsor & Wyatt 2012). A recent study modelled the destruction, tidal disruption and total sublimation, of minor planetary bodies on highly eccentric orbits for a range of white dwarf temperatures and parent body properties (Brown, Veras & Gänsicke 2017). It was found that tidal disruption and therefore disk formation only occurs for rocky and icy bodies $\geq$ 10 km, whereas all small bodies will completely sublimate prior to impact with the star. Subsequent to tidal disruption, the eventual formation of the observed debris disks is an ongoing area of study (Debes 2011; Veras et al. 2014, 2015). But once formed, if the disk is collisionless the solids will evolve primarily through PR-drag, whether optically thick or optically thin to starlight (Rafikov 2011*a*; Bochkarev & Rafikov 2011). For disks in which collisions play an important role, or where gas is co-spatial with the dust, other mechanisms may play

important roles (Rafikov 2011*b*; Metzger, Rafikov & Bochkarev 2012; Kenyon & Bromley 2017*c*).

A key prediction made by dynamical models of planetary body perturbation into the Roche limit of the host white dwarf, is that the frequency of atmospheric metals and circumstellar debris disks is somewhat dependent on the white dwarf cooling age (Debes et al. 2012; Mustill et al. 2014; Petrovich & Muñoz 2017; Smallwood et al. 2018). The distribution of planetary destruction frequency over cooling age differs between models and therefore unbiased, empirical rates of atmospheric metals and infrared excesses are needed over a wide range of white dwarf ages in order to test models.

Previous Surveys of White Dwarf Planetary Systems

Observationally, the unbiased frequency of photospheric metals in $T_{\rm eff} \leq 25\,000$ K white dwarfs has been robustly shown to be at least 20−30 per cent via multiple surveys (Zuckerman et al. 2003, 2010; Koester et al. 2014). For circumstellar debris disks, on the other hand, the bulk of existing *Spitzer* studies have targeted stars with known atmospheric metals in order to formalise the link between disks and pollution (Debes, Sigurdsson & Hansen 2007; Jura, Farihi & Zuckerman 2007*a*; Farihi et al. 2010), and therefore planetary debris frequencies that may be derived from these works are biased towards detections of disks. Later studies have used wide-field surveys such as SDSS and *WISE* in order to determine the infrared excess frequency using the largest possible number of white dwarfs (Debes et al. 2011; Girven et al. 2011), but these studies can suffer from limited sensitivity and poor sample characterisation (Barber et al. 2012). Multiple *Spitzer* studies have constrained the debris disk frequency detected via an infrared excess to between 1 and 4 per cent (Mullally et al. 2007; Farihi, Jura & Zuckerman 2009; Rocchetto et al. 2015). However, as the majority of published work suffers from selection biases, sensitivity issues, or insufficient statistics (or a combination of these), an unbiased *Spitzer* survey is needed to robustly determine the frequency of infrared excesses. Furthermore, in order to potentially test dynamical models, a sufficiently large survey is needed so that frequencies at specific cooling age bins can be determined robustly.

This study analyses *Spitzer* Infrared Array Camera (IRAC; Fazio et al. 2004) observations of 236 white dwarfs selected in an unbiased manner over a wide range of cooling ages. The same stars were part of several *HST* Cosmic Origins Spectrograph (COS) Snapshots, thereby providing a double-blind study of metal pollution and infrared excess frequency.

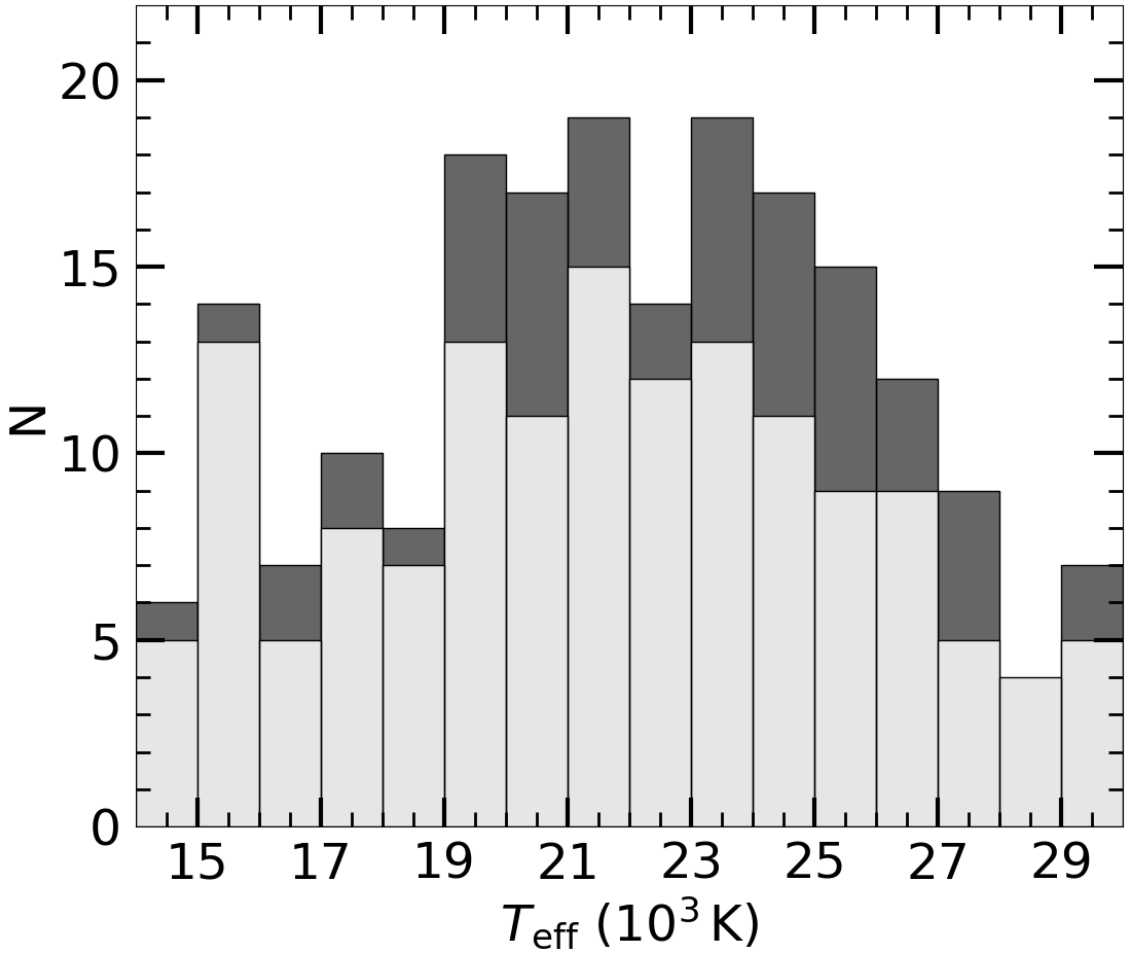

Figure 4.1. $T_{\rm eff}$ histogram for the single white dwarfs in this study. All stars were observed with *Spitzer* and are shown in dark grey, while the subset observed by *HST* are shown in light grey. The same number of targets was observed with both telescopes in the 28 000−29 000 K range, whereas in all other temperature bins more white dwarfs were observed by *Spitzer*.

These observations form an extended sample to previous studies (Koester et al. 2014; Rocchetto et al. 2015) in order to search for infrared excesses and atmospheric metals in hotter and cooler white dwarfs resulting in the largest double-blind search for debris disks around white dwarfs.

The sample selection and *Spitzer* observations are presented in Section 4.2, with the data analysis given in Section 4.3. The results and notes on individual targets are given in Section 4.4, with conclusions in Section 4.5.

4.2 Observations

4.2.1 Sample Selection Criteria

The observations primarily presented in this study are one part of a double-blind survey to determine the planetary debris disk frequency as a function of white dwarf cooling age, or effective temperature. In order to determine the infrared excess frequency, the *Spitzer* observations are analysed here, whereas *HST* observations of the same sample will be analysed in order to constrain the atmospheric metal frequency over cooling age and will be presented elsewhere. The stars in the sample were selected from catalogues of nearby white dwarfs (Liebert, Bergeron & Holberg 2005; Koester et al. 2009; Gianninas, Bergeron & Ruiz 2011) by the following criteria:

i) hydrogen rich atmospheres, and therefore relatively short diffusion timescales (Koester 2009);

ii) $F_\lambda(1300\,\text{Å}) > 5 \times 10^{-14}\,\text{erg}\,\text{cm}^{-2}\,\text{s}^{-1}\,\text{Å}^{-1}$;

iii) white dwarf effective temperatures in the range 14 000 to 31 000 K.

These criteria were chosen so that atmospheric metals observed with *HST* can be confidently ascribed to current accretion from the circumstellar debris disk. The flux limit was chosen in order to provide high S/N observations of any potential atmospheric metals, and the temperature range was selected in order to probe planetary systems around white dwarfs in the age range 9 to 230 Myr.

Using these selection criteria 236 stars were chosen. A literature and database search revealed that 40 targets are in confirmed or candidate binary systems, resulting in 196 apparently single stars in the survey. Photometry of all stars is attempted regardless of binarity, however the single star sample is the main focus of this study as the larger sample size allows a more robust determination of debris disk frequency statistics. The binary subsample contains systems of various companion types and separations, including a subsample that are spatially-resolved. Analysis of these systems is particularly interesting as, to date, the unbiased planetary debris disk frequency of wide binaries has not be established, and therefore this subsample is also discussed below. Table 4.6 lists all stars

for which IRAC photometry was attempted, with binaries noted.

4.2.2 *Spitzer* Observations

Infrared photometry was obtained for all stars in the survey using IRAC onboard the *Spitzer Space Telescope*, analysis of which is the main focus of this study. Of the sample, 168 stars were observed by *HST* COS as part of multiple Snapshot programmes. Warm *Spitzer* IRAC observations of 168 sample stars were taken in Cycles 8 and 12 for Programme 80149 and 12103, respectively. The objects were observed in the medium-size, cycling dither pattern with 20 frames of 30 s each taken at both 3.6 and 4.5 μm resulting in a total exposure time of 600 s in each warm IRAC channel. To complete the sample, archival IRAC observations (cryogenic or warm) for 68 sources were retrieved and analysed. A breakdown of the number of white dwarfs observed by *Spitzer* and *HST* binned by temperature is presented in Fig. 4.1.

4.2.3 Photometry Reduction

Single, fully processed, and calibrated 0.6 arcsec pixel^{-1} mosaic images were extracted by the IRAC calibration pipeline S19.2.0 for all stars at all observed wavelengths. Using the standard IRAF task APPHOT aperture photometry was conducted with aperture radii of 2.4 or 3.6 arcsec, depending on target brightness and the presence of additional nearby sources, and $14.4 - 24.0$ arcsec sky annuli. Aperture correction was done using conversion factors listed in the IRAC Data Handbook, but the fluxes were not corrected for colour. Flux uncertainties were calculated by the summation in quadrature of the error in the measured flux with the calibration uncertainty, taken to be 5 per cent (Farihi, Zuckerman & Becklin 2008). The measured fluxes and corresponding errors are presented in Table 4.6. Some targets have sufficiently bright neighbouring sources (including binary companions) in the IRAC observations, which could lead to photometric contamination when aperture photometry is performed. For these stars, PSF-fitting photometry was conducted using APEX. Flux upper limits were calculated by conducting aperture photometry at the published target coordinates using a 2.4 arcsec radius and performing aperture correction. The resulting value was compared to the sky noise per pixel multiplied by the aperture area, with the larger value reported as the upper limit. One target (1339+346) was irreversibly contaminated by a nearby background source, and is not considered further.

It has been shown that the measured infrared flux from *Spitzer* observations can be

altered by a few per cent, especially in channel 1, due to intra-pixel variations in the IRAC detectors (Mighell, Glaccum & Hoffmann 2008). It is important to understand how these variations affect the photometry as the calculated excesses may also be altered. The pixel-phase response (the variance of which is the cause of the observed flux variation) can be modelled by a 2D Gaussian offset from the centre of the pixel. Therefore, if one knows the position of the peak of the PSF in the pixel, the flux variation can be determined. In order to test that the observations taken for this study are robust to intra-pixel flux variation the pixel-phase response was modelled at 20 random intra-pixel positions. It was found that the average flux variation was 0.1 per cent, and therefore, photometry of objects done on mosaicked frames that are comprised of a sufficient number of individual frames will not be significantly affected by intra-pixel flux variation. For stars in this the study, the flux uncertainties will be dominated by measurement and calibration errors.

4.2.4 Spectral Energy Distribution Construction

For all stars, SEDs were constructed using additional photometric data from various catalogues including; AAVSO Photometric All-Sky Survey (APASS; Henden et al. 2016), Deep Near Infrared Survey of the Southern Sky (DENIS; Epchtein et al. 1999), Panoramic Survey Telescope and Rapid Response System (Pan-STARRS; Chambers et al. 2016), SDSS, 2MASS, and UKIDSS. Near-infrared photometry for several sources were taken from the literature (Farihi 2009; Barber et al. 2012). White dwarf atmospheric models (Koester 2010) were fitted to the optical and near-infrared fluxes using a least-squares algorithm.

In order to accurately determine infrared excesses, knowledge of the effective temperatures of the white dwarfs is crucial as, when fitted to optical and near-infrared data, cooler or hotter white dwarf models result in an inaccurate determination of the white dwarf photosphere at infrared wavelengths. Therefore, to test the effective temperatures taken from the parent surveys for all stars, atmospheric model fitting to the available photometry was conducted using a range of temperatures centred on the literature value and varying up to $\pm 2\,000$ K in steps of 500 K. For each star in the survey the temperature with the smallest model fitting error was chosen. This was typically within 1 000 K of the published temperature and it was found that for a 500 K deviation away from the best-fit temperature, the model fitting error increased by 7 per cent of the smallest value on average.

4.3 Data Analysis

The following infrared excesses determination analysis is conducted on single and binary targets in which reliable photometry of the white dwarf was obtained. This results in 195 apparently single stars and 15 white dwarfs in *Spitzer* IRAC spatially-resolved binary systems. Targets in known binaries whose *Spitzer* photometry is contaminated by unresolved or marginally resolved companions are not considered in the following analysis. However, these systems may be spatially-resolved in corresponding *HST* observations and therefore may be probed for atmospheric metals.

In order to comprehensively establish the frequency of debris disks two infrared excess determination methods were used. First, by comparing the measured flux to the predicted photospheric flux in each IRAC channel, and second, by calculating the colour excess. For all excess determination methods presented below, the photospheric model flux was determined by performing synthetic photometry of the atmospheric model over the *Spitzer* bandpasses.

Prior to the application of the two infrared excess methods, it can be useful to determine how sensitive the observations are in detecting a circumstellar debris disk. This can be done by calculating the minimum detectable excess, $\phi_{\rm excess}$, for each star in the survey. $\phi_{\rm excess}$ is defined as the significance limit of the detection (3σ, where σ is the summation in quadrature of the flux and model uncertainties) divided by the model flux at the same wavelength as the observations. If it is assumed that potential excesses are produced by flat, opaque disks with $T_{\rm in} = 1\,400\,{\rm K}$ and $T_{\rm out} = 300\,{\rm K}$, then the $\phi_{\rm excess}$ values of the observations can be compared against the flat disk model in order to determine the inclination, i, at which a debris disk is no longer observable (Bonsor et al. 2017). On average, in both warm IRAC channels it was found that all disks with $i < 89^\circ$ should be detected.

4.3.1 Flux Excess

Previous work studying dust around 180 000 *Kepler* field stars has used a flux excess method to determine infrared excesses (Kennedy & Wyatt 2012). In this study, the observations were compared to the calculated synthetic model fluxes by calculating the flux excess, χ, using the following:

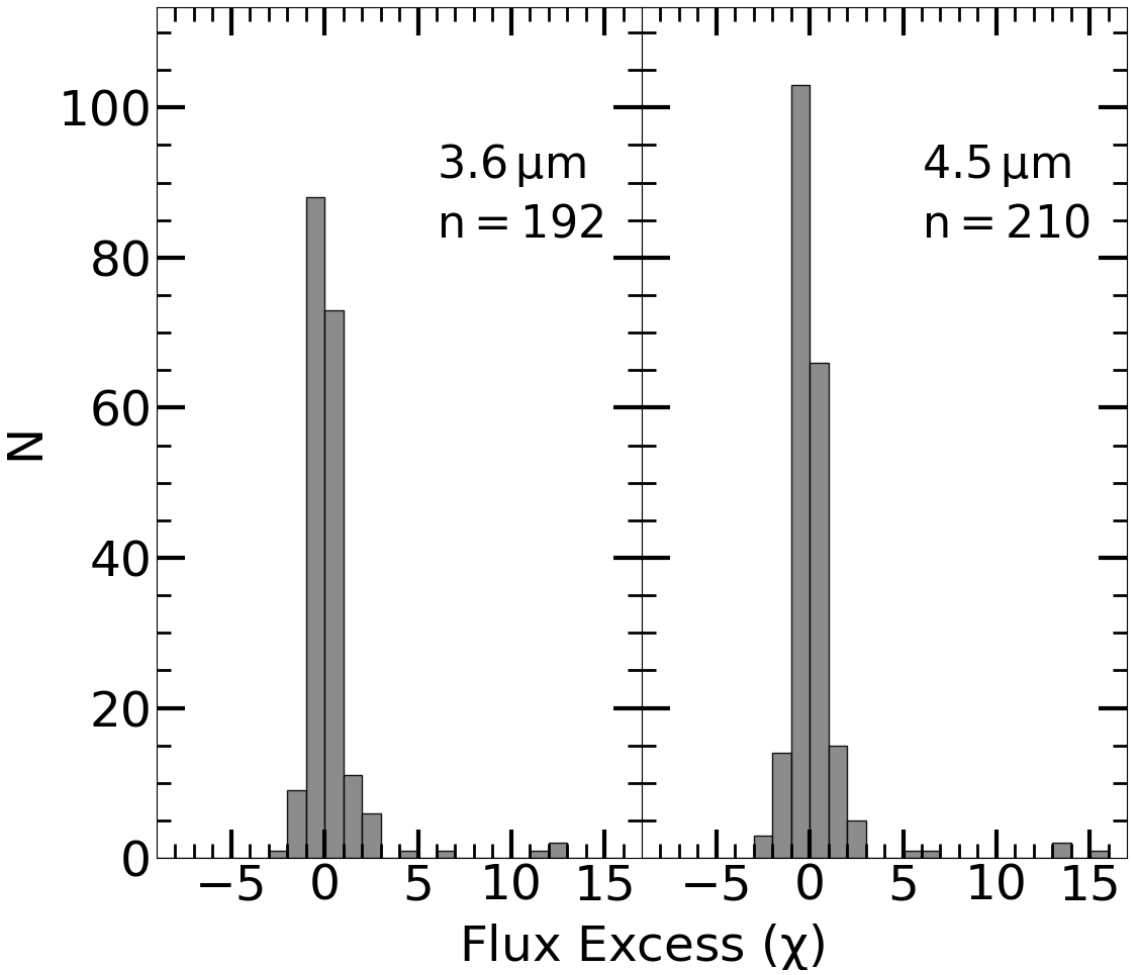

Figure 4.2. Histograms of flux excess values, χ, as determined by equation (4.1) for both warm IRAC channels. At 3.6 μm 192 stars were observed, whereas at 4.5 μm 210 targets have photometry. It should be noted that not all stars have 3.6 μm data, as some archival targets only have 4.5 and 7.9 μm observations.

$$\chi = \frac{\mathrm{F_{obs}} - \mathrm{F_{mod}}}{\sqrt{\sigma_{\mathrm{obs}}^2 + \sigma_{\mathrm{mod}}^2}} \tag{4.1}$$

where $\mathrm{F_{obs}}$ and $\mathrm{F_{mod}}$ are the observed and model fluxes, σ_{obs} and σ_{mod} are the corresponding errors, respectively. Photometric and calibration uncertainties are represented by σ_{obs} with errors in the model fitting to the short wavelength data given as σ_{mod} and are typically 1 per cent of F_{mod}.

Fig. 4.2 shows histograms of χ for each warm IRAC channel. For channel 1, the mean and standard deviation in χ is 0.15 and 1.07, and for channel 2 the corresponding values

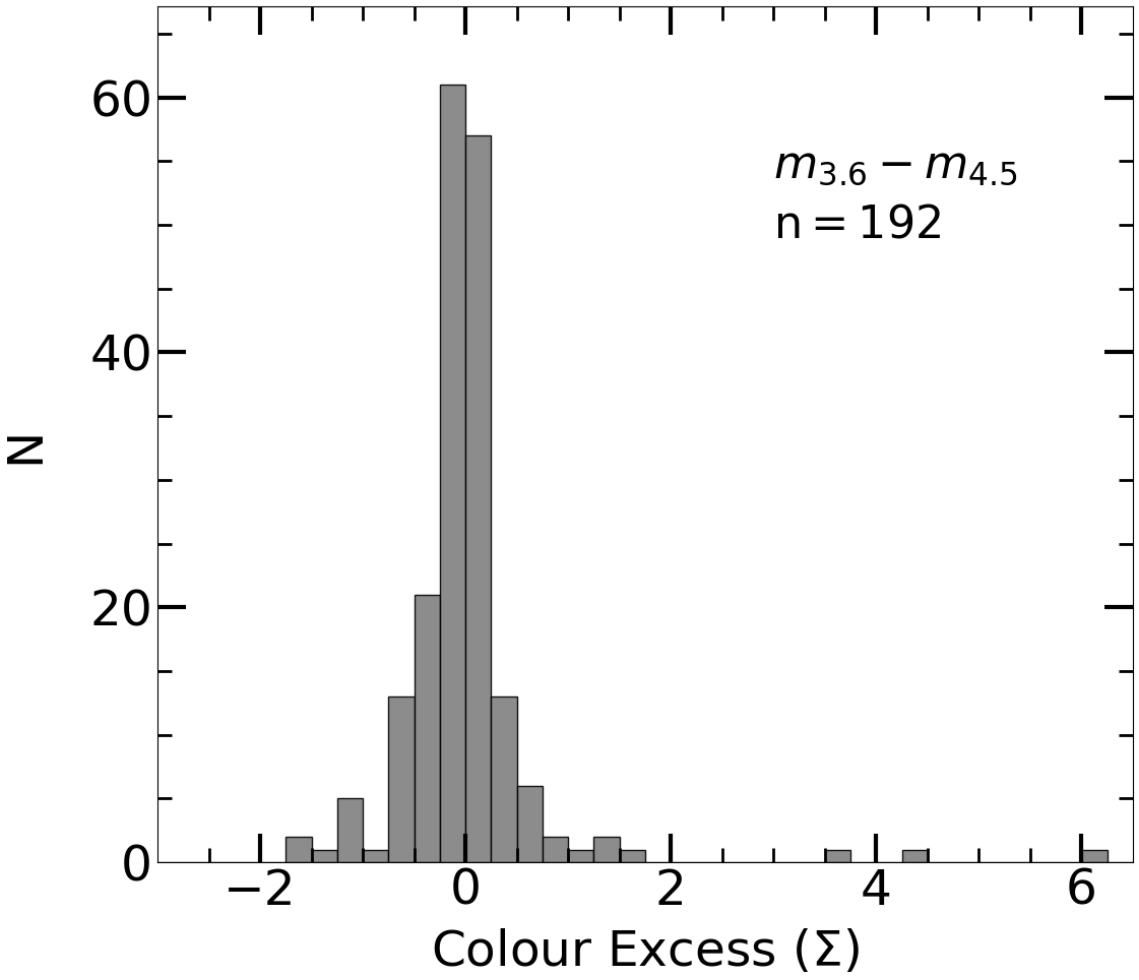

Figure 4.3. Histogram of $m_{3.6} - m_{4.5}$ colour excess values, Σ, as determined by equation (4.2) for the 192 stars in the sample observed in both warm IRAC channels.

are 0.05 and 1.15. These are broadly consistent with Gaussian distributions.

Significant infrared excesses were identified if a star has $\chi \geq 3$ in any channel. Five stars, WD 0843+516, WD 1015+161, WD 1018+410, WD 1457−086, and WD 2328+107, with previously discovered significant infrared excesses were recovered using this analysis, with χ values in the range 5−15. Of the remaining 190 single sources, two systems exhibit excess in both warm IRAC channels. However, the SEDs for these stars appear to be better fit either by a cooler temperature model, or possibly by a binary companion. These two sources are discussed in Section 4.4.1. No other sources with reliable flux measurements have a $\chi \geq 3$ at any wavelength. The χ values of white dwarfs with a significant infrared excess are presented in Table 4.1.

4.3.2 Colour Excess

Infrared colour was also used to search for infrared excesses, and therefore the presence of debris disks. By searching for colour excesses, faint debris disks could potentially be discovered that might be missed whilst searching for flux excesses. Single- and weighted-colour excesses have been previously used to detect faint debris disks around main sequence stars using *WISE* photometry (Patel, Metchev & Heinze 2014; Patel et al. 2017). In this study, the first large search for infrared colour excesses, Σ, at white dwarfs is conducted.

Single-Colour Excess Determination

It is worth noting that, following the method outlined in previous studies, the observed and model fluxes, and corresponding errors, have been converted into magnitudes. The single-colour excesses, Σ, were determined using the following:

$$\Sigma_{\mathrm{m_i - m_j}} = \frac{\mathrm{m_{i,obs}} - \mathrm{m_{j,obs}} - \mathrm{m_{ij,mod}}}{\sqrt{\sigma^2_{\mathrm{m(i,obs)}} + \sigma^2_{\mathrm{m(j,obs)}} + \sigma^2_{\mathrm{m(ij,mod)}}}} \tag{4.2}$$

where i and j are the IRAC channels such that i = 1, 2, 3, j = 2, 3, 4, and $i < j$. The numerator in the above equation is photospheric model colour, $\mathrm{m_{ij,mod}}$, subtracted from the observed colour. The uncertainties in the observed magnitudes are added in quadrature with the uncertainty in the model colour, $\sigma_{\mathrm{m(ij,mod)}}$.

Weighted-Colour Excess Determination

If sources have infrared photometry in three or more bandpasses, it is possible to construct an excess statistic based on a weighting of the various colours. The weighted-colour excesses, $\Sigma_{\overline{\mathrm{m_j}}}$, can be calculated by the weighted sum of single-colour excesses, $\overline{\Sigma[\mathrm{m_j}]}$:

$$\overline{\Sigma[\mathrm{m_j}]} = \frac{1}{\mathrm{C}} \sum_{\mathrm{i=1}}^{\mathrm{j-1}} \frac{\mathrm{m_{i,obs}} - \mathrm{m_{j,obs}} - \mathrm{m_{ij,mod}}}{\sigma^2_{\mathrm{m(i,obs)}}} \tag{4.3}$$

divided by the uncertainty of the weighted average, $\sigma_{\overline{\Sigma[\mathrm{m_j}]}}$:

$$\Sigma_{\overline{m_j}} = \frac{\overline{\Sigma[m_j]}}{\sigma_{\overline{\Sigma[m_j]}}} = \frac{\overline{\Sigma[m_j]}}{\sqrt{\sigma^2_{m(j,obs)} + 1/C}} \tag{4.4}$$

where the terms in the summation are the same as in equation 4.2, and C is the normalisation constant, $\sum_{i=1}^{j-1} \frac{1}{\sigma^2_{m(i,obs)}}$.

It is worth noting that hereafter Σ is used to represent either single- or weighted-colour excesses in general, with the values calculated using either equation 4.2 or 4.4. References to specific colour excesses will either be stated explicitly in text or as a subscript to Σ. For this study the single- and weighted-colour excesses were calculated for all white dwarfs with reliable *Spitzer* photometry in multiple channels. The histogram of the $3.6 - 4.5\,\mu$m single-colour excesses is shown in Fig. 4.3. The mean and standard deviation of this single-colour excess are 0.02 and 0.79. It is worth noting that < 20 per cent of stars were observed in either longer wavelength channel and so any statistical analysis of colour excesses in these channels might not as be robust. However, for individual targets with reliable photometry at these wavelengths single- and weighted-colour excesses can be determined in order to find debris disks.

A white dwarf was determined to have a colour excess if the star had $\Sigma \geq 3$. Using this criterion, the infrared colour excess method returned three white dwarfs; WD 0843+516, WD 1015+161, and WD 1018+410. All three degenerates are known to have debris disks. The Σ values of white dwarfs with a significant infrared excess are presented in Table 4.1.

It is worth noting that, while this technique can discover faint debris disks, it is also biased towards stars with observations at multiple wavelengths, and therefore faint disks at white dwarfs only observed in the channels 1 and 2 might be missed. This point is highlighted by the fact that the infrared flux excesses at WD 1457−086 and WD 2328+107 are not detected as having $\Sigma \geq 3$. Indeed, only white dwarfs with a highly significant infrared flux excess, $\chi > 10$, were seen to have a $3.6 - 4.5\,\mu$m single-colour excess, $\Sigma \geq 3$. However, it should be noted that due to an additional flux uncertainty term in the denominator of equation 4.2 compared to equation 4.1, the Σ values are typically lower than the corresponding χ. This results in a more conservative excess detection using the colour method.

Calculating Colour Excesses with Additional $JHK-$band Photometry

To underline the benefit of multiple wavelength observations for determining significant colour excesses, the weighted-colour excesses for all four *Spitzer* channels were calculated for the entire sample using archival UKIDSS and 2MASS $JHK-$band, and *WISE* W1 and W2 photometry. It was found that only stars with a significant flux or colour excesses as determined above have a significant weighted-colour excess using additional shorter wavelength data. This provides confidence in our excess determination methods. The weighted-colour excess values of white dwarfs with a significant infrared excess are presented in Table 4.2. It can be seen that the white dwarfs with confirmed debris disks have a weighted-colour excess greater than 5σ in at least one *Spitzer* channel, whereas stars with a potential companion or background contamination, as will be discussed in Section 4.4.1, have a weighted-colour excess below this value. Using this method, future ground-based near-infrared observations could complement archival space-based observations at longer wavelengths in order to search for debris disks. Therefore, future studies utilising near- and mid-infrared observations could potentially find faint debris disks using this method.

4.3.3 Infrared Excess Determination of Known White Dwarf Debris Disks

As can be seen in Table 4.1, if the flux excess, χ, and the colour excess, Σ, are compared for stars in this survey, then only WD 0843+516, WD 1015+161, and WD 1018+410 have a significant, $> 3\sigma$, excess for both methods.

In order to test the analysis methods further, the infrared excesses of all white dwarfs with a previously known infrared excess, and *Spitzer* IRAC observations, are determined. It can be seen in Table 4.3 that 30 out of 32 stars, 94 per cent, have a significant excess for both methods. The two degenerates that have only a significant flux excess, WD 0246+734 and WD 2132+096, only have observations in the shortest two IRAC channels. However, with additional observations at longer (or shorter) wavelengths a weighted colour excess could potentially be significant. Indeed, this is the case for several other stars. For example, WD 0106−328, has a non-significant $3.6 - 4.5\,\mu$m single-colour excess, but significant weighted-colour channel 3 and channel 4 excesses.

Table 4.1. Infrared excesses, in σ, as determined via the methods presented in Sections 4.3.1 & 4.3.2 for targets in this survey with at least one significant infrared excess. Wch3 and Wch4 represent the weighted channel 3 and 4 excesses as determined by equation 4.4.

		Flux (χ)				Colour (Σ)							
WD Name	Name	ch1	ch2	ch3	ch4	ch1-ch2	ch1-ch3	ch1-ch4	ch2-ch3	ch2-ch4	ch3-ch4	Wch3	Wch4
0843+516		12.9	15.4	11.4	15.8	6.2	7.0	20.7	1.8	14.9	11.0	5.0	5.1
1015+161		11.9	13.8	13.7	14.6	3.7	7.3	12.9	3.8	9.5	5.5	6.6	11.9
1018+410		12.3	13.2	–	–	4.4	–	–	–	–	–	–	–
1457−086		6.8	6.8	3.3	–	0.2	0.5	–	0.4	–	–	0.3	–
2328+107		6.2	6.8	–	–	0.6	–	–	–	–	–	–	–
1132+470		8.4	8.0	–	–	0.0	–	–	–	–	–	–	–
2218−271	HE 2218−2706	7.2	8.7	–	–	1.9	–	–	–	–	–	–	–

Table 4.2. Weighted colour infrared excesses, in σ, as determined by equation 4.4 using additional near-infrared photometry from UKIDSS, 2MASS, and *WISE*. Wch1, Wch2, Wch3, and Wch4 represent the weighted colour excesses for the four *Spitzer* channels.

WD Name	Name	Wch1	Wch2	Wch3	Wch4
0843+516		7.9	9.7	7.1	23.2
1015+161		9.0	9.1	9.8	15.3
1018+410		2.0	6.1	–	–
1457−086		3.1	2.8	1.5	–
2328+107		3.0	3.3	–	–
1132+470		0.8	0.4	–	–
2218−271	HE 2218−2706	2.6	4.5	–	–

To test whether this more stringent $5\,\sigma$ sensitivity limit should be used, weighted-colour excesses calculated for degenerates with known debris disks for all *Spitzer* channels using shorter wavelength UKIDSS, 2MASS, and *WISE* photometry. Interestingly, 27 out of 32 stars, 84 per cent, have an excess $\geq 5\sigma$ in at least one *Spitzer* channel, as can be seen in Table 4.4. Out of the five degenerates with an excess $\leq 5\sigma$, four have either no shorter wavelength data or poor S/N *WISE* W1 photometry, and therefore the large W1 errors could lead to a non-significant weighted-colour excess. Therefore, this seems to be a robust limit and can be used to identify bona fide debris disks. As future, more sensitive telescopes will facilitate the search for fainter and narrower debris disks, tools will be needed in order to find these disks and to avoid potential false positives. Using the two methods of infrared excess determination presented here in combination, with additional near- and mid-infrared observations, could provide a more reliable overall method to accurately find white dwarf debris disks.

Table 4.3: Same as Table 4.1, but for all white dwarfs not in this study with previously known debris disks and *Spitzer* IRAC observations. Wch3 and Wch4 represent the weighted channel 3 and 4 excesses as determined by equation 4.4.

		Flux (χ)				Colour (Σ)							
WD Name	Name	ch1	ch2	ch3	ch4	ch1-ch2	ch1-ch3	ch1-ch4	ch2-ch3	ch2-ch4	ch3-ch4	Wch3	Wch4
0106−328	HE 0106−3253	5.6	7.3	7.4	7.6	1.7	3.2	5.3	1.6	3.9	2.3	3.1	5.0
0110−565	HE 0110−5630	10.1	12.9	–	–	4.3	–	–	–	–	–	–	–
0146+187	GD 16	14.3	16.5	17.3	18.2	6.4	11.3	18.0	4.9	11.7	6.7	10.0	16.0
0246+734		3.9	5.4	–	–	1.4	–	–	–	–	–	–	–
0300−013	GD 40	10.9	13.2	13.7	16.0	3.9	7.1	15.1	3.3	11.3	7.8	7.6	15.8
0307+077		2.3	3.7	3.4	5.3	1.2	2.3	5.8	1.4	5.1	3.3	1.9	5.5
0408−041	GD 56	18.0	18.8	19.1	19.4	7.1	12.9	19.5	5.8	12.4	6.6	11.6	16.7
0420+520		13.5	–	–	–	–	–	–	–	–	–	–	–
0435+410	GD 61	7.0	9.6	–	12.8	2.7	–	9.7	–	6.9	–	–	10.6
0735+187	SDSS J0738	15.8	16.9	–	–	4.6	–	–	–	–	–	–	–
0842+231	Ton 345	–	16.6	–	16.8	–	–	–	–	9.5	–	–	–
0956−017	SDSS J0959	15.5	16.5	–	–	4.6	–	–	–	–	–	–	–
1041+091		11.5	11.0	5.8	9.4	-0.3	0.3	8.8	0.5	9.0	6.5	0.4	12.9
1116+026	GD 133	9.6	12.6	14.5	16.9	4.4	8.8	16.7	4.4	12.3	7.8	8.3	16.1
1145+017		–	14.0	–	–	–	–	–	–	–	–	–	–
1150−153		16.6	18.0	18.2	18.7	7.4	13.5	21.3	6.2	14.0	7.7	12.1	19.3

Table 4.3 – continued from previous page

		Flux (χ)				Colour (Σ)							
WD Name	Name	ch1	ch2	ch3	ch4	ch1-ch2	ch1-ch3	ch1-ch4	ch2-ch3	ch2-ch4	ch3-ch4	Wch3	Wch4
1219+130	SDSS J1221	17.2	18.1	–	–	5.4	–	–	–	–	–	–	–
1225−079		-0.3	1.1	0.2	4.4	1.0	0.3	4.1	-0.5	3.3	3.6	-0.2	4.5
1226+110	SDSS J1228	16.6	17.9	18.3	18.8	6.3	12.7	21.0	6.5	14.7	8.1	13.0	31.3
1349−230	HE 1349−2305	–	16.0	–	–	–	–	–	–	–	–	–	–
1455+298	EGGR 298	-0.7	0.1	2.3	8.0	0.5	2.2	7.7	1.7	7.2	5.4	2.3	8.8
1541+650		13.9	16.4	–	–	7.0	–	–	–	–	–	–	–
1551+175		6.0	9.3	–	–	3.8	–	–	–	–	–	–	–
1554+094	SDSS J1557	16.7	18.0	–	–	7.1	–	–	–	–	–	–	–
1615+164	SDSS J1617	14.5	15.7	–	–	3.6	–	–	–	–	–	–	–
1729+371	GD 362	14.7	16.8	17.2	19.3	6.8	13.2	31.1	6.6	24.4	17.3	12.2	31.3
1929+011	GALEX 1931	13.2	15.3	–	–	4.8	–	–	–	–	–	–	–
2115−560	GJ 4191	9.9	13.1	15.2	17.0	5.1	10.2	16.7	5.0	11.5	6.5	9.4	15.2
2132+096		2.6	5.9	–	–	2.8	–	–	–	–	–	–	–
2207+121	SDSS J2209	15.8	17.1	–	–	5.1	–	–	–	–	–	–	–
2221−165	HE 2221−1630	8.1	11.0	12.1	12.9	3.8	7.5	11.9	3.9	8.4	4.5	7.0	11.0
2326+049	G 29−38	16.6	18.1	18.7	19.3	7.5	12.3	20.5	4.8	13.1	8.2	10.1	17.7

Table 4.4. Same as Table 4.2, but for all white dwarfs with previously known debris disks, and *Spitzer* IRAC and additional near-infrared observations. In order to avoid repetition the five previously known white dwarfs with infrared excesses in this study have been omitted. Wch1, Wch2, Wch3, and Wch4 represent the weighted colour excesses for the four *Spitzer* channels.

WD Name	Name	Wch1	Wch2	Wch3	Wch4
0106−328	HE 0106−3253	4.4	4.4	4.9	6.5
0110−565	HE 0110−5630	7.5	6.4	–	–
0146+187	GD 16	15.0	17.1	17.8	23.7
0246+734		0.1	1.7	–	–
0300−013	GD 40	8.9	9.2	10.1	18.9
0307+077		1.9	1.8	2.2	6.0
0408−041	GD 56	32.0	28.2	27.3	30.4
0420+520		16.1	–	–	–
0435+410	GD 61	5.4	6.8	–	14.6
0735+187	SDSS J0738	0.6	5.0	–	–
0842+231	Ton 345	–	12.9	–	14.8
0956−017	SDSS J0959	31.8	28.1	–	–
1041+091		19.2	14.0	6.4	12.9
1116+026	GD 133	7.8	12.1	14.7	23.5
1145+017		–	24.5	–	–
1150−153		13.4	14.4	16.3	21.7
1219+130	SDSS J1221	33.1	29.3	–	–
1225−079		1.4	2.4	1.1	5.8
1226+110	SDSS J1228	29.3	30.7	36.0	41.0
1349−230	HE 1349−2305	–	2.3	–	–
1455+298	EGGR 298	-0.1	0.6	2.6	9.7
1541+650		12.9	17.1	–	–
1551+175		–	3.8	–	–
1554+094	SDSS J1557	27.0	31.7	–	–
1615+164	SDSS J1617	0.7	4.2	–	–
1729+371	GD 362	11.2	12.9	15.6	30.1
1929+011	GALEX 1931	16.4	17.1	–	–
211−560	GJ 4191	7.9	13.4	16.7	24.1
2132+096		0.5	3.6	–	–
2207+121	SDSS J2209	0.3	5.4	–	–
2221−165	HE 2221−1630	5.7	7.5	10.3	13.8
2326+049	G 29–38	15.6	24.6	23.7	34.1

4.3.4 Atmospheric Metals

A subsample of the survey was observed with *HST* COS in the far-ultraviolet in order to search for atmospheric metals, with spectra of 168 (of 236) stars taken. To conduct a thorough analysis of this data detailed atmospheric modelling that includes the effects of

radiative levitation must be carried out, which is beyond the scope of this study. Analysis of a subset of this survey has previously been conducted Koester et al. (2014), with the full sample to be published in an upcoming paper. However, in order to determine the planetary debris disk frequency from this data a simple visual inspection of the data was done, and the absence or presence of Si II was noted. Among 168 observed stars, 78 exhibit photospheric silicon.

4.4 Results

Prior to discussing the infrared excess and atmospheric metal frequencies for the 195 apparently single white dwarfs and the 40 stars confirmed or suspected to be in binary systems, the individual objects with a significant infrared excess via at least one method are reviewed. The 4.5μm excesses of systems with a significant excess as determined via at least one of the methods presented above are shown in Fig. 4.4. However, it should be noted that not all infrared excesses are indicative of planetary debris disks, and caution must be exercised when interpreting observed excesses and the derived debris disk frequencies. There are three potential causes of infrared excesses; circumstellar debris disks, binary companions, or background contamination. As will be discussed below, following scrutiny, the infrared excesses of four stars may be explained by a binary companion or contamination instead of a planetary debris disk.

4.4.1 Stars with Infrared Excesses

Seven systems are identified to have a significant infrared excesses via either the flux or colour methods. Of these stars, five white dwarfs have previously known infrared excesses due to a circumstellar debris disk (Jura et al. 2007*a*; Farihi et al. 2009; Xu & Jura 2012; Rocchetto et al. 2015). The two remaining stars are new infrared excesses, but as detailed below, are not thought to be due to debris disks. Out of the five previously known white dwarfs with an infrared excess, four stars (WD 0843+516, WD 1015+161, WD 1018+410, and WD 1457−086) exhibit atmospheric metal absorption features in the *HST* COS spectra. However, one of these targets has a modest flux excess, and no colour excess, and is discussed below. Finally, one of the stars with a previously known infrared excesses (WD 2328+107) does not have atmospheric metals as seen by *HST* COS and therefore the cause of the excess in this system is also discussed below.

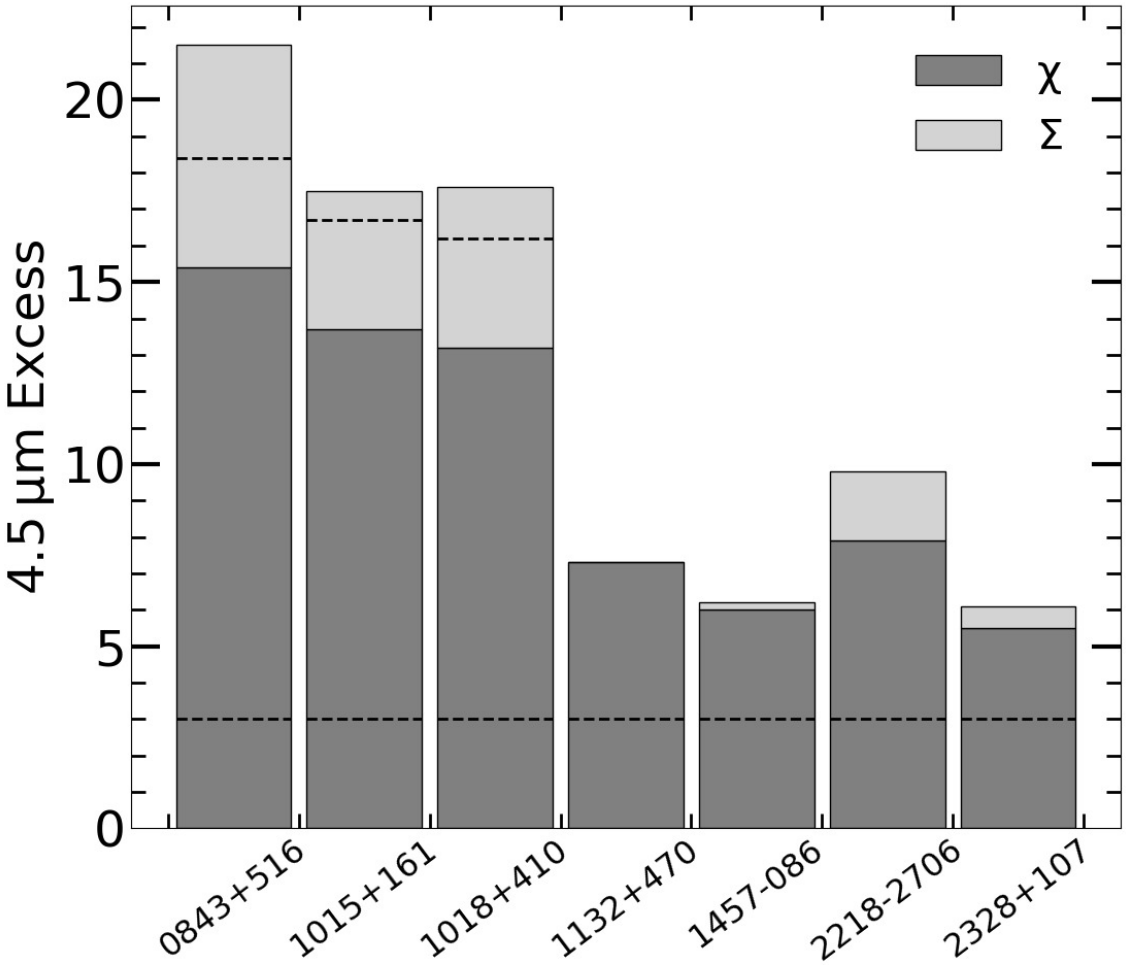

Figure 4.4. Photometric excesses at 4.5 μm as determined by both the flux excess, χ, and colour excess, Σ, methods. The black dashed lines represent 3σ for each method. Only three stars with bona fide debris disks have a significant infrared excess using both methods.

If the excesses at the four stars (WD 1132+470, WD 1457−086, WD 2218−271, and WD 2328+107) are caused by companions or contamination, then only three stars remain as having an excess due to a debris disk. Interestingly, these three systems (WD 0843+516, WD 1015+161, and WD 1018+410) are the only stars in the entire sample to have significant excesses identified via both flux and colour methods, whereas the other four stars only have significant flux excesses. The potential link between bona fide disks and the presence of significant flux and colour excesses is evident in Fig. 4.4. As mentioned above, vast majority of stars with known debris disks have significant flux and colour excesses, highlighting that by using both methods together real disks are retrieved and false positives may be detected.

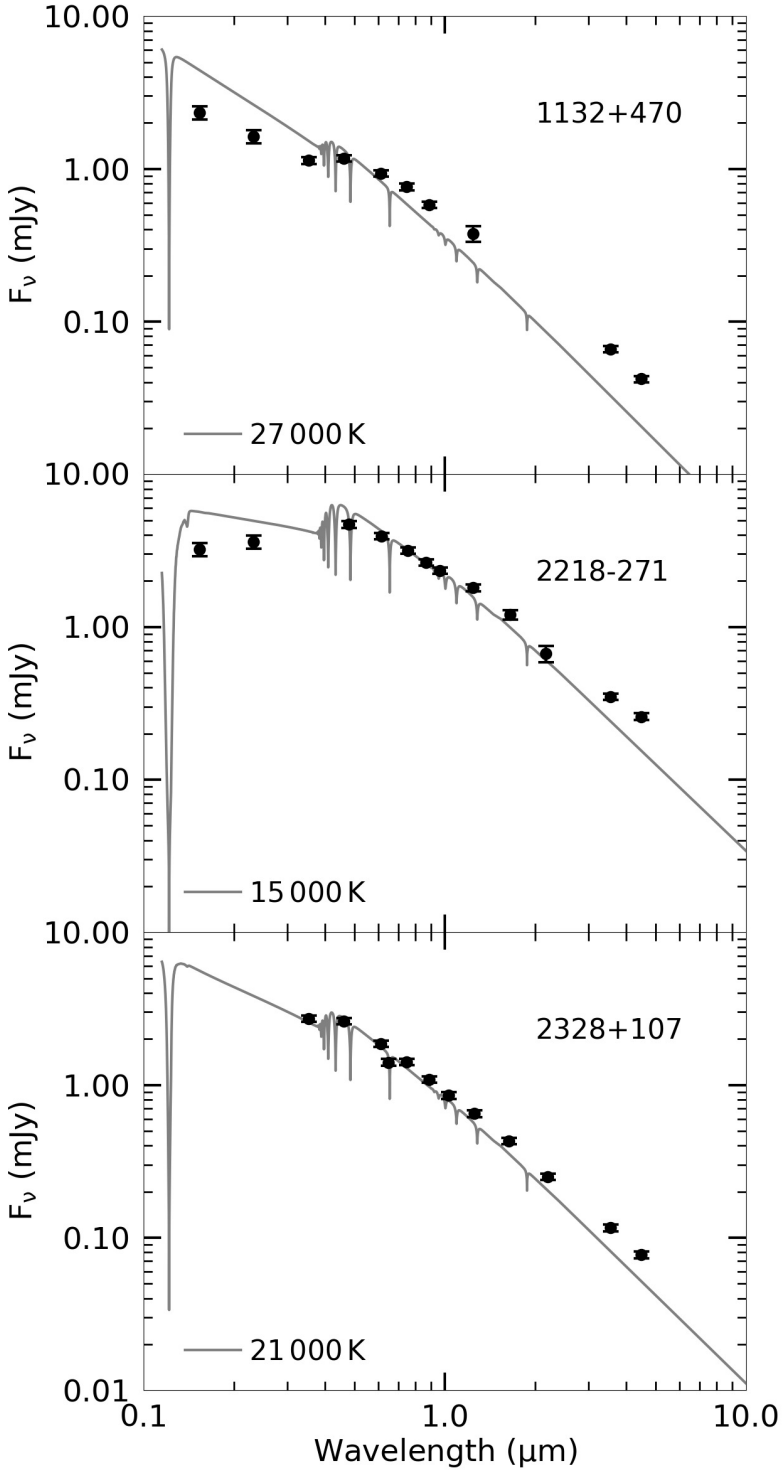

Figure 4.5. SEDs of three stars with significant infrared flux excesses. Data points with error bars are the *Spitzer* photometry together with shorter wavelength fluxes taken from the literature, and the grey lines represent the white dwarf atmospheric models. All models have $\log g = 8$ with $T_{\rm eff}$ given in the plots. *GALEX* photometry is shown, but excluded from the fitting process, as observations can suffer from interstellar extinction.

WD 1132+470

This star has been previously observed as a part of the United States Naval Observatory (USNO) parallax programme and it was seen to have clear residual astrometric motion with a periodicity of several years (Subasavage et al. 2009), indicating the presence of an unresolved companion. During SED fitting it was noted that the atmospheric model for the previously reported temperature was a poor fit to the optical and near-infrared photometry, which led to the flux excess, as can be seen in Fig. 4.5. In a recent study, it was found that the photometric and spectroscopic effective temperatures are significantly discrepant (Bédard, Bergeron & Fontaine 2017), with the conclusion that this system may be a double degenerate.

WD 2218−271

As can be seen in Fig. 4.5, this target exhibits a significant infrared excess at the *Spitzer* wavelengths, however in corresponding *HST* observations no atmospheric metals were seen, indicating that this excess may not be due to a debris disk. To test for background contamination in the *Spitzer* images, the PSF roundness of the target was measured on the IRAC 4.5 μm image using the IRAF task DAOFIND. For WD 2218−271, the roundness is 0.06, where the average of 20 field stars in the same image is 0.08 ± 0.10 (a value of 0 is perfectly round). Furthermore, the entire unbiased sample of single stars has an average roundness of 0.09 ± 0.05, and therefore the excesses is likely due to an unresolved companion rather than contamination.

This system was observed twice as a part of the ESO SPY (Napiwotzki et al. 2003) to search for short-period radial velocity variations. No significant radial velocity variation of the H α line is seen in the Ultraviolet-Visual Echelle Spectrograph (UVES) heliocentric-corrected spectra in the 16 days between observations. Moreover, the *Gaia* Data Release 2 (DR2) astrometric data are consistent with a single source. However, a potential 5.3 hr periodic signal is observed in Catalina Real-time Transient Survey (CRTS; Drake et al. 2009) photometric data. To assess if the observed infrared excess could be due to a potential companion, published infrared photometry of a range of brown dwarfs (Patten et al. 2006) was compared to the *Spitzer* data. Typical near-infrared and IRAC bands absolute magnitudes were converted to fluxes and scaled to the distance of WD 2218−271. Interestingly, it was found that a source of spectral type mid-T-dwarf can reproduce the observed

excess, however further observations of this system are needed in order to confirmed the candidate photometric period and the spectral type of a potential companion.

WD 2328+107

The infrared excess at this star has been previously discovered and was attributed to a narrow circumstellar debris disk (Rocchetto et al. 2015). However, in the corresponding *HST* COS ultraviolet spectrum no atmospheric metals are seen suggesting that the infrared excess may not be due to a debris disk, but instead may be caused via other means such as contamination or a binary companion. First, to assess contamination, a check of the IRAC 4.5 μm PSF roundness is conducted in the same manner as was done for WD 2218−271. A roundness value of 0.02 was determined, that agrees well with the 20 field stars in the same image (0.09 ± 0.04) and the value for the single stars in this study, presented above. Therefore, whilst a possibility, it does not seem that the infrared excess is due to contamination.

Second, to check for binarity a literature search was conducted, and returned no previously evidence of this source being in a binary system. Additionally, no significant H α radial velocity variation between two heliocentric-corrected SPY UVES spectra separated by 3 days was seen, and no obvious periodic photometric variability is found in the CRTS data. *Gaia* DR2 astrometry is consistent with that of a single source. As for WD 2218−271, a range of brown dwarfs were compared to the excess using the method outlined above. It was found that the presence of a T-dwarf can reproduce the observed excess, and therefore further observations are needed to confirm or refute this potential binarity to probe the possible phase space for companions to this white dwarf.

WD 1457−086

This star has a previously known infrared excess (Farihi et al. 2009) and is highly metal polluted (Koester et al. 2005*b*), however, archival near-infrared VLT Nasmyth Adaptive Optics System-Near-Infrared Imager and Spectrograph (NACO) images taken in 2010 and 2013 reveal that there is a background source within 0.4 arcsec (Dennihy et al. 2017). This nearby source has currently only been detected in the *J*-band and is posited to be the source of the infrared excess at this wavelength throwing into contention the validity of the debris disk, although it is unclear how much the background source contributes to the observed flux at *Spitzer* bandpasses. In order to determine whether or not this source

is detected at 4.5 μm, the PSF roundness of this target is examined both in the initial 2006 image analysed in this study, and a second 2017 image, photometrically analysed in Chapter 5. In the 2006 epoch, the star has a roundness of 0.07, which is comparable to the 20 field stars in the image (0.05 ± 0.04) and to the entire single star sample in this study. For the 2017 epoch, it is important to note that whilst the infrared flux did not change compared to 2006, the PSF roundness increased to 0.54. The 20 field stars in the 2017 image have an average roundness of 0.06 ± 0.05, and therefore the elongated PSF is real.

By using the *Gaia* DR2 proper motion of WD 1457−086 together with the 2010 and 2013 NACO images, the separation of the target and the background source over time can be calculated. In the 2006 IRAC image the separation should be 0.1 arcsec, whereas in 2017 it should be 0.7 arcsec. This is consistent with the roundness values over time. From knowledge of the on-sky density of galaxies at specific brightnesses at the *Spitzer* wavelengths it is possible to calculate the chance that the observed infrared excess is due to a background galaxy within 2.4 arcsec^2 of the target (Farihi et al. 2008). The odds that the 30 μJy excess at 4.5 μm is produced by a galaxy is one out of 760. Furthermore, the probability that at least one star in the entire single star sample is contaminated to the level potentially seen at WD 1457−086 is 23 per cent. Therefore, contamination via the background source is a possibility, but it should be noted that even if the infrared excess is not due to circumstellar debris disk, the presence of atmospheric metals indicates that accretion from a debris disk is ongoing.

4.4.2 Planetary Debris Disk Frequencies in Single Stars

The analysis presented here is constrained to the 195 apparently single white dwarfs for which there is reliable warm IRAC photometry, and the 143 star subsample that have *HST* data, see Table 4.5. The infrared and far-ultraviolet data are analysed independently, but as both infrared excesses and atmospheric metals are tracers of circumstellar debris disks, the frequencies of both observables are thought to be indicative of the frequency of planetary debris disks and therefore can be compared in order to understand planetary systems around single white dwarfs.

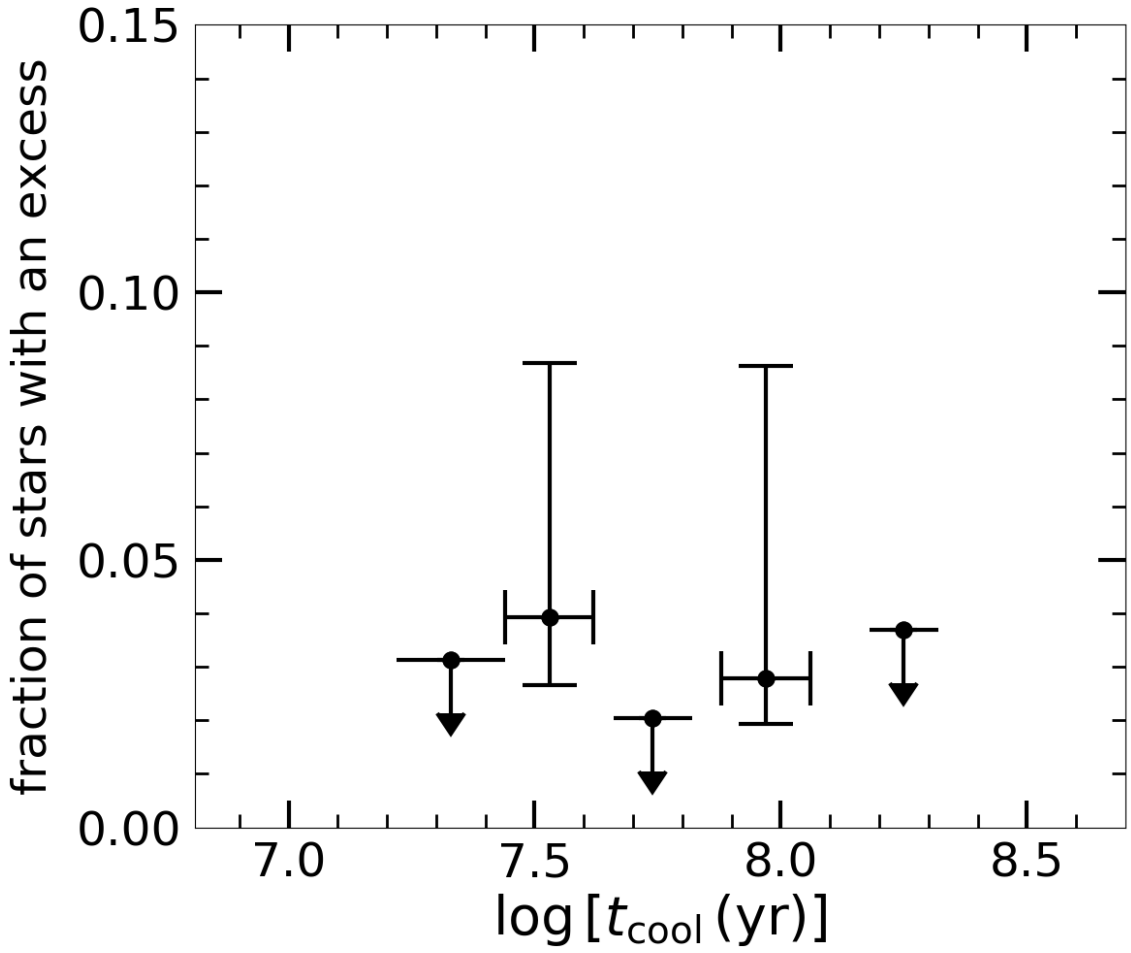

Figure 4.6. The fraction of single stars in the sample with an infrared excess due to a debris disk, with 1σ binomial probability errors and upper limits, for several cooling age bins.

Infrared Excess Frequency in the Unbiased Sample

In the single star sample, three out of 195 white dwarfs have an infrared excess due to a debris disk, resulting in a nominal unbiased frequency of $1.5^{+1.5}_{-0.5}$ per cent, whereas, 65/143 (45 ± 4 per cent) stars have atmospheric metals. The uncertainties in these fractions, and those presented hereafter, are calculated via the binomial probability distribution with a 1σ confidence level (Burgasser et al. 2003). The binomial distribution gives the probability of a certain number of successes in a given sample size, i.e. in this study it is the number of stars with an infrared excess or atmospheric metals over the sample. The binomial probability distribution is calculated using the total sample size, the number of successes, and over a range of success fractions from 0 to 1, with the peak of the probability distribution at the true success fraction. By integrating over the central 68 per cent of this

distribution, corresponding to a 1σ confidence level, the lower and upper success fraction limits can be determined (Burgasser et al. 2003).

The frequency of infrared excess due to planetary debris in the 143 star *HST* sub-sample is calculated to be $1.4^{+1.8}_{-0.4}$ per cent, in excellent agreement with the entire sample. By comparing the frequencies it is clear to see that the vast majority, $\sim$90 per cent, of white dwarfs with a circumstellar debris disk do not exhibit an observable infrared excess. Potential reasons for this are discussed below.

Previously Determined Infrared Excess Frequencies

The nominal unbiased frequency of infrared excesses due to debris disks presented in this study is in broad agreement with previous studies that cover the same cooling age range, but not with the same breadth. Prior work has utilised wide-field surveys such as UKIDSS and *WISE* to determine infrared excess frequencies of $0.4 - 1.9$ per cent (Debes et al. 2011; Girven et al. 2011). However, while these frequencies are similar to this work, they are potentially biased as half of all debris disks seen at *Spitzer* wavelengths are not observable in the $K-$band (Farihi et al. 2012*a*), whereas the large beam size of *WISE* observations means that false positives due to background contamination can occur. Since launch *Spitzer* has been used to determine the infrared excess frequency in multiple studies (Mullally et al. 2007; Barber et al. 2012) yielding frequencies as high as 4.3 per cent. It is thought that the potentially biased selection criteria of selecting stars on the presence of a $K-$band brightness and within a temperature range in which debris disks are now known to be more common may be the cause of higher frequencies. A subset of this sample covering a narrower temperature range has reported an infrared excess frequency of 3.7 per cent (Rocchetto et al. 2015). This study highlights that in order to robustly determine the debris disk frequency a large sample of stars selected in an unbiased manner was needed.

Infrared Excess Frequency over Cooling Age

The combined size and wide temperature range of this unbiased sample is unprecedented and allows for a somewhat robust determination of infrared excess frequency due to debris disks as a function of white dwarf cooling age for the first time. All single stars in the survey were separated into cooling age bins and plotted against the infrared excess frequency in Fig. 4.6, with the uncertainties taken from the binomial probability distribution with a 1σ

confidence level. It can be seen that the infrared excess frequency is non-variant across a large range of cooling ages and of the order a few per cent, in agreement with the sample as a whole and previous work covering this temperature range.

While the results of a direct comparison should be taken with caution, it is noteworthy that in the study of Zuckerman et al. (2003) for stars cooler and older than the present study with $T_{\rm eff} < 14\,000\,{\rm K}$, one star out of 70 had a newly discovered infrared excess ($1.4^{+3.1}_{-0.5}$ per cent), but 18/70 were seen to have metal absorption features (26^{+6}_{-4} per cent). A recent study used *Gaia* and *WISE* data to identify candidate debris disks around $5\,000 < T_{\rm eff} < 7\,000\,{\rm K}$ white dwarfs based on infrared colour (Debes et al. 2019). Although this method also returned a contaminated object and white dwarf binaries, it was found that $0.3{\pm}0.7$ per cent of degenerates in this temperature range may have a candidate disk. These frequencies are broadly consistent with the findings here for warmer and younger white dwarfs, although, in this cooling age range, other studies searching for debris disks have only have one or two possible bona fide infrared excesses suggesting that the frequency may decrease with cooling age (Farihi et al. 2008; Xu & Jura 2012; Bergfors et al. 2014).

Atmospheric Metal Frequency

For the entire sample of 143 single white dwarfs observed with *HST*, 45 ± 4 per cent show evidence of atmospheric metals. However, it is important to note that the observed atmospheric metals in $T_{\rm eff} > 25\,000\,{\rm K}$ white dwarfs may not be indicative of ongoing accretion from a circumstellar debris disk, but could be supported by radiative levitation. Detailed modelling is needed to determine whether or not atmospheric metals in this systems are due to a currently accreting debris disk and is beyond the scope of this study. The nominal unbiased frequency presented here agrees with previous ground-based studies searching for Ca II lines in single DA and DB white dwarfs (Zuckerman et al. 2003, 2010). As well as a subset of the *HST* observations previously published (Koester et al. 2014).

Comparing Debris Disk Frequencies Determined via Infrared Excesses and Atmospheric Metals

One of the main findings of this study is that the overwhelming majority of white dwarfs with circumstellar debris disks do not exhibit an observable debris disk. Multiple potential explanations for the lack of infrared excesses have previously been proposed. It has been proposed that around hotter stars debris disks do not form as the radius at which rapid

sublimation occurs is greater than the Roche limit radius (von Hippel et al. 2007; Bonsor et al. 2017). Interestingly, recent planetestimal disruption simulations have shown that for certain white dwarf temperatures and minor planetary body orbital and physical parameters, small asteroids and comets are completely sublimated as they enter the vicinity of the white dwarf, whereas larger bodies will fragment to form debris disks (Brown et al. 2017). It was also postulated that the lack of observed infrared excesses around intermediate temperature and cooler degenerates could be due to the tidal disruption of a planetesimal forming an optically thin disk rather than optically thick (Bonsor et al. 2017). Regardless of the exact cause, it seems that circumstellar debris disks are typically tenuous or in general narrow. Observationally, a narrow, eccentric ring of debris has been seen around WD 1145+017 (Redfield et al. 2017; Cauley et al. 2018). If this is a common occurrence it would explain the dearth of observable circumstellar debris disks in the infrared.

Inferring Planetary System Architecture using Theoretical Planetary Dynamics Models

By assessing the nominal debris disk frequency from atmospheric metals it may be possible to shed light onto the dynamical processes perturbing minor planetary bodies past the Roche limit of the host white dwarf. Interestingly, the unbiased atmospheric metal frequency may be reproduced by asteroids perturbed into Roche limit crossing orbits via interactions with Super Earth to Saturn mass planets (Mustill et al. 2017). Although, it should be noted that there are many other dynamical studies that have proposed other mechanisms (Debes et al. 2012; Veras et al. 2013; Mustill et al. 2014).

4.4.3 Planetary Debris Disk Frequencies in Binary White Dwarfs

Observationally, the frequency of planetary debris disks around single white dwarfs is now well constrained from the work presented above and previous studies (Mullally et al. 2007; Zuckerman et al. 2010; Koester et al. 2014; Rocchetto et al. 2015). However, to date, only one such study exists for the debris disk frequency in binary white dwarf systems (Zuckerman 2014), although it should be noted that the selection criteria may result in a biased frequency.

Dynamical Perturbation Models of Minor Planetary Bodies in Binary Systems

From a theoretical perspective, several long-term dynamical processes that include a stellar binary companion have been proposed to deliver minor planetary bodies past the Roche limit of the target white dwarf, and therefore are a potential cause of atmospheric pollution (Bonsor & Veras 2015; Hamers & Portegies Zwart 2016; Petrovich & Muñoz 2017; Stephan et al. 2017; Smallwood et al. 2018). However, how much each of these methods may potentially contribute to observed atmospheric pollution is not currently known. It is important to note that heavy elements observed in the atmospheres of white dwarfs in short-period binaries may originate from the stellar wind from a companion (Debes 2006; Tappert et al. 2011). However, for stars in sufficiently wide binary systems any observed atmospheric metals must be due to the perturbation of planetary bodies to the vicinity of the white dwarf (Farihi et al. 2013*a*; Veras et al. 2018). In the detection of companions to white dwarfs, it should be noted that only the coldest and lowest mass substellar stars are undetectable to ground-based observations due to the Earth-sized radii and blue-peaked stellar continua of white dwarfs (Farihi, Becklin & Zuckerman 2005).

Resolved Wide Binaries in the Unbiased Sample

Over the entire sample of 236 stars, 40 white dwarfs are in published or candidate binary systems and are noted in Table 4.6. A literature and *Gaia* DR2 archive search recovered a subsample of 22 known spatially-resolved and common proper-motion binaries, with the remaining 18 white dwarfs in confirmed or suspected short-period binary systems. For the study of infrared excesses it is important to have reliable photometry and that the bare photosphere of the target white dwarf can be analysed. Therefore, the 25 objects that are spatially-unresolved or marginally-resolved in the *Spitzer* observations (including all confirmed or suspected short-period binaries) are removed from the infrared excess analysis subsample. This results in 15 stars in wide binary systems that can be analysed to detect infrared excesses indicative of a circumstellar debris disk. On the other hand, for determining the frequency of debris disks via atmospheric metal pollution, all 22 spatially-resolved systems seen in *Gaia* DR2 can be probed, as in the far-ultraviolet *HST* spectra only white dwarfs will be observable. In the following, the frequencies of infrared excesses and atmospheric metals in the wide binary subsamples are discussed separately. These subsamples are also compared to independent white dwarf samples in order to draw con-

Table 4.5. Single and binary sample statistics for infrared excess and pollution in white dwarfs.

Description	n	m	m/n
Singles in this study:			
Significant infrared excess	195	3	0.015
Atmospheric metals detected by *HST*	143	65	0.455
Binaries in this study:			
Significant infrared excess	15	0	0
Atmospheric metals detected by *HST*	12	8	0.667
Published data:			
Wide companions to stars with debris disks	40	0	0
20 pc sample:			
Atmospheric metals among known binary stars	29	5	0.172
Binaries among known polluted stars	23	5	0.217
Binaries in the 20 pc stars	139	29	0.209

Notes. The second and third columns give the various subsample sizes and the number of objects that meet the criterion, respectively, with the final column providing the fraction of targets of the previous two columns.

clusions about any potential relationship between wide binaries and circumstellar debris disks. All subsamples are listed in Table 4.5.

Infrared Excess Frequency

First, the infrared excess frequency in the wide binary subsample is presented. For all targets in this subsample the photometry and infrared excess analysis was conducted in an identical manner to the single stars in the main sample. It should be noted that while 15 white dwarfs in wide binaries were observed, both stars in WD 2220+217 have *Spitzer* data, resulting in 14 systems, however as both stars are spatially-resolved, infrared excesses are searched for at both targets. It was found that no objects exhibit a significant flux or colour excess, that yields a binomial probability upper limit of 8 per cent for infrared excesses due to debris disks around white dwarfs with a wide binary companion. Although the targets were chosen in an unbiased manner, the small sample size means this result is not as robust as the infrared excess frequency for single stars, however the values are in agreement. Future unbiased studies with a larger sample size of wide binaries will test this value.

A Search for Binaries in the Known Dusty White Dwarf Sample

To further assess the relationship between wide binaries and infrared excesses due to circumstellar debris disks it is possible search known debris disk hosting white dwarfs for wide companions. As the theoretical studies mentioned above focus on the dynamical delivery of minor planetary bodies via wide binary companions any discovery of wide binarity in this systems could inform models. *Gaia* DR2 was used to search for common parallax and proper-motion companions to a sample of 40 polluted white dwarfs with published infrared excesses. In the sample, no bona fide, co-moving companions were found, resulting in a binomial probability upper limit of 3 per cent. It should be noted that one system, SDSS J155720.77+091624.6 (hereafter SDSS 1557), is believed to be a short-period binary where the disk is circumbinary (Farihi, Parsons & Gänsicke 2017), and therefore the companion is not thought to be the cause of the dynamical perturbations needed to bring minor planetary bodies within the Roche limit of the white dwarf. Therefore, it seems that the dynamical delivery of planetary bodies that results in the formation of white dwarf circumstellar debris disks is not dependent on the presence of a wide binary companion.

As a side note, during this analysis it was found that one debris disk hosting star, SDSS J073842.57+183509.6 ($\varpi = 5.8 \pm 0.2$ mas, $\mu = (12.8 \pm 0.3, -24.1 \pm 0.2)$ mas year^{-1}), may have a quasi-co-moving companion at a projected separation of 0.54 pc and of approximate mid-M spectral type ($\varpi = 5.9 \pm 0.1$ mas, $\mu = (9.8 \pm 0.1, -23.7 \pm 0.1)$ mas year^{-1}). No claim of binarity is made, but even if the pair were previously bound, it is likely that the white dwarf and the orbiting planetary system evolved effectively in isolation.

Atmospheric Metal Frequency

Second, the frequency of debris disks as detected via atmospheric pollution for the wide binary subsample is discussed. Of the 22 white dwarfs in wide binaries in the main sample, 12 were either observed with *HST* or have published ultraviolet observations with eight stars exhibiting atmospheric metals, resulting in an unbiased frequency of 67^{+10}_{-15} per cent. As with the determination of the frequency of infrared excesses in wide binaries in this study, the sample suffers from small number statistics, but this frequency is within 2σ of the atmospheric metal frequency for single stars in this study and in other works (Zuckerman et al. 2010; Koester et al. 2014). However, this is significantly greater than a

previous study of atmospheric pollution in wide binaries (Zuckerman 2014), although the selection criteria may be biased.

A Search for Polluted Wide Binaries within 20 pc

In addition to studying atmospheric metal pollution in wide binaries in the sample presented here, it is possible to make an independent assessment using the 20 pc white dwarf sample constructed from *Gaia* DR2 data as it is thought to be complete (Hollands et al. 2018*b*). This can be done in two ways; the probability of atmospheric metal pollution given binarity and the probability of binarity given atmospheric pollution. In the 20 pc sample there are 29 binaries that contain at least one white dwarf, and five of these have a degenerate with atmospheric metal pollution. This results in a 17^{+9}_{-4} per cent probability of pollution among white dwarfs in wide binaries. Although this is a lower limit as not all stars have ultraviolet observations.

In the 20 pc sample there are 23 white dwarfs with atmospheric metals, of which five are in binaries, yielding a polluted degenerate multiplicity percentage of 22^{+11}_{-6} per cent. Interestingly, within 20 pc there are 29 multiple star systems out of 139, resulting in a field multiplicity percentage of 21^{+4}_{-3} per cent. These fractions are in excellent agreement with each other and with the field multiplicity fraction of a deeper survey that includes a larger number of stars (Farihi et al. 2005). Therefore, it seems that, as the atmospheric metal pollution frequency in wide binaries is the same as for single stars, binarity is not important in dynamic perturbation of minor planetary bodies that results in the atmospheric pollution of white dwarf stars. Furthermore, polluted white dwarfs are in binary systems at the same fraction as field stars.

4.5 Summary and Conclusions

This chapter presents the largest, unbiased sample of white dwarfs that has been used to determine the frequency of planetary debris disks via infrared excesses using *Spitzer* photometry and atmospheric metals using *HST* spectroscopy. The main focus of this study is the determination of infrared excesses using the flux excess and colour excess methods. Seven stars have a significant flux excess, with five of these previously known. Interestingly, only three stars were determined to have a significant colour excess. The four stars that do not have a colour excess may have a flux excess due to background contamination or the

presence of a binary companion. If this is correct, then only WD 0843+516, WD 1015+161, and WD 1018+410 remain as bona fide disk detections and are the only stars in the sample with greater than 3σ excesses via both methods. Colour excesses were determined for all white dwarfs with previously discovered debris disks and it was seen that 94 per cent have a significant colour excess, confirming that the colour method can be used to detect real debris disks. Therefore, with future, more sensitive telescopes facilitating the search for narrower and fainter disks using both flux and colour excess determination methods in combination could be a useful tool in finding bona fide disks and avoiding false positives.

Single White Dwarf Planetary Debris Disk Frequencies

Over the entire single white dwarf sample the frequency of planetary debris disks as observed via infrared excesses is $1.5^{+1.5}_{-0.5}$ per cent. This is in broad agreement with previous surveys, but due to the larger size, unbiased selection, and observational sensitivity this result should be fairly definitive. In contrast, the frequency of planetary debris disks as observed via atmospheric metals is 45 ± 4 per cent indicating that the vast majority of circumstellar disks are unobservable in the infrared with current facilities. Prior studies that noticed this dearth have proposed that this could be due to narrow, optically thin, or completely gaseous disks, although circumstellar gas has only been detected in nine systems to date.

Binary White Dwarf Planetary Debris Disk Frequencies

For white dwarfs in wide binary systems, no significant infrared excesses were discovered resulting in an upper limit of 8 per cent, whereas 67^{+10}_{-15} per cent were observed to have atmospheric metals. Both of these frequencies are consistent with those determined for the single white dwarf sample. Interestingly, the fraction of nearby white dwarfs that is both in a binary system and exhibits atmospheric metals is exactly the same as the fraction of field white dwarfs in binary systems (22 per cent). Furthermore, it was found that no known white dwarf hosting a circumstellar debris disk as observed via an infrared excess has a co-moving companion (binomial probability upper limit of 2.8 per cent), which is in strong disagreement with the binary fraction of the field white dwarfs. Therefore, it seems that binarity is not linked at all to the formation of circumstellar debris disks and the atmospheric pollution of white dwarfs. This means that the processes that deliver minor planetary bodies beyond the Roche limit of white dwarfs is likely controlled by major

planetary bodies.

Table 4.6: *Spitzer* IRAC fluxes for white dwarfs in this sample, together with an indication of atmospheric Si II observed by *HST* COS. Stellar parameters and binary type are taken from the literature.

WD Name	$T_{\rm eff}$ (K)	m mag)	log $[t_{\rm cool}\,({\rm year})]$	$F_{3.6\,\mu{\rm m}}$ (μJy)	$F_{4.5\,\mu{\rm m}}$ (μJy)	$F_{5.7\,\mu{\rm m}}$ (μJy)	$F_{7.9\,\mu{\rm m}}$ (μJy)	Si II	Binarity
0000+171	20 200	15.8	7.76	64 ± 3	44 ± 2	–	–	Y	–
0002+165	25 900	15.7	7.28	65 ± 3	40 ± 2	–	–	Y	–
0004+061	24 400	16.1	7.91	55 ± 3	33 ± 2	–	–	N	–
0013−241	18 500	15.4	8.00	103 ± 5	66 ± 4	–	–	N	–
0017+061[b]	28 100	15.2	7.08	2400 ± 100	1620 ± 80	–	–	–	MS, 1
0018−339	20 600	14.6	7.69	200 ± 10	120 ± 6	–	–	N	–
0028−474[c]	17 400	15.2	7.87	166 ± 8	104 ± 5	–	–	N	WD, 2
0047−524	18 800	14.2	7.83	–	190 ± 10	–	66 ± 3	N	–
0048−544	17 900	15.2	7.87	125 ± 6	81 ± 4	–	–	–	–
0048+202	20 400	15.4	7.83	102 ± 5	65 ± 3	–	–	–	–
0052−147	26 700	15.1	7.68	106 ± 5	68 ± 3	–	–	N	–
0059+257	21 400	15.9	7.77	68 ± 4	44 ± 2	–	–	Y	–
0102+095	24 800	14.4	7.45	220 ± 10	147 ± 7	–	–	Y	–
0106−358[a]	30 900	14.7	7.04	159 ± 8	91 ± 5	–	–	Y	MS, 3
0110−139	26 300	15.8	7.38	60 ± 3	40 ± 2	–	–	–	–
0114−605[c]	24 700	15.1	7.30	113 ± 6	75 ± 4	–	–	Y	WD, 4

Table 4.6 – continued from previous page

WD Name	$T_{\rm eff}$ (K)	m (mag)	log $[t_{\rm cool}\,({\rm year})]$	$F_{3.6\,\mu{\rm m}}$ (μJy)	$F_{4.5\,\mu{\rm m}}$ (μJy)	$F_{5.7\,\mu{\rm m}}$ (μJy)	$F_{7.9\,\mu{\rm m}}$ (μJy)	Si II	Binarity
0124−257	23 000	16.2	7.43	36 ± 2	26 ± 1	–	–	N	–
0127−050	16 800	14.9	8.16	177 ± 9	112 ± 6	–	–	–	–
0127+270	24 900	15.9	7.36	55 ± 3	33 ± 2	25	38	–	–
0129−205	20 000	15.3	7.79	104 ± 5	68 ± 4	–	–	–	–
0131+018[c]	15 200	14.5	8.40	340 ± 20	220 ± 10	–	–	N	WD, 2
0136+768	16 900	14.8	7.95	230 ± 10	151 ± 8	–	–	N	–
0140−392	21 800	14.4	7.62	250 ± 10	165 ± 8	–	–	Y	–
0145−257[b]	26 700	14.5	7.20	8100 ± 400	5400 ± 300	–	–	–	MS, 5
0155+069	22 000	15.5	7.41	108 ± 6	68 ± 3	–	–	N	–
0200+248	23 300	15.7	7.79	110 ± 10	71 ± 8	–	–	N	–
0201−052	24 600	16.0	7.32	41 ± 2	28 ± 2	–	–	–	–
0216+143	26 900	14.6	7.26	210 ± 10	130 ± 7	80 ± 10	33	N	–
0221−055[b]	25 800	16.2	7.52	62 ± 3	42 ± 2	–	–	–	WD, 4
0222−265	23 200	15.7	7.60	76 ± 4	51 ± 3	–	–	–	–
0227+050	19 300	12.8	7.83	–	780 ± 40	–	260 ± 10	–	–
0229+270	24 200	15.5	7.36	80 ± 4	51 ± 3	–	–	–	–
0231−054	17 300	14.3	8.86	–	240 ± 10	–	71 ± 4	N	–

Table 4.6 – continued from previous page

WD Name	$T_{\rm eff}$ (K)	m (mag)	log $[t_{\rm cool}\,({\rm year})]$	$F_{3.6\,\mu{\rm m}}$ (μJy)	$F_{4.5\,\mu{\rm m}}$ (μJy)	$F_{5.7\,\mu{\rm m}}$ (μJy)	$F_{7.9\,\mu{\rm m}}$ (μJy)	Si II	Binarity
0242−174	20 700	15.4	7.79	96 ± 5	62 ± 3	–	–	Y	–
0300−232	22 400	15.7	8.03	72 ± 4	44 ± 2	–	–	–	–
0305−117	26 800	16.0	7.18	53 ± 3	33 ± 2	–	–	N	–
0307+149[a]	21 400	15.4	7.61	112 ± 6	71 ± 4	–	–	Y	WD, 6
0308−230	23 600	15.1	8.14	108 ± 5	70 ± 4	–	–	N	–
0308+188	18 500	14.2	7.89	320 ± 20	200 ± 10	–	–	N	–
0316+345	15 400	14.2	7.98	–	230 ± 10	–	74 ± 9	N	–
0331+226	21 500	15.3	7.43	110 ± 6	71 ± 4	–	–	–	–
0341+021[c]	22 200	15.4	7.27	102 ± 5	61 ± 3	–	–	Y	WD, 7
0345+134	25 100	16.1	7.56	46 ± 2	29 ± 2	–	–	–	–
0349−256	21 000	15.7	7.73	72 ± 4	47 ± 2	–	–	–	–
0352+018	22 100	15.6	7.28	79 ± 4	50 ± 3	–	–	Y	–
0358−514	23 400	15.7	7.46	70 ± 4	47 ± 2	–	–	N	–
0400+148	14 600	14.9	8.54	200 ± 10	130 ± 7	–	–	N	–
0403−414	22 700	16.4	7.54	41 ± 2	26 ± 1	–	–	Y	–
0406+169	15 800	15.3	8.46	126 ± 6	78 ± 4	53 ± 5	44 ± 6	N	–
0410+117[a]	21 100	13.9	7.58	–	250 ± 10	–	64 ± 3	Y	MS, 6

Table 4.6 – continued from previous page

WD Name	$T_{\rm eff}$ (K)	m (mag)	log $[t_{\rm cool}\,({\rm year})]$	$F_{3.6\,\mu{\rm m}}$ (μJy)	$F_{4.5\,\mu{\rm m}}$ (μJy)	$F_{5.7\,\mu{\rm m}}$ (μJy)	$F_{7.9\,\mu{\rm m}}$ (μJy)	Si II	Binarity
0414−406	20 900	16.1	7.79	48 ± 3	30 ± 2	–	–	N	–
0416−105	24 900	15.4	7.26	87 ± 4	53 ± 3	–	–	Y	–
0418−534	27 100	16.4	7.15	32 ± 2	21 ± 1	–	–	Y	–
0418−103	23 400	15.7	7.94	70 ± 4	44 ± 2	–	–	N	–
0421+162	19 600	14.3	7.93	280 ± 10	172 ± 9	115 ± 6	60 ± 5	Y	–
0431+126	21 400	14.2	7.75	–	177 ± 9	–	34 ± 7	Y	–
0452−347	21 200	16.1	7.62	57 ± 3	37 ± 2	–	–	Y	–
0455−532	24 400	16.8	7.22	31 ± 2	18 ± 1	–	–	–	–
0507+045A[a]	20 800	14.2	7.82	–	210 ± 10	–	140 ± 10	Y	WD, 8
0730+487	14 900	14.8	8.78	210 ± 10	129 ± 7	86 ± 6	56	N	–
0732−427	15 600	14.2	8.39	–	250 ± 10	–	90 ± 20	N	–
0816+297	16 700	15.8	8.06	78 ± 4	52 ± 3	26	26	N	–
0817+386	25 200	15.8	7.30	65 ± 4	42 ± 2	–	–	N	–
0821+632	16 800	15.9	8.01	72 ± 4	46 ± 2	–	–	N	–
0839+231	25 800	14.5	7.20	210 ± 10	131 ± 7	–	–	Y	–
0843+516	23 900	16.0	7.56	136 ± 7	137 ± 7	102 ± 7	159 ± 9	Y	–
0846+557	27 400	16.4	7.11	33 ± 2	18 ± 1	–	–	N	–

Table 4.6 – continued from previous page

WD Name	$T_{\rm eff}$ (K)	m (mag)	log $[t_{\rm cool}\,({\rm year})]$	$F_{3.6\,\mu{\rm m}}$ (μJy)	$F_{4.5\,\mu{\rm m}}$ (μJy)	$F_{5.7\,\mu{\rm m}}$ (μJy)	$F_{7.9\,\mu{\rm m}}$ (μJy)	Si II	Binarity
0854+404	22 300	14.8	7.58	156 ± 8	97 ± 5	–	–	Y	–
0859−039	23 700	13.2	7.38	700 ± 40	440 ± 20	–	–	–	–
0859+337	25 400	16.6	7.49	32 ± 2	19 ± 1	–	–	–	–
0904+391	26 200	16.3	7.40	33 ± 3	23 ± 2	–	–	N	–
0915+526	15 600	15.5	8.27	107 ± 5	65 ± 3	–	–	N	–
0920+363	24 100	16.1	7.22	56 ± 3	35 ± 2	–	–	Y	–
0922+183	24 700	16.4	7.48	40 ± 2	24 ± 2	–	–	–	–
0933+025[b]	22 400	15.9	7.78	3600 ± 200	2500 ± 100	–	–	N	MS, 10
0938+550	18 500	14.8	8.04	200 ± 10	123 ± 6	–	–	–	–
0944+192	17 400	14.5	8.16	250 ± 10	159 ± 8	–	–	N	–
0947+325	22 100	15.5	8.04	87 ± 4	57 ± 3	–	–	N	–
0954+697	21 400	16.0	7.60	63 ± 3	44 ± 2	–	–	Y	–
0956+020	15 700	15.7	8.13	88 ± 5	54 ± 3	–	–	N	–
1003−023	20 600	15.3	7.83	121 ± 6	73 ± 4	–	–	–	–
1005+642	19 700	13.7	7.88	460 ± 20	290 ± 10	–	–	N	–
1012−008	23 200	15.6	7.72	80 ± 4	49 ± 3	–	–	–	–
1013+256	22 000	16.3	7.68	42 ± 2	23 ± 1	–	–	Y	–

Table 4.6 – continued from previous page

WD Name	$T_{\rm eff}$ (K)	m (mag)	log $[t_{\rm cool}\,({\rm year})]$	$F_{3.6\,\mu{\rm m}}$ (μJy)	$F_{4.5\,\mu{\rm m}}$ (μJy)	$F_{5.7\,\mu{\rm m}}$ (μJy)	$F_{7.9\,\mu{\rm m}}$ (μJy)	Si II	Binarity
1015+161	20 000	15.6	7.99	200 ± 10	167 ± 8	142 ± 8	124 ± 7	Y	–
1016−308	16 300	14.6	8.37	240 ± 10	153 ± 8	–	–	–	–
1017+125[a]	21 400	15.7	7.73	73 ± 4	49 ± 3	28 ± 3	19 ± 6	Y	WD, 3
1018+410	23 700	16.4	7.82	86 ± 4	76 ± 4	–	–	–	–
1020−207	19 900	15.0	7.78	130 ± 7	84 ± 4	–	–	Y	–
1034+492	20 700	15.4	7.97	101 ± 5	59 ± 3	49 ± 4	30	Y	–
1038+633	24 500	15.2	8.00	109 ± 5	67 ± 3	57 ± 4	27	Y	–
1049−158	20 600	14.4	8.24	260 ± 10	155 ± 8	–	–	N	–
1049+103[c]	20 600	15.8	7.71	3700 ± 200	2600 ± 100	–	–	N	MS, 1
1052+273	23 100	14.1	8.04	300 ± 10	190 ± 10	130 ± 7	59 ± 7	N	–
1058−129	24 300	14.9	8.20	128 ± 7	82 ± 4	42 ± 6	30 ± 8	N	–
1102+748	19 700	15.1	8.24	136 ± 7	90 ± 5	–	–	N	–
1104+602	17 900	13.7	8.11	460 ± 20	290 ± 10	–	–	N	–
1105−048[a]	15 100	13.1	8.18	–	640 ± 30	–	260 ± 20	–	MS, 11
1113+413	25 400	15.4	7.30	96 ± 5	61 ± 3	–	–	Y	–
1115+166	22 100	15.1	7.72	134 ± 7	86 ± 4	65 ± 6	44	N	–
1117−023	14 700	14.5	8.31	290 ± 10	180 ± 9	–	–	N	–

Table 4.6 – continued from previous page

WD Name	$T_{\rm eff}$ (K)	m (mag)	log $[t_{\rm cool}\,({\rm year})]$	$F_{3.6\,\mu{\rm m}}$ (μJy)	$F_{4.5\,\mu{\rm m}}$ (μJy)	$F_{5.7\,\mu{\rm m}}$ (μJy)	$F_{7.9\,\mu{\rm m}}$ (μJy)	Si II	Binarity
1120+439	27 000	15.4	7.63	84 ± 4	48 ± 3	55	50	–	–
1122−324	21 700	15.8	7.58	62 ± 3	40 ± 2	–	–	–	–
1126+384	25 200	14.9	7.34	127 ± 6	76 ± 4	–	–	Y	–
1128+564	26 600	16.5	7.18	30 ± 2	19 ± 1	–	–	N	–
1129+155	17 700	14.1	7.98	380 ± 20	230 ± 10	159 ± 9	78 ± 7	Y	–
1132+470	27 500	16.4	8.28	66 ± 3	42 ± 2	–	–	–	–
1133+293	23 000	14.9	7.52	147 ± 7	91 ± 8	64 ± 7	44 ± 8	Y	–
1134+300	21 300	12.5	8.22	1380 ± 70	890 ± 40	–	–	–	–
1136+139	23 900	16.8	7.43	23 ± 3	16 ± 2	–	–	–	–
1143+321[a]	15 900	13.7	8.25	740 ± 40	480 ± 30	–	–	N	MS, 12
1145+187	26 600	14.2	7.18	240 ± 10	143 ± 7	–	–	Y	–
1152+371	27 400	14.7	8.47	13 ± 2	10 ± 1	–	–	–	–
1201−001	19 800	15.2	8.17	124 ± 6	80 ± 4	48 ± 3	18 ± 4	–	–
1202+308	28 900	16.3	7.04	40 ± 2	26 ± 2	–	–	N	–
1204−322	21 300	15.6	7.79	80 ± 4	52 ± 3	–	–	–	–
1220+234	26 500	15.6	7.74	67 ± 3	43 ± 2	–	–	N	–
1224+309[c]	28 800	16.2	7.08	610 ± 30	410 ± 20	–	–	Y	MS, 13

Table 4.6 – continued from previous page

WD Name	$T_{\rm eff}$ (K)	m (mag)	log $[t_{\rm cool}\,({\rm year})]$	$F_{3.6\,\mu{\rm m}}$ (μJy)	$F_{4.5\,\mu{\rm m}}$ (μJy)	$F_{5.7\,\mu{\rm m}}$ (μJy)	$F_{7.9\,\mu{\rm m}}$ (μJy)	Si II	Binarity
1229−012	19 400	14.5	7.60	240 ± 10	153 ± 8	91 ± 6	64 ± 8	N	–
1230−308	22 800	15.7	7.41	70 ± 4	46 ± 2	–	–	N	–
1232+479	14 400	14.5	8.31	280 ± 10	173 ± 9	–	–	–	–
1233−164[c]	24 900	15.1	7.66	114 ± 6	73 ± 4	–	–	N	WD, 4
1241+235	26 700	15.7	7.20	76 ± 4	53 ± 3	–	–	–	–
1243+015	21 600	16.5	7.72	34 ± 2	23 ± 1	–	–	Y	–
1247−115	28 100	15.3	7.23	88 ± 4	54 ± 3	–	–	Y	–
1249+160	25 600	14.7	7.24	177 ± 9	107 ± 5	–	–	Y	–
1249+182	19 900	15.2	7.74	95 ± 5	60 ± 3	–	–	Y	–
1257+047[a]	21 800	14.9	7.61	151 ± 8	98 ± 5	–	–	Y	MS, 3
1305+018[b]	29 000	15.2	7.26	110 ± 6	77 ± 4	–	–	–	MS, 14
1308−301	15 300	15.2	8.34	155 ± 8	96 ± 5	–	–	Y	–
1310−305	20 400	14.5	7.83	220 ± 10	143 ± 7	–	–	Y	–
1314−153	15 700	14.9	8.16	210 ± 10	134 ± 7	–	–	N	–
1323−514	19 400	14.4	7.80	280 ± 10	176 ± 9	–	–	Y	–
1325−089	17 000	15.0	8.01	165 ± 8	107 ± 5	–	–	Y	–
1325+279	21 300	15.8	7.91	64 ± 7	42 ± 5	–	–	Y	–

Table 4.6 – continued from previous page

WD Name	$T_{\rm eff}$ (K)	m (mag)	log $[t_{\rm cool}\,({\rm year})]$	$F_{3.6\,\mu{\rm m}}$ (μJy)	$F_{4.5\,\mu{\rm m}}$ (μJy)	$F_{5.7\,\mu{\rm m}}$ (μJy)	$F_{7.9\,\mu{\rm m}}$ (μJy)	Si II	Binarity
1330+473	22 500	15.2	7.57	106 ± 6	70 ± 4	–	–	N	–
1333+497	29 300	15.7	7.08	58 ± 3	36 ± 2	–	–	–	–
1334−160[a]	18 700	15.4	8.27	116 ± 7	94 ± 6	–	–	–	MS, 6
1334+070[c]	16 900	15.4	7.63	162 ± 8	99 ± 5	–	–	N	WD, 2
1335+369	20 500	14.8	7.62	210 ± 10	135 ± 7	–	–	–	–
1337+705	20 500	12.6	7.76	–	710 ± 40	–	250 ± 10	–	–
1338+081	24 400	16.4	7.34	31 ± 2	19 ± 1	–	–	–	–
1339+346[d]	16 000	15.9	8.08	1030	–	–	–	N	–
1349+144[c]	16 600	15.3	8.16	134 ± 7	84 ± 4	–	–	N	WD, 15
1353+409	23 500	15.5	7.38	77 ± 4	50 ± 3	33 ± 5	26 ± 5	N	–
1408+323	18 200	14.0	7.97	–	250 ± 10	–	92 ± 7	Y	–
1412−109[b]	25 700	15.9	7.38	760 ± 40	530 ± 30	330 ± 20	220 ± 20	Y	MS, 16
1421+318	27 200	15.4	7.23	82 ± 4	52 ± 3	–	–	Y	–
1433+538[c]	22 400	16.1	7.43	900 ± 50	600 ± 30	–	–	–	MS, 17
1449+168	22 400	15.4	7.58	91 ± 5	58 ± 3	–	–	–	–
1451+006	25 500	15.3	7.30	99 ± 5	63 ± 3	–	–	Y	–
1452−042	23 500	16.3	7.83	51 ± 3	36 ± 2	–	–	–	–

Table 4.6 – continued from previous page

WD Name	$T_{\rm eff}$ (K)	m (mag)	log $[t_{\rm cool}\,({\rm year})]$	$F_{3.6\,\mu{\rm m}}$ (μJy)	$F_{4.5\,\mu{\rm m}}$ (μJy)	$F_{5.7\,\mu{\rm m}}$ (μJy)	$F_{7.9\,\mu{\rm m}}$ (μJy)	Si II	Binarity
1452+553	28 300	16.1	7.60	43 ± 2	28 ± 2	–	–	Y	–
1457−086	20 400	15.8	7.72	114 ± 6	74 ± 4	49 ± 6	53	Y	–
1459+347	21 500	15.8	8.20	66 ± 3	41 ± 2	–	–	N	–
1507+220	19 900	15.0	7.80	151 ± 8	97 ± 5	–	–	–	–
1508+548	17 000	15.7	8.13	80 ± 4	50 ± 3	–	–	N	–
1511+009	27 600	15.9	7.26	56 ± 3	34 ± 2	–	–	–	–
1513+442	29 200	15.2	7.15	82 ± 4	52 ± 3	–	–	Y	–
1517+373	25 400	16.3	7.38	41 ± 2	29 ± 2	–	–	–	–
1518−003	15 400	15.2	8.16	122 ± 6	78 ± 4	–	–	N	–
1524−749	23 100	16.0	7.36	64 ± 3	39 ± 2	–	–	N	–
1525+257	22 300	15.7	7.97	70 ± 4	45 ± 2	–	–	N	–
1527+090	21 200	14.3	7.72	260 ± 10	165 ± 8	–	–	Y	–
1531−022	18 600	14.0	7.92	–	240 ± 10	–	103 ± 8	N	–
1533−057	20 000	15.4	8.07	95 ± 5	58 ± 3	–	–	Y	–
1535+293	24 500	15.9	7.40	51 ± 3	30 ± 2	–	–	N	–
1539+530[b]	26 800	15.6	7.43	5200 ± 300	3400 ± 200	–	–	–	MS, 3
1547+057	24 400	15.9	8.00	57 ± 3	36 ± 2	–	–	N	–

Table 4.6 – continued from previous page

WD Name	$T_{\rm eff}$ (K)	m (mag)	log $[t_{\rm cool}\,({\rm year})]$	$F_{3.6\,\mu{\rm m}}$ (μJy)	$F_{4.5\,\mu{\rm m}}$ (μJy)	$F_{5.7\,\mu{\rm m}}$ (μJy)	$F_{7.9\,\mu{\rm m}}$ (μJy)	Si II	Binarity
1548+149	21 500	15.2	7.74	123 ± 6	77 ± 4	–	–	Y	–
1550+183	14 300	14.8	8.62	220 ± 10	136 ± 7	95 ± 7	53 ± 6	N	–
1553+353	25 600	14.8	7.30	169 ± 8	105 ± 5	62 ± 5	43	–	–
1554+215[a]	26 300	15.2	7.26	105 ± 6	63 ± 4	–	–	–	MS, 6
1555−089[a]	14 600	14.8	8.30	220 ± 13	134 ± 8	–	–	N	MS, 18
1601+581	14 700	13.8	8.27	520 ± 30	330 ± 10	–	–	Y	–
1609+044	29 100	15.2	7.08	96 ± 5	59 ± 3	–	–	N	–
1614−128	16 600	15.0	8.01	161 ± 8	104 ± 5	–	–	N	–
1614+136	22 000	15.2	7.23	113 ± 6	68 ± 4	54 ± 5	16 ± 6	–	–
1619+123[a]	16 400	14.6	8.03	230 ± 10	149 ± 8	–	–	N	MS, 3
1620−391[a]	24 700	11.0	7.38	5000 ± 200	3100 ± 200	1900 ± 100	1070 ± 50	–	MS, 6
1620+260	28 300	15.6	7.15	76 ± 4	46 ± 2	–	–	N	–
1633+676	23 700	16.3	7.53	34 ± 2	22 ± 1	–	–	N	–
1641+387	15 600	14.6	8.31	250 ± 10	156 ± 8	–	–	Y	–
1643+143[c]	26 800	15.4	7.26	5700 ± 300	3800 ± 200	–	–	–	MS, 19
1647+375	22 000	14.9	7.59	138 ± 7	86 ± 4	–	–	Y	–
1713+332	22 100	14.4	7.32	–	185 ± 9	–	57 ± 6	Y	–

Table 4.6 – continued from previous page

WD Name	$T_{\rm eff}$ (K)	m (mag)	log $[t_{\rm cool}\,({\rm year})]$	$F_{3.6\,\mu{\rm m}}$ (μJy)	$F_{4.5\,\mu{\rm m}}$ (μJy)	$F_{5.7\,\mu{\rm m}}$ (μJy)	$F_{7.9\,\mu{\rm m}}$ (μJy)	Si II	Binarity
1713+695	15 900	13.2	8.26	820 ± 40	520 ± 30	–	–	N	–
1739+804	26 500	15.6	7.45	82 ± 4	50 ± 3	–	–	N	–
1755+194	24 400	16.0	7.46	55 ± 3	34 ± 2	–	–	Y	–
1914−598	19 800	14.4	7.88	290 ± 10	200 ± 10	–	–	Y	–
1919+145	15 300	13.0	8.40	1120 ± 60	690 ± 30	1180	741	N	–
1943+163	19 800	14.0	7.71	–	230 ± 10	–	101 ± 8	Y	–
1953−715	19 300	15.1	7.96	133 ± 7	84 ± 4	–	–	Y	–
2009+622[c]	26 500	15.3	7.15	1330 ± 70	900 ± 50	–	–	Y	MS, 20
2018−233	15 700	15.1	8.27	170 ± 9	111 ± 6	–	–	N	–
2021−128	20 800	15.2	7.78	113 ± 6	74 ± 4	–	–	N	–
2032+188	18 200	15.3	7.58	125 ± 6	81 ± 4	–	–	N	–
2039−682	17 100	13.3	8.51	–	490 ± 30	–	160 ± 10	N	–
2039−202	19 700	12.3	7.82	–	1040 ± 50	–	370 ± 20	–	–
2043−635	27 700	15.6	7.89	72 ± 4	49 ± 3	–	–	N	–
2046−220	23 400	15.4	7.45	89 ± 5	56 ± 3	–	–	Y	–
2056+073	27 300	15.4	7.75	80 ± 4	53 ± 3	–	–	N	–
2058+181	17 400	15.2	8.07	149 ± 8	97 ± 5	–	–	Y	–

Table 4.6 – continued from previous page

WD Name	$T_{\rm eff}$ (K)	m (mag)	log $[t_{\rm cool}\,({\rm year})]$	$F_{3.6\,\mu{\rm m}}$ (μJy)	$F_{4.5\,\mu{\rm m}}$ (μJy)	$F_{5.7\,\mu{\rm m}}$ (μJy)	$F_{7.9\,\mu{\rm m}}$ (μJy)	Si II	Binarity
2115+010	25 200	15.6	7.30	70 ± 4	43 ± 2	–	–	–	–
2134+218	18 000	14.5	8.06	–	159 ± 8	–	61 ± 7	Y	–
2143+353	26 100	15.9	7.38	51 ± 3	35 ± 2	–	–	N	–
2149+021	17 900	12.8	8.07	–	780 ± 40	–	270 ± 10	–	–
2152−045	19 800	15.7	7.44	84 ± 4	53 ± 3	–	–	Y	–
2200−136[c]	25 800	15.3	7.19	107 ± 5	65 ± 3	–	–	–	WD, 2
2204+070	25 600	15.8	7.49	70 ± 5	43 ± 2	–	–	–	–
2204+071	24 500	15.8	7.34	69 ± 4	42 ± 2	–	–	–	–
2205−139	26 000	15.0	7.69	120 ± 6	72 ± 4	–	–	N	–
2210+233	23 200	15.8	7.97	60 ± 3	35 ± 2	–	–	N	–
2218−271	15 000	14.7	8.14	350 ± 20	260 ± 10	–	–	N	–
2220+133	22 600	15.6	8.03	75 ± 4	46 ± 2	–	–	N	–
2220+217A[a]	18 700	15.5	8.29	80 ± 4	46 ± 2	–	–	–	WD, 2
2220+217B[a]	14 600	15.2	8.13	73 ± 4	43 ± 2	–	–	–	WD, 2
2225+219	26 000	15.8	7.30	60 ± 3	36 ± 2	–	–	Y	–
2226+061	15 300	14.8	7.93	200 ± 10	126 ± 6	73 ± 7	41	N	–
2229+235	19 300	16.0	8.03	59 ± 3	39 ± 2	24 ± 2	–	Y	–

Table 4.6 – continued from previous page

WD Name	$T_{\rm eff}$ (K)	m (mag)	log $[t_{\rm cool}\,({\rm year})]$	$F_{3.6\,\mu{\rm m}}$ (μJy)	$F_{4.5\,\mu{\rm m}}$ (μJy)	$F_{5.7\,\mu{\rm m}}$ (μJy)	$F_{7.9\,\mu{\rm m}}$ (μJy)	Si II	Binarity
2231−267	21 600	15.0	7.79	162 ± 8	109 ± 5	–	–	Y	–
2238−045	17 500	16.9	8.39	23 ± 1	13 ± 1	–	–	N	–
2244+210	24 100	16.5	7.41	35 ± 2	21 ± 1	–	–	Y	–
2248−504[c]	16 300	15.0	8.19	159 ± 8	100 ± 5	–	–	N	WD, 4
2257+162[c]	24 600	16.0	7.24	420 ± 20	290 ± 10	200 ± 10	128 ± 8	Y	MS, 9
2306+124	20 400	15.1	7.87	124 ± 6	77 ± 4	–	–	Y	–
2312−356	15 100	15.5	8.28	126 ± 6	83 ± 4	–	–	–	–
2318−226	29 900	16.1	7.15	40 ± 2	24 ± 1	–	–	–	–
2322−181	21 700	15.3	7.57	100 ± 5	62 ± 3	–	–	Y	–
2328+107	21 000	15.8	7.74	116 ± 6	77 ± 4	–	–	N	–
2331+290	27 300	15.7	6.96	69 ± 4	43 ± 2	29	14	–	–
2345−481	29 400	15.5	6.86	54 ± 3	32 ± 2	–	–	N	–
2345+304	29 100	16.4	7.06	43 ± 2	27 ± 2	–	–	N	–
2347−192	27 400	16.1	7.23	41 ± 2	23 ± 1	–	–	–	–
2350−248	29 700	15.4	7.54	77 ± 4	50 ± 3	–	–	Y	–
2359−324[c]	22 500	16.3	7.38	43 ± 2	28 ± 2	–	–	N	WD, 4

Table 4.6 – continued from previous page

WD Name	$T_{\rm eff}$ (K)	m (mag)	log $[t_{\rm cool}\,({\rm year})]$	$F_{3.6\,\mu{\rm m}}$ (μJy)	$F_{4.5\,\mu{\rm m}}$ (μJy)	$F_{5.7\,\mu{\rm m}}$ (μJy)	$F_{7.9\,\mu{\rm m}}$ (μJy)	Si II	Binarity

Notes. Cooling ages are calculated using white dwarf evolutionary models (Fontaine, Brassard & Bergeron 2001) with stellar parameters derived from *Gaia* DR2 (Gentile Fusillo et al. 2019). Fluxes without reported errors are upper limits. Confirmed and candidate companions are labelled as MS (= main sequence star, most of which are M-dwarfs), and WD (= white dwarf).

[a] Common proper-motion binary resolved in IRAC images. Reliable photometry was recovered for the target via aperture photometry or APEX.

[b] Common proper-motion binary resolved in *Gaia* DR2. IRAC images fail to reveal both sources, and thus the point-source photometry reported may not be reliable.

[c] Confirmed or candidate short-period binary. *Gaia* DR2 does not resolve any additional components, and IRAC images are point-like.

[d] Photometry contaminated by background source.

References. (1) Zuckerman & Becklin (1992); (2) Koester et al. (2009); (3) Farihi et al. (2005); (4) Maoz & Hallakoun (2017); (5) Mueller & Bues (1987); (6) El-Badry & Rix (2018); (7) Maxted, Marsh & Moran (2000); (8) Jordan et al. (1998); (9) Wachter et al. (2003); (10) Schultz et al. (1996); (11) Greenstein (1984); (12) Eggen & Greenstein (1965*b*); (13) Ferguson, Green & Liebert (1984); (14) Cheselka et al. (1993); (15) Karl et al. (2003); (16) Hoard et al. (2007); (17) Greenstein (1976); (18) Eggen & Greenstein (1965*a*); (19) Kidder, Holberg & Mason (1991); (20) Greenstein (1974).

This page was intentionally left blank

Chapter 5

Debris Disk Variation around White Dwarf Stars

Asteroids are nature's way of asking,
"How's that space program going?"

Paul Winchester Chodas (2014)

5.1 Introduction

From over a decade of research a body of compelling evidence has accumulated that shows that planetary systems around intermediate mass stars can survive the post-main sequence stellar phases (Zuckerman et al. 2003, 2010; Koester et al. 2014). Polluted white dwarfs with atmospheric metals have been observed to host orbiting circumstellar dust, and occasionally gas, disks which originate from the tidal disruption of asteroids, planetesimals, and comets after perturbation past the Roche limit (Zuckerman & Becklin 1987; Becklin et al. 2005; Gänsicke et al. 2006; von Hippel et al. 2007; Farihi et al. 2008; Farihi, Parsons & Gänsicke 2017; Xu et al. 2017).

5.1.1 White Dwarf Planetary Debris Disk Variability

Upon studying these systems recent observations have discovered both optical and infrared flux variations, and spectroscopic emission and absorption variations. Variation of the Ca II emission triplet, due to circumstellar gas, has been observed in several stars (Gänsicke et al. 2008; Wilson et al. 2014; Manser et al. 2016*a*,*b*; Dennihy et al. 2018). Whereas, optical flux and spectroscopic absorption variations, thought to be due to a disintegrating planetesimal, have been seen in one degenerate, WD 1145+017 (Vanderburg et al. 2015; Gänsicke et al. 2016; Redfield et al. 2017).

Infrared Flux Variability

Until recently, only one white dwarf has been observed to have infrared flux variation due to changes in the circumstellar dust disk. A 35 per cent infrared flux decrease was seen in WD J0959−0200 on the timescale of a year (Xu & Jura 2014). However, over the last couple of years infrared photometric variability has been shown to be more common than previously thought. By monitoring the white dwarf GD 56 over 11 years with the *Spitzer* and *WISE* space telescopes the infrared flux was observed to increase and subsequently decrease by 20 per cent (Farihi et al. 2018). It is thought that the flux increase is caused by the production of dust in the circumstellar debris disk by collisions that increase the surface area of the disk. Interestingly, spectroscopic observations of GD 56 over the same period show no variation in the atmospheric metal absorption features indicating that any gas produced by the collisions is either recondensed into dust or accretes onto the white dwarf on timescales longer than observed.

Furthermore, recent *Spitzer* observations of SDSS J1228+1040 showed a 20 per cent decrease in infrared flux (Xu et al. 2018). Interestingly, variation in the Ca II emission triplet has been seen in this system (Manser et al. 2016*b*) making it the first white dwarf planetary system with variation in both the observed circumstellar dust and gas. Using archival *WISE* observations of 35 white dwarfs with circumstellar debris disks over 7 years it has been shown that most of these systems show flux variation in one infrared band (Swan, Farihi & Wilson 2019).

Interestingly, as well as flux variability in white dwarfs, a flux decrease similar to WD J0959−0200 has been seen at the Sun-like star, TYC 8241−2652−1 (Melis et al. 2012*b*). This could potentially due to relaxation of the disk to return to a geometrically

thin nature after an asteroid disruption event or accretion onto the host star. Furthermore, *Spitzer* observations of five Sun-like stars that host debris disks with high fractional luminosities, so called "extreme debris disks", have shown significant infrared flux variation on the timescales of less than a year (Meng et al. 2015). This is over shorter time periods than the flux variation typically seen at white dwarfs, although further observations of debris disks around white dwarfs at short cadences need to be taken in order to probe these timescales. It was proposed that the observed flux variation is due to large-scale collisions between rocky parent bodies, however it should be noted that the characteristics of variation, such as variability timescales and disk temperature and surface area variation, in the five Sun-like stars differs from system to system (Meng et al. 2015), therefore suggesting that different physical processes maybe be the cause of the observed variation. Indeed, whilst colour variation has been observed in debris disks around main sequence stars potentially due to changes in disk temperature, surface area, or both (Meng et al. 2014, 2015), to date no significant colour variation has been observed in debris disks around white dwarfs (Farihi et al. 2018; Swan et al. 2019).

Theoretically Proposed Causes of Infrared Variation

Accompanying the observational research there have been recent theoretical work studying potential physical processes of the infrared variability in debris disks (Wyatt et al. 2014; Kenyon & Bromley 2017*a*,*c*). By modelling the stochastic accretion of metals onto a white dwarf atmosphere it was found that observed photospheric metal masses can be reproduced by the accretion of minor planetary bodies on year to decade timescales (Wyatt et al. 2014). This near-continuous replenishment of the circumstellar debris disk by the disruption of minor planetary bodies will cause variation in the debris disk surface area that could potentially be observed as infrared flux variation.

As was shown in Chapter 4, roughly 90 per cent of polluted white dwarfs do not exhibit a debris disk currently observable in the infrared. It has been proposed that this is due to some white dwarfs hosting optically thin disks (Bonsor et al. 2017), as opposed to the canonical flat, optically thick disk. If this is the case then PR-drag should result in the accretion of micron-sized dust on the timescale of a decade (Rafikov 2011*a*). Therefore, if optically thin disks are common, with or without an additional optically thick component, infrared flux variation should occur. Furthermore, it was found that for disks whose largest body has a radius greater than 10 km, collisional cascades can result in periodic brightening

and fading of disk luminosity due to the creation and destruction of small dust particles (Kenyon & Bromley 2017*a*). Destruction could be caused by additional collisions or by accretion by PR-drag. This view of disk evolution also supports a variable gas component to the circumstellar dust disk, such as those seen in multiple white dwarfs.

In this section recent and archival *Spitzer* observations are combined with *WISE* photometry of all known dusty white dwarfs at 3.5 and 4.6μm in order to better probe temporal infrared flux variations and potentially constrain physical models of the circumstellar environment. The *Spitzer* and *WISE* observations of all dusty white dwarfs are presented in Section 5.2. The data analysis, including differential photometry, is described in Section 5.3. The results are reported in Section 5.4 with the conclusions given in Section 5.5.

5.2 Observations

To study debris disk variation over the maximum possible baseline, new and archival *Spitzer Space Telescope* IRAC (Fazio et al. 2004; Werner et al. 2004) and *WISE* (Wright et al. 2010; Mainzer et al. 2011) observations of known dusty white dwarfs were retrieved and analysed. Both *Spitzer* and *WISE* have taken photometry at multiple infrared bandpasses, however following the loss of cryogen in both spacecraft observations were only taken at the shorter wavelengths. Therefore, in order to compare fluxes over as long as baseline as possible, photometry is only conducted on images taken at 3.4/3.6μm and 4.5/4.6μm. The cadence of *WISE* observations coupled with the legacy *Spitzer* data result in an unprecedented trove of photometry with the majority of targets detected at > 10 epochs spanning 9 to 14 years.

5.2.1 *Spitzer*

Data of 44 degenerates were obtained for Programme 13216 and processed by the IRAC calibration pipeline S19.2.0. Targets were observed at 3.6 and 4.5 μm with 10 or 20 images of 12 or 30 s each taken in a medium-sized, cycling dither pattern resulting in total exposure times of 120, 300, or 600 s. Archival IRAC observations of the sample of dusty white dwarfs taken during multiple programmes[1] taken in a plethora of exposure times and observing patterns were retrieved and processed by the IRAC calibration pipeline.

[1]ID# 23, 275, 2313, 3548, 20026, 30807, 30856, 40048, 40369, 50060, 50118, 50340, 60046, 60113, 60119, 60161, 61070, 70012, 70021, 70023, 70037, 70055, 70116, 80134, 80149, 90095, 90102, 10032, 10175, 11182, 12106, 12128

Data reduction using 1.2 arcsec pixel^{-1} CBCD (Corrected Basic Calibrated Data) frames was conducted using MOPEX standard pipelines with 0.6 arcsec pixel^{-1} mosaics created following best practices outlined in the *Spitzer* Data Analysis Cookbook. Aperture photometry was performed using APEX with aperture radii of 2.4 or 3.6 arcsec and $14.4 - 24.0$ arcsec sky annuli. In order to provide confidence in the reported fluxes aperture photometry using the standard IRAF task APPHOT was conducted on fully processed and calibrated 0.6 arcsec pixel^{-1} mosaics. For each object the aperture radii and sky annuli were kept constant for both methods. The average flux difference between the two methods was 0.8 per cent at 3.6 μm and 0.7 per cent at 4.5 μm.

Using conversion factors listed in the IRAC Data Handbook the fluxes were corrected for aperture size, but not for colour. As this study is interested in the flux variability of each source over multiple epochs the calibration uncertainty can be ignored. The reported flux error is solely the photometric measurement uncertainty.

5.2.2 *WISE*

In addition to the dedicated *Spitzer* observations, dusty white dwarfs have also been observed 3.4 and 4.6 μm by the *WISE* spacecraft during the initial Cryogenic, 3-band, and Near-Earth Object WISE (NEOWISE) surveys in 2010 and 2011 (Wright et al. 2010). Following a period of hibernation the *WISE* spacecraft was reactivated in 2013 for the NEOWISE-Reactivation mission and commenced observations (Mainzer et al. 2011, 2014) with subsequent data releases covering photometry taken between 2013 and 2017. The *WISE* orbit means that the telescope scans the entire sky in great circles over the course of a year, resulting in targets being observed every six months. During every visit, or epoch, targets are typically observed 12 times depending on the position, with the single frame exposure time being 7.7 s in each channel. For both the *WISE* and NEOWISE missions, photometry is conducted on the individual frames using the *WISE* data reduction pipeline with the determined fluxes and uncertainties reported in the AllWISE Multi-epoch Photometry Table and the NEOWISE-Reactivation Single Exposure Source Table, respectively.

The *WISE* and *NEOWISE* fluxes were retrieved for all 44 dusty white dwarfs observed by *Spitzer* and passed through several checks in order to obtain a sample of clean photometry. First, observations that were flagged with poor image and photometry quality were rejected along with any data in which the objects were undetected, reported in the tables

as upper limits. Second, photometry with coordinates 5σ away from the proper motion corrected published target coordinates were rejected, where σ is the average of the differences between the photometry coordinates for each epoch and the corrected published object coordinates. Finally, due to the relatively large *WISE* PSF Full Width at Half Maximum (FWHM) compared to *Spitzer*, typically 6 arcsec versus 2 arcsec, contamination due to a nearby object, either physically bound to the target or unrelated, can occur. Therefore, to mitigate this issue, the *Spitzer* IRAC images of white dwarfs taken nearest to the *WISE* and NEOWISE observations were searched for any potential contamination sources. If a source with a significant S/N was seen within 10 arcsec of the target in the *Spitzer* images, the *WISE* photometry at that epoch was rejected. It should be noted that whilst a target might be contaminated in all *WISE* and NEOWISE photometry that does not mean that it was removed from the sample as the majority of dusty white dwarfs now have two or more *Spitzer* observations and therefore can be analysed for potential variability.

As all targets are observed multiple times per epoch the photometry from the single frames can be co-added to produce deeper observations comparable to *Spitzer*. Following the checks, photometry was weighted averaged for each epoch in both *WISE* channels for every target. Typically, this resulted in 10 or 11 flux measurements over 8 years for each star, that, when combined with the dedicated *Spitzer* observations, produce the largest dataset of infrared observations of white dwarf debris disks covering the longest timescales to date allowing for a detailed study of debris disk variation.

5.2.3 Control Sample of Non-Debris Disk Hosting White Dwarfs

In order to study the potential infrared flux variation of the dusty white dwarf sample, a control sample of metal polluted white dwarfs that have been observed to not have a infrared excess is selected for comparison. To accurately determine the flux variation only single stars or those in *WISE* spatially-resolved binaries were chosen (Koester et al. 2005*b*; Dufour et al. 2007; Giammichele et al. 2012; Hollands et al. 2017), therefore both *Spitzer* and *WISE* observations will measure the flux of the bare white dwarf atmosphere. Archival *Spitzer* observations were taken from multiple programs[2]. A literature search and a common parallax and proper-motion search of *Gaia* DR2 data were conducted in order

[2]ID# 25, 33, 2313, 3548, 3655, 20567, 30208, 30298, 30807, 50340, 60046, 60161, 70055, 70116, 90095, 90102, 11161, 13207

to confirm that the sample does not contain any short-period binaries. Additionally, any known variable stars, or stars observed to vary in optical photometry (e.g. CRTS) due to stellar pulsations, were rejected. Furthermore, any stars with infrared contamination due to one or more nearby background sources or binary companions are rejected. This was checked by; first, a visual inspection of sources within 1.5 times the *WISE* PSF FWHM, typically 10 arcsec, was conducted in the same manner as for the white dwarfs with known debris disks described above. Second, using IRAF IMEXAM, the FWHM and shape of the stellar PSFs in the *Spitzer* observations were determined in order to check any contamination affecting the *Spitzer* photometry. White dwarfs with non-typical FWHM or shape values indicating an elongated PSF were rejected. The average IRAC PSF FWHM for the clean sample was 2.9±0.2 pixels, where the PSF FWHM of a single star is typically $2.8 - 3.1$ pixels, and the average shape is 0.09±0.11, where 0 indicates a perfectly round PSF. This resulted in a control sample of 31 white dwarfs.

Following these checks, aperture photometry using APEX was conducted on the *Spitzer* observations for all white dwarfs as detailed above. *WISE* photometry was also completed for all degenerates using the method outlined previously, including all photometric checks. Photometry of a clean sample of 31 stars that spans timescales up to 14 years is obtained and provides an ample control sample to the known dusty white dwarfs.

As a final check, SEDs were constructed for all comparison white dwarfs using literature ultraviolet, optical, and near-infrared data, and the determined *Spitzer* and *WISE* fluxes. White dwarf atmospheric models of $\log g = 8$ and effective temperatures taken from the literature were fitted to the optical photometry, and infrared flux excesses at the *Spitzer* and *WISE* wavelengths were calculated. The average flux excesses at 3.6 and 4.5 μm were 0.01σ and -0.12σ, respectively, indicating that the observed fluxes are indicative of the white dwarf atmospheric model and that the observations are of the bare white dwarf atmosphere.

5.3 Data Analysis

5.3.1 Differential Photometry

As reliable infrared photometry has been obtained for both the dusty white dwarf and control star samples over decade timescales, analysis can be done in order to probe potential infrared flux variability. It should be noted that whilst all 44 dusty white dwarfs in

the sample were observed by *Spitzer*, two stars (WD 1225−079 and WD 1455+298) only have an infrared excess beyond 5 μm. Therefore, as this study focuses on the infrared variation of debris disks at 3.4/3.6 μm and 4.5/4.6 μm, these two stars are removed from the sample and not considered during the analysis, as observations at these wavelengths will probe the white dwarf atmosphere. This results in a sample of 42 stars with debris disks at shorter infrared wavelengths.

To better understand the infrared variability in the systems in both samples, differential photometry was conducted using photometrically stable comparison stars. By selecting stars in the same *Spitzer* mosaics and *WISE* scans as the targets any photometric variations caused by observational effects are accounted for, and therefore any observed flux variation is due to intrinsic infrared variability at the object. Five bright, isolated, field stars detected at all epochs and in all short wavelength channels (3.4/3.6 μm and 4.5/4.6 μm) were chosen for each target. For the *Spitzer* observations, fluxes were determined via aperture photometry performed on the MOPEX constructed mosaics, whereas for *WISE* observations, the weighted averaged fluxes taken from *WISE* and NEOWISE catalogues, following the same procedures outlined above.

For each white dwarf in both samples, the flux of the target is divided by each of the five comparison field stars to produce a flux ratio, with the uncertainties calculated by the summation in quadrature of the target and comparison star measurement errors. The weighted average and error of the five flux ratios are determined for each epoch that is then normalised over all epochs. Across both samples the average flux variation of the comparison field stars at all wavelength bandpasses is on the order of one per cent.

5.3.2 Variability Metrics

The Significance and Percentage Change

When studying infrared variability there are two important metrics to consider for each system: the significance and the percentage change. The significance is determined by the difference in flux between two epochs divided by the summation in quadrature of the flux uncertainties for those epochs. This metric is used to ascertain whether or not the observed variation is significant and is measured in σ, the flux uncertainties of both epoch summed in quadrature. In this study, flux variability is considered significant if this value is greater than 3. On the other hand, the percentage change is simply the flux difference

between two epochs divided by the average flux of those epochs. This metric can be useful in measuring the flux change of the system, potentially due to physical changes in the debris disk.

As the significance of the variation is dependent on the flux uncertainties it is therefore also dependent on the sensitivity of the observations (for example, the telescope used, the exposure time, etc.). Therefore, a possible scenario is that the percentage change of a system is large indicating that there is variation, but if there are large uncertainties then the variation may not be determined to be significant. The opposite scenario, is that with very sensitive observations, flux variations with a small percentage change may be determined to be significant. Therefore, by using both metrics together, one can establish if a system is significantly varying and by how much.

The Minimum Detectable Fractional Flux Variation

Thus, as both these metrics are useful in the study of infrared flux variation, it could be useful to define a new metric that encapsulates both the information of the physical flux variation and whether or not the variation is significant. One can therefore introduce a new metric; the minimum detectable fractional flux variation, $\phi_{\rm var}$:

$$\phi_{\rm var} = \frac{3\sqrt{\sigma_{\rm i}^2 + \sigma_{\rm j}^2}}{0.5({\rm F_i} + {\rm F_j})} \tag{5.1}$$

where $F_{\rm i}$ and $F_{\rm j}$ are the fluxes at the i and j epochs, with the uncertainties given as $\sigma_{\rm i}$ and $\sigma_{\rm j}$. As the total error is $\sqrt{\sigma_1^2 + \sigma_2^2}$, the numerator in this equation is simply the 3σ level, above which any flux variation is considered significant. When this is divided by the average flux, this results in the minimum fractional change in flux that is considered real. This metric can be useful for two reasons:

i) it can reveal how significant the physical flux variation is by dividing the observed fractional flux variation by $\phi_{\rm var}$. If this ratio is equal or greater than one then the flux variation is significant;

ii) It can shed light on how sensitive the observations are to flux variation as observations with facilities that have lower uncertainties will yield lower $\phi_{\rm var}$ values. This will

put variability detection limits on *Spitzer* and *WISE*.

The Stetson Index and a Chi-Squared Variance Test

In addition to using the significance to establish whether or not a flux variation is real, previous work has used the Stetson index and a chi-squared variance test to verify flux variation (Meng et al. 2015). The Stetson index (Stetson 1996) measures the correlation in the flux observed at two wavelengths over several epochs. This correlation metric can be useful in detecting flux variation at targets as, over time, processes that cause bona fide physical variation are likely to produce correlated (or indeed anti-correlated) flux increases or decreases (Flaherty et al. 2013; Rebull et al. 2014; Meng et al. 2015). Whereas variation due to noise is statistically unlikely to be correlated over time. Therefore, if a large positive or negative Stetson index is seen in the 3.6 and 4.5 μm flux, then the correlated or anti-correlated flux is likely indicative of real variation. The Stetson index can only be used to infer flux variation, and cannot be used to determine potential colour variation. This metric can be calculated by:

$$\mathrm{S} = \frac{\sum_{\mathrm{k}=1}^{\mathrm{N}} \mathrm{g_k sign(P_k)}\sqrt{|\mathrm{P_k}|}}{\sum_{\mathrm{k}=1}^{\mathrm{N}} \mathrm{g_k}} \tag{5.2}$$

where g_{k} is the weight of the k epoch, taken in this work to be equal to one, and $P_{\mathrm{k}} = \delta_{\lambda_1,\mathrm{k}}\delta_{\lambda_2,\mathrm{k}}$, where λ_1 and λ_2 are the two wavelengths at which the observations are taken, and:

$$\delta_{\lambda,\mathrm{k}} = \sqrt{\frac{\mathrm{N}}{\mathrm{N}-1}}\frac{\mathrm{F_k} - \langle \mathrm{F} \rangle}{\sigma_{\mathrm{k}}} \tag{5.3}$$

where N is the number of observations, $\langle F \rangle$ is the mean flux, and F_{k} and σ_{k} is the flux and uncertainty at the k epoch, respectively. In order to determine whether or not the (anti-)correlated flux is indicative of real variation previous work has used absolute S value thresholds of 0.45, 0.5, and 0.9 (Flaherty et al. 2013; Rebull et al. 2014; Meng et al. 2015). It has been shown that a S value of 0.9 corresponds to a 6σ variation detection assuming a Gaussian distribution of correlations (Rebull et al. 2014). Therefore, to be rigorous,

flux variation is thought to be significant via this method if the absolute Stetson index is greater than 1.0.

In addition, a chi-squared variance test can be conducted on the stars in the sample in order to determine any variability using the following:

$$\chi^2 = \frac{1}{\mathrm{N}-1}\sum_{\mathrm{k}=1}^{\mathrm{N}}\left(\frac{\mathrm{F_k}-\langle\mathrm{F}\rangle}{\sigma_\mathrm{k}}\right)^2 \tag{5.4}$$

where the parameters are defined the same as above. Previous work has defined that variation can be confidently detected for χ^2 equal or greater than three or five (Flaherty et al. 2013; Rebull et al. 2014; Meng et al. 2015). By comparison with the Stetson index it was found that a S value of 0.9 (and a 6σ variation detection) corresponds roughly to a χ^2 of five (Rebull et al. 2014), and therefore, for this study, flux variation is considered real if this value is greater than five.

Furthermore, as well as studying flux variations in one wavelength, it is also possible to analyse colour variations by determining how the ratio of the longer wavelength (4.5 or 4.6μm) flux to the shorter wavelength flux (3.4 or 3.6μm) changes between epoch. Potential colour variation can be probed by using the significance, percentage change, and chi-squared variance metrics. While the presence of infrared flux variation may give hints to the physical processes occurring in debris disks, observations of colour variation can be clear indicators of either a changing dust area, changing dust temperature, or both, as has been inferred to be the case for disks around multiple main sequence stars (Meng et al. 2014, 2015).

By using the significance, Stetson index, and the chi-squared variance test it is possible to confidently conclude that any potential infrared flux and colour variation at a white dwarf is real, which then can be studied using the percentage change and minimum detectable fractional flux variation metrics.

5.4 Results

Both the sample of 42 white dwarfs with known debris disks and the control sample of 31 single, metal polluted degenerates with no observed infrared excesses are put through the analysis methods detailed above in order to first determine if a system exhibits real

flux or colour variation, and then to analyse the change in flux or colour that potentially could be due to physical changes in the debris disk. In the dusty white dwarf sample there are four known ZZ Ceti stars (WD 1116+026, WD 1150−153, WD 1541+650, and WD 2326+049) (McGraw & Robinson 1975; Vauclair et al. 2000; Gianninas et al. 2006; Silvotti et al. 2006). It should be noted that any observed infrared variability in these stars may be due to the thermal re-radiation of the stellar optical pulsations rather than a physical change in the surface area of the disk. This will be discussed in more detail below. Representative normalised light curves of dusty white dwarfs for channel 1 and 2 fluxes, and colours are shown in Figs. 5.6 & 5.7, with typical normalised light curves of the control white dwarf sample given in Figs. 5.8 & 5.9. As the data points shown were calculated using differential photometry they are unitless.

It is interesting to note that nine stars in the dusty white dwarf sample have observed circumstellar gas, typically seen via the Ca II triplet (Gänsicke et al. 2006, 2007, 2008; Dufour et al. 2010; Farihi et al. 2012*a*; Melis et al. 2012*a*; Wilson et al. 2014; Guo et al. 2015), but in one system gas has been observed via absorption features (Xu et al. 2016; Redfield et al. 2017). The production method(s) of the gas has not been confirmed empirically to date, although possible processes include: the collision between the dust disk and an additional incoming asteroid (Jura 2008; Wilson et al. 2014), intra-disk collisions caused by the general relativistic precession of dust (Manser et al. 2016*b*), from collisions in a currently, or recently, disintegrating planetesimal (Xu et al. 2016), or from a collisional cascade of dust within the disk (Kenyon & Bromley 2017*b*). In all systems the gas has been observed to be co-spatial with the circumstellar debris disks. Any of these processes may increase or decrease the emitting surface area of the dust disk, and therefore infrared flux, and it may be useful to highlight these stars in the following subsections. Interestingly, a recent spectroscopic survey to search for the Ca II triplet at all known dusty white dwarfs found no new circumstellar gas disks (Dennihy 2018). As these emission features have been observed to be transient on the scale of years or decades (Manser et al. 2016*b*; Dennihy et al. 2018) this raises two possibilities; either the systems with observed Ca II emission are undergoing a (currently unknown) process that does not occur at the other disks or it is possible that all disks can produce gas emission in sporadic episodes. To understand the process(es) that produce circumstellar gas and the transient nature it may be beneficial to study how the infrared flux varies in these systems.

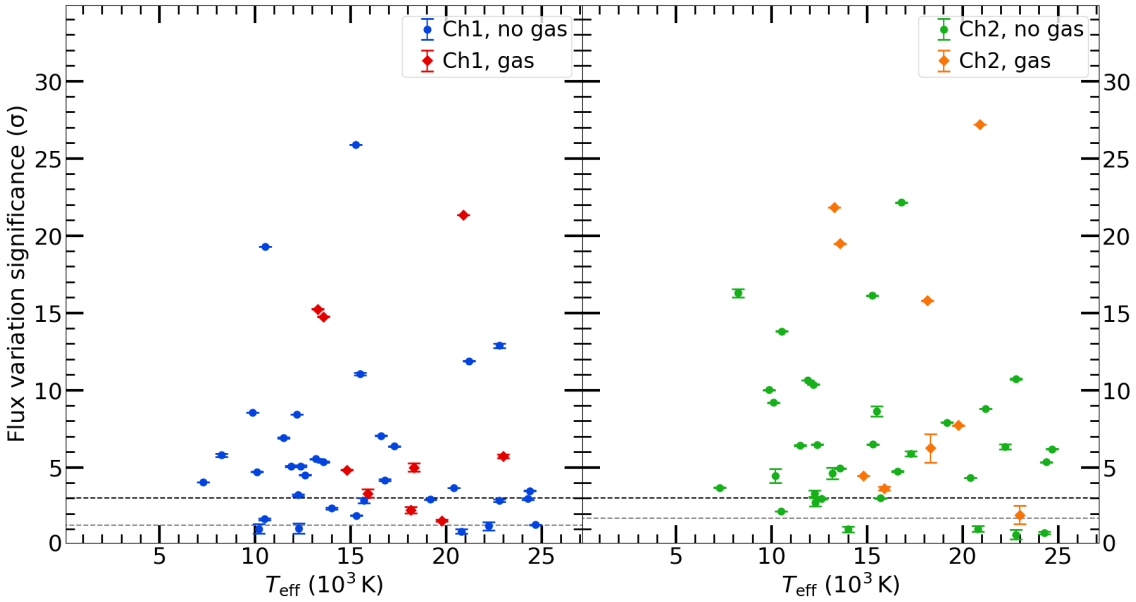

Figure 5.1. The flux variation significance plotted against the effective temperature of the host star with the white dwarfs with observed circumstellar gas highlighted. The black line is 3σ and the grey line is the average flux variance significance for the control sample.

5.4.1 Flux Variation

Using the three flux variation methods detailed above it is seen that at least 28 out of 42 dusty white dwarfs have flux variation at channel 1 (3.4 or 3.6μm) and at least 30 out of 42 at channel 2 (4.5 or 4.6μm). This is good agreement with a previous study that used *WISE* 3.4μm observations (Swan et al. 2019). For the subsample of dusty white dwarfs with circumstellar gas, at least six out of nine were determined to have flux variations at both channel 1 and 2. As a fraction, is this indistinct to the whole dusty white dwarf sample. For the control sample, on the other hand, between 10 and 39 per cent exhibit flux variation. By comparing the samples, it can be seen that the dusty white dwarfs have a significantly higher fraction of variation than the metal polluted white dwarfs with no debris disk. This is the first study to show that the majority of debris disks vary at 4.5 and 4.6μm. The sample statistics for all methods are reported in Table 5.1, with the significance values for the individual targets in both samples given in Tables 5.2 & 5.3. For the dusty white dwarf sample, and the subsample with circumstellar gas, the percentage of systems that significantly vary agree across all three determination methods. However, for the control sample there seems to be a discrepancy in the number of varying stars

Table 5.1. Sample statistics for flux and colour variation.

	Dusty	with circumstellar gas	Control
N	42	9	31
Significance			
ch1	29 (69^{+6}_{-8} per cent)	7 (78^{+8}_{-18} per cent)	12 (39^{+9}_{-8} per cent)
ch2	34 (81^{+5}_{-7} per cent)	8 (89^{+4}_{-18} per cent)	12 (39^{+9}_{-8} per cent)
ch2/ch1	13 (31^{+8}_{-6} per cent)	1 (11^{+18}_{-4} per cent)	1 (3^{+7}_{-1} per cent)
Stetson			
ch1 & ch2	36 (86^{+4}_{-7} per cent)	6 (67^{+11}_{-17} per cent)	4 (13^{+8}_{-4} per cent)
Variance			
ch1	28 (67^{+6}_{-8} per cent)	7 (78^{+8}_{-18} per cent)	4 (13^{+8}_{-4} per cent)
ch2	30 (71^{+6}_{-8} per cent)	7 (78^{+8}_{-18} per cent)	3 (10^{+8}_{-3} per cent)
ch2/ch1	18 (43^{+8}_{-7} per cent)	3 (33^{+17}_{-11} per cent)	1 (3^{+7}_{-1} per cent)

between the significance, and the Stetson and variance methods. Although for all methods the percentage of significantly varying systems in the control sample is lower than for the dusty white dwarf sample.

For the entire dusty white dwarf sample, the flux variation significances for both channel 1 and 2 are plotted in Fig. 5.1. The average significance for the control sample in both channels is plotted for comparison (1.3±1.4 for channel 1 and 1.7±1.3 for channel 2). It can be seen that, as well as more dusty white dwarfs varying significantly, the absolute value of flux variation significance is typically higher than for the control sample in both channels. The average significance for the dusty white dwarf sample is 6.5±5.7 in channel 1 and 8.0±6.4 in channel 2, whereas for the stars with observed circumstellar gas it is 8.2±7.0 and 12.0±9.2, with the high standard deviations due to the large significance range as can be seen in Fig. 5.1. As the control sample consists of metal polluted white dwarfs with no debris disk, this finding confirms that the cause of the infrared flux variation is the circumstellar debris disk and that the majority of white dwarfs debris disks vary.

5.4.2 Colour Variation

Due to the high S/N *Spitzer* observations taken at both channels, the colour variation of dusty white dwarfs can be probed for the first time. Previous work has commented that, although some potential colour variation is seen, due the low S/N of *WISE* channel 2 confident conclusions about colour variability cannot be drawn (Swan et al. 2019). In this

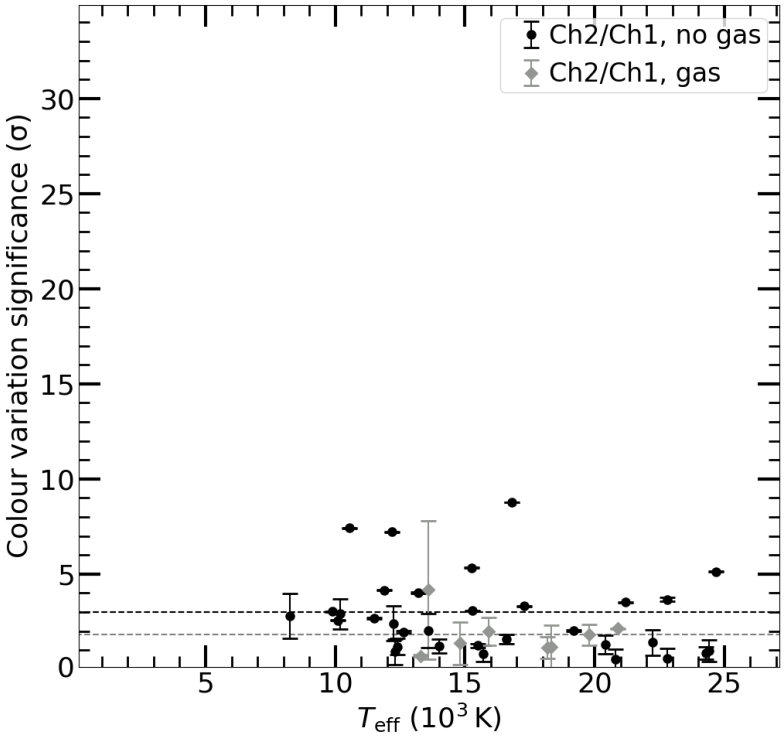

Figure 5.2. The colour variation significance plotted against the effective temperature of the host star with the white dwarfs with observed circumstellar gas highlighted. The black line is 3σ and the grey line is the average flux variance significance for the control sample.

study, *WISE* photometry is included for completeness, although as will be discussed below the maximum colour variation significance typically comes from the *Spitzer* observations. It should be noted that while the *Spitzer* and *WISE* bandpasses are similar, the filter sets are different, and therefore the flux ratios of the two channels (i.e. the colour) cannot be directly compared (Farihi et al. 2018). Where possible, the variation determination metrics detailed above are used on the *Spitzer* and *WISE* photometry separately for each star. Indeed, after the aforementioned photometric checks, several stars do not have clean photometry in both channels at multiple epochs when the *Spitzer* and *WISE* data are analysed separately.

By using the significance and variance tests it can be seen that at least 13 out of 42 dusty white dwarfs exhibit colour variability, whereas in the subset of these that have observed circumstellar gas at least one out of nine show colour variations. It should be noted that the Stetson index cannot be used to probe colour variations as the test searches for flux variation assuming a correlation between wavelength channels (i.e. no

colour variation). For the control sample, only one out of 31 stars have a significant colour variation. This shows that the observed colour variability is due to the circumstellar debris disks, although there does not seem to be a link between colour variability and observed circumstellar gas. The colour variation frequency for each sample is reported in Table 5.1, with the significance values for the individual targets in both samples given in Tables 5.2 & 5.3. For all samples the frequencies agree using both methods.

As can be seen in Fig. 5.2, while there are five stars with a highly significant colour variation (greater than 5σ), the majority of white dwarfs in the dusty sample, the circumstellar gas subsample, and the control sample have similar average significances (2.6 ± 1.9, 1.8 ± 1.0, and 1.8 ± 0.9, respectively). This raises the interesting question as to whether the observed colour variation is due to a specific process(es) occurring in some disks or if it is intrinsic to all disks (as flux variation seems to be), and the sensitivities of current facilities are the limiting factor in determining the significance of the colour variation.

5.4.3 Flux and Colour Percentage Variation

After using the variation determination methods to establish flux and colour variation at dusty white dwarfs, one can potentially use the flux and colour percentage change to analyse the nature of the debris disks. While the processes governing the creation and destruction of dust in circumstellar debris disks around white dwarfs are currently unknown (although methods involving tidal disruption, collisions, and PR-drag have been proposed), knowledge about these systems can be gained by studying the flux and colour percentage variation. This is because a change in flux is interpreted as a change in the observable emitting surface area which could be caused by dust creation and destruction.

Using the Minimum Detectable Fractional Flux Variation to Probe Sensitivity

Prior to discussing the observed flux percentage change, it can be useful to discuss the minimum detectable fractional flux variation of the dusty white dwarfs and the sample as a whole, in order to place the flux variation into context. By using equation 5.4, $\phi_{\rm var}$ was determined using the normalised differential photometry from both *Spitzer* and *WISE* observations for all dusty white dwarfs. The $\phi_{\rm var}$ values are useful in understanding variation for two reasons. First, as data from two facilities is analysed in this study, $\phi_{\rm var}$ can be used to probe how sensitive both telescopes are to flux variation and therefore, variability detection limits can be placed in *Spitzer* and *WISE*. This is because $\phi_{\rm var}$ is

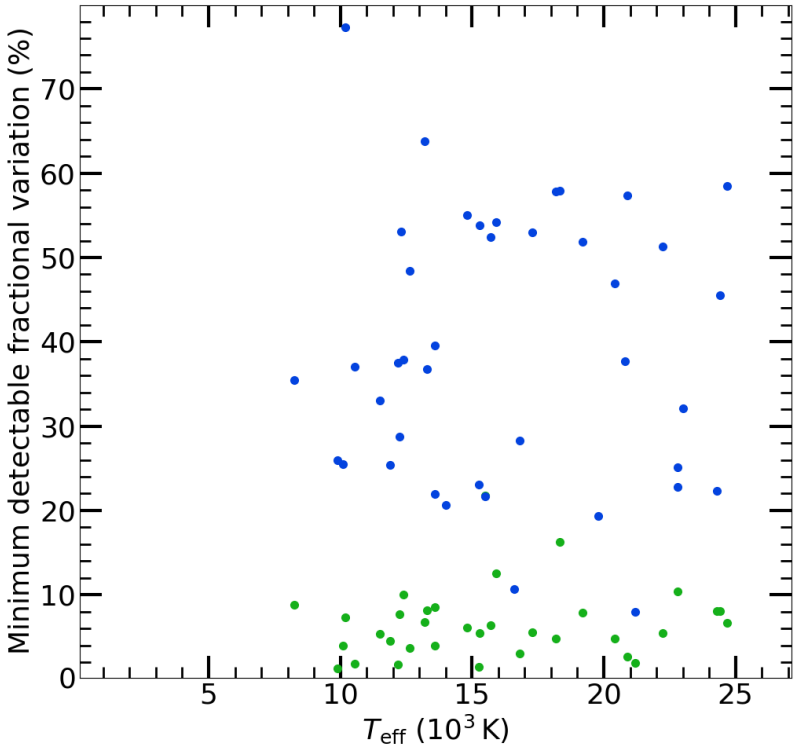

Figure 5.3. The minimum detectable fractional variation, $\phi_{\rm var}$, in channel 1 for the dusty white dwarfs in the sample. The green points are from the *Spitzer* observations, whereas blue points are from the *WISE* photometry.

dependent on the flux uncertainties. In Fig. 5.3, the $\phi_{\rm var}$ values for observations of all dusty white dwarfs taken in channel 1 are presented, with the green and blue points representing values calculated from *Spitzer* and *WISE* data, respectively. Whilst there is an overlap, a clear clustering into two groups can be seen. $\phi_{\rm var}$ values from *Spitzer* observations are typically below 10 per cent, that means that the upper limit of flux uncertainties are about 2 per cent. For the *WISE* photometry, the minimum detectable fractional variability is, in general, between 20 and 60 per cent, indicating flux uncertainties of between 5 and 14 per cent in this study. This shows the usefulness of *Spitzer* in studying flux variability of white dwarf debris disks, with future facilities expecting to push these detection limits lower.

Comparing the Minimum Detectable Fractional Flux Variation Against the Observed Variation

Second, by calculating the average $\phi_{\rm var}$ values for both spacecraft at both flux channels and for the colour, one can compare them against the observed flux and colour percentage variations. These values are plotted against the time between observational epochs in

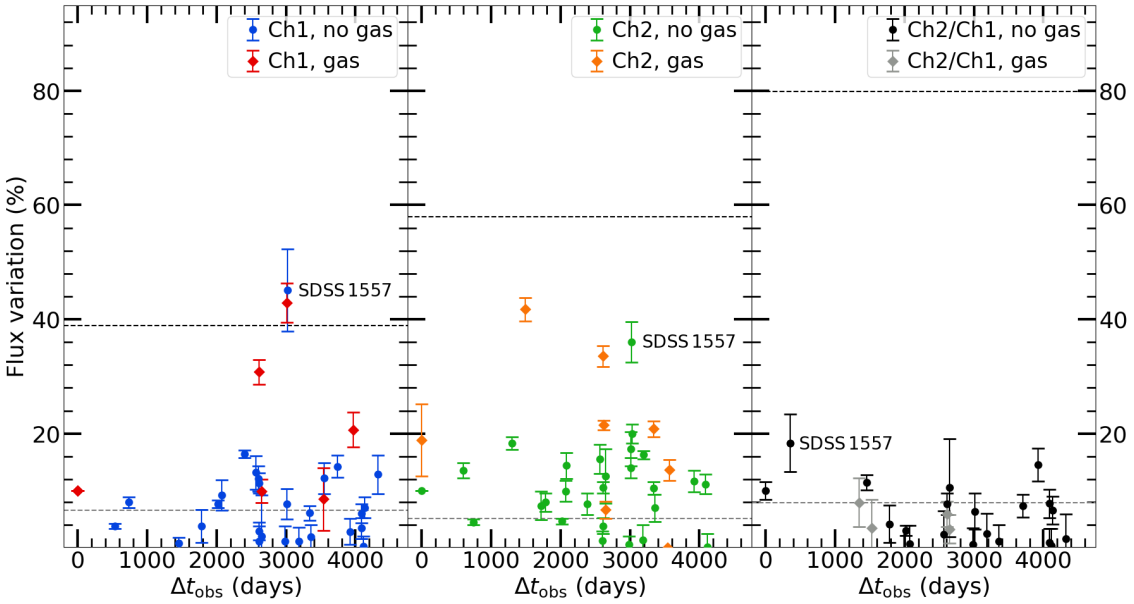

Figure 5.4. The maximum flux variation, $\phi_{\rm var}$, determined for all known dusty white dwarfs. The black and grey lines are the average minimum detectable fractional variations, $\phi_{\rm var}$, for *WISE* and *Spitzer*, respectively.

Fig. 5.4. This comparison is useful as it combines the physical flux and colour variation occurring at these systems with a measure of the significance, above which flux and colour variation could be considered real. Therefore, it can be seen that as the average *WISE* $\phi_{\rm var}$ value in channel 1 is roughly 40 per cent, only two stars have observed flux variation above this value and have bona fide variations. Whereas, the average *Spitzer* $\phi_{\rm var}$ value is about 7 per cent and therefore more systems are determined to have a significant flux variation. Obviously, there are ranges of $\phi_{\rm var}$ values, as is seen in Fig. 5.3, and so some flux variations below the average $\phi_{\rm var}$ values will be significant. Therefore, caution needs to be taken when directly interpreting Fig. 5.4. Interestingly, whilst the average *Spitzer* $\phi_{\rm var}$ values remain similar for channels 1 and 2, and the colour, indicating that more disks are varying significantly at channel 2 and fewer have real colour variations, the average *WISE* $\phi_{\rm var}$ values for channel 2 and the colour are much higher. This is because the S/N in *WISE* channel 2 is, in general, much lower than in channel 1 (Swan et al. 2019), and therefore, no significant channel 2 flux or colour variations are seen with *WISE*.

An interesting point, is that, in general, the systems with observed circumstellar gas have a greater flux percentage variation than the dusty white dwarf sample as a whole. In both channels 1 and 2, all systems that vary by more than 20 per cent have observed

circumstellar gas, with the exception being SDSS 1557, that varies by 45 per cent in channel 1 and by 36 per cent in channel 2, as clearly seen in Fig. 5.4. This white dwarf is in a known close binary system with a L-type brown dwarf companion (Farihi et al. 2017), and therefore the observed flux variation is not believed to be partly or wholly due to a physical change in the observed emitting surface area of the disk, but also due to the companion. Therefore, excluding this close binary, one can see that all highly varying disks have observed circumstellar gas. Although the sample size of stars with circumstellar gas is small, this finding provides a tenuous link between the infrared flux variation potentially caused by physical disk changes such as collisions, tidal disruption, and PR-drag, and the presence of circumstellar gas potentially caused by a collisional cascade, intra-disk collisions via general relativity precession, and tidal disruption. This is especially interesting as a recent survey found that the rest of the dusty white dwarf sample does not currently have observable Ca II triplet emission (Dennihy 2018). It should be noted that no correlation is seen between colour variation and the presence of circumstellar gas.

Flux Variation of ZZ Ceti Stars in the Sample

Whilst there have been substantial optical and ultraviolet studies (Tucker et al. 2018), the infrared flux variation of ZZ Ceti stars (pulsating white dwarfs) is currently not well known or constrained, and the amplitude of variations in the infrared have not been constrained via models. This makes the interpretation of the observed flux variation at the four ZZ Cetis in the sample (WD 1116+026, WD 1150−153, WD 1541+650, and WD 2326+049) potentially challenging. From *Spitzer* observations of WD 2326+049 taken in 2004 a significant pulsation amplitude of 4 per cent was seen in channel 1 with no significant variation above 5 per cent in channel 2 (Reach et al. 2009). Optical observations of this star show variations with an amplitude of 20 per cent (McGraw & Robinson 1975). In this study, the infrared flux variation is 8±1 per cent in channel 1 and 14±1 per cent in channel 2. Therefore, it is not possible to rule out that the observed flux variation is due to heating of the disk by stellar pulsations.

However, for the three remaining stars, no corresponding *Spitzer* study has been conducted. From the observations of WD 2326+049 taken in channel 1, and assuming they are indicative of the infrared pulsations at all ZZ Cetis, it has been speculated that the amplitude of flux variation in the infrared would be 10−20 per cent of the optical flux variation amplitude (Kilic et al. 2008, 2012). By being conservative and assum-

ing that the infrared flux variation due to the heating of dust via stellar pulsations is 20 per cent of the optical pulsations (Vauclair et al. 2000; Gianninas et al. 2006; Silvotti et al. 2006), it can be estimated that the infrared flux amplitude for WD 1116+026, WD 1150−153, and WD 1541+650 is 0.1 per cent, 0.2 per cent, and 0.9 per cent, respectively. For WD 1116+026 and WD 1150−153, these values are roughly two orders of magnitude smaller than the observed flux variation in this study and therefore it is believed that the variability is due to processes occurring within the disk. For WD 1541+650, the estimated flux variation due to stellar pulsations is roughly one third of the observed flux variation in channel 1, but only 10 per cent of the flux change in channel 2. Therefore while, the channel 1 variability might be caused by the stellar pulsations, it seems that in channel 2 the flux variation is due to physical processes in the disk.

Flux Variation Trends over Time

As a side note, due to the large number of epochs observed for each white dwarf it is possible to plot the observed flux variation against the time between observations in an attempt to determine any variation trends. In this sample, it was found that there appears to be no correlation between flux variation and time between epochs. This is unsurprising as many processes acting on different timescales could potentially cause flux variation (Farihi et al. 2018), and even if a standard variation process exists for all debris disks the observations here are too sparse to determine such a process.

5.4.4 Relationship between Fractional Luminosity and Flux Variation

When fitting a flat, opaque disk model to an observed infrared flux excess in order to determine the physical properties of a disk there is a degeneracy between the inner and outer radius (i.e. radial width) and the disk inclination. In order to somewhat break this degeneracy, one could use the fractional luminosity of the disk (the ratio of disk and stellar luminosities) as a proxy for the observable emitting surface area (Rocchetto et al. 2015; Dennihy et al. 2017). A low fractional luminosity could be caused by either a wide, edge-on disk or a narrow, face-on disk, whereas a high factional luminosity would be caused by a wide, face-on disk.

Therefore, by using the fractional luminosity as a proxy for observable emitting surface area it can be compared against the observed flux percentage variation in order to potentially learn about the nature of the variations. If it is assumed that the process(es)

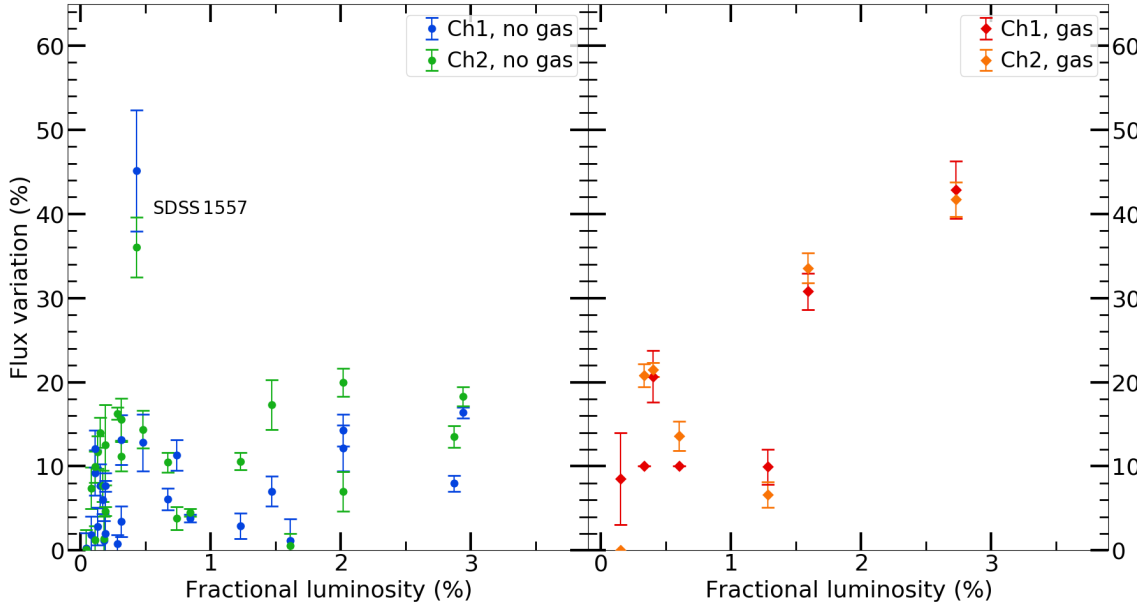

Figure 5.5. The fractional luminosity of known debris disks plotted against the observed flux variation for all stars and those with observed circumstellar gas.

that govern dust production and destruction (and therefore flux variation) occur for all disks in the same overall manner then it may be reasonable to assume that as the observable emitting surface area of a disk increases, the observed flux percentage variation also increases. In Fig. 5.5, the fractional luminosity of stars in the sample is plotted against the observed flux percentage variation. It can be seen that, in general, for stars with no observed circumstellar gas the flux variation does not increase with fractional luminosity (although a shallow positive trend may exist), and remains below 20 per cent. The exception is SDSS 1557, that has a large flux variation due to the close brown dwarf companion, as clearly seen in Fig. 5.5.

For the circumstellar gas subsample, there seems to be a strong correlation between the observable emitting surface area and the flux percentage variation, suggesting that the process(es) that increase the observable emitting surface area and flux variation are related, if these process(es) are common for all disks. It should be noted that as the fluxes of the debris disks (and therefore disk luminosities) vary, so do the fractional luminosities, however, on average these values only change by 0.1 per cent for the entire dusty white dwarf sample, and so this variation does not affect this result.

5.5 Discussion and Conclusions

In this chapter, *Spitzer* and *WISE* observations of a sample of 42 dusty white dwarfs are presented. Due to the increasing number of epochs and temporal baselines, typically more than ten observations over nine years, the flux and colour variation of the debris disks can be probed in more detail. For comparison, a control sample of 31 metal polluted, but non-debris disk hosting white dwarfs were selected. In order to detect as small a variation as possible, differential photometry was conducted on all white dwarfs using five nearby, comparison stars. Flux and colour variability was then determined via three methods; the significance, the Stetson index, and a chi-squared variance test.

Significant Flux Variation seen in the Majority of Dusty White Dwarfs

It was found that at least 67 per cent, and potentially up to 86 per cent, of dusty white dwarfs have bona fide flux variations. This is significantly higher than the frequency of stars in the control sample that exhibit flux variations, indicating that the cause of the flux variations are the circumstellar debris disks. These percentages are similar to those found in a recent study using solely *WISE* channel 1 observations (Swan et al. 2019). The absolute value of variation in both wavelength channels in the dusty white dwarfs is also significantly higher than for the control sample.

Whilst additional observations over a range of cadences are needed in order to fit debris disk variation models it is worth discussing processes that may govern such variations. As mentioned above there are several possible processes that may cause the production, destruction, or movement of circumstellar dust; intra-disk collisions, tidal disruption of additional incoming minor planetary bodies, and PR-drag. These processes are important for both flux and colour variation. Their typical timescales have been discussed in detail in relation to the flux variation at WD 0408−041 (Farihi et al. 2018), but in theory they should apply to all varying debris disks. The collisional cascade of small minor planetary bodies in a disk has been modelled and can theoretically produce a flux increase on the timescale of years (Kenyon & Bromley 2017*b*), however the rate at which the disk would need to be replenished is higher than the typically accretion rate of metals onto the white dwarf atmosphere. The stochastic tidal disruption of additional bodies has been proposed (Wyatt et al. 2014), and may be the solution for the source of additional material, however observational monitoring of flux variation events is needed to constrain any models.

Significant Colour Variation Detected for the First Time

Interestingly, in a pioneering discovery, significant colour variations have been seen in white dwarf debris disks, with it occurring in at least 31 per cent of the disks. For comparison, only one star in the control sample showed a significant colour variation. Therefore, in addition to confirming the presence of significant colour variation in white dwarf planetary debris disks, it seems that disk colour variation is common. To confirm this finding additional *Spitzer* observations are needed as the *WISE* channel 2 observations typically have low S/N and are not sensitive enough to determine colour variations (Swan et al. 2019). Differences in the observed colour may be caused by a significant change in the radial distance, and temperature, of the dust. Such a change could be caused by PR-drag, however in order to undergo this affect dust must be optically thin, and therefore either the debris disk is radially optically thin, or the dust is above or below the plane of a radially optically thick disk. However, it has been shown that destruction of dust via collisional processes occur on timescales an order of magnitude shorter than accretion of the dust onto the star via PR-drag (Farihi et al. 2018). Therefore, interpretation of colour variation is not straight forward and further work is needed.

Empirical Flux Percentage Variation

As well as detecting variability using the three methods outlined above, it is also possible to analyse the debris disks by studying the flux percentage variation as this may provide information about the physical change in the observable emitting surface area of the debris disk. A new metric, the minimum detectable fractional variation, was defined to probe how sensitive *Spitzer* and *WISE* are to variations. In general, *Spitzer* can significantly detect variability below 10 per cent for all stars in the sample, down to below 1 per cent for the highest S/N observations. However, for this study, *WISE* observations can only confidently detect variability in the range 20−60 per cent. This outlines how important *Spitzer* and future, more sensitive, telescopes are to detecting debris disk variability.

Flux Variation in White Dwarfs with Circumstellar Gas

Interestingly, it was found that, with the exception of known close binary SDSS 1557, all dusty white dwarfs with no observed circumstellar gas vary by less than 20 per cent in both channels 1 and 2. Whereas all stars that vary by more than 20 per cent have observed circumstellar gas. Furthermore, by plotting the observed flux percentage variation in

channels 1 and 2 against the fractional luminosity of the disks (which can be used as a proxy for observable emitting surface area), there seems to be a correlation between the flux variation and the fractional luminosity for systems with circumstellar gas. No such correlation was seen in white dwarfs with no circumstellar gas, although a shallow trend may exist. There was also no difference in the colour percentage variation between systems with and without circumstellar gas.

If one assumes that the processes that govern flux variation occur for all disks, conclusions may be drawn by interpreting the relationship between flux variation and fractional luminosity for the entire sample. The observed correlation seems to suggest that as the observable emitting surface area increases so does the observed flux variation. This correlation appears to be stronger for stars with circumstellar gas than those without. Therefore, one can ask; "*is the difference in correlation real?*" And if so, "*can it provide information about the different processes occurring in disks with and without circumstellar gas, if such exist?*" It is worth noting again, that a recent survey found no new gas disks in the current dusty white dwarf sample (Dennihy 2018), and therefore to increase the sample size and potentially answer these questions large infrared photometric surveys are needed to find more debris disks which then need to be followed up to determine if they have circumstellar gas.

It is now well established that the circumstellar environment around white dwarfs is dynamical in nature. From the disappearance of circumstellar gas on year to decade timescales to the seemingly sporadic creation, destruction, and possible movement of dust on varying timescales it is clear that the evolution of these disks is worthy of further research. It is important to understand what processes govern the varying nature of these disks. If the cause of the flux variation is due to additional asteroid accretion events then a lot can be learnt about the dynamical nature of minor planetary bodies in white dwarf systems, including what will occur in the end state of the Solar System. If, on the other hand, the flux variations are caused by intra-disk processes then knowledge could be gained by drawing parallels to other disk and ring systems around planets and main sequence stars as these are known to be dynamical in nature as well. Therefore, study of the evolution of the planetary debris disk after the destruction of a minor planetary body can help bring insight into planetary systems in general.

Table 5.2. The infrared flux and colour variation at 3.6 and 4.5 μm for all dusty white dwarfs in the sample with an infrared excess at these wavelengths.

WD Name	Name	Ch1 (σ)	Ch2 (σ)	Ch2 / Ch1 (σ)
0106−328	HE 0106−3253	2.76±0.17	3.00±0.02	0.83±0.43
0110−565	HE 0110−5630	2.92±0.03	7.90±0.02	2.01±0.04
0146+187	GD 16	6.91±0.05	6.41±0.03	2.68±0.04
0246+734	EGGR 474	5.79±0.12	16.28±0.27	2.81±1.17
0300−013	GD 40	1.87±0.02	6.49±0.02	3.06±0.03
0307+077		1.02±0.30	4.46±0.45	2.91±0.79
0408−041	GD 56	25.87±0.01	16.11±0.01	5.34±0.02
0420+520		2.96±0.06	0.76±0.09	0.84±0.33
0420−731		7.47±0.05	0.86±0.22	0.68±0.47
0435+410	GD 61	4.18±0.06	22.14±0.01	8.77±0.02
0539−479		2.84±0.08	0.66±0.32	0.58±0.53
0735+187[a]	SDSS J0738	14.74±0.02	19.47±0.02	4.17±3.64
0842+231[a]	Ton 345	1.55±0.06	7.72±0.02	1.81±0.55
0842+572	SDSS J0846	2.35±0.07	1.00±0.18	1.20±0.36
0843+516		1.28±0.02	6.19±0.02	5.14±0.04
0956−017[a]	SDSS J0959	15.24±0.03	21.83±0.02	0.70±0.06
1015+161		3.67±0.02	4.33±0.02	1.30±0.50
1018+410		3.48±0.03	5.34±0.02	0.96±0.57
1041+091[a]		5.00±0.27	6.25±0.92	1.37±0.08
1116+026	GD 133	5.08±0.07	6.46±0.02	1.19±0.42
1141+057[a]	SDSS J1144	5.71±0.12	1.92±0.60	1.87±0.74
1145+017[b]		3.32±0.25	3.64±0.11	1.99±0.73
1145+288	SDSS J1147	1.06±0.33	2.74±0.26	0.91±0.66
1150−153		4.50±0.03	2.97±0.02	1.96±0.06
1219+130	SDSS J1221	3.20±0.06	3.31±0.21	2.41±0.91
1226+110[a]	SDSS J1228	21.33±0.01	27.19±0.01	2.15±0.02
1232+563		5.37±0.04	4.93±0.02	2.01±0.89
1349−230[a]	HE 1349−2305	2.25±0.20	15.78±0.01	1.13±0.55
1457−086		1.19±0.25	6.32±0.15	1.41±0.67
1536+520	SDSS J1537	0.86±0.15	1.02±0.20	0.51±0.54
1541+650		5.06±0.05	10.63±0.01	4.16±0.03
1551+175		11.05±0.08	8.62±0.33	1.24±0.12
SDSS 1557	SDSS J1557	12.88±0.15	10.72±0.03	3.67±0.09
1615+164[a]	SDSS J1617	4.83±0.02	4.45±0.01	1.30±0.03
1729+371	GD 362	19.29±0.01	13.81±0.01	7.42±0.02
1929+011	GALEX 1931	11.89±0.01	8.80±0.01	3.51±0.01
2115−560	GJ 4191	8.55±0.01	10.01±0.01	3.03±0.01
2132+096		5.55±0.02	4.62±0.37	4.03±0.03
2207+121	SDSS J2209	6.36±0.02	5.89±0.17	3.32±0.03
2221−165	HE 2221−1630	4.71±0.01	9.19±0.01	2.57±0.02
2326+049	G 29−38	8.42±0.01	10.36±0.01	7.22±0.03
2329+407	EGGR 160	7.05±0.04	4.73±0.05	1.60±0.24

Notes. [a] Circumstellar gas observed Ca II triplet emission.
[b] Circumstellar gas observed via absorption features.

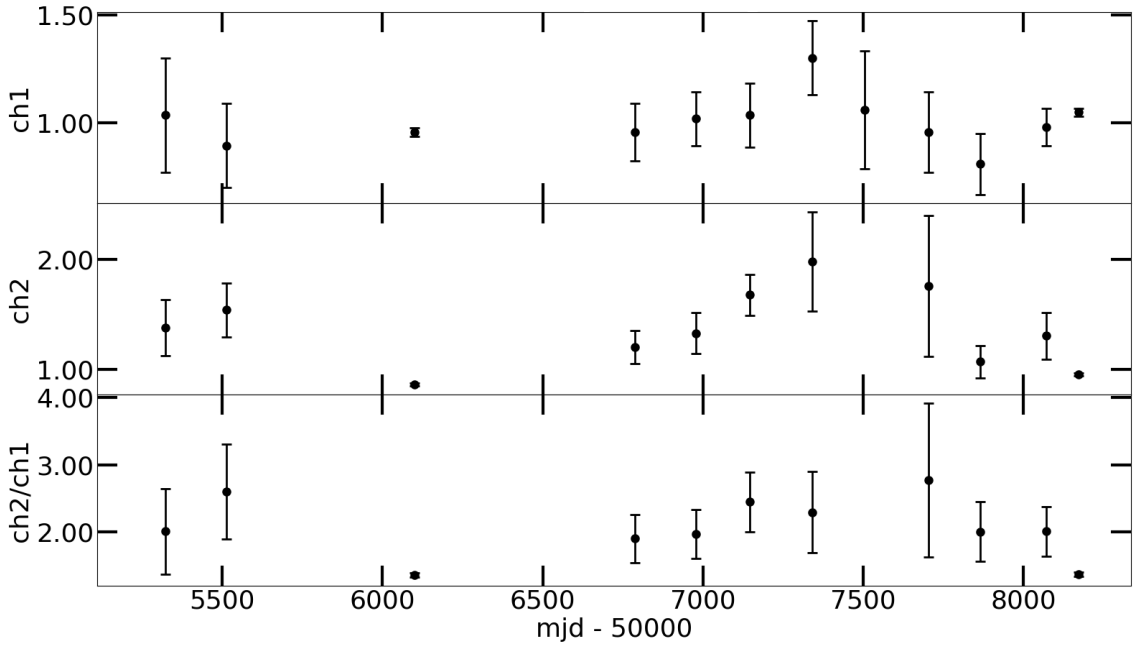

Figure 5.6. The *Spitzer* and *WISE* combined normalised light curve of the dusty white dwarf WD 1018+410 showing: (top panel) the channel 1 fluxes; (middle panel) the channel 2 fluxes; and (bottom panel) the colours.

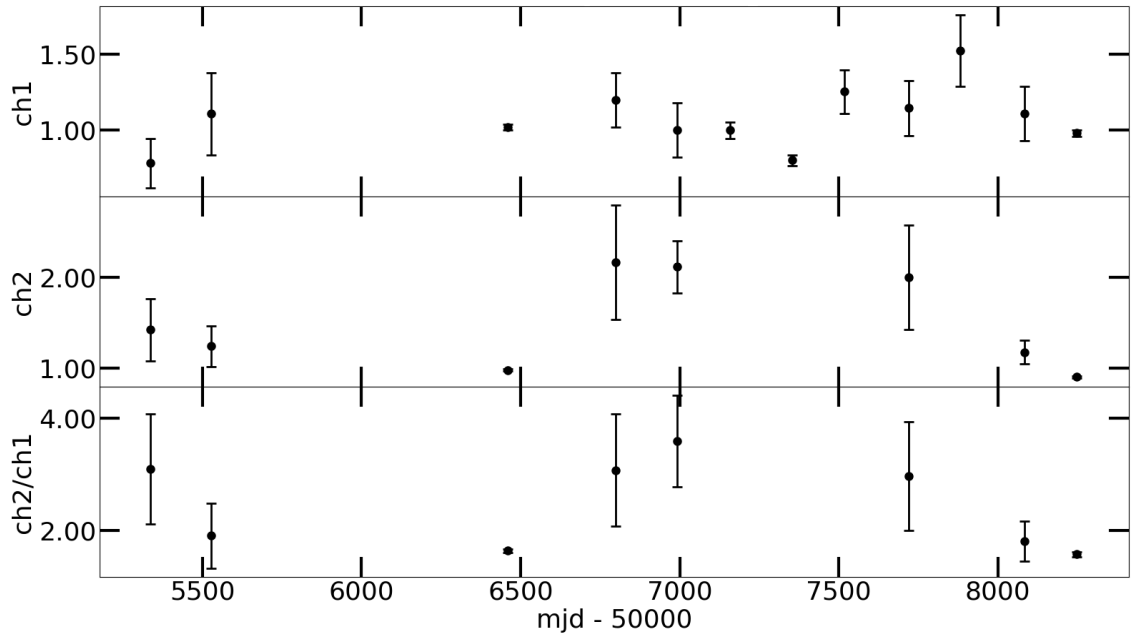

Figure 5.7. The *Spitzer* and *WISE* combined normalised light curve of the dusty white dwarf WD 1232+563 showing: (top panel) the channel 1 fluxes; (middle panel) the channel 2 fluxes; and (bottom panel) the colours.

Table 5.3. The infrared flux and colour variation at 3.6 and 4.5 μm for the polluted white dwarf control sample.

WD Name	Name	Ch1 (σ)	Ch2 (σ)	Ch2 / Ch1 (σ)
0046+051		0.11±0.10	0.72±0.03	1.92±0.98
0208+396		0.19±0.12	0.65±0.07	4.81±0.63
0243−026		0.01±0.18	1.06±0.25	2.03±0.49
0245+541		0.60±0.06	0.58±0.10	1.89±0.09
0322−019		3.07±0.10	3.04±0.30	1.73±0.26
0552−041		0.31±0.08	0.29±0.05	1.26±0.10
0738−172		3.08±0.03	3.17±0.08	2.19±0.08
0802+386		0.13±0.24	0.44±0.09	1.34±0.57
0816−310		0.21±0.35	0.41±0.01	2.70±0.72
0840−136		0.06±0.09	1.30±0.01	1.89±0.26
0843+358		0.04±0.15	0.12±0.02	0.87±0.42
0953+594		3.18±0.22	1.14±0.09	0.93±0.50
1202−232		3.03±0.14	3.70±0.07	1.23±0.43
1208+576		0.60±0.22	0.52±0.03	0.95±0.17
1212−022		0.42±0.25	0.36±0.25	2.54±0.89
1257+278		0.28±0.01	3.02±0.02	2.82±0.02
1311+578		0.35±0.28	0.61±0.39	1.85±0.77
1328+307		0.47±0.29	3.62±0.02	1.67±0.45
1349+431		0.11±0.32	1.55±0.06	0.96±0.37
1532+129		3.10±0.01	3.08±0.02	0.51±0.35
1626+368		3.12±0.08	3.82±0.01	1.62±0.50
1632+177		3.08±0.19	3.20±0.13	2.36±0.33
1633+433		3.27±0.19	1.13±0.01	1.26±0.26
1653+385		0.26±0.18	0.68±0.02	0.55±0.47
1705+030		0.15±0.71	0.54±0.01	0.45±0.18
2105−820		3.02±0.27	3.53±0.15	0.89±0.38
2216−657		3.06±0.55	3.04±0.01	2.01±0.56
2251−070		0.05±0.49	0.55±0.05	2.16±0.28
2312−024		3.10±0.22	3.18±0.06	2.82±0.30
2322+118		0.11±0.13	0.47±0.04	1.27±0.49
2345−447		3.17±0.33	3.15±0.04	2.32±0.48

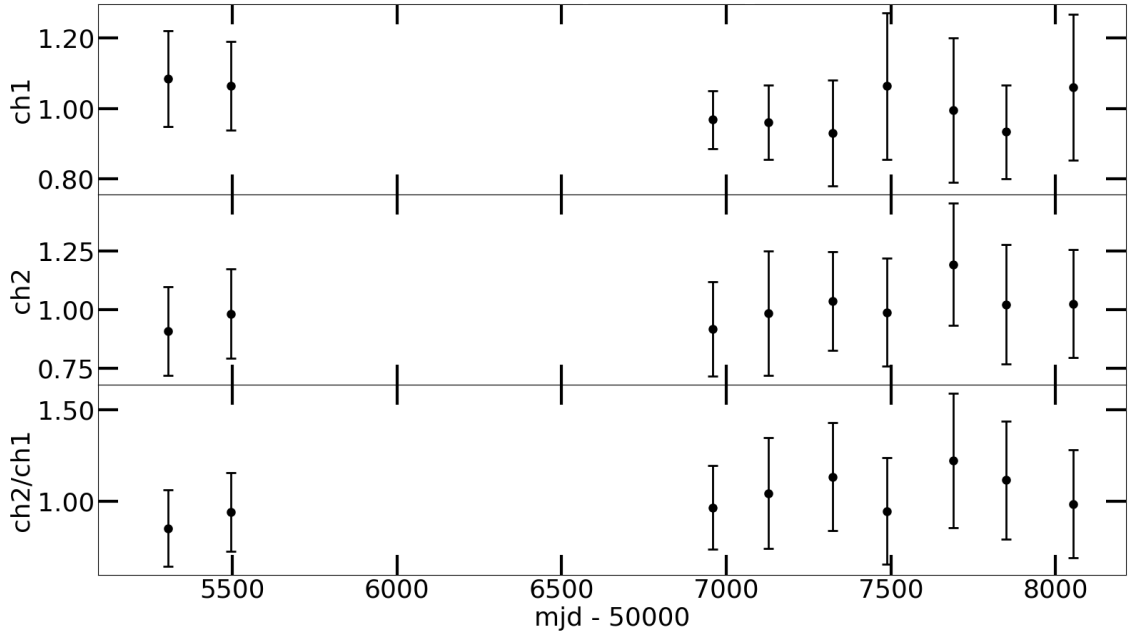

Figure 5.8. The *Spitzer* and *WISE* combined normalised light curve of the control white dwarf WD 0843+358 showing: (top panel) the channel 1 fluxes; (middle panel) the channel 2 fluxes; and (bottom panel) the colours.

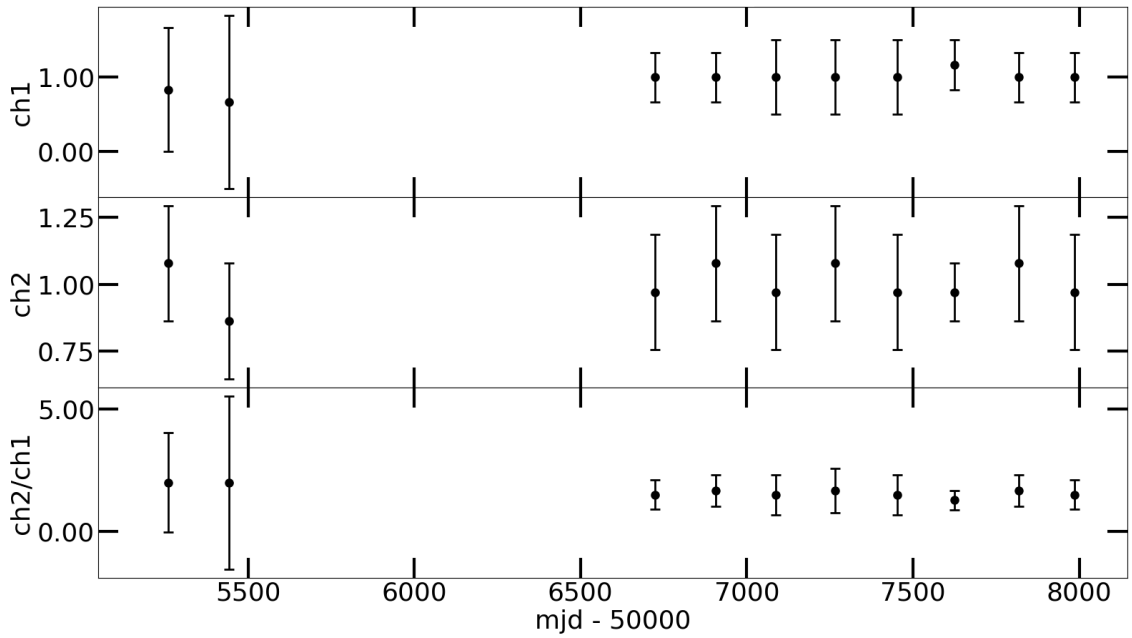

Figure 5.9. The *Spitzer* and *WISE* combined normalised light curve of the control white dwarf WD 1705+030 showing: (top panel) the channel 1 fluxes; (middle panel) the channel 2 fluxes; and (bottom panel) the colours.

Chapter 6

Conclusions

Equipped with his five senses, man explores the universe around him and calls the adventure Science.

Edwin Powell Hubble (1929)

This thesis presents work into the formation, evolution, and destruction of minor planetary bodies in both the Solar System and exoplanetary systems around white dwarf stars. In the search for a holistic picture of the nature of planetary bodies during every stage of their lifetimes it is important, and indeed necessary, to tie knowledge gained from Solar System research to exoplanetary system studies, and vice versa. For example, by studying Solar System comets, one could determine the molecular abundances and conditions of the nascent Solar System protoplanetary disk, which can be compared to submillimetre observations of molecules in exoprotoplanetary disks. However, when doing these comparisons it is important to know what cometary observations are indeed indicative of the early Solar System, and how the evolutionary processes of comets may change the composition relative to the protoplanetary disk. On the other hand, observations of the destruction of minor planetary bodies as they are gravitationally perturbed beyond the Roche limit of their host stars greatly benefits from the understanding of planetary dynamics honed from observations of Solar System planets, comets, and asteroids. Furthermore, research into the destruction, and subsequent debris disk evolution, of minor planetary bodies provides

insight into the ultimate fate of Solar System asteroids following the giant phases of the Sun. Therefore, research focused on both the Solar System and exoplanetary systems can help shed light on a greater understanding of the formation, evolution, and destruction of minor planetary bodies.

Chapter 2

In Chapter 2, a combined chemical and physical model that simulates the collapse of a molecular cloud into the formation of a proto-Solar and protoplanetary disk was used to probe the O_2/H_2O, N_2/H_2O, N_2/CO, and CO/H_2O ratios seen in the coma of comet 67P. Under the assumption that the molecular abundance ratios have remained unchanged since comet formation in the protoplanetary disk and by tracking the physical conditions and molecular abundances throughout the collapse model to the protoplanetary disk phase, the initial physical and chemical conditions of the pre-Solar System molecular cloud were inferred. It was found that a broad range of conditions such as final temperature and density, free-fall collapse retardation rate, and cosmic ray ionisation rate can reproduce the O_2/H_2O and CO/H_2O ratios seen in 67P. This result suggests that a primordial origin of these molecules is possible and such analysis permits the study of the nascent Solar System using cometary molecules as a tracer. For N_2/H_2O and N_2/CO, the best-fit scenario of low collapse retardation and cosmic ray ionisation rates over-estimates these ratios. However, it is possible that 67P has a non-typical nitrogen abundance as other comets and TNOs have been observed to have a significantly higher abundance.

Interestingly, upon passing a density threshold during the collapse, the freeze out of molecules produced via gas-phase chemistry occurred rapidly due to the higher extinction and low temperatures reducing the desorption rate and allowing ices to form. Another main finding of this study is that it is possible to determine the history of the abundances of the molecules in the collapse phase. It was found that during the collapse phase there are strong transient peaks in the molecular abundances that typically occur when the threshold density mentioned above has been reached. Therefore, the molecules are frozen out and retained as ices due to low desorption rates which means that the final solid-phase abundances can reveal information about the abundance of the molecules in the gas-phase. Additionally, as the freeze out of molecules results in stratified ices, the layers of the ices encode information about the specific gas-phase abundance of the molecules at the time of freeze out. Therefore, the molecular abundances in the ices can reveal the chemical

evolution of the collapse of the molecular cloud.

It has been shown that, by using a physical and chemical Solar System formation model, the molecular abundances observed in cometary comae can reveal information of both the initial conditions of the early Solar System and the physical and chemical evolution during the formation of the proto-Solar and protoplanetary disk. Therefore, in future work this analysis could be conducted for a larger sample of comets and for comets from different dynamical families in order to constrain the formation conditions of minor planetary bodies in the Solar System.

Chapter 3

In Chapter 3, *Herschel* SPIRE spectroscopic observations of comets Hartley 2, Tempel 2, 45P, and C/2009 P1 were analysed in order to study H_2O in their comae. A radiative transfer model, CRETE, was, in part, developed (De Val-Borro & Wilson 2016) and utilised to interpret the submillimetre rotational line emission of ortho- and para-H_2O. Whilst, the derived H_2O production rates for all comets agree with previous observations, non-typical H_2O OPRs were determined for three comets. It had previously been proposed that the OPR could be used as a proxy for cometary formation temperature and therefore radial location from the Sun, however recent laboratory experiments have shown that during comet formation the OPR is normalised to the statistical equilibrium (Hama et al. 2016). By comparing the comae OPR determined in this study to literature values of observations of comet nuclei a potential dependence on the nucleocentric distance may be seen. This suggests that OPR variation could be indicative of processes in the comae, however it has been noted that the typical densities observed are not high enough to cause OPR changes via collisional processes (Mumma et al. 1987). Therefore, the interpretation of these non-typical OPR is challenging.

Future observations of ortho- and para-H_2O at a range of nucleocentric distances, as well as further laboratory studies and theoretical work, are needed in order to shed more light on these results. As noted previously, the OPR was used to probe comet formation, with further research this ratio may be useful in understanding cometary evolution.

Chapter 4

In Chapter 4, the largest, double-blind, unbiased survey of hydrogen rich atmosphere white dwarfs studied to determine the frequency of circumstellar planetary debris disks is

presented. *Spitzer* IRAC photometric observations of 236 stars were analysed via flux and colour methods in order to determine infrared excesses that are indicative of dust disks. A subsample of 168 stars were observed with *HST* COS in order to search for atmospheric metals that would infer the presence of an accreting debris disk. For the single star sample, it was found that whilst 45±4 per cent of white dwarfs have atmospheric metals, only $1.5^{+1.5}_{-0.5}$ per cent have a significant infrared excess. In the study, 22 stars are in spatially-resolved binaries and were analysed for the presence or absence of a debris disk. For the first time, the unbiased debris disk frequency of wide binary systems is reported, and it agrees with the single star sample. Interestingly, using *Gaia* data it was found that the binary fraction of metal polluted white dwarfs is the same as field degenerates, however no white dwarf with a circumstellar debris disk has a binary companion. Therefore, it seems that there is no connection between the binarity of a white dwarf and if it exhibits atmospheric metals or a circumstellar disk. This means that the main driver of the perturbation of minor planetary bodies beyond the Roche limit of the host star is likely to be a planet(s).

The main finding of this study confirms previous findings of studies with smaller and biased samples, that the vast majority of white dwarfs with planetary systems, as detected via accreted metals, do not have observable infrared excesses. Future observations using more sensitive facilities are needed to determine whether or not these systems are void of optically thick disks or if they are simply below current sensitivity limits. The answer to this question is important in understanding the nature of the destruction of minor planetary bodies.

Chapter 5

In Chapter 5, a study of the infrared photometry of all known planetary debris disk hosting white dwarfs over the longest timescales to date is reported. *Spitzer* and *WISE* observations of 42 degenerates were analysed in order to determine any potential flux or colour variation. In order to probe as small a variation as possible differential photometry was conducted on each target which was analysed using three methods in order to confidently detect variation; the significance, the Stetson index, and a chi-squared variance test. For comparison, a control sample of 31 metal polluted white dwarfs with no observable debris disk in the infrared were analysed in the same manner. It was found that majority of planetary debris disks are varying at both wavelength channels used; at least 67 per cent

and 71 per cent, whereas for the control sample only 10−39 per cent show flux variations. For the first time, it was shown that debris disks around white dwarfs significantly vary in colour with at least 31 per cent exhibiting such a variation. There are multiple proposed processes that could cause flux variation, such as tidal disruption, collisional cascades, and PR-drag, however to properly constrain models further observations at a shorter cadence are needed. The observed colour variation is difficult to interpret as the method that could cause it, PR-drag, has been shown to act on timescales an order of magnitude longer than collisional, destruction processes. Therefore, further theoretical work is also needed to understand this result.

An additional, interesting finding is that by studying the flux percentage variation, it can be seen that only white dwarfs with circumstellar gas, typically observed via Ca II triplet emission, vary by more than 20 per cent. If it is assumed that the variation processes ongoing at the majority disks are occurring in the same manner then this difference could potentially inform circumstellar gas generation methods.

Future Work

From the work presented in this thesis there are several avenues that could be explored to further the study of the formation, evolution, and destruction of minor planetary bodies. First, on the topic of comet formation, it would be interesting to see if the physical and chemical initial conditions needed to produce the molecular abundances ratios observed in comets of different families are the same or different. Using the model presented in Chapter 2, future work could be conducted to study this for a larger sample of comets that could provide a better understanding of the conditions in the nascent Solar System. On the study of cometary OPRs as a probe of evolutionary processes ongoing in cometary comae, there are multiple projects that could be undertaken. From an observational perspective, the determination of OPR values at a range of nucleocentric distances for a single comet (for example, using *Rosetta* data of comet 67P or a future rendezvous mission of another comet) is important as it could confirm or refute the apparent dependency of OPR with distance seen in Chapter 3. Laboratory studies, such as those conducted in Hama et al. 2016, should be continued with an emphasis on reproducing the collisional environment in the cometary comae in order to probe potential nuclear-spin conversion mechanisms that could cause the observed non-typical OPR values. Finally, theoretical work, potentially informed by the aforementioned observational future project, should be

done to find viable nuclear-spin conversion processes that could occur in the collisionless environment of the outer coma.

On the destruction of minor planetary bodies, from work reported in Chapter 4, it is apparent that the vast majority of polluted white dwarfs do not exhibit a debris disk observable in the infrared. The cause of this dearth is still unknown, but it has been proposed that the lack of infrared flux is due to either narrow dust rings or completely gaseous disks. Utilising future, more sensitive facilities, observational studies may be able to determine between these possibilities. It has been shown in Chapter 4 that in white dwarf binary systems, the companion does not appear to have a major role in the pollution of the central degenerate. To date, there are no theoretical dynamical models of the pollution of a white dwarf in a binary that does not invoke the gravitational perturbation of a planetary body by the companion star. Therefore, future work could be conducted to see if the dynamical models of planetary bodies around a single star are applicable to white dwarfs in wide binaries, and if they can reproduce the observed frequency of atmospheric metals.

Finally, for white dwarfs with a known debris disk observable in the infrared, it has been seen that the majority of these disks vary in flux. Whilst multiple mechanisms have been proposed to explain the flux variation, the true cause is still unknown. A detailed, shorter cadence observing campaign should be conducted in order to better constrain the timescales of the observed brightening and dimming events, that could subsequently be modelled to determine the likely ongoing processes. Furthermore, in Chapter 5, there appears to be an interesting correlation between the percentage of flux variation and the presence of circumstellar gas. The process(es) governing the production and destruction of the gas in these systems is not known and this tentative link provides a potential connection between methods of flux variation and gas generation. For example, as flux variation is due to a changing of the dust emitting surface area a potential dust destruction or creation mechanism could produce the observed gas. Any observing campaign to study flux variation should focus on these systems with concurrent (or semi-concurrent) infrared photometric and optical spectroscopic observations being taken to track the dust and gas in the systems over several epochs. Interestingly, in Chapter 5, colour variation of debris disks is seen for the first time. This is likely due to changes in the dust temperature or location, however as debris disk variation is a burgeoning area of research both further observational and theoretical work is needed to understand the evolution of planetary

debris disks around white dwarf stars.

The work presented in this thesis has contributed in advancing the knowledge of both Solar System science and exoplanetary studies, and therefore, taken together, helps in understanding the overall picture of the nature of minor planetary bodies.

This page was intentionally left blank

Appendix A

Complete Proto-Solar/Protoplanetary Formation Model Results

Presented here are the results of the physical and chemical collapse model reported in Chapter 2 for all combinations of parameters in the ranges: $B = 0.1{-}1.0$, $n_{\rm III} = 10^7{-}10^{11}\,{\rm cm}^{-3}$, $T_{\rm III} = 10{-}20\,{\rm K}$, $\zeta/\zeta_0 = 0.1{-}10.0$, where $\zeta_0 = 1.3 \times 10^{-17}\ {\rm s}^{-1}$, and $G/G_0 = 0.5{-}10.0$. *** represents abundance ratios $\geq 10^4$.

Table A.1: Full results from the model. The abundance ratios in the ice for each molecular pair are reported at two times: (a) at the end of the collapse phase (Phase II) and (b) 10^8 years into the final steady-state phase (Phase III).

B	n_{III} (cm^{-3})	T_{III} (K)	ζ/ζ_0	G/G_0	O_2/H_2O (per cent)		N_2/H_2O (per cent)		N_2/CO (per cent)		CO/H_2O (per cent)	
					a	b	a	b	a	b	a	b
0.1	10^7	10	0.1	0.5	3.14	3.12	3.76	3.73	2.69	2.72	139.73	137.25
				1.0	3.14	3.09	4.31	4.28	3.08	3.12	139.78	137.30
				5.0	3.08	3.07	6.05	6.00	4.32	4.37	139.83	137.35
				10.0	3.09	3.07	6.88	6.83	4.92	4.97	139.86	137.37
			1.0	0.5	2.86	2.03	10.63	6.50	10.78	24.38	98.60	26.65
				1.0	2.89	2.03	10.44	6.32	10.28	23.26	101.59	27.18
				5.0	2.94	2.03	10.42	6.20	9.68	21.72	107.68	28.55
				10.0	2.96	2.03	10.53	6.23	9.65	21.71	109.16	28.72
			10.0	0.5	0.60	0.17	4.47	0.00	2209.61	7.17	0.20	0.02
				1.0	0.65	0.18	4.70	0.00	1982.27	7.01	0.24	0.02
				5.0	0.75	0.21	5.23	0.00	1307.83	7.46	0.40	0.02
				10.0	0.78	0.22	5.57	0.00	946.19	7.81	0.59	0.02
		20	0.1	0.5	3.74	3.73	5.66	5.64	4.00	4.03	141.59	139.85
				1.0	3.72	3.71	6.49	6.46	4.58	4.62	141.72	139.97
				5.0	3.71	3.70	8.93	8.90	6.30	6.35	141.87	140.12

Table A.1 – continued from previous page

B	n_{III} (cm^{-3})	T_{III} (K)	ζ/ζ_0	G/G_0	O_2/H_2O (per cent)		N_2/H_2O (per cent)		N_2/CO (per cent)		CO/H_2O (per cent)	
					a	b	a	b	a	b	a	b
				10.0	3.71	3.71	10.08	10.04	7.10	7.16	141.90	140.15
			1.0	0.5	3.20	2.42	11.53	7.57	11.76	20.63	98.09	36.70
				1.0	3.30	2.47	11.57	7.53	11.40	19.95	101.52	37.76
				5.0	3.46	2.55	12.05	7.71	11.13	19.37	108.32	39.79
				10.0	3.51	2.57	12.38	7.89	11.22	19.47	110.31	40.51
			10.0	0.5	0.31	0.10	3.97	0.00	2693.28	1.70	0.15	0.03
				1.0	0.37	0.11	4.24	0.00	2226.05	1.78	0.19	0.03
				5.0	0.51	0.15	4.89	0.00	1263.78	1.98	0.39	0.03
				10.0	0.56	0.17	5.27	0.00	912.88	2.03	0.58	0.03
	10^8	10	0.1	0.5	3.14	3.15	3.76	3.77	2.69	2.70	139.82	139.75
				1.0	3.11	3.12	4.31	4.33	3.08	3.10	139.88	139.81
				5.0	3.08	3.10	6.05	6.07	4.32	4.34	139.93	139.86
				10.0	3.09	3.10	6.88	6.91	4.92	4.94	139.95	139.89
			1.0	0.5	2.90	2.84	10.82	10.42	10.59	12.04	102.11	86.58
				1.0	2.94	2.87	10.64	10.23	10.09	11.45	105.40	89.35
				5.0	2.99	2.91	10.60	10.16	9.52	10.77	111.42	94.33

Table A.1 – continued from previous page

B	n_{III} (cm^{-3})	T_{III} (K)	ζ/ζ_0	G/G_0	O_2/H_2O (per cent)		N_2/H_2O (per cent)		N_2/CO (per cent)		CO/H_2O (per cent)	
					a	b	a	b	a	b	a	b
				10.0	3.01	2.93	10.74	10.28	9.47	10.71	113.39	95.97
			10.0	0.5	0.62	0.54	6.08	1.00	567.57	9386.68	1.07	0.01
				1.0	0.67	0.59	6.42	1.05	497.93	8934.68	1.29	0.01
				5.0	0.78	0.69	7.07	1.17	313.42	8790.01	2.25	0.01
				10.0	0.81	0.71	7.35	1.22	229.28	8869.56	3.20	0.01
		20	0.1	0.5	3.74	3.76	5.66	5.69	4.00	4.01	141.65	141.67
				1.0	3.72	3.74	6.49	6.52	4.58	4.60	141.78	141.80
				5.0	3.71	3.73	8.93	8.97	6.29	6.32	141.94	141.96
				10.0	3.72	3.73	10.08	10.13	7.10	7.13	141.97	141.99
			1.0	0.5	3.23	3.24	11.69	11.49	11.62	12.86	100.58	89.39
				1.0	3.34	3.33	11.74	11.53	11.26	12.44	104.25	92.64
				5.0	3.50	3.49	12.22	11.96	11.00	12.12	111.06	98.70
				10.0	3.55	3.54	12.57	12.29	11.08	12.20	113.41	100.78
			10.0	0.5	0.32	0.28	5.35	0.90	1260.10	7207.89	0.42	0.01
				1.0	0.38	0.34	5.73	0.97	982.74	7258.59	0.58	0.01
				5.0	0.52	0.46	6.56	1.12	517.67	7680.58	1.27	0.01

Table A.1 – continued from previous page

B	n_{III} (cm^{-3})	T_{III} (K)	ζ/ζ_0	G/G_0	O_2/H_2O (per cent)		N_2/H_2O (per cent)		N_2/CO (per cent)		CO/H_2O (per cent)	
					a	b	a	b	a	b	a	b
				10.0	0.58	0.51	6.89	1.17	389.32	7738.88	1.77	0.02
	10^9	10	0.1	0.5	3.14	3.15	3.76	3.78	2.69	2.70	139.83	140.01
				1.0	3.11	3.13	4.31	4.34	3.08	3.10	139.89	140.07
				5.0	3.08	3.10	6.05	6.08	4.32	4.34	139.94	140.12
				10.0	3.09	3.10	6.88	6.92	4.92	4.94	139.96	140.14
			1.0	0.5	2.90	3.03	10.84	11.31	10.57	11.21	102.50	100.89
				1.0	2.94	3.07	10.66	11.12	10.08	10.67	105.82	104.31
				5.0	2.99	3.13	10.62	11.09	9.50	10.03	111.84	110.48
				10.0	3.02	3.15	10.77	11.23	9.45	9.98	113.86	112.55
			10.0	0.5	0.62	0.62	6.34	5.31	481.25	***	1.32	0.00
				1.0	0.68	0.68	6.70	5.62	420.24	***	1.59	0.00
				5.0	0.79	0.80	7.37	6.26	255.28	***	2.89	0.00
				10.0	0.82	0.84	7.65	6.56	193.22	***	3.96	0.00
		20	0.1	0.5	3.74	3.76	5.66	5.69	4.00	4.01	141.66	141.86
				1.0	3.72	3.74	6.49	6.52	4.58	4.59	141.79	143.42
				5.0	3.71	3.73	8.93	8.89	6.29	6.32	141.94	142.15

Table A.1 – continued from previous page

B	n_{III} (cm^{-3})	T_{III} (K)	ζ/ζ_0	G/G_0	O_2/H_2O (per cent)		N_2/H_2O (per cent)		N_2/CO (per cent)		CO/H_2O (per cent)	
					a	b	a	b	a	b	a	b
				10.0	3.72	3.73	10.08	10.14	7.10	7.13	141.98	142.18
			1.0	0.5	3.24	3.39	11.70	12.24	11.61	12.28	100.85	99.68
				1.0	3.34	3.50	11.76	12.30	11.25	11.88	104.54	103.50
				5.0	3.51	3.67	12.23	12.80	10.99	11.58	111.36	110.56
				10.0	3.56	3.73	12.59	13.17	11.07	11.65	113.75	113.04
			10.0	0.5	0.32	0.32	5.56	4.65	1147.94	***	0.48	0.00
				1.0	0.39	0.38	5.96	4.99	897.40	***	0.66	0.00
				5.0	0.53	0.53	6.83	5.75	469.38	***	1.46	0.00
				10.0	0.58	0.59	7.14	6.05	351.49	***	2.03	0.00
	10^{10}	10	0.1	0.5	3.14	3.15	3.76	3.78	2.69	2.70	139.83	140.04
				1.0	3.11	3.13	4.31	4.34	3.08	3.09	139.89	140.09
				5.0	3.08	3.10	6.05	6.08	4.32	4.34	139.94	140.15
				10.0	3.09	3.10	6.88	6.92	4.92	4.94	139.96	140.17
			1.0	0.5	2.90	3.06	10.84	11.41	10.57	11.13	102.54	102.48
				1.0	2.94	3.10	10.66	11.23	10.07	10.59	105.87	105.98
				5.0	2.99	3.15	10.63	11.19	9.50	9.96	111.93	112.31

Table A.1 – continued from previous page

B	n_{III} (cm^{-3})	T_{III} (K)	ζ/ζ_0	G/G_0	O_2/H_2O (per cent)		N_2/H_2O (per cent)		N_2/CO (per cent)		CO/H_2O (per cent)	
					a	b	a	b	a	b	a	b
				10.0	3.02	3.18	10.77	11.34	9.45	9.50	113.91	114.44
			10.0	0.5	0.62	0.63	6.37	6.34	473.92	***	1.34	0.00
				1.0	0.68	0.69	6.73	6.71	414.64	***	1.62	0.00
				5.0	0.79	0.81	7.40	7.48	252.64	***	2.93	0.00
				10.0	0.82	0.85	7.68	7.85	190.08	***	4.04	0.00
		20	0.1	0.5	3.74	3.76	5.66	5.69	4.00	4.01	141.66	141.88
				1.0	3.72	3.74	6.49	6.52	4.58	4.59	141.79	142.01
				5.0	3.71	3.73	8.93	8.98	6.29	6.32	141.95	142.17
				10.0	3.72	3.74	10.08	10.14	7.10	7.13	141.98	142.20
			1.0	0.5	3.24	3.41	11.71	12.33	11.60	12.23	100.88	100.79
				1.0	3.34	3.52	11.76	12.39	11.25	11.83	104.57	104.68
				5.0	3.51	3.70	12.24	12.89	10.99	11.53	111.39	111.86
				10.0	3.56	3.75	12.59	13.27	11.07	11.60	113.78	114.38
			10.0	0.5	0.32	0.32	5.59	5.51	1141.02	***	0.49	0.00
				1.0	0.39	0.39	5.99	5.92	891.09	***	0.67	0.00
				5.0	0.53	0.53	6.86	6.83	464.16	***	1.48	0.00

Table A.1 – continued from previous page

B	n_{III} (cm^{-3})	T_{III} (K)	ζ/ζ_0	G/G_0	O_2/H_2O (per cent)		N_2/H_2O (per cent)		N_2/CO (per cent)		CO/H_2O (per cent)	
					a	b	a	b	a	b	a	b
				10.0	0.58	0.60	7.17	7.19	347.50	***	2.06	0.00
	10^{11}	10	0.1	0.5	3.14	3.15	3.76	3.78	2.69	2.70	139.83	140.04
				1.0	3.11	3.13	4.31	4.34	3.08	3.09	139.89	140.10
				5.0	3.08	3.10	6.05	6.08	4.32	4.34	139.94	140.15
				10.0	3.09	3.10	6.88	6.92	4.92	4.94	139.96	140.17
			1.0	0.5	2.90	3.06	10.84	11.42	10.57	11.13	102.54	102.65
				1.0	2.94	3.10	10.66	11.24	10.07	10.59	105.87	106.16
				5.0	2.99	3.16	10.63	11.20	9.50	9.96	111.89	112.50
				10.0	3.02	3.18	10.77	11.35	9.45	9.90	113.91	114.63
			10.0	0.5	0.62	0.63	6.37	6.45	472.87	***	1.35	0.00
				1.0	0.68	0.69	6.73	6.83	413.02	***	1.63	0.00
				5.0	0.79	0.81	7.41	7.62	252.27	***	2.94	0.00
				10.0	0.82	0.85	7.68	7.99	189.46	***	4.05	0.00
		20	0.1	0.5	3.74	3.76	5.66	5.69	4.00	4.01	141.66	141.88
				1.0	3.72	3.74	6.49	6.52	4.58	4.59	141.79	142.01
				5.0	3.71	3.73	8.93	8.98	6.29	6.32	141.95	142.17

Table A.1 – continued from previous page

B	n_{III} (cm^{-3})	T_{III} (K)	ζ/ζ_0	G/G_0	O_2/H_2O (per cent)		N_2/H_2O (per cent)		N_2/CO (per cent)		CO/H_2O (per cent)	
					a	b	a	b	a	b	a	b
				10.0	3.72	3.74	10.08	10.14	7.10	7.13	141.98	142.20
			1.0	0.5	3.24	3.41	11.71	12.33	11.60	12.22	100.88	100.91
				1.0	3.34	3.52	11.76	12.39	11.24	11.83	104.58	104.80
				5.0	3.51	3.70	12.24	12.90	10.99	11.52	111.39	111.99
				10.0	3.56	3.75	12.59	13.28	11.07	11.60	113.78	114.51
			10.0	0.5	0.32	0.33	5.59	5.61	1135.48	***	0.49	0.00
				1.0	0.39	0.39	5.99	6.02	889.99	***	0.67	0.00
				5.0	0.53	0.54	6.86	6.95	464.36	***	1.48	0.00
				10.0	0.58	0.60	7.17	7.31	349.99	***	2.05	0.00
1.0	10^7	10	0.1	0.5	0.80	0.80	6.80	6.76	5.43	5.49	125.20	123.05
				1.0	0.80	0.80	7.77	7.72	6.20	6.27	125.36	123.20
				5.0	0.81	0.80	9.93	9.87	7.92	8.02	125.28	123.13
				10.0	0.80	0.80	10.72	10.66	8.58	8.67	125.04	122.89
			1.0	0.5	1.89	1.24	8.87	5.05	7.12	15.70	124.70	32.16
				1.0	1.78	1.17	9.68	5.52	7.80	17.23	124.02	32.02
				5.0	1.55	1.03	11.53	6.60	9.45	20.92	122.00	31.56

Table A.1 – continued from previous page

B	n_{III} (cm^{-3})	T_{III} (K)	ζ/ζ_0	G/G_0	O_2/H_2O (per cent)		N_2/H_2O (per cent)		N_2/CO (per cent)		CO/H_2O (per cent)	
					a	b	a	b	a	b	a	b
				10.0	1.46	0.97	12.17	6.98	10.04	22.24	121.19	31.40
			10.0	0.5	1.68	0.32	12.22	0.00	15.50	10.74	78.83	0.01
				1.0	1.76	0.34	12.30	0.00	15.32	10.54	80.30	0.01
				5.0	1.80	0.34	12.43	0.00	15.34	10.30	81.02	0.02
				10.0	1.79	0.34	12.52	0.00	15.40	10.40	81.26	0.02
		20	0.1	0.5	1.01	1.01	6.20	6.18	4.94	4.98	125.66	124.15
				1.0	1.02	1.01	6.97	6.95	5.51	5.56	126.52	125.00
				5.0	1.02	1.02	8.90	8.87	6.99	7.05	127.35	125.82
				10.0	1.03	1.03	9.71	9.67	7.62	7.69	127.39	127.24
			1.0	0.5	1.75	1.25	8.22	5.11	6.75	11.62	121.83	44.01
				1.0	1.67	1.19	8.79	5.46	7.18	12.37	122.45	44.10
				5.0	1.53	1.08	10.43	6.46	8.49	14.63	122.94	44.17
				10.0	1.49	1.06	11.14	6.90	9.06	15.59	122.97	44.28
			10.0	0.5	1.11	0.23	11.84	0.00	15.83	2.93	74.78	0.02
				1.0	1.20	0.24	11.94	0.00	15.47	2.90	77.20	0.02
				5.0	1.28	0.26	12.02	0.00	15.10	2.75	79.58	0.02

Table A.1 – continued from previous page

B	n_{III} (cm^{-3})	T_{III} (K)	ζ/ζ_0	G/G_0	O_2/H_2O (per cent)		N_2/H_2O (per cent)		N_2/CO (per cent)		CO/H_2O (per cent)	
					a	b	a	b	a	b	a	b
				10.0	1.29	0.26	12.09	0.00	15.05	2.81	80.36	0.02
	10^8	10	0.1	0.5	0.80	0.80	6.80	6.83	5.43	5.46	125.25	125.14
				1.0	0.80	0.81	7.77	7.80	6.19	6.22	125.40	125.29
				5.0	0.81	0.81	9.93	9.97	7.92	7.96	125.33	125.22
				10.0	0.80	0.80	10.72	10.77	8.57	8.62	125.08	124.98
			1.0	0.5	1.90	1.83	8.89	8.43	7.08	7.96	125.54	105.89
				1.0	1.78	1.72	9.70	9.20	7.77	8.73	124.86	105.33
				5.0	1.55	1.50	11.56	10.98	9.41	10.59	122.84	103.70
				10.0	1.46	1.41	12.19	11.59	10.00	11.25	121.93	102.97
			10.0	0.5	1.77	1.07	13.05	1.53	13.87	9112.86	94.13	0.02
				1.0	1.87	1.12	13.20	1.53	13.65	8916.68	96.74	0.02
				5.0	1.93	1.14	13.46	1.55	13.54	8825.05	99.47	0.02
				10.0	1.92	1.13	13.57	1.56	13.57	8829.68	100.01	0.02
		20	0.1	0.5	1.01	1.02	6.20	6.23	4.94	4.96	125.69	125.65
				1.0	1.02	1.02	6.97	7.00	5.51	5.53	126.55	126.51
				5.0	1.02	1.03	8.90	8.94	6.99	7.02	127.38	127.35

Table A.1 – continued from previous page

B	n_{III} (cm^{-3})	T_{III} (K)	ζ/ζ_0	G/G_0	O_2/H_2O (per cent)		N_2/H_2O (per cent)		N_2/CO (per cent)		CO/H_2O (per cent)	
					a	b	a	b	a	b	a	b
				10.0	1.03	1.03	9.71	9.75	7.62	7.65	127.42	127.39
			1.0	0.5	1.75	1.73	8.24	8.01	6.73	7.37	122.42	108.68
				1.0	1.67	1.65	8.81	8.56	7.16	7.84	123.05	109.23
				5.0	1.53	1.51	10.45	10.16	8.46	9.26	123.55	109.66
				10.0	1.49	1.47	11.16	10.39	9.03	9.89	123.52	109.65
			10.0	0.5	1.16	0.77	12.48	1.66	14.50	7189.14	86.10	0.02
				1.0	1.26	0.82	12.63	1.66	14.13	7004.75	89.43	0.02
				5.0	1.36	0.87	12.84	1.66	13.67	6812.95	93.89	0.02
				10.0	1.37	0.88	12.94	1.66	13.59	6814.06	95.20	0.02
	10^9	10	0.1	0.5	0.80	0.80	6.80	6.83	5.43	5.45	125.25	125.35
				1.0	0.80	0.81	7.77	7.81	6.19	6.22	125.40	125.51
				5.0	0.81	0.81	9.93	9.98	7.92	7.96	125.33	125.43
				10.0	0.80	0.80	10.72	10.78	8.57	8.61	125.09	125.19
			1.0	0.5	1.90	1.98	8.89	9.26	7.08	7.43	125.62	124.59
				1.0	1.78	1.86	9.70	10.10	7.77	8.15	124.95	123.90
				5.0	1.56	1.62	11.56	12.04	9.40	9.88	122.93	121.83

Table A.1 – continued from previous page

B	n_{III} (cm^{-3})	T_{III} (K)	ζ/ζ_0	G/G_0	O_2/H_2O (per cent)		N_2/H_2O (per cent)		N_2/CO (per cent)		CO/H_2O (per cent)	
					a	b	a	b	a	b	a	b
				10.0	1.46	1.53	12.19	12.70	9.99	10.51	122.01	120.89
			10.0	0.5	1.79	2.08	13.25	12.92	13.65	151.30	97.08	8.54
				1.0	1.89	2.18	13.41	12.98	13.42	139.03	99.92	9.34
				5.0	1.96	2.23	13.71	13.15	13.29	126.27	103.13	10.42
				10.0	1.95	2.22	13.83	13.22	13.32	125.80	103.78	10.51
		20	0.1	0.5	1.01	1.02	6.20	6.24	4.94	4.96	125.69	125.80
				1.0	1.02	1.02	6.97	7.01	5.51	5.53	126.55	126.67
				5.0	1.02	1.03	8.90	8.95	6.99	7.02	127.38	127.50
				10.0	1.03	1.03	9.71	9.75	7.62	7.65	127.43	127.55
			1.0	0.5	1.75	1.83	8.24	8.60	6.73	7.05	122.48	122.02
				1.0	1.67	1.75	8.81	9.20	7.16	7.50	123.11	122.67
				5.0	1.53	1.60	10.45	10.92	8.46	8.86	123.61	123.20
				10.0	1.49	1.56	11.16	11.65	9.03	9.46	123.57	123.16
			10.0	0.5	1.17	1.49	12.62	13.48	14.34	86.56	87.97	15.57
				1.0	1.27	1.60	12.78	13.55	13.97	77.68	91.47	17.44
				5.0	1.37	1.70	13.01	13.60	13.50	68.59	96.34	19.83

Table A.1 – continued from previous page

B	n_{III} (cm^{-3})	T_{III} (K)	ζ/ζ_0	G/G_0	O_2/H_2O (per cent)		N_2/H_2O (per cent)		N_2/CO (per cent)		CO/H_2O (per cent)	
					a	b	a	b	a	b	a	b
				10.0	1.39	1.71	13.12	13.66	13.42	67.09	97.72	20.36
	10^{10}	10	0.1	0.5	0.80	0.80	6.80	6.84	5.43	5.45	125.25	125.38
				1.0	0.80	0.81	7.77	7.81	6.19	6.22	125.40	125.53
				5.0	0.81	0.81	9.93	9.98	7.92	7.95	125.33	125.46
				10.0	0.80	0.80	10.72	10.78	8.57	8.61	125.09	125.21
			1.0	0.5	1.90	1.99	8.89	9.35	7.08	7.38	125.63	126.73
				1.0	1.78	1.88	9.70	10.20	7.76	8.10	124.96	126.03
				5.0	1.56	1.64	11.56	12.16	9.40	9.81	122.94	123.91
				10.0	1.46	1.54	12.19	12.83	9.99	10.43	122.01	122.94
			10.0	0.5	1.80	2.88	13.27	20.94	13.62	27.33	97.40	76.60
				1.0	1.90	3.05	13.43	21.21	13.40	26.35	100.27	80.49
				5.0	1.96	3.15	13.74	21.71	13.27	25.56	103.54	84.93
				10.0	1.95	3.14	13.86	21.90	13.30	25.56	103.54	84.93
		20	0.1	0.5	1.01	1.02	6.20	6.24	4.94	4.96	125.69	125.82
				1.0	1.02	1.02	6.97	7.01	5.51	5.53	126.55	126.68
				5.0	1.02	1.03	8.90	8.95	6.99	7.02	127.38	127.52

Table A.1 – continued from previous page

B	n_{III} (cm^{-3})	T_{III} (K)	ζ/ζ_0	G/G_0	O_2/H_2O (per cent)		N_2/H_2O (per cent)		N_2/CO (per cent)		CO/H_2O (per cent)	
					a	b	a	b	a	b	a	b
				10.0	1.03	1.03	9.71	9.76	7.62	7.65	127.43	127.57
			1.0	0.5	1.75	1.84	8.24	8.66	6.73	7.02	122.48	123.49
				1.0	1.67	1.76	8.81	9.27	7.16	7.46	123.12	124.16
				5.0	1.53	1.61	10.45	11.00	8.46	8.82	123.62	124.69
				10.0	1.49	1.57	11.16	11.74	9.03	9.42	123.58	124.65
			10.0	0.5	1.18	1.92	12.63	20.33	14.33	29.83	88.17	68.15
				1.0	1.27	2.09	12.79	20.63	13.95	28.17	91.69	73.24
				5.0	1.37	2.26	13.03	21.06	13.49	26.18	96.61	80.44
				10.0	1.39	2.29	13.14	21.23	13.41	25.76	97.99	82.40
	10^{11}	10	0.1	0.5	0.80	0.80	6.80	6.84	5.43	5.45	125.25	125.38
				1.0	0.80	0.81	7.77	7.81	6.19	6.22	125.40	125.53
				5.0	0.81	0.81	9.93	9.98	7.92	7.95	125.33	125.46
				10.0	0.80	0.80	10.72	10.78	8.57	8.61	125.09	125.21
			1.0	0.5	1.90	2.00	8.89	9.36	7.08	7.38	125.63	126.95
				1.0	1.78	1.88	9.70	10.21	7.76	8.09	124.96	126.24
				5.0	1.56	1.64	11.56	12.17	9.40	9.81	122.94	124.12

Table A.1 – continued from previous page

B	n_{III} (cm^{-3})	T_{III} (K)	ζ/ζ_0	G/G_0	O_2/H_2O (per cent)		N_2/H_2O (per cent)		N_2/CO (per cent)		CO/H_2O (per cent)	
					a	b	a	b	a	b	a	b
				10.0	1.46	1.54	12.19	12.84	9.99	10.43	122.02	123.15
			10.0	0.5	1.80	3.08	13.27	22.75	13.62	24.38	97.44	93.32
				1.0	1.90	3.27	13.44	23.10	13.40	24.54	100.14	98.16
				5.0	1.96	3.39	13.74	23.71	13.27	22.86	103.58	103.72
				10.0	1.95	3.37	13.86	23.93	13.30	22.83	104.23	104.83
		20	0.1	0.5	1.01	1.02	6.20	6.24	4.94	4.96	125.69	125.82
				1.0	1.02	1.02	6.97	7.01	5.51	5.53	126.55	126.68
				5.0	1.02	1.03	8.90	8.95	6.99	7.02	127.38	127.52
				10.0	1.03	1.03	9.71	9.76	7.62	7.65	127.43	127.57
			1.0	0.5	1.75	1.85	8.24	8.67	6.73	7.01	122.48	123.64
				1.0	1.67	1.76	8.81	9.27	7.16	7.46	123.12	124.31
				5.0	1.53	1.61	10.45	11.01	8.46	8.82	123.62	124.84
				10.0	1.49	1.57	11.16	11.75	9.03	9.42	123.58	124.80
			10.0	0.5	1.18	2.01	12.63	21.57	14.33	27.54	88.19	78.35
				1.0	1.27	2.18	12.79	21.93	13.95	26.03	91.71	84.24
				5.0	1.37	2.37	13.03	22.45	13.48	24.25	96.63	92.56

Table A.1 – continued from previous page

B	n_{III} (cm^{-3})	T_{III} (K)	ζ/ζ_0	G/G_0	O_2/H_2O (per cent)		N_2/H_2O (per cent)		N_2/CO (per cent)		CO/H_2O (per cent)	
					a	b	a	b	a	b	a	b
				10.0	1.39	2.40	13.14	22.66	13.40	23.87	98.02	94.91

This page was intentionally left blank

Bibliography

Abouaf-Marguin, L., Vasserot, A.-M., Pardanaud, C. & Michaut, X., 2007, *Chemical Physics Letters*, **447**(4), 232
URL: *http://www.sciencedirect.com/science/article/pii/S0009261407012377*

Abouaf-Marguin, L., Vasserot, A.-M., Pardanaud, C. & Michaut, X., 2009, *Chemical Physics Letters*, **480**(1), 82
URL: *http://www.sciencedirect.com/science/article/pii/S0009261409010847*

Agarwal, J., Müller, M. & Grün, E., 2007, *Space Science Reviews*, **128**, 79

A'Hearn, M. F., Millis, R. C., Schleicher, D. O., Osip, D. J. & Birch, P. V., 1995, *Icarus*, **118**, 223

A'Hearn, M. F. & Millis, R. L., 1980, *AJ*, **85**, 1528

Ahn, C. P., Alexandroff, R., Allende Prieto, C., Anderson, S. F., Anderton, T., Andrews, B. H., Aubourg, É., Bailey, S., Balbinot, E., Barnes, R. & et al., 2012, *ApJSS*, **203**, 21

Althaus, L. G., Córsico, A. H., Isern, J. & García-Berro, E., 2010, *The Astronomy and Astrophysics Review*, **18**(4), 471

Altwegg, K., Balsiger, H., Bar-Nun, A., Berthelier, J. J., Bieler, A., Bochsler, P., Briois, C., Calmonte, U., Combi, M., De Keyser, J., Eberhardt, P., Fiethe, B., Fuselier, S., Gasc, S., Gombosi, T. I., Hansen, K., Hässig, M., Jäckel, A., Kopp, E., Korth, A., LeRoy, L., Mall, U., Marty, B., Mousis, O., Neefs, E., Owen, T., Rème, H., Rubin, M., Sémon, T., Tzou, C.-Y., Waite, H. & Wurz, P., 2015, *Science*, **347**(6220)
URL: *http://science.sciencemag.org/content/347/6220/1261952*

Altwegg, K., Balsiger, H., Bar-Nun, A., Berthelier, J.-J., Bieler, A., Bochsler, P., Briois, C., Calmonte, U., Combi, M. R., Cottin, H., De Keyser, J., Dhooghe, F., Fiethe, B., Fuselier, S. A., Gasc, S., Gombosi, T. I., Hansen, K. C., Haessig, M., Ja ckel, A., Kopp, E., Korth, A., Le Roy, L., Mall, U., Marty, B., Mousis, O., Owen, T., Reme, H., Rubin, M., Semon, T., Tzou, C.-Y., Waite, J. H. & Wurz, P., 2016, *Science Advances*, **2**, e1600285

Altwegg, K., Balsiger, H., Berthelier, J. J., Bieler, A., Calmonte, U., De Keyser, J., Fiethe, B., Fuselier, S. A., Gasc, S. & Gombosi, T. I., 2017, *Philosophical Transactions of the Royal Society of London Series A*, **375**(2097), 20160253

Arpigny, C., Jehin, E., Manfroid, J., Hutsemékers, D., Schulz, R., Stüwe, J. A., Zucconi, J.-M. & Ilyin, I., 2003, *Science*, **301**, 1522

Balsiger, H., 1990, *Measurements of ion species within the coma of comet Halley from Giotto.* (Ellis Horwood Ltd), volume 1, chapter 2, pp. 129–146

Balsiger, H., Altwegg, K., Bar-Nun, A., Berthelier, J. J., Bieler, A., Bochsler, P., Briois, C., Calmonte, U., Combi, M. & De Keyser, J., 2015, *Science Advances*, **1**(8), e1500377

Balsiger, H., Altwegg, K., Bochsler, P., Eberhardt, P., Fischer, J., Graf, S., Jäckel, A., Kopp, E., Langer, U., Mildner, M., Müller, J., Riesen, T., Rubin, M., Scherer, S., Wurz, P., Wüthrich, S., Arijs, E., Delanoye, S., de Keyser, J., Neefs, E., Nevejans, D., Rème, H., Aoustin, C., Mazelle, C., Médale, J.-L., Sauvaud, J. A., Berthelier, J.-J., Bertaux, J.-L., Duvet, L., Illiano, J.-M., Fuselier, S. A., Ghielmetti, A. G., Magoncelli, T., Shelley, E. G., Korth, A., Heerlein, K., Lauche, H., Livi, S., Loose, A., Mall, U., Wilken, B., Gliem, F., Fiethe, B., Gombosi, T. I., Block, B., Carignan, G. R., Fisk, L. A., Waite, J. H., Young, D. T. & Wollnik, H., 2007, *Space Science Reviews*, **128**, 745

Balsiger, H., Altwegg, K. & Geiss, J., 1995, *Journal of Geophysical Research*, **100**, 5827

Barber, S. D., Belardi, C., Kilic, M. & Gianninas, A., 2016, *MNRAS*, **459**(2), 1415

Barber, S. D., Kilic, M., Brown, W. R. & Gianninas, A., 2014, *ApJ*, **786**, 77

Barber, S. D., Patterson, A. J., Kilic, M., Leggett, S. K., Dufour, P., Bloom, J. S. & Starr, D. L., 2012, *ApJ*, **760**, 26

Becklin, E. E., Farihi, J., Jura, M., Song, I., Weinberger, A. J. & Zuckerman, B., 2005, *ApJL*, **632**, L119

Bédard, A., Bergeron, P. & Fontaine, G., 2017, *ApJ*, **848**, 11

Beduz, C., Carravetta, M., Chen, J. Y.-C., Concistrè, M., Denning, M., Frunzi, M., Horsewill, A. J., Johannessen, O. G., Lawler, R., Lei, X., Levitt, M. H., Li, Y., Mamone, S., Murata, Y., Nagel, U., Nishida, T., Ollivier, J., Rols, S., Rõõm, T., Sarkar, R., Turro, N. J. & Yang, Y., 2012, *Proceedings of the National Academy of Sciences*, **109**(32), 12894 **URL:** *https://www.pnas.org/content/109/32/12894*

Bensch, F. & Bergin, E. A., 2004, *ApJ*, **615**, 531

Bentley, M. S., Schmied, R., Mannel, T., Torkar, K., Jeszenszky, H., Romstedt, J., Levasseur-Regourd, A.-C., Weber, I., Jessberger, E. K. & Ehrenfreund, P., 2016, *Nature*, **537**(7618), 73

Bergeron, P., Saffer, R. A. & Liebert, J., 1992, *ApJ*, **394**, 228

Bergfors, C., Farihi, J., Dufour, P. & Rocchetto, M., 2014, *MNRAS*, **444**, 2147

Bergin, E. A., Blake, G. A., Ciesla, F., Hirschmann, M. M. & Li, J., 2015, *Proceedings of the National Academy of Science*, **112**, 8965

Bertaux, J.-L., Combi, M. R., Quémerais, E. & Schmidt, W., 2014, *Planetary Space Science*, **91**, 14

Bieler, A., Altwegg, K., Balsiger, H., Bar-Nun, A., Berthelier, J.-J., Bochsler, P., Briois, C., Calmonte, U., Combi, M., de Keyser, J., van Dishoeck, E. F., Fiethe, B., Fuselier, S. A., Gasc, S., Gombosi, T. I., Hansen, K. C., Hässig, M., Jäckel, A., Kopp, E., Korth, A., Le Roy, L., Mall, U., Maggiolo, R., Marty, B., Mousis, O., Owen, T., Rème, H., Rubin, M., Sémon, T., Tzou, C.-Y., Waite, J. H., Walsh, C. & Wurz, P., 2015, *Nature*, **526**, 678

Biraud, F., Bourgois, G., Crovisier, J., Fillit, R., Gerard, E. & Kazes, I., 1974, *A&A*, **34**, 163

Biver, N., 1997, *Molècules mères cométaires: observations et modélisations*, Ph.D. thesis, Univ. Paris 7-Diderot

Biver, N. & Bockelée-Morvan, D., 2016, *IAU Focus Meeting*, **29**(27), 228

Biver, N., Bockelee-Morvan, D., Colom, P., Crovisier, J., Davies, J. K., Dent, W. R. F., Despois, D., Gerard, E., Lellouch, E., Rauer, H., Moreno, R. & Paubert, G., 1997*a*, *Science*, **275**, 1915

Biver, N., Bockelée-Morvan, D., Colom, P., Crovisier, J., Germain, B., Lellouch, E., Davies, J. K., Dent, W. R. F., Moreno, R., Paubert, G., Wink, J., Despois, D., Lis, D. C., Mehringer, D., Benford, D., Gardner, M., Phillips, T. G., Gunnarsson, M., Rickman, H., Winnberg, A., Bergman, P., Johansson, L. E. B. & Rauer, H., 1997*b*, *Earth Moon and Planets*, **78**, 5

Biver, N., Bockelée-Morvan, D., Colom, P., Crovisier, J., Henry, F., Lellouch, E., Winnberg, A., Johansson, L. E. B., Gunnarsson, M., Rickman, H., Rantakyrö, F., Davies, J. K., Dent, W. R. F., Paubert, G., Moreno, R., Wink, J., Despois, D., Benford, D. J., Gardner, M., Lis, D. C., Mehringer, D., Phillips, T. G. & Rauer, H., 2002*a*, *Earth Moon and Planets*, **90**, 5

Biver, N., Bockelée-Morvan, D., Colom, P., Crovisier, J., Lecacheux, A., Frisk, U., Hjalmarson, Å., Olberg, M. & Sandqvist, A., 2009, *A&A*, **501**, 359

Biver, N., Bockelée-Morvan, D., Crovisier, J., Colom, P., Henry, F., Moreno, R., Paubert, G., Despois, D. & Lis, D. C., 2002*b*, *Earth Moon and Planets*, **90**, 323

Biver, N., Bockelée-Morvan, D., Crovisier, J., Davies, J. K., Matthews, H. E., Wink, J. E., Rauer, H., Colom, P., Dent, W. R. F., Despois, D., Moreno, R., Paubert, G., Jewitt, D. & Senay, M., 1999, *AJ*, **118**, 1850

Biver, N., Bockelée-Morvan, D., Crovisier, J., Lecacheux, A., Frisk, U., Hjalmarson, Å., Olberg, M., Florén, H.-G., Sandqvist, A. & Kwok, S., 2007, *Planetary Space Science*, **55**, 1058

Biver, N., Crovisier, J., Bockelée-Morvan, D., Szutowicz, S., Lis, D. C., Hartogh, P., de Val-Borro, M., Moreno, R., Boissier, J., Kidger, M., Küppers, M., Paubert, G., Dello Russo, N., Vervack, R. & Weaver, H., 2012, *A&A*, **539**, A68

Biver, N., Rauer, H., Despois, D., Moreno, R., Paubert, G., Bockelée-Morvan, D., Colom, P., Crovisier, J., Gérard, E. & Jorda, L., 1996, *Nature*, **380**, 137

Blum, J., Gundlach, B., Krause, M., Fulle, M., Johansen, A., Agarwal, J., von Borstel, I., Shi, X., Hu, X. & Bentley, M. S., 2017, *MNRAS*, **469**, S755

Bochkarev, K. V. & Rafikov, R. R., 2011, *ApJ*, **741**, 36

Bockelée-Morvan, D., 1987, *A&A*, **181**, 169

Bockelée-Morvan, D. & Biver, N., 2017, *Philosophical Transactions of the Royal Society of London Series A*, **375**(2097), 20160252

Bockelée-Morvan, D., Biver, N., Crovisier, J., Lis, D. C., Hartogh, P., Moreno, R., de Val-Borro, M., Blake, G. A., Szutowicz, S., Boissier, J., Cernicharo, J., Charnley, S. B., Combi, M., Cordiner, M. A., de Graauw, T., Encrenaz, P., Jarchow, C., Kidger, M., Küppers, M., Milam, S. N., Müller, H. S. P., Phillips, T. G. & Rengel, M., 2014, *A&A*, **562**, A5

Bockelée-Morvan, D., Biver, N., Swinyard, B., de Val-Borro, M., Crovisier, J., Hartogh, P., Lis, D. C., Moreno, R., Szutowicz, S., Lellouch, E., Emprechtinger, M., Blake, G. A., Courtin, R., Jarchow, C., Kidger, M., Küppers, M., Rengel, M., Davis, G. R., Fulton, T., Naylor, D., Sidher, S. & Walker, H., 2012, *A&A*, **544**, L15

Bockelée-Morvan, D., Calmonte, U., Charnley, S., Duprat, J., Engrand, C., Gicquel, A., Hässig, M., Jehin, E., Kawakita, H., Marty, B., Milam, S., Morse, A., Rousselot, P., Sheridan, S. & Wirström, E., 2015*a*, *Space Science Reviews*, **197**, 47

Bockelée-Morvan, D. & Crovisier, J., 1989, *A&A*, **216**, 278

Bockelée-Morvan, D., Crovisier, J., Colom, P. & Despois, D., 1994, *A&A*, **287**, 647

Bockelée-Morvan, D., Debout, V., Erard, S., Leyrat, C., Capaccioni, F., Filacchione, G., Fougere, N., Drossart, P., Arnold, G. & Combi, M., 2015*b*, *A&A*, **583**, A6

Bockelée-Morvan, D., Gautier, D., Lis, D. C., Young, K., Keene, J., Phillips, T., Owen, T., Crovisier, J., Goldsmith, P. F., Bergin, E. A., Despois, D. & Wootten, A., 1998, *Icarus*, **133**, 147

Bockelée-Morvan, D., Henry, F., Biver, N., Boissier, J., Colom, P., Crovisier, J., Despois, D., Moreno, R. & Wink, J., 2009, *A&A*, **505**, 825

Bockelée-Morvan, D., Lis, D. C., Wink, J. E., Despois, D., Crovisier, J., Bachiller, R., Benford, D. J., Biver, N., Colom, P., Davies, J. K., Gérard, E., Germain, B., Houde, M., Mehringer, D., Moreno, R., Paubert, G., Phillips, T. G. & Rauer, H., 2000, *A&A*, **353**, 1101

Boehnhardt, H., Bibring, J.-P., Apathy, I., Auster, H. U., Ercoli Finzi, A., Goesmann, F., Klingelhöfer, G., Knapmeyer, M., Kofman, W. & Krüger, H., 2017, *Philosophical Transactions of the Royal Society of London Series A*, **375**(2097), 20160248

Boissier, J., Bockelée-Morvan, D., Biver, N., Crovisier, J., Lellouch, E., Moreno, R. & Zakharov, V., 2012, *A&A*, **542**, A73

Bonev, B. P., Mumma, M. J., Gibb, E. L., DiSanti, M. A., Villanueva, G. L., Magee-Sauer, K. & Ellis, R. S., 2009, *ApJ*, **699**(2), 1563

Bonev, B. P., Mumma, M. J., Kawakita, H., Kobayashi, H. & Villanueva, G. L., 2008*a*, *Icarus*, **196**, 241

Bonev, B. P., Mumma, M. J., Radeva, Y. L., DiSanti, M. A., Gibb, E. L. & Villanueva, G. L., 2008*b*, *ApJL*, **680**, L61

Bonev, B. P., Mumma, M. J., Villanueva, G. L., Disanti, M. A., Ellis, R. S., Magee-Sauer, K. & Dello Russo, N., 2007, *ApJL*, **661**, L97

Bonev, B. P., Villanueva, G. L., DiSanti, M. A., Boehnhardt, H., Lippi, M., Gibb, E. L., Paganini, L. & Mumma, M. J., 2017, *AJ*, **153**, 241

Bonev, B. P., Villanueva, G. L., Paganini, L., DiSanti, M. A., Gibb, E. L., Keane, J. V., Meech, K. J. & Mumma, M. J., 2013, *Icarus*, **222**, 740

Bonsor, A., Farihi, J., Wyatt, M. C. & van Lieshout, R., 2017, *MNRAS*, **468**, 154

Bonsor, A. & Veras, D., 2015, *MNRAS*, **454**, 53

Bonsor, A. & Wyatt, M. C., 2012, *MNRAS*, **420**, 2990

Brahe, T., 1603, *De mundi aetherei recentioribus phaenomenis liber secundus de cometa anni 1577*

Brasser, R. & Morbidelli, A., 2013, *Icarus*, **225**, 40

Brinkworth, C. S., Gänsicke, B. T., Marsh, T. R., Hoard, D. W. & Tappert, C., 2009, *ApJ*, **696**(2), 1402

Brown, J. C., Veras, D. & Gänsicke, B. T., 2017, *MNRAS*, **468**, 1575

Brown, R. H., Lauretta, D. S., Schmidt, B. & Moores, J., 2012, *Planetary Space Science*, **60**, 166

Brownlee, D. E., Tsou, P., Anderson, J. D., Hanner, M. S., Newburn, R. L., Sekanina, Z., Clark, B. C., Hörz, F., Zolensky, M. E., Kissel, J., McDonnell, J. A. M., Sandford, S. A. & Tuzzolino, A. J., 2003, *Journal of Geophysical Research (Planets)*, **108**(E10), 8111

Brugger, B., Mousis, O., Morse, A., Marboeuf, U., Jorda, L., Guilbert-Lepoutre, A., Andrews, D., Barber, S., Lamy, P. & Luspay-Kuti, A., 2016, *ApJ*, **822**(2), 98

Buntkowsky, G., Limbach, H.-H., Walaszek, B., Adamczyk, A., Xu, Y., Breitzke, H., Schweitzer, A., Gutmann, T., Wächtler, M., Amadeu, N. et al., 2008, *Z Phys Chem*, **222**(7), 1049
URL: *https://www.researchgate.net/publication/228565826_Mechanisms_of_Dipolar_OrthoPara-H2O_Conversion_in_Ice*

Burgasser, A. J., Kirkpatrick, J. D., Reid, I. N., Brown, M. E., Miskey, C. L. & Gizis, J. E., 2003, *ApJ*, **586**, 512

Burns, J. A., Lamy, P. L. & Soter, S., 1979, *Icarus*, **40**(1), 1

Cacciani, P., Cosléou, J. & Khelkhal, M., 2012, *Physical Review A*, **85**(1), 012521

Calmonte, U., Altwegg, K., Balsiger, H., Berthelier, J. J., Bieler, A., Cessateur, G., Dhooghe, F., van Dishoeck, E. F., Fiethe, B., Fuselier, S. A., Gasc, S., Gombosi, T. I., Hässig, M., Le Roy, L., Rubin, M., Sémon, T., Tzou, C.-Y. & Wampfler, S. F., 2016, *MNRAS*, **462**, S253

Capaccioni, F., Coradini, A., Filacchione, G., Erard, S., Arnold, G., Drossart, P., De Sanctis, M. C., Bockelee-Morvan, D., Capria, M. T. & Tosi, F., 2015, *Science*, **347**(6220), aaa0628

Capria, M. T., Cremonese, G., Bhardwaj, A. & de Sanctis, M. C., 2005, *A&A*, **442**, 1121

Cauley, P. W., Farihi, J., Redfield, S., Bachman, S., Parsons, S. G. & Gänsicke, B. T., 2018, *ApJL*, **852**, L22

Ceccarelli, C., Caselli, P., Bockelée-Morvan, D., Mousis, O., Pizzarello, S., Robert, F. & Semenov, D., 2014, *Protostars and Planets VI*, 859

Ceponkus, J., Uvdal, P. & Nelander, B., 2010, *The Journal of Chemical Physics*, **133**(7), 074301
URL: *https://doi.org/10.1063/1.3460457*

Chambers, K. C., Magnier, E. A., Metcalfe, N., Flewelling, H. A., Huber, M. E., Waters, C. Z., Denneau, L., Draper, P. W., Farrow, D., Finkbeiner, D. P., Holmberg, C., Koppenhoefer, J., Price, P. A., Saglia, R. P., Schlafly, E. F., Smartt, S. J., Sweeney, W., Wainscoat, R. J., Burgett, W. S., Grav, T., Heasley, J. N., Hodapp, K. W., Jedicke, R., Kaiser, N., Kudritzki, R.-P., Luppino, G. A., Lupton, R. H., Monet, D. G., Morgan, J. S., Onaka, P. M., Stubbs, C. W., Tonry, J. L., Banados, E., Bell, E. F., Bender, R., Bernard, E. J., Botticella, M. T., Casertano, S., Chastel, S., Chen, W.-P., Chen, X., Cole, S., Deacon, N., Frenk, C., Fitzsimmons, A., Gezari, S., Goessl, C., Goggia, T., Goldman, B., Grebel, E. K., Hambly, N. C., Hasinger, G., Heavens, A. F., Heckman, T. M., Henderson, R., Henning, T., Holman, M., Hopp, U., Ip, W.-H., Isani, S., Keyes, C. D., Koekemoer, A., Kotak, R., Long, K. S., Lucey, J. R., Liu, M., Martin, N. F., McLean, B., Morganson, E., Murphy, D. N. A., Nieto-Santisteban, M. A., Norberg, P., Peacock, J. A., Pier, E. A., Postman, M., Primak, N., Rae, C., Rest, A., Riess, A., Riffeser, A., Rix, H. W., Roser, S., Schilbach, E., Schultz, A. S. B., Scolnic, D., Szalay, A., Seitz, S., Shiao, B., Small, E., Smith, K. W., Soderblom, D., Taylor, A. N., Thakar, A. R., Thiel, J., Thilker, D., Urata, Y., Valenti, J., Walter, F., Watters, S. P., Werner, S., White, R., Wood-Vasey, W. M. & Wyse, R., 2016, *ArXiv e-prints*

Chapovsky, P. L., 1991, *Phys. Rev. A*, **43**, 3624
URL: *https://link.aps.org/doi/10.1103/PhysRevA.43.3624*

Chapovsky, P. L. & Ilisca, E., 2001, *Physical Review A*, **63**(6), 062505

Cheselka, M., Holberg, J. B., Watkins, R., Collins, J. & Tweedy, R. W., 1993, *AJ*, **106**, 2365

Chiang, E. I. & Goldreich, P., 1997, *ApJ*, **490**(1), 368

Chiu, K., Neufeld, D. A., Bergin, E. A., Melnick, G. J., Patten, B. M., Wang, Z. & Bockelée-Morvan, D., 2001, *Icarus*, **154**, 345

Choi, Y., van der Tak, F. F. S., Bergin, E. A. & Plume, R., 2014, *A&A*, **572**, L10

Cleeves, L. I., Bergin, E. A. & Adams, F. C., 2014, *ApJ*, **794**(2), 123

Cochran, A. L., 1987, *AJ*, **93**, 231

Cochran, A. L., 2008, *Icarus*, **198**, 181

Cochran, A. L., Barker, E. S. & Gray, C. L., 2012, *Icarus*, **218**, 144

Cochran, A. L. & Cochran, W. D., 2001, *Icarus*, **154**, 381

Colangeli, L., Epifani, E., Brucato, J. R., Bussoletti, E., De Sanctis, C., Fulle, M., Mennella, V., Palomba, E., Palumbo, P. & Rotundi, A., 1999, *A&A*, **343**, L87

Combi, M. R., Bertaux, J.-L., Quémerais, E., Ferron, S. & Mäkinen, J. T. T., 2011, *ApJL*, **734**, L6

Combi, M. R., Cochran, A. L., Cochran, W. D., Lambert, D. L. & Johns-Krull, C. M., 1999, *ApJ*, **512**, 961

Combi, M. R., Harris, W. M. & Smyth, W. H., 2004, *Gas dynamics and kinetics in the cometary coma: theory and observations* (University of Arizona Press), chapter 6, pp. 523–552

Combi, M. R., Mäkinen, J. T. T., Bertaux, J.-L., Quémerais, E., Ferron, S. & Fougere, N., 2013, *Icarus*, **225**, 740

Combi, M. R., Reinard, A. A., Bertaux, J.-L., Quemerais, E. & Mäkinen, T., 2000, *Icarus*, **144**, 191

Coradini, A., Capaccioni, F., Drossart, P., Arnold, G., Ammannito, E., Angrilli, F., Barucci, A., Bellucci, G., Benkhoff, J., Bianchini, G., Bibring, J. P., Blecka, M., Bockelee-Morvan, D., Capria, M. T., Carlson, R., Carsenty, U., Cerroni, P., Colangeli, L., Combes, M., Combi, M., Crovisier, J., De Sanctis, M. C., Encrenaz, E. T., Erard, S., Federico, C., Filacchione, G., Fink, U., Fonti, S., Formisano, V., Ip, W. H., Jaumann, R., Kuehrt, E., Langevin, Y., Magni, G., McCord, T., Mennella, V., Mottola, S., Neukum, G., Palumbo, P., Piccioni, G., Rauer, H., Saggin, B., Schmitt, B., Tiphene, D. & Tozzi, G., 2007, *Space Science Reviews*, **128**(1-4), 529

Cordiner, M. A., Boissier, J., Charnley, S. B., Remijan, A. J., Mumma, M. J., Villanueva, G., Lis, D. C., Milam, S. N., Paganini, L., Crovisier, J., Bockelee-Morvan, D., Kuan, Y.-J., Biver, N. & Coulson, I. M., 2017, *ApJ*, **838**, 147

Cordiner, M. A., Remijan, A. J., Boissier, J., Milam, S. N., Mumma, M. J., Charnley, S. B., Paganini, L., Villanueva, G., Bockelée-Morvan, D., Kuan, Y.-J., Chuang, Y.-L., Lis, D. C., Biver, N., Crovisier, J., Minniti, D. & Coulson, I. M., 2014, *ApJL*, **792**, L2

Crifo, J. F., 1992, *ApJ*, **391**, 336

Crifo, J. F. & Slanina, Z., 1991, *ApJ*, **383**, 351

Crovisier, J., 1984, *A&A*, **130**, 361

Crovisier, J., 1989, *A&A*, **213**, 459

Crovisier, J., 1998, *Faraday Discussions*, **109**, 437

Crovisier, J., Biver, N., Bockelée-Morvan, D., Boissier, J., Colom, P. & Lis, D. C., 2009, *Earth Moon and Planets*, **105**, 267

Crovisier, J., Biver, N., Bockelee-Morvan, D., Colom, P., Jorda, L., Lellouch, E., Paubert, G. & Despois, D., 1995, *Icarus*, **115**, 213

Crovisier, J., Bockelée-Morvan, D., Biver, N., Colom, P., Despois, D. & Lis, D. C., 2004, *A&A*, **418**, L35

Crovisier, J., Colom, P., Gérard, E., Bockelée-Morvan, D. & Bourgois, G., 2002, *A&A*, **393**, 1053

Crovisier, J. & Encrenaz, T., 1983, *A&A*, **126**, 170

Crovisier, J., Encrenaz, T., Lellouch, E., Bockelée-Morvan, D., Altieri, B., Leech, K., Salama, A., Griffin, M. J., de Graauw, T., van Dishoeck, E. F., Knacke, R. & Brooke, T. Y., 1999, in P. Cox & M. Kessler (eds.), *The Universe as Seen by ISO* (ESA-SP), volume 427 of *ESA Special Publication*, p. 161

Crovisier, J. & Le Bourlot, J., 1983, *A&A*, **123**, 61

Crovisier, J., Leech, K., Bockelee-Morvan, D., Brooke, T. Y., Hanner, M. S., Altieri, B., Keller, H. U. & Lellouch, E., 1997, *Science*, **275**, 1904

Curl, R. F., Kasper, J. V. V. & Pitzer, K. S., 1967, *The Journal of Chemical Physics*, **46**(8), 3220
URL: *https://doi.org/10.1063/1.1841193*

Cutri, R. M., Skrutskie, M. F., van Dyk, S., Beichman, C. A., Carpenter, J. M., Chester, T., Cambresy, L., Evans, T., Fowler, J., Gizis, J., Howard, E., Huchra, J., Jarrett, T., Kopan, E. L., Kirkpatrick, J. D., Light, R. M., Marsh, K. A., McCallon, H., Schneider, S., Stiening, R., Sykes, M., Weinberg, M., Wheaton, W. A., Wheelock, S. & Zacarias, N., 2003, *VizieR Online Data Catalog*, **2246**

Danks, A. C., Lambert, D. L. & Arpigny, C., 1974, *ApJ*, **194**, 745

Davidsson, B. J. R., Sierks, H., Güttler, C., Marzari, F., Pajola, M., Rickman, H., A'Hearn, M. F., Auger, A. T., El-Maarry, M. R. & Fornasier, S., 2016, *A&A*, **592**, A63

Davies, J. K., Roush, T. L., Cruikshank, D. P., Bartholomew, M. J., Geballe, T. R., Owen, T. & de Bergh, C., 1997, *Icarus*, **127**, 238

de Pater, I., Palmer, P. & Snyder, L. E., 1991, in R. L. Newburn, Jr., M. Neugebauer & J. Rahe (eds.), *IAU Colloq. 116: Comets in the post-Halley era*, volume 167 of *Astrophysics and Space Science Library*, pp. 175–207

De Sanctis, M. C., Capaccioni, F., Ciarniello, M., Filacchione, G., Formisano, M., Mottola, S., Raponi, A., Tosi, F., Bockelée-Morvan, D. & Erard, S., 2015, *Nature*, **525**(7570), 500

De Val-Borro, M., Bockelée-Morvan, D., Jehin, E., Hartogh, P., Opitom, C., Szutowicz, S., Biver, N., Crovisier, J., Lis, D. C., Rezac, L., de Graauw, T., Hutsemékers, D., Jarchow, C., Kidger, M., Küppers, M., Lara, L. M., Manfroid, J., Rengel, M., Swinyard, B. M., Teyssier, D., Vandenbussche, B. & Waelkens, C., 2014, *A&A*, **564**, A124

De Val-Borro, M., Hartogh, P., Crovisier, J., Bockelée-Morvan, D., Biver, N., Lis, D. C., Moreno, R., Jarchow, C., Rengel, M., Szutowicz, S., Banaszkiewicz, M., Bensch, F., Błęcka, M. I., Emprechtinger, M., Encrenaz, T., Jehin, E., Küppers, M., Lara, L.-M., Lellouch, E., Swinyard, B. M., Vandenbussche, B., Bergin, E. A., Blake, G. A., Blommaert, J. A. D. L., Cernicharo, J., Decin, L., Encrenaz, P., de Graauw, T., Hutsemékers, D., Kidger, M., Manfroid, J., Medvedev, A. S., Naylor, D. A., Schieder, R., Stam, D., Thomas, N., Waelkens, C., Szczerba, R., Saraceno, P., di Giorgio, A. M., Philipp, S., Klein, T., Ossenkopf, V., Zaal, P. & Shipman, R., 2010, *A&A*, **521**, L50

De Val-Borro, M., Rezac, L., Hartogh, P., Biver, N., Bockelée-Morvan, D., Crovisier, J., Küppers, M., Lis, D. C., Szutowicz, S., Blake, G. A., Emprechtinger, M., Jarchow, C.,

Jehin, E., Kidger, M., Lara, L.-M., Lellouch, E., Moreno, R. & Rengel, M., 2012, *A&A*, **546**, L4

De Val-Borro, M. & Wilson, T. G., 2016, *CRETE: Comet RadiativE Transfer and Excitation*, Astrophysics Source Code Library

Debes, J. H., 2006, *ApJ*, **652**, 636

Debes, J. H., 2011, *The Origin and Evolution of White Dwarf Dust Disks* (Wiley), chapter 6, pp. 173–202

Debes, J. H., Hoard, D. W., Wachter, S., Leisawitz, D. T. & Cohen, M., 2011, *ApJSS*, **197**, 38

Debes, J. H. & Sigurdsson, S., 2002, *ApJ*, **572**(1), 556

Debes, J. H., Sigurdsson, S. & Hansen, B., 2007, *AJ*, **134**, 1662

Debes, J. H., Thévenot, M., Kuchner, M. J., Burgasser, A. J., Schneider, A. C., Meisner, A. M., Gagné, J., Faherty, J. K., Rees, J. M., Allen, M., Caselden, D., Cushing, M., Wisniewski, J., Allers, K., The Backyard Worlds: Planet 9 Collaboration & The Disk Detective Collaboration, 2019, *ApJL*, **872**, L25

Debes, J. H., Walsh, K. J. & Stark, C., 2012, *ApJ*, **747**, 148

Decock, A., Jehin, E., Rousselot, P., Hutsemékers, D., Manfroid, J., Raghuram, S., Bhardwaj, A. & Hubert, B., 2015, *A&A*, **573**, A1

Dello Russo, N., Bonev, B. P., DiSanti, M. A., Mumma, M. J., Gibb, E. L., Magee-Sauer, K., Barber, R. J. & Tennyson, J., 2005, *ApJ*, **621**, 537

Dello Russo, N., Kawakita, H., Vervack, R. J. & Weaver, H. A., 2016*a*, *Icarus*, **278**, 301

Dello Russo, N., Vervack, R. J., J., Weaver, H. A., Montgomery, M. M., Deshpande, R., Fernández, Y. R. & Martin, E. L., 2008, *ApJ*, **680**(1), 793

Dello Russo, N., Vervack, R. J., Kawakita, H., Cochran, A., McKay, A. J., Harris, W. M., Weaver, H. A., Lisse, C. M., DiSanti, M. A., Kobayashi, H., Biver, N., Bockelée-Morvan, D., Crovisier, J., Opitom, C. & Jehin, E., 2016*b*, *Icarus*, **266**, 152

Dello Russo, N., Vervack, R. J., Weaver, H. A., Biver, N., Bockelée-Morvan, D., Crovisier, J. & Lisse, C. M., 2007, *Nature*, **448**(7150), 172

Dello Russo, N., Vervack, R. J., Weaver, H. A., Lisse, C. M., Kawakita, H., Kobayashi, H., Cochran, A. L., Harris, W. M., Bockelée-Morvan, D., Biver, N., Crovisier, J. & McKay, A. J., 2013, *Icarus*, **222**, 707

Dello Russo, N., Vervack, Jr., R. J., Lisse, C. M., Weaver, H. A., Kawakita, H., Kobayashi, H., Cochran, A. L., Harris, W. M., McKay, A. J., Biver, N., Bockelée-Morvan, D. & Crovisier, J., 2011, *ApJL*, **734**, L8

Dennihy, E., Clemens, J. C., Debes, J. H., Dunlap, B. H., Kilkenny, D., O'Brien, P. C. & Fuchs, J. T., 2017, *ApJ*, **849**, 77

Dennihy, E., Clemens, J. C., Dunlap, B. H., Fanale, S. M., Fuchs, J. T. & Hermes, J. J., 2018, *ApJ*, **854**, 40

Dennihy, E. D., 2018, *Explorations of the Remnant Exoplanetary Debris Disks Around White Dwarf Stars*, Ph.D. thesis, The University of North Carolina at Chapel Hill

Despois, D., Crovisier, J., Bockelee-Morvan, D., Gerard, E. & Schraml, J., 1986, *A&A*, **160**, L11

DiSanti, M. A., Bonev, B. P., Villanueva, G. L. & Mumma, M. J., 2013, *ApJ*, **763**, 1

DiSanti, M. A., Villanueva, G. L., Paganini, L., Bonev, B. P., Keane, J. V., Meech, K. J. & Mumma, M. J., 2014, *Icarus*, **228**, 167

Dones, L., Brasser, R., Kaib, N. & Rickman, H., 2015, *Space Science Reviews*, **197**(1-4), 191

Draine, B. T., 1978, *ApJSS*, **36**, 595

Drake, A. J., Djorgovski, S. G., Mahabal, A., Beshore, E., Larson, S., Graham, M. J., Williams, R., Christensen, E., Catelan, M., Boattini, A., Gibbs, A., Hill, R. & Kowalski, R., 2009, *ApJ*, **696**, 870

Dufour, P., Bergeron, P., Liebert, J., Harris, H. C., Knapp, G. R., Anderson, S. F., Hall, P. B., Strauss, M. A., Collinge, M. J. & Edwards, M. C., 2007, *ApJ*, **663**, 1291

Dufour, P., Kilic, M., Fontaine, G., Bergeron, P., Lachapelle, F. R., Kleinman, S. J. & Leggett, S. K., 2010, *ApJ*, **719**, 803

Dulieu, F., Minissale, M. & Bockelée-Morvan, D., 2017, *A&A*, **597**, A56

Eberhardt, P., 1999, *Space Science Reviews*, **90**, 45

Eberhardt, P., Krankowsky, D., Schulte, W., Dolder, U., Lammerzahl, P., Berthelier, J. J., Woweries, J., Stubbemann, U., Hodges, R. R., Hoffman, J. H. & Illiano, J. M., 1987, *A&A*, **187**, 481

Eberhardt, P., Reber, M., Krankowsky, D. & Hodges, R. R., 1995, *A&A*, **302**, 301

Eggen, O. J. & Greenstein, J. L., 1965*a*, *ApJ*, **142**, 925

Eggen, O. J. & Greenstein, J. L., 1965*b*, *ApJ*, **141**, 83

El-Badry, K. & Rix, H.-W., 2018, *MNRAS*, **480**, 4884

El-Badry, K., Rix, H.-W. & Weisz, D. R., 2018, *ApJ*, **860**(2), L17

Emprechtinger, M., Lis, D. C., Bell, T., Phillips, T. G., Schilke, P., Comito, C., Rolffs, R., van der Tak, F., Ceccarelli, C., Aarts, H., Bacmann, A., Baudry, A., Benedettini, M., Bergin, E. A., Blake, G., Boogert, A., Bottinelli, S., Cabrit, S., Caselli, P., Castets, A., Caux, E., Cernicharo, J., Codella, C., Coutens, A., Crimier, N., Demyk, K., Dominik, C., Encrenaz, P., Falgarone, E., Fuente, A., Gerin, M., Goldsmith, P., Helmich, F., Hennebelle, P., Henning, T., Herbst, E., Hily-Blant, P., Jacq, T., Kahane, C., Kama, M., Klotz, A., Kooi, J., Langer, W., Lefloch, B., Loose, A., Lord, S., Lorenzani, A., Maret, S., Melnick, G., Neufeld, D., Nisini, B., Ossenkopf, V., Pacheco, S., Pagani, L., Parise, B., Pearson, J., Risacher, C., Salez, M., Saraceno, P., Schuster, K., Stutzki, J., Tielens, X., van der Wiel, M., Vastel, C., Viti, S., Wakelam, V., Walters, A., Wyrowski, F. & Yorke, H., 2010, *A&A*, **521**, L28

Epchtein, N., Deul, E., Derriere, S., Borsenberger, J., Egret, D., Simon, G., Alard, C., Balázs, L. G., de Batz, B., Cioni, M.-R., Copet, E., Dennefeld, M., Forveille, T., Fouqué, P., Garzón, F., Habing, H. J., Holl, A., Hron, J., Kimeswenger, S., Lacombe, F., Le Bertre, T., Loup, C., Mamon, G. A., Omont, A., Paturel, G., Persi, P., Robin, A. C., Rouan, D., Tiphène, D., Vauglin, I. & Wagner, S. J., 1999, *A&A*, **349**, 236

Farihi, J., 2009, *MNRAS*, **398**, 2091

Farihi, J., Becklin, E. E. & Zuckerman, B., 2005, *ApJSS*, **161**, 394

Farihi, J., Bond, H. E., Dufour, P., Haghighipour, N., Schaefer, G. H., Holberg, J. B., Barstow, M. A. & Burleigh, M. R., 2013*a*, *MNRAS*, **430**, 652

Farihi, J., Brinkworth, C. S., Gänsicke, B. T., Marsh, T. R., Girven, J., Hoard, D. W., Klein, B. & Koester, D., 2011, *ApJ*, **728**(1), L8

Farihi, J., Gänsicke, B. T. & Koester, D., 2013*b*, *Science*, **342**(6155), 218

Farihi, J., Gänsicke, B. T., Steele, P. R., Girven, J., Burleigh, M. R., Breedt, E. & Koester, D., 2012*a*, *MNRAS*, **421**, 1635

Farihi, J., Gänsicke, B. T., Wyatt, M. C., Girven, J., Pringle, J. E. & King, A. R., 2012*b*, *MNRAS*, **424**, 464

Farihi, J., Jura, M., Lee, J.-E. & Zuckerman, B., 2010, *ApJ*, **714**, 1386

Farihi, J., Jura, M. & Zuckerman, B., 2009, *ApJ*, **694**, 805

Farihi, J., Parsons, S. G. & Gänsicke, B. T., 2017, *Nature Astronomy*, **1**, 0032

Farihi, J., van Lieshout, R., Cauley, P. W., Dennihy, E., Su, K. Y. L., Kenyon, S. J., Wilson, T. G., Toloza, O., Gänsicke, B. T., von Hippel, T., Redfield, S., Debes, J. H., Xu, S., Rogers, L., Bonsor, A., Swan, A., Pala, A. F. & Reach, W. T., 2018, *MNRAS*, **481**, 2601

Farihi, J., Wyatt, M. C., Greaves, J. S., Bonsor, A., Sibthorpe, B. & Panić, O., 2014, *MNRAS*, **444**(2), 1821

Farihi, J., Zuckerman, B. & Becklin, E. E., 2008, *ApJ*, **674**, 431

Fatuzzo, M. & Adams, F. C., 2014, *ApJ*, **787**(1), 26

Fazio, G. G., Hora, J. L., Allen, L. E., Ashby, M. L. N., Barmby, P., Deutsch, L. K., Huang, J.-S., Kleiner, S., Marengo, M., Megeath, S. T., Melnick, G. J., Pahre, M. A., Patten, B. M., Polizotti, J., Smith, H. A., Taylor, R. S., Wang, Z., Willner, S. P., Hoffmann, W. F., Pipher, J. L., Forrest, W. J., McMurty, C. W., McCreight, C. R., McKelvey, M. E., McMurray, R. E., Koch, D. G., Moseley, S. H., Arendt, R. G., Mentzell,

J. E., Marx, C. T., Losch, P., Mayman, P., Eichhorn, W., Krebs, D., Jhabvala, M., Gezari, D. Y., Fixsen, D. J., Flores, J., Shakoorzadeh, K., Jungo, R., Hakun, C., Workman, L., Karpati, G., Kichak, R., Whitley, R., Mann, S., Tollestrup, E. V., Eisenhardt, P., Stern, D., Gorjian, V., Bhattacharya, B., Carey, S., Nelson, B. O., Glaccum, W. J., Lacy, M., Lowrance, P. J., Laine, S., Reach, W. T., Stauffer, J. A., Surace, J. A., Wilson, G., Wright, E. L., Hoffman, A., Domingo, G. & Cohen, M., 2004, *ApJSS*, **154**, 10

Feaga, L. M., A'Hearn, M. F., Farnham, T. L., Bodewits, D., Sunshine, J. M., Gersch, A. M., Protopapa, S., Yang, B., Drahus, M. & Schleicher, D. G., 2014, *AJ*, **147**, 24

Feldman, P. D., 2005, *Physica Scripta Volume T*, **119**, 7

Feldman, P. D., Cochran, A. L. & Combi, M. R., 2004, *Spectroscopic investigations of fragment species in the coma* (University of Arizona Press), chapter 2, pp. 425–447

Feldman, P. D., Festou, M. C., Tozzi, P. & Weaver, H. A., 1997, *ApJ*, **475**, 829

Feldman, P. D., Lupu, R. E., McCandliss, S. R. & Weaver, H. A., 2009, *ApJ*, **699**, 1104

Ferguson, D. H., Green, R. F. & Liebert, J., 1984, *ApJ*, **287**, 320

Festou, M. C., 1990, *Variations of the Gaseous Output of the Nucleus of Comet Halley* (Ellis Horwood Ltd), chapter 3, p. 245

Festou, M. C., 1998, in W. Wamsteker, R. Gonzalez Riestra & B. Harris (eds.), *Ultraviolet Astrophysics Beyond the IUE Final Archive*, volume 413 of *ESA Special Publication*, p. 45

Filacchione, G., Raponi, A., Capaccioni, F., Ciarniello, M., Tosi, F., Capria, M. T., De Sanctis, M. C., Migliorini, A., Piccioni, G. & Cerroni, P., 2016, *Science*, **354**(6319), 1563

Fink, U., 2009, *Icarus*, **201**, 311

Fink, U., Doose, L., Rinaldi, G., Bieler, A., Capaccioni, F., Bockelée-Morvan, D., Filacchione, G., Erard, S., Leyrat, C., Blecka, M., Capria, M. T., Combi, M., Crovisier, J., De Sanctis, M. C., Fougere, N., Taylor, F., Migliorini, A. & Piccioni, G., 2016, *Icarus*, **277**, 78

Fink, U. & Hicks, M. D., 1996, *ApJ*, **459**, 729

Flaherty, K. M., Muzerolle, J., Rieke, G., Gutermuth, R., Balog, Z., Herbst, W. & Megeath, S. T., 2013, *AJ*, **145**, 66

Fontaine, G., Brassard, P. & Bergeron, P., 2001, *PASP*, **113**, 409

Fougere, N., Altwegg, K., Berthelier, J. J., Bieler, A., Bockelée-Morvan, D., Calmonte, U., Capaccioni, F., Combi, M. R., De Keyser, J. & Debout, V., 2016, *MNRAS*, **462**, S156

Frewen, S. F. N. & Hansen, B. M. S., 2014, *MNRAS*, **439**, 2442

Fulle, M., 2004, *Motion of cometary dust*, p. 565

Fulle, M., Della Corte, V., Rotundi, A., Rietmeijer, F. J. M., Green, S. F., Weissman, P., Accolla, M., Colangeli, L., Ferrari, M. & Ivanovski, S., 2016, *MNRAS*, **462**, S132

Gänsicke, B. T., Aungwerojwit, A., Marsh, T. R., Dhillon, V. S., Sahman, D. I., Veras, D., Farihi, J., Chote, P., Ashley, R., Arjyotha, S., Rattanasoon, S., Littlefair, S. P., Pollacco, D. & Burleigh, M. R., 2016, *ApJL*, **818**, L7

Gänsicke, B. T., Koester, D., Farihi, J., Girven, J., Parsons, S. G. & Breedt, E., 2012, *MNRAS*, **424**, 333

Gänsicke, B. T., Koester, D., Marsh, T. R., Rebassa-Mansergas, A. & Southworth, J., 2008, *MNRAS*, **391**, L103

Gänsicke, B. T., Marsh, T. R. & Southworth, J., 2007, *MNRAS*, **380**, L35

Gänsicke, B. T., Marsh, T. R., Southworth, J. & Rebassa-Mansergas, A., 2006, *Science*, **314**, 1908

Gentile Fusillo, N. P., Tremblay, P.-E., Gänsicke, B. T., Manser, C. J., Cunningham, T., Cukanovaite, E., Hollands, M., Marsh, T., Raddi, R., Jordan, S., Toonen, S., Geier, S., Barstow, M. & Cummings, J. D., 2019, *MNRAS*, **482**, 4570

Giammichele, N., Bergeron, P. & Dufour, P., 2012, *ApJSS*, **199**, 29

Gianninas, A., Bergeron, P. & Fontaine, G., 2006, *AJ*, **132**, 831

Gianninas, A., Bergeron, P. & Ruiz, M. T., 2011, *ApJ*, **743**, 138

Gianninas, A., Dufour, P. & Bergeron, P., 2004, *ApJ*, **617**(1), L57

Gibb, E. L., Bonev, B. P., Villanueva, G., DiSanti, M. A., Mumma, M. J., Sudholt, E. & Radeva, Y., 2012, *ApJ*, **750**(2), 102

Gibb, E. L., Mumma, M. J., Dello Russo, N., DiSanti, M. A. & Magee-Sauer, K., 2003, *Icarus*, **165**, 391

Gicquel, A., Milam, S. N., Villanueva, G. L., Remijan, A. J., Coulson, I. M., Chuang, Y.-L., Charnley, S. B., Cordiner, M. A. & Kuan, Y.-J., 2014, *ApJ*, **794**, 1

Gicquel, A., Vincent, J.-B., Agarwal, J., A'Hearn, M. F., Bertini, I., Bodewits, D., Sierks, H., Lin, Z.-Y., Barbieri, C., Lamy, P. L., Rodrigo, R., Koschny, D., Rickman, H., Keller, H. U., Barucci, M. A., Bertaux, J.-L., Besse, S., Cremonese, G., Da Deppo, V., Davidsson, B., Debei, S., Deller, J., De Cecco, M., Frattin, E., El-Maarry, M. R., Fornasier, S., Fulle, M., Groussin, O., Gutiérrez, P. J., Gutiérrez-Marquez, P., Güttler, C., Höfner, S., Hofmann, M., Hu, X., Hviid, S. F., Ip, W.-H., Jorda, L., Knollenberg, J., Kovacs, G., Kramm, J.-R., Kührt, E., Küppers, M., Lara, L. M., Lazzarin, M., Moreno, J. J. L., Lowry, S., Marzari, F., Masoumzadeh, N., Massironi, M., Moreno, F., Mottola, S., Naletto, G., Oklay, N., Pajola, M., Pommerol, A., Preusker, F., Scholten, F., Shi, X., Thomas, N., Toth, I. & Tubiana, C., 2016, *MNRAS*, **462**, S57

Gillon, M., Triaud, A. H. M. J., Demory, B.-O., Jehin, E., Agol, E., Deck, K. M., Lederer, S. M., de Wit, J., Burdanov, A., Ingalls, J. G., Bolmont, E., Leconte, J., Raymond, S. N., Selsis, F., Turbet, M., Barkaoui, K., Burgasser, A., Burleigh, M. R., Carey, S. J., Chaushev, A., Copperwheat, C. M., Delrez, L., Fernandes, C. S., Holdsworth, D. L., Kotze, E. J., Van Grootel, V., Almleaky, Y., Benkhaldoun, Z., Magain, P. & Queloz, D., 2017, *Nature*, **542**, 456

Girven, J., Brinkworth, C. S., Farihi, J., Gänsicke, B. T., Hoard, D. W., Marsh, T. R. & Koester, D., 2012, *ApJ*, **749**(2), 154

Girven, J., Gänsicke, B. T., Steeghs, D. & Koester, D., 2011, *MNRAS*, **417**, 1210

Goldsmith, P. F., Liseau, R., Bell, T. A., Black, J. H., Chen, J.-H., Hollenbach, D., Kaufman, M. J., Li, D., Lis, D. C. & Melnick, G., 2011, *ApJ*, **737**(2), 96

Gomes, R., Levison, H. F., Tsiganis, K. & Morbidelli, A., 2005, *Nature*, **435**(7041), 466

Greenstein, J. L., 1974, *AJ*, **79**, 964

Greenstein, J. L., 1976, *AJ*, **81**, 323

Greenstein, J. L., 1984, *ApJ*, **276**, 602

Griffin, M. J., Abergel, A., Abreu, A., Ade, P. A. R., André, P., Augueres, J.-L., Babbedge, T., Bae, Y., Baillie, T., Baluteau, J.-P., Barlow, M. J., Bendo, G., Benielli, D., Bock, J. J., Bonhomme, P., Brisbin, D., Brockley-Blatt, C., Caldwell, M., Cara, C., Castro-Rodriguez, N., Cerulli, R., Chanial, P., Chen, S., Clark, E., Clements, D. L., Clerc, L., Coker, J., Communal, D., Conversi, L., Cox, P., Crumb, D., Cunningham, C., Daly, F., Davis, G. R., de Antoni, P., Delderfield, J., Devin, N., di Giorgio, A., Didschuns, I., Dohlen, K., Donati, M., Dowell, A., Dowell, C. D., Duband, L., Dumaye, L., Emery, R. J., Ferlet, M., Ferrand, D., Fontignie, J., Fox, M., Franceschini, A., Frerking, M., Fulton, T., Garcia, J., Gastaud, R., Gear, W. K., Glenn, J., Goizel, A., Griffin, D. K., Grundy, T., Guest, S., Guillemet, L., Hargrave, P. C., Harwit, M., Hastings, P., Hatziminaoglou, E., Herman, M., Hinde, B., Hristov, V., Huang, M., Imhof, P., Isaak, K. J., Israelsson, U., Ivison, R. J., Jennings, D., Kiernan, B., King, K. J., Lange, A. E., Latter, W., Laurent, G., Laurent, P., Leeks, S. J., Lellouch, E., Levenson, L., Li, B., Li, J., Lilienthal, J., Lim, T., Liu, S. J., Lu, N., Madden, S., Mainetti, G., Marliani, P., McKay, D., Mercier, K., Molinari, S., Morris, H., Moseley, H., Mulder, J., Mur, M., Naylor, D. A., Nguyen, H., O'Halloran, B., Oliver, S., Olofsson, G., Olofsson, H.-G., Orfei, R., Page, M. J., Pain, I., Panuzzo, P., Papageorgiou, A., Parks, G., Parr-Burman, P., Pearce, A., Pearson, C., Pérez-Fournon, I., Pinsard, F., Pisano, G., Podosek, J., Pohlen, M., Polehampton, E. T., Pouliquen, D., Rigopoulou, D., Rizzo, D., Roseboom, I. G., Roussel, H., Rowan-Robinson, M., Rownd, B., Saraceno, P., Sauvage, M., Savage, R., Savini, G., Sawyer, E., Scharmberg, C., Schmitt, D., Schneider, N., Schulz, B., Schwartz, A., Shafer, R., Shupe, D. L., Sibthorpe, B., Sidher, S., Smith, A., Smith, A. J., Smith, D., Spencer, L., Stobie, B., Sudiwala, R., Sukhatme, K., Surace, C., Stevens, J. A., Swinyard, B. M., Trichas, M., Tourette, T., Triou, H., Tseng, S., Tucker, C., Turner, A., Vaccari, M., Valtchanov, I., Vigroux, L., Virique, E., Voellmer, G., Walker, H., Ward, R., Waskett, T., Weilert, M., Wesson, R., White, G. J., Whitehouse, N., Wilson, C. D., Winter, B., Woodcraft, A. L., Wright, G. S., Xu, C. K., Zavagno, A., Zemcov, M., Zhang, L. & Zonca, E., 2010, *A&A*, **518**, L3

Guilbert-Lepoutre, A., Besse, S., Mousis, O., Ali-Dib, M., Höfner, S., Koschny, D. & Hager, P., 2015, *Space Science Reviews*, **197**(1-4), 271

Gulkis, S., Allen, M., von Allmen, P., Beaudin, G., Biver, N., Bockelée-Morvan, D., Choukroun, M., Crovisier, J., Davidsson, B. J. R. & Encrenaz, P., 2015, *Science*,

347(6220), aaa0709

Guo, J., Tziamtzis, A., Wang, Z., Liu, J., Zhao, J. & Wang, S., 2015, *ApJL*, **810**, L17

Hallakoun, N., Xu, S., Maoz, D., Marsh, T. R., Ivanov, V. D., Dhillon, V. S., Bours, M. C. P., Parsons, S. G., Kerry, P. & Sharma, S., 2017, *MNRAS*, **469**(3), 3213

Hallam, H., 1973, *Vibrational Spectroscopy of Trapped Species: Infrared and Raman Studies of Matrix-isolated Molecules, Radicals and Ions*, A Wiley-Interscience publication (J. Wiley)
URL: *https://books.google.co.uk/books?id=HCBPAQAAIAAJ*

Halley, E., 1705, *A Synopsis of the Astronomy of Comets*

Hama, T., Kouchi, A. & Watanabe, N., 2016, *Science*, **351**, 65

Hama, T., Kouchi, A. & Watanabe, N., 2018, *ApJL*, **857**(2), L13

Hama, T. & Watanabe, N., 2013, *Chem. Rev.*, **113**, 8783

Hamers, A. S. & Portegies Zwart, S. F., 2016, *MNRAS*, **462**, L84

Hansen, B. M. S., Kulkarni, S. & Wiktorowicz, S., 2006, *AJ*, **131**(2), 1106

Hartogh, P., Crovisier, J., de Val-Borro, M., Bockelée-Morvan, D., Biver, N., Lis, D. C., Moreno, R., Jarchow, C., Rengel, M., Emprechtinger, M., Szutowicz, S., Banaszkiewicz, M., Bensch, F., Blecka, M. I., Cavalié, T., Encrenaz, T., Jehin, E., Küppers, M., Lara, L.-M., Lellouch, E., Swinyard, B. M., Vandenbussche, B., Bergin, E. A., Blake, G. A., Blommaert, J. A. D. L., Cernicharo, J., Decin, L., Encrenaz, P., de Graauw, T., Hutsemekers, D., Kidger, M., Manfroid, J., Medvedev, A. S., Naylor, D. A., Schieder, R., Thomas, N., Waelkens, C., Roelfsema, P. R., Dieleman, P., Güsten, R., Klein, T., Kasemann, C., Caris, M., Olberg, M. & Benz, A. O., 2010, *A&A*, **518**, L150

Hartogh, P., Lellouch, E., Crovisier, J., Banaszkiewicz, M., Bensch, F., Bergin, E. A., Billebaud, F., Biver, N., Blake, G. A., Blecka, M. I., Blommaert, J., Bockelée-Morvan, D., Cavalié, T., Cernicharo, J., Courtin, R., Davis, G., Decin, L., Encrenaz, P., Encrenaz, T., González, A., de Graauw, T., Hutsemékers, D., Jarchow, C., Jehin, E., Kidger, M., Küppers, M., de Lange, A., Lara, L.-M., Lis, D. C., Lorente, R., Manfroid, J., Medvedev, A. S., Moreno, R., Naylor, D. A., Orton, G., Portyankina, G., Rengel, M., Sagawa, H.,

Sánchez-Portal, M., Schieder, R., Sidher, S., Stam, D., Swinyard, B., Szutowicz, S., Thomas, N., Thornhill, G., Vandenbussche, B., Verdugo, E., Waelkens, C. & Walker, H., 2009, *Planetary Space Science*, **57**, 1596

Hartogh, P., Lis, D. C., Bockelée-Morvan, D., de Val-Borro, M., Biver, N., Küppers, M., Emprechtinger, M., Bergin, E. A., Crovisier, J., Rengel, M., Moreno, R., Szutowicz, S. & Blake, G. A., 2011, *Nature*, **478**, 218

Haser, L., 1957, *Bulletin de la Societe Royale des Sciences de Liege*, **43**, 740

Hässig, M., Altwegg, K., Balsiger, H., Bar-Nun, A., Berthelier, J. J., Bieler, A., Bochsler, P., Briois, C., Calmonte, U., Combi, M., De Keyser, J., Eberhardt, P., Fiethe, B., Fuselier, S. A., Galand, M., Gasc, S., Gombosi, T. I., Hansen, K. C., Jäckel, A., Keller, H. U., Kopp, E., Korth, A., Kührt, E., Le Roy, L., Mall, U., Marty, B., Mousis, O., Neefs, E., Owen, T., Rème, H., Rubin, M., Sémon, T., Tornow, C., Tzou, C.-Y., Waite, J. H. & Wurz, P., 2015, *Science*, **347**(1), aaa0276

Henden, A. A., Templeton, M., Terrell, D., Smith, T. C., Levine, S. & Welch, D., 2016, *VizieR Online Data Catalog*, **2336**

Herschel Science Centre., 2014, *SPIRE Handbook 2016, Herschel Explanatory Supplement vol. 2.5*, HERSCHEL-DOC-0798

Hindmarsh, A., 1982, *ODEPACK, a Systematized Collection of ODE Solvers* (Lawrence Livermore National Laboratory)
URL: *https://books.google.co.uk/books?id=9XWPmwEACAAJ*

Hirabayashi, M., Scheeres, D. J., Chesley, S. R., Marchi, S., McMahon, J. W., Steckloff, J., Mottola, S., Naidu, S. P. & Bowling, T., 2016, *Nature*, **534**(7607), 352

Hoard, D. W., Debes, J. H., Wachter, S., Leisawitz, D. T. & Cohen, M., 2013, *ApJ*, **770**(1), 21

Hoard, D. W., Wachter, S., Sturch, L. K., Widhalm, A. M., Weiler, K. P., Pretorius, M. L., Wellhouse, J. W. & Gibiansky, M., 2007, *AJ*, **134**, 26

Hogerheijde, M. R. & van der Tak, F. F. S., 2000, *A&A*, **362**, 697

Hollands, M. A., Gänsicke, B. T. & Koester, D., 2018*a*, *MNRAS*, **477**, 93

Hollands, M. A., Koester, D., Alekseev, V., Herbert, E. L. & Gänsicke, B. T., 2017, *MNRAS*, **467**, 4970

Hollands, M. A., Tremblay, P.-E., Gänsicke, B. T., Gentile-Fusillo, N. P. & Toonen, S., 2018*b*, *MNRAS*, **480**, 3942

Hollenbach, D., Kaufman, M. J., Bergin, E. A. & Melnick, G. J., 2009, *ApJ*, **690**(2), 1497

Huggins, W., 1868, *Philosophical Transactions of the Royal Society of London Series I*, **158**, 529

Hutsemékers, D., Manfroid, J., Jehin, E., Zucconi, J.-M. & Arpigny, C., 2008, *A&A*, **490**, L31

Hyland, M. G., Fitzsimmons, A. & Snodgrass, C., 2019, *MNRAS*, 60

Ip, W. H., 2004, *Global solar wind interaction and ionospheric dynamics*, p. 605

Irvine, W. M., Schloerb, F. P., Crovisier, J., Fegley, Jr., B. & Mumma, M. J., 2000, *Comets: a Link Between Interstellar and Nebular Chemistry* (University of Arizona Press, Tucson), chapter 8, p. 1159

Jehin, E., Manfroid, J., Kawakita, H., Hutsemékers, D., Weiler, M., Arpigny, C., Cochran, A., Hainaut, O., Rauer, H., Schulz, R. & Zucconi, J.-M., 2008, in *Asteroids, Comets, Meteors 2008*, volume 1405 of *LPI Contributions*, p. 8319

Jewitt, D., Matthews, H. E., Owen, T. & Meier, R., 1997, *Science*, **278**, 90

Jones, G. H., Knight, M. M., Fitzsimmons, A. & Taylor, M. G. G. T., 2017, *Philosophical Transactions of the Royal Society of London Series A*, **375**(2097), 20170001

Jordan, S., Koester, D., Vauclair, G., Dolez, N., Heber, U., Hagen, H. J., Reimers, D., Chevreton, M. & Dreizler, S., 1998, *A&A*, **330**, 277

Jura, M., 2003, *ApJL*, **584**, L91

Jura, M., 2008, *AJ*, **135**, 1785

Jura, M., Dufour, P., Xu, S., Zuckerman, B., Klein, B., Young, E. D. & Melis, C., 2015, *ApJ*, **799**, 109

Jura, M., Farihi, J. & Zuckerman, B., 2007*a*, *ApJ*, **663**, 1285

Jura, M., Farihi, J. & Zuckerman, B., 2009, *AJ*, **137**, 3191

Jura, M., Farihi, J., Zuckerman, B. & Becklin, E. E., 2007*b*, *AJ*, **133**(5), 1927

Jura, M. & Xu, S., 2012, *AJ*, **143**(1), 6

Jura, M. & Xu, S., 2013, *AJ*, **145**(2), 30

Jura, M. & Young, E. D., 2014, *Annual Review of Earth and Planetary Sciences*, **42**, 45

Jutzi, M. & Benz, W., 2017, *A&A*, **597**, A62

Karl, C., Napiwotzki, R., Heber, U., Lisker, T., Nelemans, G., Christlieb, N. & Reimers, D., 2003, in D. de Martino, R. Silvotti, J.-E. Solheim & R. Kalytis (eds.), *NATO ASIB Proc. 105: White Dwarfs*, volume 105, p. 43

Kawakita, H., Dello Russo, N., Furusho, R., Fuse, T., Watanabe, J.-i., Boice, D. C., Sadakane, K., Arimoto, N., Ohkubo, M. & Ohnishi, T., 2006, *ApJ*, **643**(2), 1337

Kawakita, H., Dello Russo, N., Vervack, Jr., R., Kobayashi, H., DiSanti, M. A., Opitom, C., Jehin, E., Weaver, H. A., Cochran, A. L., Harris, W. M., Bockelée-Morvan, D., Biver, N., Crovisier, J., McKay, A. J., Manfroid, J. & Gillon, M., 2014, *ApJ*, **788**, 110

Kawakita, H. & Kobayashi, H., 2009, *ApJ*, **693**, 388

Kawakita, H., Kobayashi, H., Dello Russo, N., Vervack, R. J., Hashimoto, M., Weaver, H. A., Lisse, C. M., Cochran, A. L., Harris, W. M., Bockelée-Morvan, D., Biver, N., Crovisier, J. & McKay, A. J., 2013, *Icarus*, **222**, 723

Kawakita, H., Watanabe, J.-i., Ando, H., Aoki, W., Fuse, T., Honda, S., Izumiura, H., Kajino, T., Kambe, E., Kawanomoto, S., Noguchi, K., Okita, K., Sadakane, K., Sato, B., Takada-Hidai, M., Takeda, Y., Usuda, T., Watanabe, E. & Yoshida, M., 2001, *Science*, **294**, 1089

Kawakita, H., Watanabe, J.-i., Furusho, R., Fuse, T., Capria, M. T., De Sanctis, M. C. & Cremonese, G., 2004, *ApJ*, **601**, 1152

Kawakita, H., Watanabe, J.-I., FUSE, T., Furusho, R. & Abe, S., 2002, *Earth Moon and Planets*, **90**, 371

Kawka, A. & Vennes, S., 2016, *MNRAS*, **458**, 325

Keller, H. U., Mottola, S., Davidsson, B., Schröder, S. E., Skorov, Y., Kührt, E., Groussin, O., Pajola, M., Hviid, S. F. & Preusker, F., 2015, *A&A*, **583**, A34

Kennedy, G. M. & Wyatt, M. C., 2012, *MNRAS*, **426**, 91

Kenyon, S. J. & Bromley, B. C., 2017*a*, *ApJ*, **844**, 116

Kenyon, S. J. & Bromley, B. C., 2017*b*, *ApJ*, **850**, 50

Kenyon, S. J. & Bromley, B. C., 2017*c*, *ApJ*, **839**, 38

Keto, E. & Caselli, P., 2010, *MNRAS*, **402**(3), 1625

Kidder, K. M., Holberg, J. B. & Mason, P. A., 1991, *AJ*, **101**, 579

Kilic, M., Farihi, J., Nitta, A. & Leggett, S. K., 2008, *AJ*, **136**, 111

Kilic, M., Patterson, A. J., Barber, S., Leggett, S. K. & Dufour, P., 2012, *MNRAS*, **419**, L59

Kilic, M. & Redfield, S., 2007, *ApJ*, **660**(1), 641

Kilic, M., von Hippel, T., Leggett, S. K. & Winget, D. E., 2006, *ApJ*, **646**(1), 474

Kleinman, S. J., Kepler, S. O., Koester, D., Pelisoli, I., Peçanha, V., Nitta, A., Costa, J. E. S., Krzesinski, J., Dufour, P. & Lachapelle, F. R., 2013, *ApJSS*, **204**(1), 5

Knight, M. M. & Schleicher, D. G., 2013, *Icarus*, **222**, 691

Kobayashi, H., Kawakita, H., Mumma, M. J., Bonev, B. P., Watanabe, J.-i. & Fuse, T., 2007, *ApJL*, **668**, L75

Koester, D., 2009, *A&A*, **498**, 517

Koester, D., 2010, *Mem. Societa Astronomica Italiana*, **81**, 921

Koester, D., 2013, *White Dwarf Stars* (Springer Science), volume 4, chapter 11, pp. 559–612

Koester, D., Gänsicke, B. T. & Farihi, J., 2014, *A&A*, **566**, A34

Koester, D., Girven, J., Gänsicke, B. T. & Dufour, P., 2011, *A&A*, **530**, A114

Koester, D. & Kepler, S. O., 2019, *arXiv e-prints*, arXiv:1905.11174

Koester, D., Napiwotzki, R., Voss, B., Homeier, D. & Reimers, D., 2005*a*, *A&A*, **439**(1), 317

Koester, D., Provencal, J. & Shipman, H. L., 1997, *A&A*, **320**, L57

Koester, D., Rollenhagen, K., Napiwotzki, R., Voss, B., Christlieb, N., Homeier, D. & Reimers, D., 2005*b*, *A&A*, **432**, 1025

Koester, D., Voss, B., Napiwotzki, R., Christlieb, N., Homeier, D., Lisker, T., Reimers, D. & Heber, U., 2009, *A&A*, **505**, 441

Koester, D., Weidemann, V. & Zeidler, E. M., 1982, *A&A*, **116**, 147

Koester, D. & Wilken, D., 2006, *A&A*, **453**(3), 1051

Kuyanov-Prozument, K., Choi, M. Y. & Vilesov, A. F., 2010, *The Journal of Chemical Physics*, **132**(1), 014304
URL: *https://doi.org/10.1063/1.3276459*

Langland-Shula, L. E. & Smith, G. H., 2011, *Icarus*, **213**, 280

Lawrence, A., Warren, S. J., Almaini, O., Edge, A. C., Hambly, N. C., Jameson, R. F., Lucas, P., Casali, M., Adamson, A., Dye, S., Emerson, J. P., Foucaud, S., Hewett, P., Hirst, P., Hodgkin, S. T., Irwin, M. J., Lodieu, N., McMahon, R. G., Simpson, C., Smail, I., Mortlock, D. & Folger, M., 2007, *MNRAS*, **379**, 1599

Lecacheux, A., Biver, N., Crovisier, J., Bockelée-Morvan, D., Baron, P., Booth, R. S., Encrenaz, P., Florén, H.-G., Frisk, U., Hjalmarson, Å., Kwok, S., Mattila, K., Nordh, L., Olberg, M., Olofsson, A. O. H., Rickman, H., Sandqvist, A., von Schéele, F., Serra, G., Torchinsky, S., Volk, K. & Winnberg, A., 2003, *A&A*, **402**, L55

Lellouch, E., Crovisier, J., Lim, T., Bockelee-Morvan, D., Leech, K., Hanner, M. S., Altieri, B., Schmitt, B., Trotta, F. & Keller, H. U., 1998, *A&A*, **339**, L9

Liebert, J., Bergeron, P. & Holberg, J. B., 2005, *ApJSS*, **156**, 47

Limbach, H.-H., Buntkowsky, G., Matthes, J., Grndemann, S., Pery, T., Walaszek, B. & Chaudret, B., 2006, *ChemPhysChem*, **7**(3), 551
URL: *https://onlinelibrary.wiley.com/doi/abs/10.1002/cphc.200500559*

Lis, D. C., Bergin, E. A., Schilke, P. & van Dishoeck, E. F., 2013*a*, *J. Phys. Chem. A*, **117**, 9661

Lis, D. C., Biver, N., Bockelée-Morvan, D., Hartogh, P., Bergin, E. A., Blake, G. A., Crovisier, J., de Val-Borro, M., Jehin, E., Küppers, M., Manfroid, J., Moreno, R., Rengel, M. & Szutowicz, S., 2013*b*, *ApJL*, **774**, L3

Lis, D. C., Phillips, T. G., Goldsmith, P. F., Neufeld, D. A., Herbst, E., Comito, C., Schilke, P., Müller, H. S. P., Bergin, E. A., Gerin, M., Bell, T. A., Emprechtinger, M., Black, J. H., Blake, G. A., Boulanger, F., Caux, E., Ceccarelli, C., Cernicharo, J., Coutens, A., Crockett, N. R., Daniel, F., Dartois, E., de Luca, M., Dubernet, M.-L., Encrenaz, P., Falgarone, E., Geballe, T. R., Godard, B., Giesen, T. F., Goicoechea, J. R., Gry, C., Gupta, H., Hennebelle, P., Hily-Blant, P., Kołos, R., Krełowski, J., Joblin, C., Johnstone, D., Kaźmierczak, M., Lord, S. D., Maret, S., Martin, P. G., Martín-Pintado, J., Melnick, G. J., Menten, K. M., Monje, R., Mookerjea, B., Morris, P., Murphy, J. A., Ossenkopf, V., Pearson, J. C., Pérault, M., Persson, C., Plume, R., Qin, S.-L., Salez, M., Schlemmer, S., Schmidt, M., Sonnentrucker, P., Stutzki, J., Teyssier, D., Trappe, N., van der Tak, F. F. S., Vastel, C., Wang, S., Yorke, H. W., Yu, S., Zmuidzinas, J., Boogert, A., Erickson, N., Karpov, A., Kooi, J., Maiwald, F. W., Schieder, R. & Zaal, P., 2010, *A&A*, **521**, L26

Livio, M., Pringle, J. E. & Wood, K., 2005, *ApJ*, **632**(1), L37

Lodders, K., 2003, *ApJ*, **591**(2), 1220

Lupu, R. E., Feldman, P. D., Weaver, H. A. & Tozzi, G.-P., 2007, *ApJ*, **670**, 1473

Madhusudhan, N., 2019, *Ann. Rev. Astr. Astrophys.*, **57**, 617

Mainzer, A., Bauer, J., Cutri, R. M., Grav, T., Masiero, J., Beck, R., Clarkson, P., Conrow, T., Dailey, J., Eisenhardt, P., Fabinsky, B., Fajardo-Acosta, S., Fowler, J., Gelino, C., Grillmair, C., Heinrichsen, I., Kendall, M., Kirkpatrick, J. D., Liu, F., Masci, F., McCallon, H., Nugent, C. R., Papin, M., Rice, E., Royer, D., Ryan, T., Sevilla, P., Sonnett, S., Stevenson, R., Thompson, D. B., Wheelock, S., Wiemer, D., Wittman, M., Wright, E. & Yan, L., 2014, *ApJ*, **792**, 30

Mainzer, A., Bauer, J., Grav, T., Masiero, J., Cutri, R. M., Dailey, J., Eisenhardt, P., McMillan, R. S., Wright, E., Walker, R., Jedicke, R., Spahr, T., Tholen, D., Alles, R.,

Beck, R., Brandenburg, H., Conrow, T., Evans, T., Fowler, J., Jarrett, T., Marsh, K., Masci, F., McCallon, H., Wheelock, S., Wittman, M., Wyatt, P., DeBaun, E., Elliott, G., Elsbury, D., Gautier, IV, T., Gomillion, S., Leisawitz, D., Maleszewski, C., Micheli, M. & Wilkins, A., 2011, *ApJ*, **731**, 53

Mamajek, E. E., Quillen, A. C., Pecaut, M. J., Moolekamp, F., Scott, E. L., Kenworthy, M. A., Collier Cameron, A. & Parley, N. R., 2012, *AJ*, **143**(3), 72

Manca Tanner, C., Quack, M. & Schmidiger, D., 2013, *J. Phys. Chem. A*, **117**(39), 10105

Manfroid, J., Jehin, E., Hutsemékers, D., Cochran, A., Zucconi, J.-M., Arpigny, C., Schulz, R. & Stüwe, J. A., 2005, *A&A*, **432**, L5

Manser, C. J., Gänsicke, B. T., Eggl, S., Hollands, M., Izquierdo, P., Koester, D., Landstreet, J. D., Lyra, W., Marsh, T. R. & Meru, F., 2019, *Science*, **364**(6435), 66

Manser, C. J., Gänsicke, B. T., Koester, D., Marsh, T. R. & Southworth, J., 2016*a*, *MNRAS*, **462**, 1461

Manser, C. J., Gänsicke, B. T., Marsh, T. R., Veras, D., Koester, D., Breedt, E., Pala, A. F., Parsons, S. G. & Southworth, J., 2016*b*, *MNRAS*, **455**, 4467

Maoz, D. & Hallakoun, N., 2017, *MNRAS*, **467**, 1414

Maquet, L., 2015, *A&A*, **579**, A78

Marconi, M. L. & Mendis, D. A., 1984, *ApJ*, **287**, 445

Marty, B., Altwegg, K., Balsiger, H., Bar-Nun, A., Bekaert, D. V., Berthelier, J.-J., Bieler, A., Briois, C., Calmonte, U., Combi, M., De Keyser, J., Fiethe, B., Fuselier, S. A., Gasc, S., Gombosi, T. I., Hansen, K. C., Hässig, M., Jäckel, A., Kopp, E., Korth, A., Le Roy, L., Mall, U., Mousis, O., Owen, T., Rème, H., Rubin, M., Sémon, T., Tzou, C.-Y., Waite, J. H. & Wurz, P., 2017, *Science*, **356**, 1069

Massironi, M., Simioni, E., Marzari, F., Cremonese, G., Giacomini, L., Pajola, M., Jorda, L., Naletto, G., Lowry, S. & El-Maarry, M. R., 2015, *Nature*, **526**(7573), 402

Mathis, J. S., Mezger, P. G. & Panagia, N., 1983, *A&A*, **128**, 212

Maxted, P. F. L., Marsh, T. R. & Moran, C. K. J., 2000, *MNRAS*, **319**, 305

Mayor, M. & Queloz, D., 1995, *Nature*, **378**, 355

McCook, G. P. & Sion, E. M., 1999, *ApJSS*, **121**(1), 1

McGraw, J. T. & Robinson, E. L., 1975, *ApJL*, **200**, L89

McKay, A. J., Chanover, N. J., Morgenthaler, J. P., Cochran, A. L., Harris, W. M. & Russo, N. D., 2012, *Icarus*, **220**, 277

McKay, A. J., Cochran, A. L., DiSanti, M. A., Dello Russo, N., Weaver, H., Vervack, R. J., Harris, W. M. & Kawakita, H., 2018, *Icarus*, **309**, 1

McKay, A. J., Cochran, A. L., DiSanti, M. A., Villanueva, G., Russo, N. D., Vervack, R. J., Morgenthaler, J. P., Harris, W. M. & Chanover, N. J., 2015, *Icarus*, **250**, 504

Meech, K. J., A'Hearn, M. F., Adams, J. A., Bacci, P., Bai, J., Barrera, L., Battelino, M., Bauer, J. M., Becklin, E., Bhatt, B., Biver, N., Bockelée-Morvan, D., Bodewits, D., Böhnhardt, H., Boissier, J., Bonev, B. P., Borghini, W., Brucato, J. R., Bryssinck, E., Buie, M. W., Canovas, H., Castellano, D., Charnley, S. B., Chen, W. P., Chiang, P., Choi, Y.-J., Christian, D. J., Chuang, Y.-L., Cochran, A. L., Colom, P., Combi, M. R., Coulson, I. M., Crovisier, J., Dello Russo, N., Dennerl, K., DeWahl, K., DiSanti, M. A., Facchini, M., Farnham, T. L., Fernández, Y., Florén, H. G., Frisk, U., Fujiyoshi, T., Furusho, R., Fuse, T., Galli, G., García-Hernández, D. A., Gersch, A., Getu, Z., Gibb, E. L., Gillon, M., Guido, E., Guillermo, R. A., Hadamcik, E., Hainaut, O., Hammel, H. B., Harker, D. E., Harmon, J. K., Harris, W. M., Hartogh, P., Hashimoto, M., Häusler, B., Herter, T., Hjalmarson, A., Holland, S. T., Honda, M., Hosseini, S., Howell, E. S., Howes, N., Hsieh, H. H., Hsiao, H.-Y., Hutsemékers, D., Immler, S. M., Jackson, W. M., Jeffers, S. V., Jehin, E., Jones, T. J., de Juan Ovelar, M., Kaluna, H. M., Karlsson, T., Kawakita, H., Keane, J. V., Keller, L. D., Kelley, M. S., Kinoshita, D., Kiselev, N. N., Kleyna, J., Knight, M. M., Kobayashi, H., Kobulnicky, H. A., Kolokolova, L., Kreiny, M., Kuan, Y.-J., Küppers, M., Lacruz, J. M., Landsman, W. B., Lara, L. M., Lecacheux, A., Levasseur-Regourd, A. C., Li, B., Licandro, J., Ligustri, R., Lin, Z.-Y., Lippi, M., Lis, D. C., Lisse, C. M., Lovell, A. J., Lowry, S. C., Lu, H., Lundin, S., Magee-Sauer, K., Magain, P., Manfroid, J., Mazzotta Epifani, E., McKay, A., Melita, M. D., Mikuz, H., Milam, S. N., Milani, G., Min, M., Moreno, R., Mueller, B. E. A., Mumma, M. J., Nicolini, M., Nolan, M. C., Nordh, H. L., Nowajewski, P. B., Odin Team, Ootsubo, T.,

Paganini, L., Perrella, C., Pittichová, J., Prosperi, E., Radeva, Y. L., Reach, W. T., Remijan, A. J., Rengel, M., Riesen, T. E., Rodenhuis, M., Rodríguez, D. P., Russell, R. W., Sahu, D. K., Samarasinha, N. H., Sánchez Caso, A., Sandqvist, A., Sarid, G., Sato, M., Schleicher, D. G., Schwieterman, E. W., Sen, A. K., Shenoy, D., Shi, J.-C., Shinnaka, Y., Skvarc, J., Snodgrass, C., Sitko, M. L., Sonnett, S., Sosseini, S., Sostero, G., Sugita, S., Swinyard, B. M., Szutowicz, S., Takato, N., Tanga, P., Taylor, P. A., Tozzi, G.-P., Trabatti, R., Trigo-Rodríguez, J. M., Tubiana, C., de Val-Borro, M., Vacca, W., Vandenbussche, B., Vaubaillion, J., Velichko, F. P., Velichko, S. F., Vervack, Jr., R. J., Vidal-Nunez, M. J., Villanueva, G. L., Vinante, C., Vincent, J.-B., Wang, M., Wasserman, L. H., Watanabe, J., Weaver, H. A., Weissman, P. R., Wolk, S., Wooden, D. H., Woodward, C. E., Yamaguchi, M., Yamashita, T., Yanamandra-Fischer, P. A., Yang, B., Yao, J.-S., Yeomans, D. K., Zenn, T., Zhao, H. & Ziffer, J. E., 2011, *ApJL*, **734**, L1

Meidt, S. E., Hughes, A., Dobbs, C. L., Pety, J., Thompson, T. A., García-Burillo, S., Leroy, A. K., Schinnerer, E., Colombo, D., Querejeta, M., Kramer, C., Schuster, K. F. & Dumas, G., 2015, *ApJ*, **806**(1), 72

Meier, R. & A'Hearn, M. F., 1997, *Icarus*, **125**, 164

Meier, R., Owen, T. C., Matthews, H. E., Jewitt, D. C., Bockelee-Morvan, D., Biver, N., Crovisier, J. & Gautier, D., 1998, *Science*, **279**, 842

Melis, C., Dufour, P., Farihi, J., Bochanski, J., Burgasser, A. J., Parsons, S. G., Gänsicke, B. T., Koester, D. & Swift, B. J., 2012*a*, *ApJ*, **751**, L4

Melis, C., Farihi, J., Dufour, P., Zuckerman, B., Burgasser, A. J., Bergeron, P., Bochanski, J. & Simcoe, R., 2011, *ApJ*, **732**(2), 90

Melis, C., Jura, M., Albert, L., Klein, B. & Zuckerman, B., 2010, *ApJ*, **722**(2), 1078

Melis, C., Zuckerman, B., Rhee, J. H., Song, I., Murphy, S. J. & Bessell, M. S., 2012*b*, *Nature*, **487**, 74

Meng, H. Y. A., Su, K. Y. L., Rieke, G. H., Rujopakarn, W., Myers, G., Cook, M., Erdelyi, E., Maloney, C., McMath, J., Persha, G., Poshyachinda, S. & Reichart, D. E., 2015, *ApJ*, **805**, 77

Meng, H. Y. A., Su, K. Y. L., Rieke, G. H., Stevenson, D. J., Plavchan, P., Rujopakarn, W., Lisse, C. M., Poshyachinda, S. & Reichart, D. E., 2014, *Science*, **345**, 1032

Meng, X., Chen, X. & Han, Z., 2008, *A&A*, **487**(2), 625

Metzger, B. D., Rafikov, R. R. & Bochkarev, K. V., 2012, *MNRAS*, **423**, 505

Mighell, K. J., Glaccum, W. & Hoffmann, W., 2008, in *Space Telescopes and Instrumentation 2008: Optical, Infrared, and Millimeter*, volume 7010 of *Proceedings of the SPIE*, p. 70102W

Migliorini, A., Piccioni, G., Capaccioni, F., Filacchione, G., Bockelée-Morvan, D., Erard, S., Leyrat, C., Combi, M. R., Fougere, N., Crovisier, J., Taylor, F. W., De Sanctis, M. C., Capria, M. T., Grassi, D., Rinaldi, G., Tozzi, G. P. & Fink, U., 2016, *A&A*, **589**, A45

Miura, R. E., Kohno, K., Tosaki, T., Espada, D., Hwang, N., Kuno, N., Okumura, S. K., Hirota, A., Muraoka, K., Onodera, S., Minamidani, T., Komugi, S., Nakanishi, K., Sawada, T., Kaneko, H. & Kawabe, R., 2012, *ApJ*, **761**(1), 37

Miyamoto, Y., Fushitani, M., Ando, D. & Momose, T., 2008, *The Journal of Chemical Physics*, **128**(11), 114502
URL: *https://doi.org/10.1063/1.2889002*

Morbidelli, A., Levison, H. F., Tsiganis, K. & Gomes, R., 2005, *Nature*, **435**(7041), 462

Morgenthaler, J. P., Harris, W. M., Combi, M. R., Feldman, P. D. & Weaver, H. A., 2009, in *AAS/Division for Planetary Sciences Meeting Abstracts #41*, volume 41 of *AAS/Division for Planetary Sciences Meeting Abstracts*, p. 15.11

Mousis, O., Ronnet, T., Brugger, B., Ozgurel, O., Pauzat, F., Ellinger, Y., Maggiolo, R., Wurz, P., Vernazza, P. & Lunine, J. I., 2016, *ApJL*, **823**(2), L41

Mueller, B. E. A. & Bues, I., 1987, *Mitteilungen der Astronomischen Gesellschaft Hamburg*, **70**, 345

Mullally, F., Kilic, M., Reach, W. T., Kuchner, M. J., von Hippel, T., Burrows, A. & Winget, D. E., 2007, *ApJSS*, **171**, 206

Müller, H. S. P., Endres, C. P., Stutzki, J. & Schlemmer, S., 2013, in J. D. Gillaspy, W. L. Wiese & Y. A. Podpaly (eds.), *American Institute of Physics Conference Series*, volume 1545 of *American Institute of Physics Conference Series*, pp. 96–109

Mumma, M. J., 1982, in M. J. Mumma, K. Fox & J. Hornstein (eds.), *Vibrational-Rotational Spectry. for Planetary Atmospheres, Vol. 2*, volume 2 of *Vibrational-Rotational Spectroscopy for Planetary Atmospheres, Volume 1*, pp. 1–10

Mumma, M. J., Blass, W. E., Weaver, H. A. & Larson, H. P., 1988, in *BAAS*, volume 20 of *BAAS*, p. 826

Mumma, M. J., Bonev, B. P., Villanueva, G. L., Paganini, L., DiSanti, M. A., Gibb, E. L., Keane, J. V., Meech, K. J., Blake, G. A., Ellis, R. S., Lippi, M., Boehnhardt, H. & Magee-Sauer, K., 2011, *ApJL*, **734**, L7

Mumma, M. J. & Charnley, S. B., 2011, *Ann. Rev. Astr. Astrophys.*, **49**, 471

Mumma, M. J., DiSanti, M. A., Dello Russo, N., Magee-Sauer, K., Gibb, E. & Novak, R., 2003, *Advances in Space Research*, **31**, 2563

Mumma, M. J., McLean, I. S., DiSanti, M. A., Larkin, J. E., Dello Russo, N., Magee-Sauer, K., Becklin, E. E., Bida, T., Chaffee, F., Conrad, A. R., Figer, D. F., Gilbert, A. M., Graham, J. R., Levenson, N. A., Novak, R. E., Reuter, D. C., Teplitz, H. I., Wilcox, M. K. & Xu, L.-H., 2001, *ApJ*, **546**, 1183

Mumma, M. J., Weaver, H. A. & Larson, H. P., 1987, *A&A*, **187**, 419

Mumma, M. J., Weissman, P. R. & Stern, S. A., 1993, in E. H. Levy & J. I. Lunine (eds.), *Protostars and Planets III*, pp. 1177–1252

Mustill, A. J., Veras, D. & Villaver, E., 2014, *MNRAS*, **437**, 1404

Mustill, A. J. & Villaver, E., 2012, *ApJ*, **761**(2), 121

Mustill, A. J., Villaver, E., Veras, D., Gänsicke, B. T. & Bonsor, A., 2017, *ArXiv e-prints*

Napiwotzki, R., Christlieb, N., Drechsel, H., Hagen, H.-J., Heber, U., Homeier, D., Karl, C., Koester, D., Leibundgut, B., Marsh, T. R., Moehler, S., Nelemans, G., Pauli, E.-M., Reimers, D., Renzini, A. & Yungelson, L., 2003, *The Messenger*, **112**, 25

Nauenberg, M., 1972, *ApJ*, **175**, 417

Nelemans, G. & Tauris, T. M., 1998, *A&A*, **335**, L85

Neufeld, D. A., Snell, R. L., Ashby, M. L. N., Bergin, E. A., Chin, G., Erickson, N. R., Goldsmith, P. F., Harwit, M., Howe, J. E., Kleiner, S. C., Koch, D. G., Patten, B. M., Plume, R., Schieder, R., Stauffer, J. R., Tolls, V., Wang, Z., Winnewisser, G., Zhang, Y. F. & Melnick, G. J., 2000, *ApJL*, **539**, L107

Newburn, R. L. & Spinrad, H., 1984, *AJ*, **89**, 289

Newburn, R. L. & Spinrad, H., 1989, *AJ*, **97**, 552

Nordhaus, J. & Spiegel, D. S., 2013, *MNRAS*, **432**(1), 500

Ootsubo, T., Kawakita, H., Hamada, S., Kobayashi, H., Yamaguchi, M., Usui, F., Nakagawa, T., Ueno, M., Ishiguro, M., Sekiguchi, T., Watanabe, J.-i., Sakon, I., Shimonishi, T. & Onaka, T., 2012, *ApJ*, **752**, 15

Owen, T., 1973, *ApJ*, **184**, 33

Paganini, L., DiSanti, M. A., Mumma, M. J., Villanueva, G. L., Bonev, B. P., Keane, J. V., Gibb, E. L., Boehnhardt, H. & Meech, K. J., 2014, *AJ*, **147**(1), 15

Paganini, L., Mumma, M. J., Boehnhardt, H., DiSanti, M. A., Villanueva, G. L., Bonev, B. P., Lippi, M., Käufl, H. U. & Blake, G. A., 2013, *ApJ*, **766**, 100

Paganini, L., Mumma, M. J., Bonev, B. P., Villanueva, G. L., DiSanti, M. A., Keane, J. V. & Meech, K. J., 2012*a*, *Icarus*, **218**, 644

Paganini, L., Mumma, M. J., Villanueva, G. L., DiSanti, M. A. & Bonev, B. P., 2015, *ApJ*, **808**, 1

Paganini, L., Mumma, M. J., Villanueva, G. L., DiSanti, M. A., Bonev, B. P., Lippi, M. & Boehnhardt, H., 2012*b*, *ApJL*, **748**, L13

Patel, R. I., Metchev, S. A. & Heinze, A., 2014, *ApJSS*, **212**, 10

Patel, R. I., Metchev, S. A., Heinze, A. & Trollo, J., 2017, *AJ*, **153**, 54

Patten, B. M., Stauffer, J. R., Burrows, A., Marengo, M., Hora, J. L., Luhman, K. L., Sonnett, S. M., Henry, T. J., Raghavan, D., Megeath, S. T., Liebert, J. & Fazio, G. G., 2006, *ApJ*, **651**, 502

Payne, M. J., Veras, D., Gänsicke, B. T. & Holman, M. J., 2017, *MNRAS*, **464**(3), 2557

Payne, M. J., Veras, D., Holman, M. J. & Gänsicke, B. T., 2016, *MNRAS*, **457**(1), 217

Pérez, C., Muckle, M. T., Zaleski, D. P., Seifert, N. A., Temelso, B., Shields, G. C., Kisiel, Z. & Pate, B. H., 2012, *Science*, **336**(6083), 897
URL: *http://science.sciencemag.org/content/336/6083/897*

Petrenko, V. & Whitworth, R., 1999, *Physics of Ice* (OUP Oxford)
URL: *https://books.google.co.uk/books?id=oC941a8lXWIC*

Petrovich, C. & Muñoz, D. J., 2017, *ApJ*, **834**, 116

Pickett, H. M., Poynter, R. L., Cohen, E. A., Delitsky, M. L., Pearson, J. C. & Müller, H. S. P., 1998, *Journal of Quantitative Spectroscopy & Radiative Transfer*, **60**, 883

Pilbratt, G. L., Riedinger, J. R., Passvogel, T., Crone, G., Doyle, D., Gageur, U., Heras, A. M., Jewell, C., Metcalfe, L., Ott, S. & Schmidt, M., 2010, *A&A*, **518**, L1

Probst, R. G., 1981, *Infrared Detection of Very Low Mass Stars.*, Ph.D. thesis, UNIVERSITY OF VIRGINIA.

Probst, R. G., 1983, *ApJSS*, **53**, 335

Protopapa, S., Sunshine, J. M., Feaga, L. M., Kelley, M. S. P., A'Hearn, M. F., Farnham, T. L., Groussin, O., Besse, S., Merlin, F. & Li, J.-Y., 2014, *Icarus*, **238**, 191

Provencal, J. L., Shipman, H. L., Koester, D., Wesemael, F. & Bergeron, P., 2002, *ApJ*, **568**(1), 324

Radeva, Y. L., Mumma, M. J., Bonev, B. P., DiSanti, M. A., Villanueva, G. L., Magee-Sauer, K., Gibb, E. L. & Weaver, H. A., 2010, *Icarus*, **206**(2), 764

Radeva, Y. L., Mumma, M. J., Villanueva, G. L., Bonev, B. P., DiSanti, M. A., A'Hearn, M. F. & Dello Russo, N., 2013, *Icarus*, **223**, 298

Rafikov, R. R., 2011*a*, *ApJL*, **732**, L3

Rafikov, R. R., 2011*b*, *MNRAS*, **416**, L55

Raponi, A., Ciarniello, M., Capaccioni, F., Filacchione, G., Tosi, F., De Sanctis, M. C., Capria, M. T., Barucci, M. A., Longobardo, A. & Palomba, E., 2016, *MNRAS*, **462**, S476

Rappaport, S., Gary, B. L., Kaye, T., Vanderburg, A., Croll, B., Benni, P. & Foote, J., 2016, *MNRAS*, **458**, 3904

Rawlings, J. M. C., Hartquist, T. W., Menten, K. M. & Williams, D. A., 1992, *MNRAS*, **255**, 471

Reach, W. T., Kuchner, M. J., von Hippel, T., Burrows, A., Mullally, F., Kilic, M. & Winget, D. E., 2005, *ApJL*, **635**, L161

Reach, W. T., Lisse, C., von Hippel, T. & Mullally, F., 2009, *ApJ*, **693**, 697

Rebull, L. M., Cody, A. M., Covey, K. R., Günther, H. M., Hillenbrand, L. A., Plavchan, P., Poppenhaeger, K., Stauffer, J. R., Wolk, S. J., Gutermuth, R., Morales-Calderón, M., Song, I., Barrado, D., Bayo, A., James, D., Hora, J. L., Vrba, F. J., Alves de Oliveira, C., Bouvier, J., Carey, S. J., Carpenter, J. M., Favata, F., Flaherty, K., Forbrich, J., Hernandez, J., McCaughrean, M. J., Megeath, S. T., Micela, G., Smith, H. A., Terebey, S., Turner, N., Allen, L., Ardila, D., Bouy, H. & Guieu, S., 2014, *AJ*, **148**, 92

Redfield, S., Farihi, J., Cauley, P. W., Parsons, S. G., Gänsicke, B. T. & Duvvuri, G. M., 2017, *ApJ*, **839**, 42

Reinhard, R., 1986, *Nature*, **321**, 313

Rocchetto, M., Farihi, J., Gänsicke, B. T. & Bergfors, C., 2015, *MNRAS*, **449**, 574

Rodgers, S. D., Charnley, S. B., Huebner, W. F. & Boice, D. C., 2004, *Physical processes and chemical reactions in cometary comae* (University of Arizona Press), chapter 5, pp. 505–522

Roettger, E. E., Feldman, P. D., A'Hearn, M. F. & Festou, M. C., 1990, *Icarus*, **86**, 100

Rotundi, A., Sierks, H., Della Corte, V., Fulle, M., Gutierrez, P. J., Lara, L., Barbieri, C., Lamy, P. L., Rodrigo, R. & Koschny, D., 2015, *Science*, **347**(6220), aaa3905

Rubin, M., Altwegg, K., Balsiger, H., Bar-Nun, A., Berthelier, J.-J., Bieler, A., Bochsler, P., Briois, C., Calmonte, U., Combi, M., De Keyser, J., Dhooghe, F., Eberhardt, P., Fiethe, B., Fuselier, S. A., Gasc, S., Gombosi, T. I., Hansen, K. C., Hässig, M., Jäckel, A., Kopp, E., Korth, A., Le Roy, L., Mall, U., Marty, B., Mousis, O., Owen, T., Rème, H., Sémon, T., Tzou, C.-Y., Waite, J. H. & Wurz, P., 2015*a*, *Science*, **348**, 232

Rubin, M., Altwegg, K., Balsiger, H., Bar-Nun, A., Berthelier, J.-J., Briois, C., Calmonte, U., Combi, M., De Keyser, J., Fiethe, B., Fuselier, S. A., Gasc, S., Gombosi, T. I., Hansen, K. C., Kopp, E., Korth, A., Laufer, D., Le Roy, L., Mall, U., Marty, B., Mousis, O., Owen, T., Rème, H., Sémon, T., Tzou, C.-Y., Waite, J. H. & Wurz, P., 2018, *Science Advances*, **4**, eaar6297

Rubin, M., Altwegg, K., van Dishoeck, E. F. & Schwehm, G., 2015*b*, *ApJL*, **815**(1), L11

Sackmann, I. J., Boothroyd, A. I. & Kraemer, K. E., 1993, *ApJ*, **418**, 457

Salinas, V. N., Hogerheijde, M. R., Bergin, E. A., Cleeves, L. I., Brinch, C., Blake, G. A., Lis, D. C., Melnick, G. J., Panić, O., Pearson, J. C., Kristensen, L., Yıldız, U. A. & van Dishoeck, E. F., 2016, *A&A*, **591**, A122

Schleicher, D. & Bair, A., 2014, in K. Muinonen, A. Penttilä, M. Granvik, A. Virkki, G. Fedorets, O. Wilkman & T. Kohout (eds.), *Asteroids, Comets, Meteors 2014*, p. 1

Schleicher, D. G. & Bair, A. N., 2011, *AJ*, **141**, 177

Schultz, G., Zuckerman, B. & Becklin, E. E., 1996, *ApJ*, **460**, 402

Schulz, R., Owens, A., Rodriguez-Pascual, P. M., Lumb, D., Erd, C. & Stüwe, J. A., 2006, *A&A*, **448**, L53

Shinnaka, Y., Kawakita, H., Jehin, E., Decock, A., Hutsemkers, D. & Manfroid, J., 2016, *MNRAS*, **462**(Suppl 1), S124
URL: *http://mnras.oxfordjournals.org/content/462/Suppl_1/S124.abstract*

Shinnaka, Y., Kawakita, H., Kobayashi, H., Jehin, E., Manfroid, J., Hutsemékers, D. & Arpigny, C., 2011, *ApJ*, **729**, 81

Sierks, H., Barbieri, C., Lamy, P. L., Rodrigo, R., Koschny, D., Rickman, H., Keller, H. U., Agarwal, J., A'Hearn, M. F. & Angrilli, F., 2015, *Science*, **347**(6220), aaa1044

Silvotti, R., Pavlov, M., Fontaine, G., Marsh, T. & Dhillon, V., 2006, *Memorie della Societa Astronomica Italiana*, **77**, 486

Sion, E. M., Greenstein, J. L., Landstreet, J. D., Liebert, J., Shipman, H. L. & Wegner, G. A., 1983, *ApJ*, **269**, 253

Sliter, R., Gish, M. & Vilesov, A. F., 2011, *The Journal of Physical Chemistry A*, **115**(34), 9682, PMID: 21671631
URL: *https://doi.org/10.1021/jp201125k*

Smallwood, J. L., Martin, R. G., Livio, M. & Lubow, S. H., 2018, *MNRAS*, **480**, 57

Snodgrass, C., A'Hearn, M. F., Aceituno, F., Afanasiev, V., Bagnulo, S., Bauer, J., Bergond, G., Besse, S., Biver, N. & Bodewits, D., 2017, *Philosophical Transactions of the Royal Society of London Series A*, **375**(2097), 20160249

Spitzer, L., 1978, *Physical processes in the interstellar medium* (Wiley)

Stawikowski, A. & Greenstein, J. L., 1964, *ApJ*, **140**, 1280

Steele, P. R., Burleigh, M. R., Farihi, J., Gänsicke, B. T., Jameson, R. F., Dobbie, P. D. & Barstow, M. A., 2009, *A&A*, **500**(3), 1207

Stephan, A. P., Naoz, S. & Zuckerman, B., 2017, *ApJL*, **844**, L16

Stetson, P. B., 1996, *PASP*, **108**, 851

Subasavage, J. P., Henry, T. J., Jao, W.-C., Nelan, E. P., Harris, H. C. & Dahn, C. C., 2009, in *Journal of Physics Conference Series*, volume 172 of *Journal of Physics Conference Series*, p. 012017

Sun, Z.-D., Takagi, K. & Matsushima, F., 2005, *Science*, **310**(5756), 1938
URL: *http://science.sciencemag.org/content/310/5756/1938*

Swan, A., Farihi, J. & Wilson, T. G., 2019, *MNRAS*

Swinyard, B. M., Polehampton, E. T., Hopwood, R., Valtchanov, I., Lu, N., Fulton, T., Benielli, D., Imhof, P., Marchili, N., Baluteau, J.-P., Bendo, G. J., Ferlet, M., Griffin, M. J., Lim, T. L., Makiwa, G., Naylor, D. A., Orton, G. S., Papageorgiou, A., Pearson, C. P., Schulz, B., Sidher, S. D., Spencer, L. D., van der Wiel, M. H. D. & Wu, R., 2014, *MNRAS*, **440**, 3658

Szutowicz, S., Biver, N., Bockelee-Morvan, D., Crovisier, J., Moreno, R., de Val-Borro, M., Hartogh, P., Rengel, M., Lis, D. C., Küppers, M., Bergin, E. A., Blake, G. A., Vandenbussche, B. & Swinyard, B., 2011, in *EPSC-DPS Joint Meeting 2011*, p. 1213

Tappert, C., Gänsicke, B. T., Schmidtobreick, L. & Ribeiro, T., 2011, *A&A*, **532**, A129

Taquet, V., Furuya, K., Walsh, C. & van Dishoeck, E. F., 2016, *MNRAS*, **462**, S99

Taylor, M. G. G. T., Altobelli, N., Buratti, B. J. & Choukroun, M., 2017, *Philosophical Transactions of the Royal Society of London Series A*, **375**(2097), 20160262

Teachey, A. & Kipping, D. M., 2018, *Science Advances*, **4**(10), eaav1784

Tenishev, V., Combi, M. R. & Rubin, M., 2011, *ApJ*, **732**, 104

Tennyson, J., Zobov, N. F., Williamson, R., Polyansky, O. L. & Bernath, P. F., 2001, *Journal of Physical and Chemical Reference Data*, **30**(3), 735
URL: *https://doi.org/10.1063/1.1364517*

Thomas, N., Sierks, H., Barbieri, C., Lamy, P. L., Rodrigo, R., Rickman, H., Koschny, D., Keller, H. U., Agarwal, J. & A'Hearn, M. F., 2015, *Science*, **347**(6220), aaa0440

Tozzi, G. P., Feldman, P. D. & Festou, M. C., 1998, *A&A*, **330**, 753

Tremblay, P. E., Gentile-Fusillo, N., Raddi, R., Jordan, S., Besson, C., Gänsicke, B. T., Parsons, S. G., Koester, D., Marsh, T. & Bohlin, R., 2017, *MNRAS*, **465**(3), 2849

Tsiganis, K., Gomes, R., Morbidelli, A. & Levison, H. F., 2005, *Nature*, **435**(7041), 459

Tucker, M. A., Fleming, S. W., Pelisoli, I., Romero, A., Bell, K. J., Kepler, S. O., Caton, D. B., Debes, J., Montgomery, M. H., Thompson, S. E., Koester, D., Million, C. & Shiao, B., 2018, *MNRAS*, **475**, 4768

Tudorie, M., Cacciani, P., Cosléou, J., Herlemont, F., Khelkhal, M., Puzzarini, C., Maret, S. & Kahane, C., 2006, *A&A*, **453**, 755

van Maanen, A., 1917, *PASP*, **29**, 258

Vanderbosch, Z., Hermes, J. J., Dennihy, E., Dunlap, B. H., Izquierdo, P., Tremblay, P. E., Cho, P. B., Gaensicke, B. T., Bell, K. J., Montgomery, M. H. & Winget, D. E., 2019, *arXiv e-prints*, arXiv:1908.09839

Vanderburg, A., Johnson, J. A., Rappaport, S., Bieryla, A., Irwin, J., Lewis, J. A., Kipping, D., Brown, W. R., Dufour, P., Ciardi, D. R., Angus, R., Schaefer, L., Latham, D. W., Charbonneau, D., Beichman, C., Eastman, J., McCrady, N., Wittenmyer, R. A. & Wright, J. T., 2015, *Nature*, **526**, 546

Vassiliadis, E. & Wood, P. R., 1993, *ApJ*, **413**, 641

Vauclair, G., Dolez, N., Fu, J.-N., Homeier, D., Roques, S., Chevreton, M. & Koester, D., 2000, *A&A*, **355**, 291

Veras, D., Leinhardt, Z. M., Bonsor, A. & Gänsicke, B. T., 2014, *MNRAS*, **445**, 2244

Veras, D., Leinhardt, Z. M., Eggl, S. & Gänsicke, B. T., 2015, *MNRAS*, **451**, 3453

Veras, D., Mustill, A. J., Bonsor, A. & Wyatt, M. C., 2013, *MNRAS*, **431**, 1686

Veras, D., Xu, S. & Rebassa-Mansergas, A., 2018, *MNRAS*, **473**, 2871

Villanueva, G. L., Mumma, M. J., Bonev, B. P., Di Santi, M. A., Gibb, E. L., Böhnhardt, H. & Lippi, M., 2009, *ApJL*, **690**, L5

Villanueva, G. L., Mumma, M. J., DiSanti, M. A., Bonev, B. P., Gibb, E. L., Magee-Sauer, K., Blake, G. A. & Salyk, C., 2011, *Icarus*, **216**(1), 227

Villanueva, G. L., Mumma, M. J., DiSanti, M. A., Bonev, B. P., Paganini, L. & Blake, G. A., 2012, *Icarus*, **220**, 291

von Hippel, T., Kuchner, M. J., Kilic, M., Mullally, F. & Reach, W. T., 2007, *ApJ*, **662**, 544

Wachter, S., Hoard, D. W., Hansen, K. H., Wilcox, R. E., Taylor, H. M. & Finkelstein, S. L., 2003, *ApJ*, **586**, 1356

Walsh, K. J., Morbidelli, A., Raymond, S. N., O'Brien, D. P. & Mandell, A. M., 2011, *Nature*, **475**(7355), 206

Weaver, H. A., 1998, in J. C. Brandt, T. B. Ake & C. C. Petersen (eds.), *The Scientific Impact of the Goddard High Resolution Spectrograph*, volume 143 of *Astronomical Society of the Pacific Conference Series*, p. 213

Weaver, H. A., A'Hearn, M. F., Arpigny, C., Combi, M. R., Feldman, P. D., Tozzi, G.-P., Dello Russo, N. & Festou, M. C., 2008, in *Asteroids, Comets, Meteors 2008*, volume 1405 of *LPI Contributions*, p. 8216

Weaver, H. A., Feldman, P. D., A'Hearn, M. F., Dello Russo, N. & Stern, S. A., 2011, *ApJL*, **734**, L5

Weaver, H. A., Feldman, P. D., McPhate, J. B., A'Hearn, M. F., Arpigny, C. & Smith, T. E., 1994, *ApJ*, **422**, 374

Weaver, H. A. & Mumma, M. J., 1984, *ApJ*, **276**, 782

Werner, M. W., Roellig, T. L., Low, F. J., Rieke, G. H., Rieke, M., Hoffmann, W. F., Young, E., Houck, J. R., Brandl, B., Fazio, G. G., Hora, J. L., Gehrz, R. D., Helou, G., Soifer, B. T., Stauffer, J., Keene, J., Eisenhardt, P., Gallagher, D., Gautier, T. N., Irace, W., Lawrence, C. R., Simmons, L., Van Cleve, J. E., Jura, M., Wright, E. L. & Cruikshank, D. P., 2004, *ApJSS*, **154**, 1

Whipple, F. L., 1950, *ApJ*, **111**, 375

Willacy, K., Alexander, C., Ali-Dib, M., Ceccarelli, C., Charnley, S. B., Doronin, M., Ellinger, Y., Gast, P., Gibb, E., Milam, S. N., Mousis, O., Pauzat, F., Tornow, C., Wirström, E. S. & Zicler, E., 2015, *Space Science Reviews*, **197**, 151

Wilson, D. J., Gänsicke, B. T., Farihi, J. & Koester, D., 2016, *MNRAS*, **459**, 3282

Wilson, D. J., Gänsicke, B. T., Koester, D., Raddi, R., Breedt, E., Southworth, J. & Parsons, S. G., 2014, *MNRAS*, **445**, 1878

Wilson, D. J., Gänsicke, B. T., Koester, D., Toloza, O., Pala, A. F., Breedt, E. & Parsons, S. G., 2015, *MNRAS*, **451**(3), 3237

Wirström, E. S., Charnley, S. B., Cordiner, M. A. & Ceccarelli, C., 2016, *ApJ*, **830**(2), 102

Wolszczan, A. & Frail, D. A., 1992, *Nature*, **355**(6356), 145

Wooden, D. H., Ishii, H. A. & Zolensky, M. E., 2017, *Philosophical Transactions of the Royal Society of London Series A*, **375**, 20160260

Woodward, C. E., Kelley, M. S., Bockelée-Morvan, D. & Gehrz, R. D., 2007, *ApJ*, **671**(1), 1065

Wright, E. L., Eisenhardt, P. R. M., Mainzer, A. K., Ressler, M. E., Cutri, R. M., Jarrett, T., Kirkpatrick, J. D., Padgett, D., McMillan, R. S., Skrutskie, M., Stanford, S. A., Cohen, M., Walker, R. G., Mather, J. C., Leisawitz, D., Gautier, III, T. N., McLean, I., Benford, D., Lonsdale, C. J., Blain, A., Mendez, B., Irace, W. R., Duval, V.,

Liu, F., Royer, D., Heinrichsen, I., Howard, J., Shannon, M., Kendall, M., Walsh, A. L., Larsen, M., Cardon, J. G., Schick, S., Schwalm, M., Abid, M., Fabinsky, B., Naes, L. & Tsai, C.-W., 2010, *AJ*, **140**, 1868

Wyatt, M. C., 2008, *Ann. Rev. Astr. Astrophys.*, **46**, 339

Wyatt, M. C., Booth, M., Payne, M. J. & Churcher, L. J., 2010, *MNRAS*, **402**(1), 657

Wyatt, M. C., Farihi, J., Pringle, J. E. & Bonsor, A., 2014, *MNRAS*, **439**, 3371

Xie, X. & Mumma, M. J., 1992, *ApJ*, **386**, 720

Xu, S., Hallakoun, N., Gary, B., Dalba, P. A., Debes, J., Dufour, P., Fortin-Archambault, M., Fukui, A., Jura, M. A. & Klein, B., 2019, *arXiv e-prints*, arXiv:1904.10896

Xu, S. & Jura, M., 2012, *ApJ*, **745**, 88

Xu, S. & Jura, M., 2014, *ApJ*, **792**(2), L39

Xu, S., Jura, M., Dufour, P. & Zuckerman, B., 2016, *ApJ*, **816**, L22

Xu, S., Jura, M., Klein, B., Koester, D. & Zuckerman, B., 2013, *ApJ*, **766**(2), 132

Xu, S., Jura, M., Koester, D., Klein, B. & Zuckerman, B., 2014, *ApJ*, **783**, 79

Xu, S., Su, K. Y. L., Rogers, L. K., Bonsor, A., Olofsson, J., Veras, D., van Lieshout, R., Dufour, P., Green, E. M., Schlawin, E., Farihi, J., Wilson, T. G., Wilson, D. J. & Gänsicke, B. T., 2018, *ApJ*, **866**, 108

Xu, S., Zuckerman, B., Dufour, P., Young, E. D., Klein, B. & Jura, M., 2017, *ApJL*, **836**, L7

Yamamoto, S., 2017, *Chemistry of Diffuse Clouds* (Springer Japan, Tokyo), chapter 4, pp. 65–90
URL: *https://doi.org/10.1007/978-4-431-54171-4-4*

Yamamoto, T., 1982, *A&A*, **109**, 326

Zakharov, V., Bockelée-Morvan, D., Biver, N., Crovisier, J. & Lecacheux, A., 2007, *A&A*, **473**, 303

Ziurys, L. M., Savage, C., Brewster, M. A., Apponi, A. J., Pesch, T. C. & Wyckoff, S., 1999, *ApJL*, **527**, L67

Zuckerman, B., 2014, *ApJL*, **791**, L27

Zuckerman, B. & Becklin, E. E., 1987, *Nature*, **330**, 138

Zuckerman, B. & Becklin, E. E., 1992, *ApJ*, **386**, 260

Zuckerman, B., Koester, D., Dufour, P., Melis, C., Klein, B. & Jura, M., 2011, *ApJ*, **739**(2), 101

Zuckerman, B., Koester, D., Melis, C., Hansen, B. M. & Jura, M., 2007, *ApJ*, **671**(1), 872

Zuckerman, B., Koester, D., Reid, I. N. & Hünsch, M., 2003, *ApJ*, **596**, 477

Zuckerman, B., Melis, C., Klein, B., Koester, D. & Jura, M., 2010, *ApJ*, **722**, 725

This is the end.

James Douglas "Jim" Morrison